The Hong Kong Polytechnic University
Department of Electronic & Information Engineering

Investigation of Spurious Waves in Thin-film Bulk Acoustic Wave Resonators

YANG Wenxia

A thesis submitted in partial fulfilment of the requirements
for the degree of Doctor of Philosophy

March 2013

CERTIFICATE OF ORIGINALITY

I hereby declare that this thesis is my own work and that, to the best of my knowledge and belief, it reproduces no material previously published or written, nor material that has been accepted for the award of any other degree or diploma, except where due acknowledgement has been made in the text.

_______________________________ (Signed)

YANG Wenxia _____________________ (Name of Student)

Abstract

With the development of the wireless communication systems, the frequency spectrum crowding increases constantly. This trend strengthens the need for high performance frequency control components steadily. Film bulk acoustic resonator (FBAR) has been widely used in the frequency control components because of its small size, low insertion loss, high quality factor and its capability of being integrated with other components on silicon substrate. However, FBARs are suffering from the laterally propagating spurious waves. These spurious waves degrade the performance of filters composed of FBARs by increasing the insertion loss, introducing ripples in their passband and narrowing the bandwidth. The goal of this study is to propose an efficient method to model the FBAR structure, aiming to investigate the lateral spurious modes generation and improve the quality factor of FBAR.

A two-dimensional finite-difference time-domain (FDTD) algorithm is proposed to model the FBAR resonators. The partial derivatives of the equations of motion and the quasi-static Maxwell's equations are discretized to centered finite differences. The free surface boundary condition is applied to the interface between the medium and air. At the interface between different materials, the material properties are averaged to ensure the stability under Courant condition. The two-dimensional fast Fourier transform (2D FFT) method is applied to extract the dispersion characteristic of the Rayleigh-Lamb modes propagating in the FBAR resonator. The proposed algorithm is validated by comparing the obtained dispersion curve with the one obtained by the effective acoustic impedance.

Wave scattering analysis for multimode excitation is developed to investigate the lateral boundaries of FBAR resonators. To validate the proposed scheme, the reflection of simultaneously excited antisymmetric Lamb wave modes at the free edge of a steel plate is simulated using the FDTD method. By using the mode power coefficients, the power of the Lamb modes is determined from the displacements on the surface of the plate. The mode conversion coefficients obtained are in good agreement with the one calculated by taking multiple measurements with single Lamb wave mode excitation

using the finite element method (FEM). The proposed scheme is then applied to investigate two generic free-standing bulk acoustic resonator (FBAR) structures. The scattering coefficients of these two FBAR structures are calculated and analyzed.

Based on the scattering analysis of the two generic FBAR structures, a new structure of FBAR resonator with frame-like airgap on bottom electrode is proposed to suppress the spurious modes and improve the quality factor. Time domain and frequency domain analysis are conducted to investigate the spurious waves in the proposed structure. From both time domain and frequency domain results, it is observed that with an airgap on the bottom electrode the excitation of the spurious waves in the active region is suppressed, and the energy leaked into the passive region is reduced as well.

The overall results of this work indicate that the FDTD scheme is an appropriate approach for modeling FBAR resonators, and the scattering analysis for multimode excitation provides a simple way to design the lateral boundaries of FBARs.

Acknowledgments

I would like to take this opportunity to express my warmest gratitude to my supervisor Dr. Wai Yip Tam. Thanks him for offering me the opportunity to study in the wonderful city Hong Kong. He introduced me into the scientific world, and encouraged me to participate in the conferences. During my study, Dr. Tam gave me suggestions whenever I encountered problems and enabled me to write scientific articles. Thanks him for his continuous patience, encouragement and guidance throughout my study period. Without his efforts, it was impossible for me to accomplish this dissertation.

I am grateful to Prof. Ken-ya Hashimoto. He kindly gave me the chance to study in the beautiful country of Japan, at Chiba University for several months. He taught me the effective acoustic impedance theory, gave me many invaluable suggestions, and inspired me in many ways. I benefited a lot from discussions with him.

I am grateful to Dr. Florian Thalmayr. It was my fortune to meet him at the 2010 IEEE international frequency control symposium. He gave me useful suggestions on my problems, shared his experience on numerical simulation, and shared his results with me as well. He encouraged me when I felt anxious.

I am grateful to Dr. Zheng Kuisong and Dr. King Yuen Wong for many helpful discussions about the finite-difference time-domain method. I wish to express gratitude to the members of the Electro-Communications Laboratory of Chiba University, especially Dr. Wang Hualei for his helpful discussions with me and encouragement. I also owe a lot of thanks to my friends, especially Miss Zhu Yaxuan, Dr. Sun Xiaocui, and Dr. Yeeyee Kong for their accompany and encouragement.

I am grateful to my dissertation committee members for the effort and advice in reviewing the dissertation.

Finally, my deepest thanks are due to my family. Although far away from home, their love and encouragement always accompany me. I furthermore want to express my gratitude to my beloved Zhou Songjian for his understanding, support and encouragement. His encouragement helped me to get through the tough times.

Contents

1 Introduction 19

1.1 Background and motivation 19

1.2 Outline of dissertation 24

2 Properties of BAW devices and design methods 26

2.1 Introduction 26

2.2 Thin-film Bulk Acoustic Wave Resonators 26

2.3 Resonator properties for filter applications 28

2.3.1 Band-pass filters based on resonators 28

2.3.2 Resonator figure of merit 30

2.4 Design methods for FBAR 35

2.4.1 Analytical method 35

2.4.2 Laser interferometry 41

2.4.3 Numerical method 42

2.4.4 Summary of the methods for FBAR design 43

3 Acoustic waves in solids and in FDTD model 47

3.1 Introduction 47

3.2 Governing equations 47

3.2.1 Governing equations for non-piezoelectric materials 47

3.2.2 Governing equations for piezoelectric materials 50

3.3 Elastic waves in two-dimensional model 53

3.3.1 Governing equations for piezoelectric material 53

3.3.2 Governing equations for metal 58

3.4 FDTD spatial and temporal discretizations 59

3.4.1 FDTD spatial discretization 60

3.4.2 FDTD temporal discretization 61

3.4.3 Governing equations of piezoelectric material in FDTD model 62

3.4.4 Governing equations of metal in FDTD model 63

3.5 Numerical analysis of the FDTD algorithm: dispersion and stability 64
    3.5.1 Numerical dispersion 64
    3.5.2 Numerical stability 65
3.6 Excitation source 65
    3.6.1 Gaussian pulse waveform 65
    3.6.2 Toneburst waveform 66
    3.6.3 Sinusoidal waveform 66
3.7 Boundary conditions 70
    3.7.1 Free surface boundary condition 70
    3.7.2 Interface boundary condition 73
3.8 2D-FFT method 75
3.9 Summary 79

4 Wave scattering analysis for multimode excitation 80
4.1 Introduction 80
    4.1.1 Nondestructive testing 80
    4.1.2 Wave scattering in FBAR 82
4.2 Methods for scattering analysis 85
    4.2.1 Torvik's method 85
    4.2.2 Time domain FEM simulation 87
    4.2.3 Frequency domain FEM simulation 89
4.3 Scattering analysis for multimode excitation 90
4.4 Validation of the scattering analysis for multimode excitation 94
4.5 Multimode wave scattering analysis in generic FBAR model 103
    4.5.1 Generic FBAR model with symmetric electrodes 103
    4.5.2 Generic FBAR model with asymmetric electrodes 114

5 FBAR with frame-like airgap on bottom electrode for suppression of spurious modes 128
5.1 Introduction 128
5.2 Time domain analysis for the proposed structure 129
    5.2.1 FBAR with different bottom electrode airgap width 133
    5.2.2 FBAR with different bottom electrode airgap depth 136
5.3 Frequency domain analysis for the proposed structure 140
    5.3.1 Power of the spurious modes for different airgap width 141
    5.3.2 Power of the spurious modes for different airgap depth 147
    5.3.3 Power of the spurious modes at different frequency 154

5.4 Discussion 162

6 Conclusion and outlook **163**

Bibliography **165**

List of Figures

1.1 Frequency allocation for different communication standards 20

1.2 Comparison the size of ceramic duplexer and FBAR duplexer (a) Ceramic duplexer, (b) FBAR duplexer 20

1.3 Configuration of film bulk acoustic resonator (a) Free-standing Bulk Acoustic Resonator (FBAR), (b) Solidly mounted resonator (SMR) 22

2.1 Comparison of two types of film bulk acoustic resonators (a) Free-standing Bulk Acoustic Resonator (FBAR), (b) Solidly mounted resonator (SMR) . . 27

2.2 Mechanical resonances in a plate of thickness d. The stress fields associated with the resonances are plotted. 27

2.3 Resonator geometry for illustrating the generation of plate waves. (a) Resonator having comparable lateral and thickness dimensions, (b) large lateral-to-thickness dimensions, (c) large lateral-to-thickness dimensions with extended plate over the active region of the resonator. 28

2.4 Schematic of filter topologies. (a) Ladder filter having series and parallel resonators. (b) Balanced lattice filter. (c) Stacked crystal filter (SCF). (d) Coupled resonator filter (CRF). 29

2.5 Admittance Y_s and Y_p of series and parallel resonators for ladder-type filter and scattering parameter $|S21|$ of the ladder-type filter. 30

2.6 Dispersion curve for the two types of FBAR resonators (a) type I dispersion (Al/ZnO/Al with thickness of $0.2\mu m/1.6\mu m/0.2\mu m$), (b) type II dispersion (Al/AlN/Al with thickness of $0.3\mu m/3\mu m/0.3\mu m$) 34

2.7 Mason model for acoustic plates: (a) piezoelectric plate, (b) pure mechanical plate. 36

2.8 Mason model for a multilayer resonator. The circuit is terminated on the left by a free surface (an acoustic short) and on the right by a semiinfinitely thick substrate. Each layer is represented by the corresponding transmission line sections with the piezoelectric layer having the electrical port associated with it. 36

2.9 Butterworth Van Dyke (BVD) model for resonators. 38

2.10 Modified Butterworth Van Dyke (mBVD) model for resonators. 39

2.11 mBVD model with additional motional branches to model some of the spurious modes. 39

2.12 A line source $T_0\delta(x_1)$ on top of a multilayer structure. 40

3.1 Traction forces acting on an infinitesimally small cube. 49

3.2 Two-dimensional schematic of a generic FBAR resonator. 53

3.3 Spatial layout of the variables in the FDTD model. 60

3.4 Gaussian pulse waveform with maximum frequency of 2GHz: (a) in the time domain, (b) in the frequency domain. 67

3.5 Toneburst waveform of five cycles at 1.315 GHz: (a) in the time domain, (b) in the frequency domain. 68

3.6 Sinusoidal waveform at 1.331 GHz: (a) in the time domain, (b) in the frequency domain. 69

3.7 FDTD grid with an extra row inserted on the top interface. 71

3.8 FDTD grid with an extra row inserted on the top interface and an extra column inserted on the left boundary. 72

3.9 Finite-difference grid at the interface between two materials. 74

3.10 2D FDTD model of FBAR resonator for dispersion analysis. 76

3.11 Dispersion curve for FBAR resonator passive region (AlN/Al with thickness of $3\mu m/0.6\mu m$: (a) obtained by 2D-FFT method, (b) obtained by the effective acoustic impedance (This graph is courtesy of F. Thalmayr, Sand 9, Inc..). 78

3.12 The proposed FDTD procedure for modeling the FBAR. 79

4.1 Schematic representation of nondestructive testing using bulk waves (a) pulse-echo mode, (b) pitch-catch mode, and (c) through-transmission mode. 81

4.2 Schematic representation of nondestructive testing using Lamb waves. . . . 82

4.3 Sketch of a thin film resonator with lateral free boundaries. 82

4.4 Dispersion curves of a FBAR with the combination of Al/AlN/Al (with thickness of $0.3\mu m/3\mu m/0.3\mu m$) (a) Active area, (b) Passive area, (c) Active area vs passive area for S_1 and pS_1 mode. 85

4.5 Lamb wave reflection at the plate free edge. 86

4.6 Schematic of different time steps in the time-domain FEM analysis for wave scattering (a) Lamb wave burst to excite the incident mode, (b) reflection of the incident mode at the right boundary, and (c) propagation of the reflected waves. 88

4.7 Schematic of the frequency-domain FEM setup for the analysis of wave scattering. 89

4.8 Schematic of the model setup for the analysis of multimode excitation wave scattering. 90

4.9 Spectrum of a typical Lamb wave measured by the transducer at P_2. Three Lamb modes are supported by the structure at the measuring frequency. . 93

4.10 Incident Lamb waves at $x_1 = 30$mm when the input A_0 and A_1 modes are excited at $x_1 = 0$. (a) Time history, (b) Wavenumber spectrum at frequency = 2.6 MHz. 96

4.11 Scattered Lamb waves at P_2. (a) Time history, (b) Frequency spectrum. . . 98

4.12 Amplitude of the conversion coefficients r_{nm} for A_0 and A_1 modes reflecting from the free edge. 99

4.13 Mode power coefficient c_n for A_0 and A_1 modes propagating in steel plate. . 101

4.14 Power scattering coefficients s_{nm} for A_0 and A_1 modes reflecting from the free edge. 101

4.15 Power scattering coefficients s_{nm} for mode A_0 reflecting from the free edge; ○ obtained by FDTD simulation, solid lines are obtained by FEM method[119]. 102

4.16 Schematic of a generic FBAR resonator with symmetric electrodes for Lamb wave scattering analysis. 104

4.17 Dispersion characteristics of FBAR resonator with symmetric electrodes. (a) Active region, (b) Passive region. 106

4.18 Incident Lamb waves at $x_1 = 50\mu$m when the input A_0 and A_1 modes are excited at $x_1 = 0$. (a) Time history, (b) Wavenumber spectrum at frequency = 1.315 GHz. 107

4.19 Scattered Lamb waves at P_2 for FBAR with symmetric electrodes. (a) Time history, (b) Frequency spectrum. 109

4.20 Mode power coefficient c_n for A_0 and A_1 modes propagating in active region for FBAR with symmetric electrodes. 110

4.21 The power scattering coefficients s^r_{nm} for A_0 and A_1 modes reflecting from the symmetric boundary at P_3. 110

4.22 Transmitted Lamb waves at P_4 for FBAR with symmetric electrodes. (a) Time history, (b) Frequency spectrum. 112

4.23 Mode power coefficient c_n for A_0 and A_1 modes propagating in passive region for FBAR with symmetric electrodes. 113

4.24 The power scattering coefficients s^t_{nm} for A_0 and A_1 modes transmitted into the passive region. 113

4.25 Schematic of a generic FBAR resonator with asymmetric electrodes for Lamb wave scattering analysis. 115

4.26 Dispersion characteristic of FBAR resonator with asymmetric electrodes in the passive region. 116

4.27 Incident Lamb waves at $x_1 = 50\mu$m when the input A_0 and A_1 modes are excited at $x_1 = 0$. (a) Time history, (b) Wavenumber spectrum at frequency = 1.315 GHz. 117

4.28 Scattered Lamb waves at P_2 for FBAR with asymmetric electrodes. (a) Time history, (b) Frequency spectrum. 119

4.29 Mode power coefficient c_n for A_0, A_1, S_0 and S_1 modes propagating active region for FBAR with asymmetric electrodes. 120

4.30 The power scattering coefficients s^{ra}_{mn} and s^{rs}_{mn} for A_0 and A_1 modes reflecting from the asymmetric boundary at P_3. 120

4.31 Transmitted Lamb waves at P_4 for FBAR with asymmetric electrodes. (a) Time history, (b) Frequency spectrum. 122

4.32 Mode power coefficient c_n for pA_0, pA_1 and pS_0 modes propagating in passive region for FBAR with asymmetric electrodes. 123

4.33 The power scattering coefficients s^{ta}_{mn} and s^{ts}_{mn} for A_0 and A_1 modes transmitted into the passive region. 123

5.1 The proposed FBAR resonator with frame-like airgap to suppress the spurious modes. 129

5.2 Observation displacement layers in the time domain analysis. 130

5.3 Displacement u_3 along the top observation layer for FBAR resonator with (w = 10 μm) and without (w = 0 μm) airgap on the bottom electrode (a) The whole structure, (b) The right passive region of the structure, (c) Active region. 132

5.4 Displacement u_3 along the bottom observation layer for FBAR resonator with (w = 10 μm) and without (w = 0 μm) airgap on the bottom electrode. 132

5.5 The FBAR resonator with airgap on the bottom electrode for time domain analysis on the effect of the airgap width. 133

5.6 Displacement u_3 along the top observation layer of the piezoelectric material for different airgap width (a) The whole structure, (b) The right passive region of the structure, (c) Active region. 135

5.7 Displacement u_3 along the top observation layer of the piezoelectric material for different airgap width. 135

5.8 Sum of the square of the displacement amplitude in the right passive region for different airgap width. 136

5.9 The FBAR resonator with airgap on the bottom electrode for time domain analysis on the effect of the airgap depth. 137

5.10 Displacement u_3 along the top observation layer of the piezoelectric material for different airgap depth (a) The whole structure, (b) The right passive region of the structure, (c) Active region. 139

5.11 Sum of the square of the displacement amplitude in the right passive region for different airgap depth. 139

5.12 Displacement u_3 along the top observation layer of the piezoelectric material for different airgap depth. 140

5.13 The FBAR resonator with airgap on the bottom electrode for frequency domain analysis on the effect of airgap width. 141

5.14 Power of Lamb modes in the active region at 1.33 GHz for different airgap width. 142

5.15 Power of Lamb modes in the active region at 1.3 GHz for different airgap width. 143

5.16 The total power of Lamb modes in the active region at 1.33 GHz for different airgap width. 143

5.17 The total power of Lamb modes in the active region at 1.3 GHz for different airgap width. 144

5.18 Power of Lamb modes in the passive region at 1.33 GHz for different airgap width. 145

5.19 The total leakage power of Lamb modes in the passive region at 1.33 GHz for different airgap width. 145

5.20 Power of Lamb modes in the passive region at 1.3 GHz for different airgap width. 146

5.21 The total leakage power of Lamb modes in the passive region at 1.3 GHz for different airgap width. 146

5.22 Amplitude of the longitudinal mode at 1.33 GHz for different airgap width. 147

5.23 The FBAR resonator with airgap on the bottom electrode for frequency domain analysis on the effect of the airgap depth. 148

5.24 Power of Lamb modes in the active region at 1.33 GHz for different airgap depth. 149

5.25 Power of Lamb modes in the active region at 1.3 GHz for different airgap depth. 149

5.26 The total power of Lamb modes in the active region at 1.33 GHz for different airgap depth. 150

5.27 The total power of Lamb modes in the active region at 1.3 GHz for different airgap depth. 150

5.28 Power of Lamb modes in the passive region at 1.33 GHz for different airgap depth. 151

5.29 The total leakage power of Lamb modes in the passive region at 1.33 GHz for different airgap depth. 152

5.30 Power of Lamb modes in the passive region at 1.3 GHz for different airgap depth. 152

5.31 The total leakage power of Lamb modes in the passive region at 1.3 GHz for different airgap depth. 153

5.32 Amplitude of the longitudinal mode at 1.33 GHz for different airgap depth. 154

5.33 Power of Lamb modes in the active region of FBAR resonator with and without airgap on the bottom electrode at different frequency (a) mode A_0, (b) mode A_1, (c) mode S_0, and (d) mode S_1. 156

5.34 Power of Lamb modes in the active region of FBAR resonator with an airgap (w = $3\mu m$, d = $0.5\mu m$) on the bottom electrode at different frequency. 157

5.35 Total power of Lamb modes in the active region of FBAR resonator with and without airgap on the bottom electrode. 157

5.36 Power of Lamb modes in the passive region of FBAR resonator with and without airgap on the bottom electrode at different frequency (a) mode pA_0, (b) mode pA_1, and (c) mode pS_0. 160

5.37 Power of Lamb modes in the passive region of FBAR resonator with an airgap (w = $3\mu m$, d = $0.5\mu m$) on the bottom electrode at different frequency. 160

5.38 Total leakage power of Lamb modes in the passive region of FBAR resonator with and without airgap on the bottom electrode. 161

5.39 Amplitude of the longitudinal mode for FBAR resonator with and without airgap on the bottom electrode at different frequency. 161

List of Tables

2.1 Summary of the advantages and disadvantages of the methods for FBAR design. 44

3.1 Elastic stiffness, mass density, permittivity and piezoelectric constants of AlN 54

3.2 Elastic stiffness, mass density, and permittivity of Al 59

3.3 Positions of the field components of the (i, j)-th cell in the finite-difference grid. 61

4.1 Energy difference between the incident modes and the reflected modes for the first set of data. 102

4.2 Energy difference between the incident modes and the reflected modes for the second set of data. 103

4.3 Power scattering coefficients of the reflected waves s^r_{mn} for FBAR with symmetric electrodes. 108

4.4 Power scattering coefficients of the transmitted waves s^t_{mn} for FBAR with symmetric electrodes. 111

4.5 Energy difference between the incident modes and the converted modes for the first set of data. 114

4.6 Energy difference between the incident modes and the converted modes for the second set of data. 114

4.7 Power scattering coefficients of the converted modes for FBAR with symmetric electrodes. 114

4.8 Power scattering coefficients of the reflected waves s^{ra}_{mn} and s^{rs}_{mn} for FBAR with asymmetric electrodes. 118

4.9 Power scattering coefficients of the transmitted waves s^{ta}_{mn} and s^{ts}_{mn} for FBAR with asymmetric electrodes. 121

4.10 Energy difference between the incident modes and the converted modes for the first set of data. 125

4.11 Energy difference between the incident modes and the converted modes for the second set of data. 126

4.12 Power scattering coefficients of the converted modes for FBAR with asymmetric electrodes. 127

List of Abbreviations

1D/2D/3D	One-dimensional/ Two-dimensional/ Three-dimensional
BAW	Bulk Acoustic wave
BFM	Brute-force method
BVD	Butterworth Van Dyke model
CMOS	Complementary metal-on-oxide semiconductor
CRF	Coupled resonator filter
DFT	Discrete Fourier transform
DOF	Degrees of freedom
ESD	Electro static discharge
FBAR	Film Bulk Acoustic Wave Resonator; the expression will be used to represent both designs of BAW devices, FBAR and SMR for the first three chapters and chapter 6 without explicit specification and it represents the free-standing bulk acoustic resonator in chapter 4 and 5
FD	Frequency Domain
FDTD	Finite-difference time-domain
FEM	Finite element method
FFT	Fast Fourier transform
FOM	Figure of merit
IDM	Injection damping mechanism
IDT	Interdigitated transducers
KLM	Krimholtz, Leedom, and Matthaei model
mBVD	Modified Butterworth Van Dyke model
MPC	Mode power coefficient
NDT	Nondestructive testing
PCS	Personal communications band (US mobile communication standard)
PDE	Partial-differential equations
PML	Perfectly matched layer

RF	Radio Frequency
RL	Rayleigh-Lamb
RX	Receive
SAW	Surface acoustic wave
SCF	Stacked crystal filter
SMR	Solidly mounted resonator
SV	Shear vertical
TCF	Temperature coefficient of frequency
TE	Thickness extensional
TX	Transmit
TD	Time domain
ZDR	Zero-drift resonator

Chapter 1

Introduction

1.1 Background and motivation

According to the propagation properties of electromagnetic waves in air, all mobile communication applications today are using frequencies between 400 MHz and 6 GHz, which is shown in Figure 1.1 [5]. The performance means that different applications require different insertion loss and steepness of the skirt for filters. For example, the PCS band has a much more stringent requirement on filter performance than the Bluetooth application. There is a strong demand to use this precious spectrum as efficiently as possible. This demand has pushed people to allocate bands closer together and re-use the spectrum as efficiently as possible [98]. In the meanwhile, the wireless communication devices usually support several communication standards simultaneously. This strengthens the need for high performance frequency-control components.

Duplexer is one of the most critical frequency-control components for overall radio performance in mobile devices. The duplexer is composed of two filters, a transmit (TX) filter and a receive (RX) filter. The popularity of slim phones with thin battery, which has limited power capacity, has pushed the duplexer to maintain low insertion loss in the pass-band. In the meanwhile, to hinder the interference of the strong transmitted signal with the received signal, a sufficient isolation is required between the RX and TX band. Before the advent of film bulk acoustic resonators (FBAR), duplexers used in cellphones consisted of ceramic and surface acoustic wave (SAW) filters.

The ceramic filters utilizing the electromagnetic waves are relatively large in size, compared with the RF filters consisted of BAW (bulk acoustic wave) /SAW resonators utilizing acoustic waves, as it is shown in Figure 1.2. Figure 1.2 is only used to illustrate the size comparison between the ceramic filters and BAW filters. This is because that the electromagnetic wavelength in the GHz range is large. Even in ceramic filters with relative permittivity $\varepsilon_r \approx 100$ the electromagnetic wavelength is still in the order of mm [6]. This

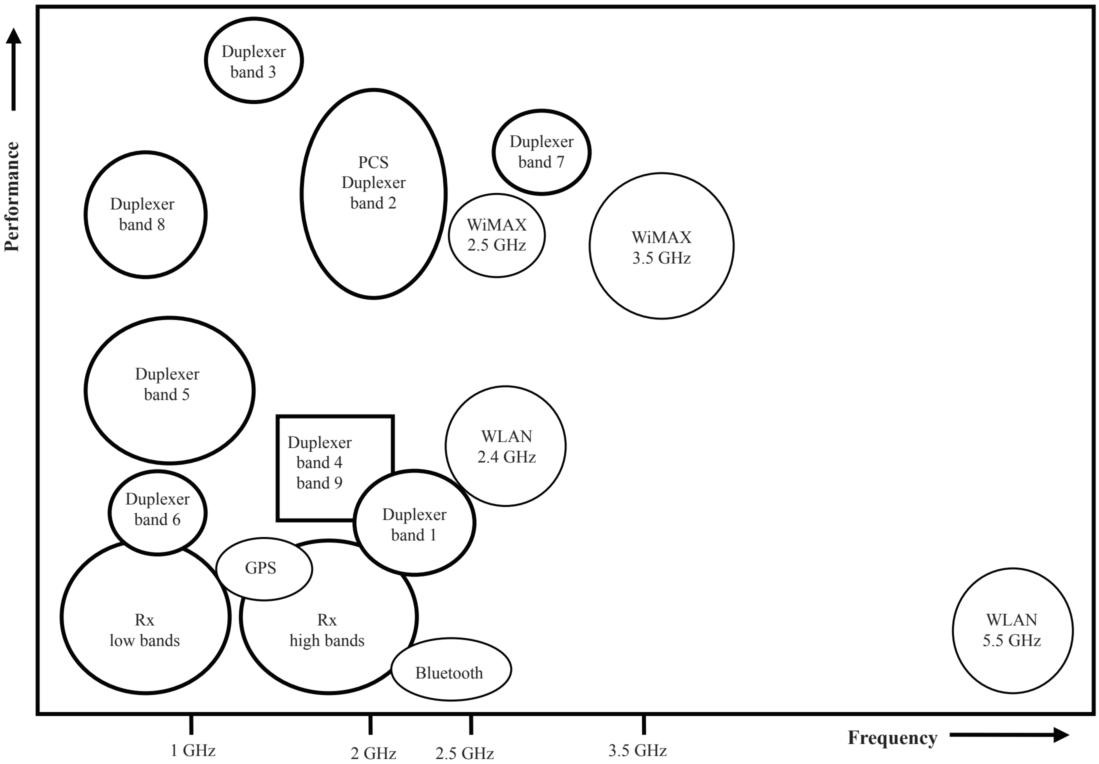

Figure 1.1: Frequency allocation for different communication standards

has limited the usage of ceramic filters in modern mobile devices, which require shrinking the size of duplexers to save place for various applications.

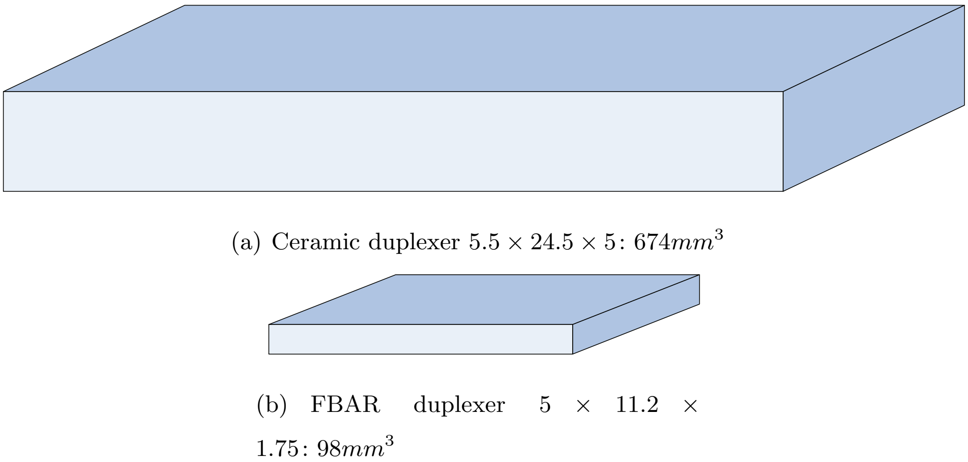
(a) Ceramic duplexer $5.5 \times 24.5 \times 5$: $674mm^3$

(b) FBAR duplexer $5 \times 11.2 \times 1.75$: $98mm^3$

Figure 1.2: Comparison the size of ceramic duplexer and FBAR duplexer (a) Ceramic duplexer, (b) FBAR duplexer

In contrast, RF filters using acoustic waves, such as SAW and BAW, instead of electromagnetic waves can be much smaller, only in the order of μm, while exhibiting high performance. This benefits from that the propagation velocity of acoustic waves in solids is approximately 10^3 to 10^5 times slower than that of electromagnetic waves.

SAW technology has entrenched position in filter applications for over 30 years [21, 93]. Several advantages of SAW technology have helped it to consolidate its position in traditional phone bands, with exception of the US-PCS band, which requires very high quality factor and low insertion loss [5]. First, the big advantage of SAW technology is that it is easy to create differential outputs without adding extra complexity to the process [5]. The differential outputs can eliminate most of the common mode contaminating the RX path. The second advantage is that filters based on SAW technology can have the flexibility in terms of relative bandwidth. This is because that SAW designers have the freedom to choose a combination of material and cut angle to obtain effective coupling coefficients k_{eff}^2 anywhere between 0.5% and 15% [81]. In a ladder filter the relative bandwidth is directly linked to the effective coupling coefficient k_{eff}^2 of the resonators. Most important of all, SAW technology has the advantage of low cost, which is owing to only few lithographic steps are necessary. Nevertheless, SAW filters for frequencies above 2 GHz are not easy to manufacture because that the lithography and patterning of the small interdigitated transducers (IDT) finger is a big challenge. Due to the small IDT finger width, the quality factor Q then drops dramatically, and to achieve high performance at high frequencies is very demanding if not impossible.

To cover the frequency range in which SAW filters can hardly fulfill the high demanding specifications, such as the US-PCS band, film bulk acoustic resonators (FBAR) have entered the market in 2001 [99–101]. Compared with SAW resonator, film bulk acoustic resonator (FBAR) is comparatively young and was demonstrated nearly simultaneously by the research groups of Grudkowski [32], Nakamura [79], and Lakin [54] in 1980. These devices were composed of the piezoelectric material zinc oxide (ZnO) and two metal electrodes, which form a resonating membrane vibrating in the thickness extensional mode. The membrane was supported by a thin silicon (Si) layer. In 1982, an increased coupling was obtained by removing the Si support layer [55]. With regard to CMOS (complementary metal-on-oxide semiconductor) compatibility, sputtered aluminum nitride (AlN) was introduced as an alternative piezoelectric material by Wang and Lakin [56, 124]. Today, AlN remains the piezoelectric material of choice in all commercially available BAW devices, owing to its low intrinsic material losses, the relatively high intrinsic coupling coefficient, the moderate dielectric constant, and the possibility to have high volume manufacturing [3].

In 1995, Lakin proposed the so called solidly mounted resonator (SMR), which uses quarter-wavelength thick layers to acoustically isolate the resonator from the substrate [52]. The isolating layer, or the Bragg reflector, is formed by an alternating sequence of high and low acoustic impedance materials. Figure 1.3 shows the configuration of the two types of film bulk acoustic resonators (FBAR), the free-standing bulk acoustic resonator (FBAR), and the SMR. FBAR stands for both the free-standing bulk acoustic resonator (FBAR) and the SMR in this chapter, if not specified. The details of the FBAR resonator working principles and the two types of FBAR resonator will be discussed in the next chapter. In 2002, SMR devices were demonstrated in high volumes by Infineon [2, 4]. There are several benefits coming from the Bragg reflector underneath the bottom electrode: better mechanical robustness, superior thermal heat transfer to the substrate, and smaller temperature coefficient of frequency (TCF) owing to the oxide material with positive TCF within the Bragg reflector [97]. However, bad effects also come along with the presence of the Bragg reflector. Compared with the free-standing bulk acoustic resonator (FBAR), SMR resonator always has some acoustic energy stored in the Bragg reflector, which result in a lower coupling coefficient and a lower quality factor [96]. In addition, the manufacturing process is more complicated due to the existence of the Bragg reflector.

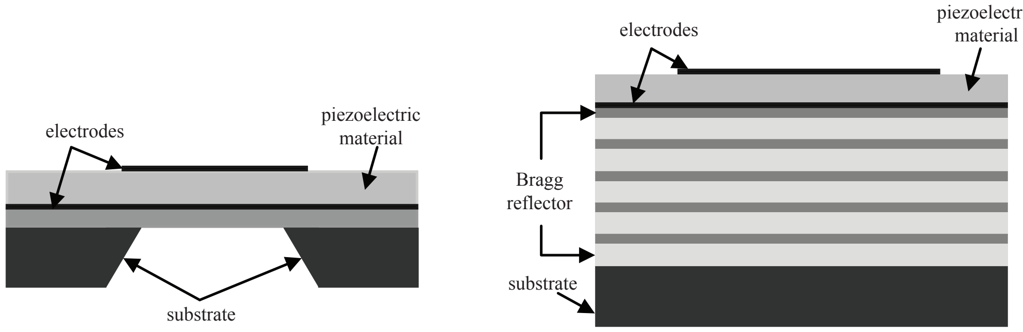

(a) (b)

Figure 1.3: Configuration of film bulk acoustic resonator (a) Free-standing Bulk Acoustic Resonator (FBAR), (b) Solidly mounted resonator (SMR)

Several advantages of BAW technology in comparison with SAW are the superior performance in terms of resistance to electro static discharge (ESD), temperature stability, and the power handling ability [5]. Nevertheless, the most important factor for the choice of BAW devices is the extremely high quality factor, which allows achieving superior filter performances. The quality factor of the resonator determines the steepness of the skirts of the filter and contributes to the improvement of the insertion loss. With the outstanding quality factor of BAW devices, the skirts of the filters are steep and the insertion loss is small. As a result, it was possible for the first time for an acoustic device to meet the high demanding requirements of the US-PCS band replacing bulky ceramic filters in cellphones [99]. Since then, FBAR has become a popular research topic. To meet the increasing demand in bandwidth by modern communication standards, the frequency usage above 2GHz is predicted to proliferate in the future. This has promised FBAR a bright future on the market. However, performance of FBAR needs to be improved to meet the more stringent new requirements.

The designing of FBAR resonators for RF filter applications is mainly determined by four aspects: large piezoelectric coupling coefficient, high quality factor (Q-value), the purity of the main resonance, and small temperature coefficient of frequency (TCF)[27]. The piezoelectric coupling coefficient is mainly determined by the piezoelectric and metal electrode materials properties. AlN is now widely used because of its high intrinsic coupling coefficient and convenient fabrication process. Metals with high acoustic impedance, such as Ru, Mo, and W, are also used as electrodes to boost the achievable effective coupling coefficient k_{eff}^2 [36, 51, 132]. The free-standing bulk acoustic resonator (FBAR) and the SMR both have laterally propagating spurious waves caused by electrode edges [113]. These spurious waves degrade the performance of filters composed of FBARs by increasing the insertion loss, introducing ripples in their passbands and narrowing the bandwidth. The conversion of modes at the electrode edges and leakage of acoustic power due to these spurious modes were studied using finite element/ boundary element method (FEM/BEM) qualitatively [87]. Several researches have been done to investigate the lateral spurious waves and to suppress them [46, 53, 60, 63, 91, 108]. One method is so-called apodization technique. Here irregular resonator shape usually a polygon with no two sides parallel is used to smear out the ripples introduced by the spurious lateral waves within the passband of the filter [58]. Another method is adding viscous acoustic materials at the perimeter of the electrodes to attenuate reflections of the lateral acoustic modes at the electrode edges back into the electrode region [23]. Combining the two methods together may have even better performance of suppressing the spurious modes. However, these two methods do not actually eliminate the spurious modes generation. They only reduce the strength of the spurious modes. The quality factor can not be improved by these two methods and the insertion loss of filters composed of these FBARs is still high. Using frame-like electrodes to eliminate the generation of the spurious modes is so far considered to be the best way to suppress the spurious waves [37]. The frame-like method adopts a proper electrode overlapping the top electrode to fulfill the boundary conditions between the main mode in the active area of the resonator and the exponentially decaying displacement amplitude outside. By satisfying the boundary conditions, the spurious modes generation is eliminated. However, this frame-like method can not suppress the lateral modes below f_s (f_s is the series resonance frequency of the FBAR) for FBARs with type II dispersion characteristic [16]. These lateral modes generate unwanted ripples in the filter passband, and they introduce significant loss below f_s. A combination of a recessed frame with a raised frame was introduced independently by Avago [102] and Infineon [116] to suppress the spurious lateral modes and improve the quality factor of FBARs with type II dispersion. However, the gasket overlapping the top electrode may even introduce more spurious waves caused by the gasket mode, which degrade the quality factor of the filters below f_s[15]. The lateral spurious modes propagating into the passive peripheral area will also introduce losses and deteriorate the quality factor of the filter. This phenomenon was qualitatively observed by numerical device analysis by various groups [74, 87, 97, 116]. To meet the temperature stability requirements for some application bands, a zero-drift resonator (ZDR) was introduced [82, 131]. As the frequency spectrum crowding increases constantly, the further enhancement of the quality factor Q for FBAR and ZDR is desired. The quality factor is currently limited by the lateral modes leaking to the passive peripheral area [103]. Thus, more investigation needs to be done regarding the origin and characteristics of the lateral waves and appropriate measures have to be taken to suppress the lateral spurious modes and improve the quality factor.

Various approaches have been introduced to model the electromechanical characteristics of the free-standing bulk acoustic resonator (FBAR) and SMR structures. For small thickness-to-width ratios piezoelectric layer, the one-dimensional (1D) Mason model [92] has been widely used to analyze the vertical structure of a given FBAR. However, the 1D model can not predict the spurious lateral resonances caused by the reflection of the electrode edges. Two-dimensional (2D) model was introduced to analyze the ripples and the energy loss of the FBAR [73]. Due to the complexity of the exact piezoelectric equations that describe the device and its loading conditions, applications of these analytical approaches are limited. One of the commonly used numerical methods to analyze a complex FBAR structure is the finite element method (FEM)[62, 66]. However, FEM needs matrix inversion and has difficulty to handle large dimensional or three dimensional problems. Therefore, the purpose of this research is to propose a more efficient method to model the FBAR structure, aiming to investigate the lateral spurious modes generation and improve the quality factor of FBAR.

1.2 Outline of dissertation

In Chapter 2, the working principle of FBAR resonator is reviewed, and the two types of FBAR structure are discussed. Following that, the resonator properties for filter application is discussed. The conventional modeling schemes of FBAR resonators are also reviewed. The limitations of these modeling schemes are discussed and served as the motivations of the developments in the rest of this dissertation.

In Chapter 3, the fundamental equations governing the elastic wave motion in solids are described. Moreover, the quasi-static approximation of the electromagnetic waves is applied to derive the governing equations for acoustic waves in piezoelectric materials. The finite-difference time-domain (FDTD) spatial and temporal discretizations of the governing equations are demonstrated. The numerical dispersion and stability of the FDTD model are discussed. The excitation source is discussed for different applications. The boundary conditions of the numerical model are presented. The 2D-FFT method is used to obtain the dispersion curve and the amplitudes of respective modes. Finally, the summary of the FDTD model for simulating the FBAR resonators is given.

In Chapter 4, the wave scattering analysis for the nondestructive testing (NDT) and FBAR is reviewed. The limitations of the existent wave scattering schemes are pointed out. The derivation of the scattering analysis for multimode excitation is presented. After checking the validity of the proposed method, the multimode wave scattering analysis is applied on two generic free-standing bulk acoustic resonator (FBAR) structures.

In Chapter 5, based on the scattering analysis of the two generic free-standing bulk acoustic resonator (FBAR) structures, a new structure of free-standing bulk acoustic resonator (FBAR) with frame-like airgap on bottom electrode is proposed to suppress the spurious modes and improve the quality factor. The proposed free-standing bulk acoustic resonator (FBAR) structure is presented. The time domain analysis developed in chapter 3 is carried out for the proposed structure. Then, the frequency domain analysis is conducted to provide a more profound understanding for the phenomenon.

Chapter 6 summarizes the dissertation and major conclusions are given.

Chapter 2

Properties of BAW devices and design methods

2.1 Introduction

In this chapter, the working principle of bulk acoustic wave (BAW) resonators is reviewed and the two types of thin-film bulk acoustic wave resonator (FBAR) structures are discussed. In this chapter, FBAR stands for both the free-standing bulk acoustic resonator (FBAR) and the SMR, is not specified. Following that, bandpass filters for high performance applications are reviewed and the related resonator properties for filter application are discussed. The conventional modeling schemes of FBAR resonators are also reviewed. The limitations of these modeling schemes are discussed and served as the motivations of the developments in the rest of this dissertation.

2.2 Thin-film Bulk Acoustic Wave Resonators

A FBAR resonator is composed of a piezoelectric material sandwiched by two metal electrodes. When an alternating electric field is applied between the electrodes, acoustic waves are excited in the piezoelectric material. To confine the acoustic waves within the resonator, highly reflective boundaries are implemented. Air is considered to be a perfect reflective boundary for acoustic waves and it is utilized as the reflective boundaries for the free-standing bulk acoustic resonator (FBAR). An airgap is formed underneath the bottom electrode of the free-standing bulk acoustic resonator (FBAR) to isolate the resonator from the substrate. Another approach to isolate the resonator from the substrate is to adopt a Bragg reflector underneath the bottom electrode, so called the solidly mounted resonator (SMR). The Bragg reflector is composed of quarter-wavelength thick layers with alternating high and low acoustic impedance. With approximately quarter-wavelength thick layer, the reflected wave from the bottom interface of the first Bragg layer will be about 180 degrees out of phase with respect to the incident wave at the interface of the bottom electrode and the first Bragg reflector layer. This destructive interference makes the first Bragg layer and each succeeding layer act like a mirror, reflecting the acoustic waves back into the resonator. SiO_2 (silicon oxide) is commonly chosen as the low-impedance layer in the Bragg reflector. As for the high-impedance layer, AlN (aluminum nitride) and W (tungsten) are frequently adopted. When metal is used for the high-impedance layer, it has to be carefully patterned to avoid the parasitic capacitance, which will degrade the effective coupling coefficient [96]. Because each layer in the Bragg reflector is not a perfect reflector, acoustic energy will penetrate into the Bragg reflector layer, which will degrade the quality factor as well. To improve the quality factor of SMR resonator, the Bragg reflector was optimized for both the longitudinal and shear waves [68]. Figure 2.1 illustrates the comparison of the two types of FBAR resonators.

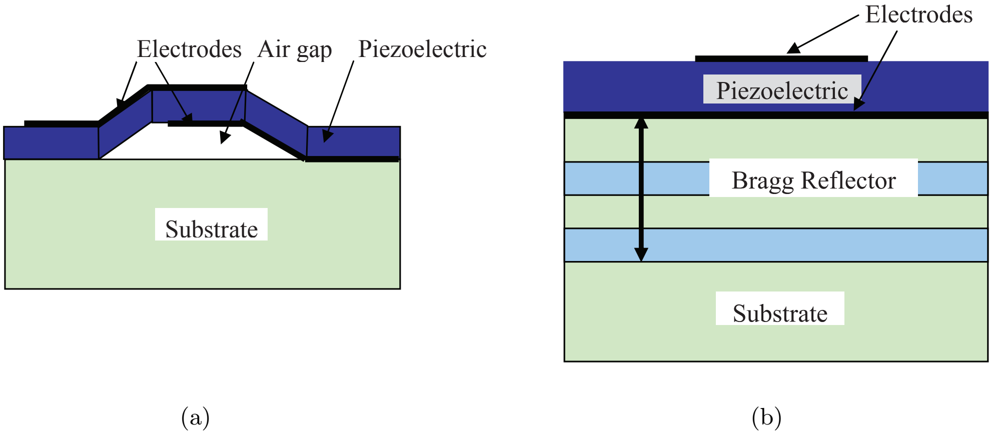

Figure 2.1: Comparison of two types of film bulk acoustic resonators (a) Free-standing Bulk Acoustic Resonator (FBAR), (b) Solidly mounted resonator (SMR)

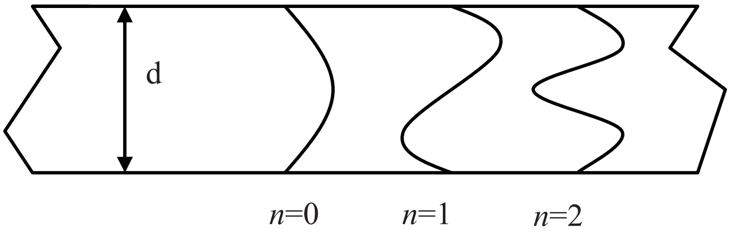

Figure 2.2: Mechanical resonances in a plate of thickness d. The stress fields associated with the resonances are plotted.

Figure 2.2 shows a prototype resonator consisting of a piezoelectric plate of thickness d sandwiched by infinitely thin electrodes. Note that only the symmetric modes can be

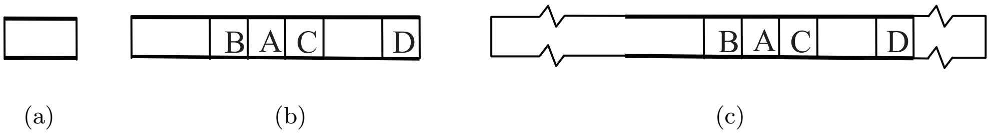

Figure 2.3: Resonator geometry for illustrating the generation of plate waves. (a) Resonator having comparable lateral and thickness dimensions, (b) large lateral-to-thickness dimensions, (c) large lateral-to-thickness dimensions with extended plate over the active region of the resonator.

excited by the electric field. FBAR utilizes the fundamental longitudinal mode ($n = 0$) in which the resonant frequency is determined by the thickness of the piezoelectric layer and the acoustic wave velocity inside the piezoelectric layer. However, lateral modes are also excited through the intrinsic Poisson coupling [49]. Figure 2.3 illustrates the generation of the lateral plate wave modes. In Figure 2.3(a) a resonator with a lateral dimension comparable to the piezoelectric plate thickness is displayed. Assuming a time harmonic electric field is applied on the electrodes, lateral vibrations will be excited in addition to the thickness vibrations, owing to the intrinsic Poisson coupling. Due to the small lateral to thickness ratio, the lateral vibration and the thickness vibration are so tightly coupled and not distinguishable in this case. However, in practical applications of FBAR resonator, the dimension of the lateral direction is usually much larger than that of the thickness direction, which is shown in figure 2.3(b). In this case, the lateral deformation of element A can be canceled by the adjacent elements B and C. However, the end element D does not have an adjacent cell on the right hand side to cancel the lateral deformation in that direction. Thus, lateral waves are generated by the end cell D. A more practical FBAR resonator model is illustrated in Figure 2.3(c). Here, the piezoelectric plate is supposed to be larger than the overlap of the electrodes region, or the active region of the FBAR resonator. Owing to the structural and electrical discontinuity, lateral modes are excited at the boundary element D in this case as well. These spurious lateral modes excited at the boundary will propagate throughout the plate, causing ripples on the impedance and degrading the quality factor of FBAR.

2.3 Resonator properties for filter applications

2.3.1 Band-pass filters based on resonators

Thin film bulk acoustic wave resonators (FBAR) are widely used as frequency control devices, such as oscillators and RF filters. RF filters composed of FBAR resonators can be grouped into two categories, the electrically coupled filters and the acoustically coupled filters. These filter configurations are shown in Figure 2.4 [47]. In Figure 2.4, the ladder and lattice filter are the electrically coupled filter, and the stacked crystal filter (SCF) and coupled resonator filter (CRF) are the acoustically coupled filter. The acoustically coupled filters usually show a wider bandwidth and a lower out-of-band rejection. They also require more complex manufacturing, because of the additional layers [48]. In contrast, the electrically coupled ladder or lattice filters have steep skirt selectivity, and high out-of-band rejection. Thus, the ladder filters with high performance are commonly used in high-end mobile communication systems.

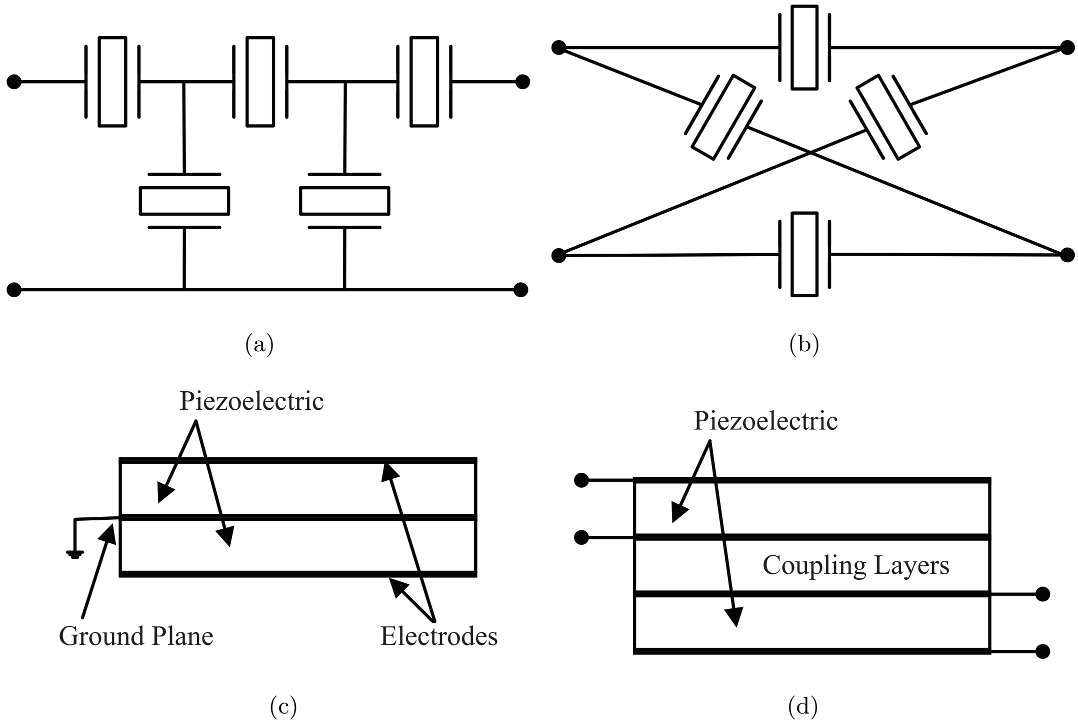

Figure 2.4: Schematic of filter topologies. (a) Ladder filter having series and parallel resonators. (b) Balanced lattice filter. (c) Stacked crystal filter (SCF). (d) Coupled resonator filter (CRF).

Figure 2.4(a) shows an unbalanced ladder-type filter consisting of three series and two parallel or shunt resonators, hence called a 3-2. All the series resonators have the same resonance and anti-resonance frequencies and likewise the shunt resonators are all identical but different from the series resonators. The center frequency f_0 of the ladder filter is at the resonance frequency of the series resonator, as is shown in Figure 2.5. The shunt resonators are mass-loaded to shift their frequency so that their anti-resonance frequency $f_{a,p}$ is approximately at the resonance frequency $f_{r,s}$ of the series resonators [50]. At the center frequency f_0, the series resonators have the lowest impedance and current flow is almost straight through the filter. To hinder the current flow to ground through the shunt resonators, the shunt resonators should have high anti-resonance resistance. The steepness of the filter skirt is also determined by the minimum resistance R_{min} at the resonance frequency and the maximum resistance R_{max} at the anti-resonance frequency. More ladder sections can be added to improve the out-of-band rejection, but it will introduce more insertion loss as well. Therefore, high-Q resonators are desired to provide low resonance impedance and high anti-resonance impedance, and to form filters with small insertion loss.

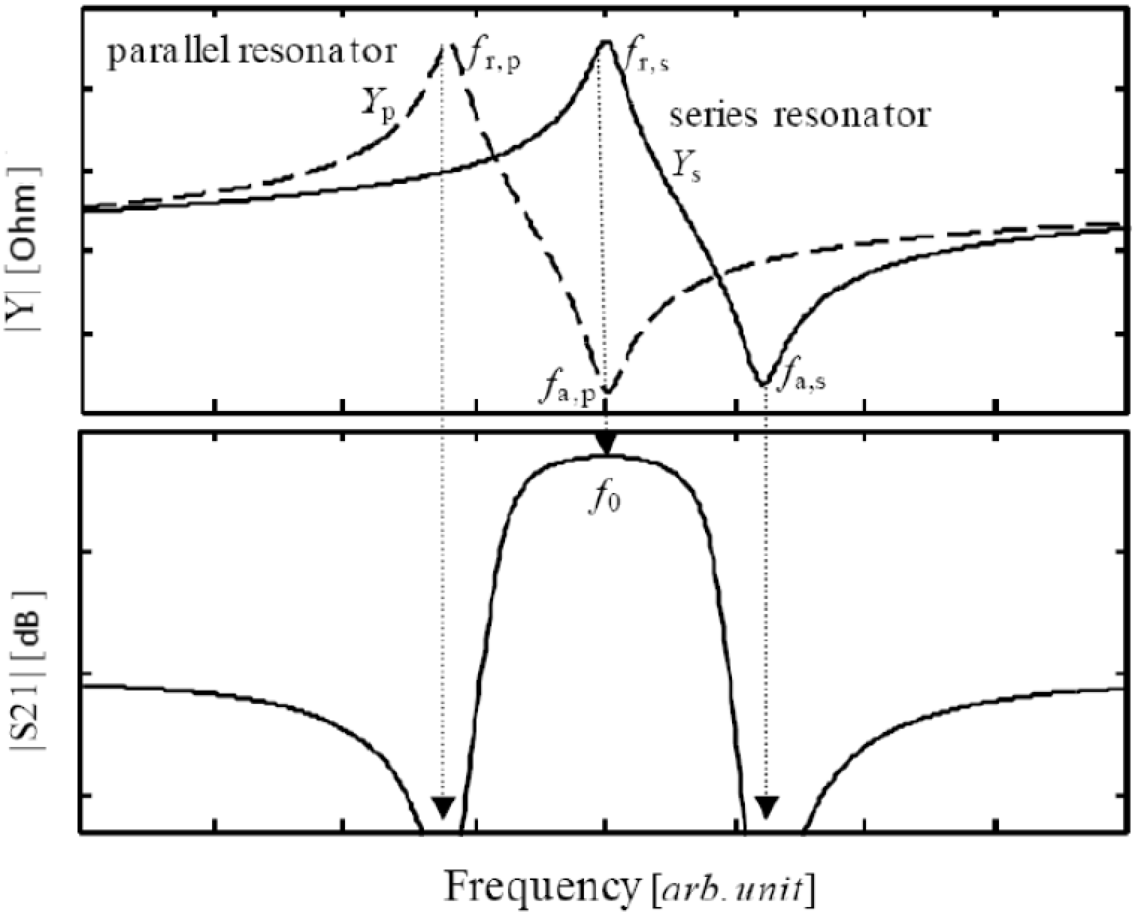

Figure 2.5: Admittance Y_s and Y_p of series and parallel resonators for ladder-type filter and scattering parameter $|S21|$ of the ladder-type filter.

2.3.2 Resonator figure of merit

As it is stated in Chapter 1, besides of temperature stability, three resonator properties have to be considered for filter applications: the effective coupling coefficient k^2_{eff}, the quality factor Q, and the spurious modes. Note, that the effective coupling coefficient k^2_{eff} is different from the material coupling coefficient K^2, which is merely related to the material itself. The effective coupling coefficient k^2_{eff} can be thought of as the ratio of the energy stored in the electric field and the energy stored in the acoustic field [92]. It is a device property, related to the material and the resonator configuration as well.

In general, the effective coupling coefficient k_{eff}^2 is a measure for the effectiveness of the electromechanical conversion that is independent of frequency, and can be obtained by the following equation [57]

$$k_{eff}^2 = \frac{\pi}{2}\frac{f_s}{f_p}\cot\left(\frac{\pi}{2}\frac{f_s}{f_p}\right) \ , \tag{2.1}$$

where f_s is the series resonance frequency of the resonator, and f_p is the parallel resonance frequency of the resonator. For small k_{eff}^2, $f_p \approx f_s$, equation (2.1) can be simplified to the following equation by a first order approximation

$$k_{eff}^2 = \left(\frac{\pi}{2}\right)^2 \frac{f_p - f_s}{f_p} \ . \tag{2.2}$$

The quality factor Q is a measure of losses for the resonator and is generally defined as the ratio of the total stored energy to the dissipated energy per cycle [27]:

$$Q = \frac{E_{tot}}{\Delta E} \ , \tag{2.3}$$

where E_{tot} is the total stored energy and ΔE is the energy lost per cycle. The quality factor Q is frequency dependent and can be obtained by the brute-force method (BFM)[28]. This method of extracting Q is first to fit the modified Butterworth Van Dyke (mBVD) model to the resonator using a least-squares algorithm. (The mBVD model will be presented in the next section.) Then the stored energy and the dissipated energy in one cycle can be calculated at each frequency. Finally, taking the ratio of these two energy, the quality factor Q can be obtained.

For filter applications, the overall figure of merit (FOM) M of the resonators is defined as [133],

$$M = \frac{k_{eff}^2}{1 - k_{eff}^2} Q \ . \tag{2.4}$$

For small k_{eff}^2, equation (2.4) can be simplified as

$$M = k_{eff}^2 Q \ , \tag{2.5}$$

which is the most commonly found formulation in literature. Since the quality factor Q is dependent on the frequency, M is also a function of frequency.

As it is mentioned before, for ladder-type filters, it is desired to have the resonance resistance R_s as small as possible and the anti-resonance resistance R_p as large as possible. These resistances can be related to the FOM as [97]

$$R_s \sim X_o / M(f_s) \ , \tag{2.6}$$

$$R_p \sim X_o \cdot M(f_p) \ , \tag{2.7}$$

where X_o is the capacitance reactance of the resonator. It can be obtained by the following equation

$$X_o = \left|\left(\omega C_0 \left(1 + k_{eff}^2\right)\right)^{-1}\right| \sim \left|\left(\omega C_0\right)^{-1}\right| \ . \tag{2.8}$$

Here, C_0 is the plate shunt capacitance, and can be obtained by $C_0 = \varepsilon_o \cdot \varepsilon_r \cdot A/d$. A is the area of the resonator; d is the thickness of the piezoelectric region; and ε_r is the relative dielectric constant of the piezoelectric material.

It can be observed from equation (2.6) and (2.7) that the small R_s and large R_p can be achieved by improving the FOM of the resonator. However, for thin-film bulk acoustic resonator (FBAR) applications, the effective coupling coefficient k_{eff}^2 is limited by the available piezoelectric material. There is only a small amount of design flexibility in adjusting k_{eff}^2. Therefore,the best approach to improve the resonator performance is to achieve as high unloaded Q as possible [97].

Spurious waves not only introduce ripples in the passband and rejection bands of the filter using FBAR resonators, but also deteriorate the quality factor Q of the filter by leaking energy into the peripheral area. The Rayleigh-Lamb (RL) modes are the main contributors of these spurious waves. When an alternating electric field is applied on the electrodes, shear vertical (SV) waves will be excited along with the longitudinal waves (also referred to as the thickness extensional (TE) waves) through the intrinsic Poisson coupling. In an infinite three-dimensional volume, these two types of waves do not interact with each other. However, in a plate, which is infinite in the lateral directions (x_1 and x_2 direction), and is finite in the thickness direction (x_3 direction), these two groups of waves will couple with each other by mutual scattering on the free boundary. After successive reflection from the top and bottom faces of the plate, these two waves will reconstruct themselves and form the so-called Rayleigh-Lamb (RL) modes [11].

The Rayleigh-Lamb modes can be further grouped into two families; the symmetric modes (S_n) and the antisymmetric modes (A_n),which are also referred to as the flexure modes. The symmetric modes are the ones that introduce ripples in the passband of the filter using FBAR resonators. Because the relative position of the electrodes is not changed for the flexure modes, the flexure modes are not coupled with the electric field and thus not visible on the electric response of the filter. However, the flexure modes also contribute to the energy leakage into the peripheral area of the resonator[118]. Thus, to enhance the quality factor Q of the resonator, both the symmetric and antisymmetric modes need to be investigated.

The dispersion property of the Rayleigh-Lamb modes can be derived based on the "transverse" resonance principle described in Bert Auld's book[11]. For an isotropic plate, the dispersion relation for the symmetric modes is as

$$\frac{\tan k_{sv} d/2}{\tan k_l d/2} = -\frac{4\beta^2 k_l k_{sv}}{(k_{sv}^2 - \beta^2)^2} \ , \tag{2.9}$$

and for antisymmetric modes as

$$\frac{\tan k_{sv} d/2}{\tan k_l d/2} = -\frac{\left(k_{sv}^2 - \beta^2\right)^2}{4\beta^2 k_l k_{sv}} \ . \tag{2.10}$$

Here, k_{sv} and k_l are the wavenumber of the shear vertical waves and the longitudinal waves respectively; d is the thickness of the plate. β is the wavenumber of the RL modes, and it is related to k_{sv} and k_l by the following equations

$$k_{sv}^2 = \left(\frac{\omega}{v_{sv}}\right)^2 - \beta^2 \ , \tag{2.11}$$

and

$$k_l^2 = \left(\frac{\omega}{v_l}\right)^2 - \beta^2 \ . \tag{2.12}$$

Here, v_{sv} is the velocity of the shear vertical wave and v_l is the velocity of the longitudinal wave; $\omega = 2\pi f$ is the angular frequency. For multilayer structures with anisotropic materials, such as AlN, the dispersion relation can be obtained by the transfer matrix scheme as described in [1, 64, 109], or by experimentally measurement as presented in [112].

The free-standing bulk acoustic resonators (FBARs) using AlN as the piezoelectric material has a type II dispersion, which is quite different from FBAR resonators using ZnO as the piezoelectric material, as it is shown in figure 2.6. Here, only the two lowest symmetric and antisymmetric modes are shown, as they are in the frequency range between f_s and f_p. Unlike type I dispersion, for type II dispersion, the S_1 mode (or often referred to as the TE1 mode) has two branches; one is with a positive group velocity (labeled as $S_1(+)$), and the other one has a negative group velocity (labeled as $S_1(-)$).The group velocity v_g can be obtained by the following equation from the dispersion curve,

$$v_g = \frac{d\omega}{d\beta} \ . \tag{2.13}$$

Here, ω is the angular frequency and β is the wavenumber of the mode.

Because of this type II dispersion characteristic, FBAR resonators with AlN as piezoelectric material suffer a big energy loss below f_s, which will in turn degrade the quality factor of the resonator. As it is mentioned in Chapter 1, several approaches have been proposed to eliminate these spurious modes. However, the quality factor of the resonator is still limited by the lateral propagating spurious modes into the passive area of the resonator[103]. Therefore, the goal of this work is to propose an efficient model to investigate these spurious modes and to enhance the quality factor of FBAR resonators.

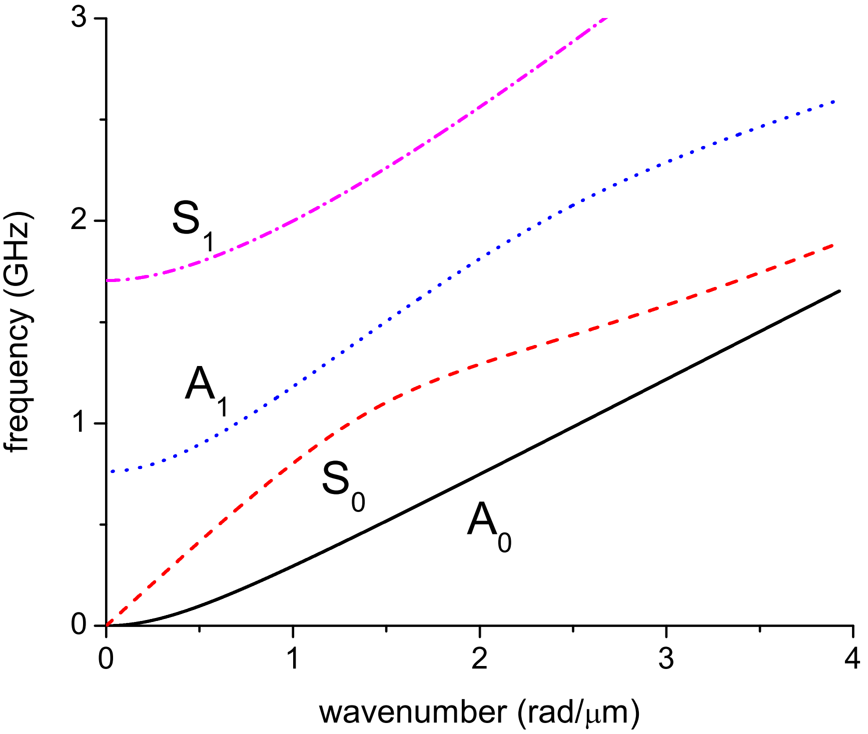

(a)

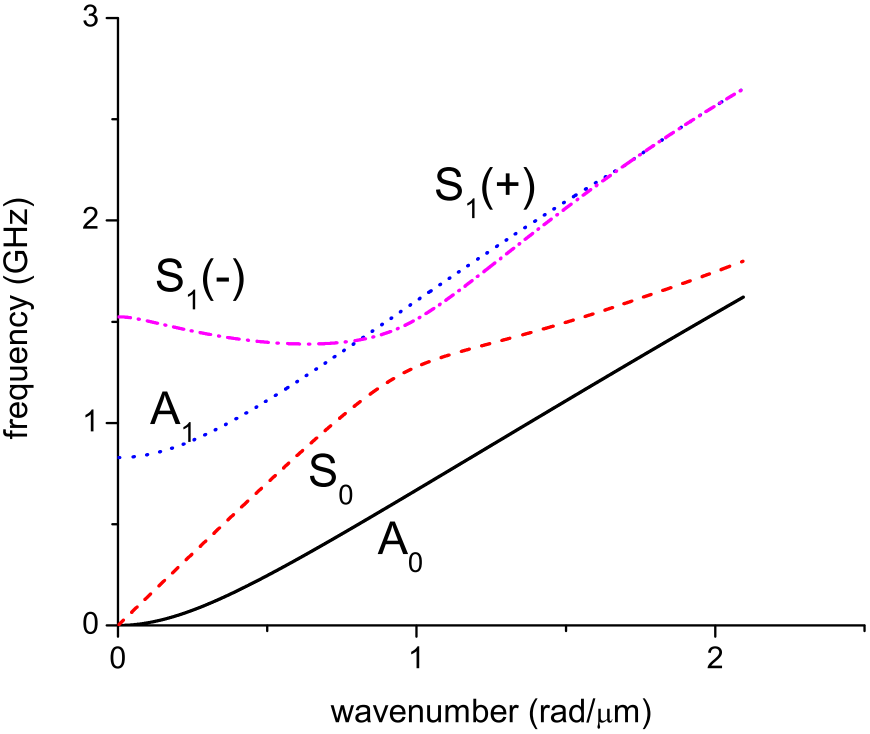

(b)

Figure 2.6: Dispersion curve for the two types of FBAR resonators (a) type I dispersion (Al/ZnO/Al with thickness of $0.2\mu m/1.6\mu m/0.2\mu m$), (b) type II dispersion (Al/AlN/Al with thickness of $0.3\mu m/3\mu m/0.3\mu m$)

2.4 Design methods for FBAR

With the popularity of the FBAR resonators, the design methods for FBAR resonators have also become a hot topic. The aim of this section is to review the most frequently used design methods for FBAR resonators. This section is divided into four parts. Firstly, three analytic methods used for FBAR resonator design are examined, which are the Mason model, the Butterworth Van Dyke (BVD) model, and the Mode Power Coefficient (MPC) scheme. Secondly, the experimental laser interferometry method is reviewed. Following that, the numerical method for FBAR resonator modeling is reviewed, which is the finite element method (FEM). Finally, these design schemes are summarized. The limitations of each scheme are discussed and served as the motivation to develop the finite-difference time-domain (FDTD) model for FBAR resonator modeling.

2.4.1 Analytical method

Three analytic methods used for FBAR resonator design are reviewed in this section, which are the Mason model, the Butterworth Van Dyke (BVD) model, and the Mode Power Coefficient (MPC) scheme.

2.4.1.1 Mason model

Mason model is a physical model, where the mechanical or the piezoelectric plate is represented as an acoustic transmission line[70, 88, 92]. Note that there are other transmission line models, such as the KLM model [42], however, all acoustic transmission line models give the equivalent results [106].

Figure 2.7 shows the representation of Mason model for the piezoelectric plate and the pure mechanical plate with thickness d. For a piezoelectric plate, the Mason model has three ports including two acoustical ports and one electrical port, as it is shown in figure 2.7(a). For a nonpiezoelectric mechanical layer, Mason model only has two acoustical ports, as it is shown in figure 2.7(b). The electrical response of the multilayer stack, such as FBAR resonators, can be obtained by cascading transmission line sections of piezoelectric and mechanical layers according to the physical stack under investigation. Figure 2.8 shows the configuration of a SMR resonator as an example. The single top electrode on the left is terminated by a free surface that is represented by an acoustic short. The substrate is assumed to be infinite, which is represented by the specific acoustic impedance Z_0 of the layer. If the substrate is finite, a mechanical transmission line section should be used again terminating the model by an acoustic short. For the free-standing bulk acoustic resonators (FBARs), the Bragg reflector layers, or the mirror layers can be removed.

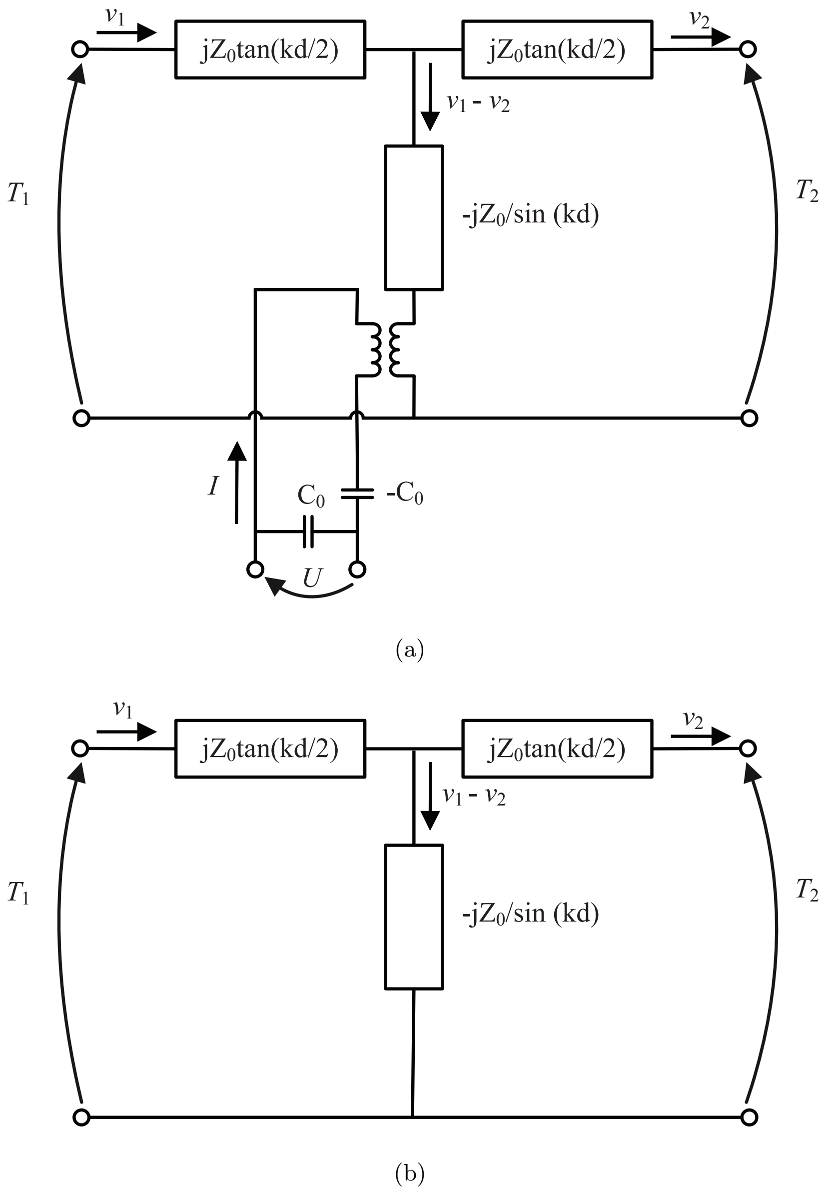

Figure 2.7: Mason model for acoustic plates: (a) piezoelectric plate, (b) pure mechanical plate.

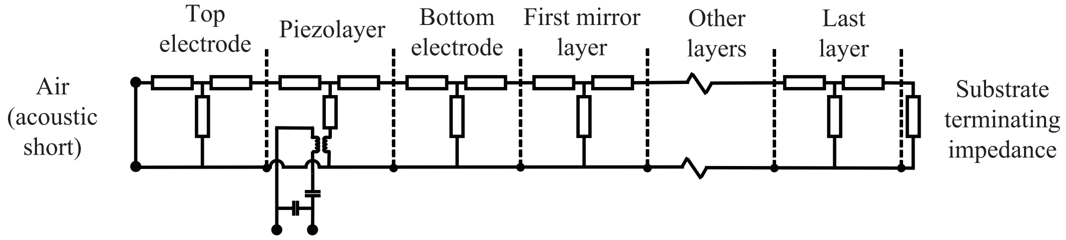

Figure 2.8: Mason model for a multilayer resonator. The circuit is terminated on the left by a free surface (an acoustic short) and on the right by a semiinfinitely thick substrate. Each layer is represented by the corresponding transmission line sections with the piezoelectric layer having the electrical port associated with it.

The electric impedance Z of the multilayer resonator can be obtained by the following equation

$$Z = \left(\frac{1}{j\omega C_0}\right)\left(1 - k_t^2 \frac{tan\phi}{\phi} Z_{in}\right) \ , \tag{2.14}$$

where

$$Z_{in} = \frac{(z_1 + z_2)\, cos^2\phi + jsin2\phi}{(z_1 + z_2)\, cos2\phi + j\,(z_1 z_2 + 1)\, sin2\phi} \ . \tag{2.15}$$

Here $z_1 = Z_1/Z_0$ and $z_2 = Z_2/Z_0$ are the normalized input impedance of the two acoustic ports, and Z_0 is the specific acoustic impedance of the piezoelectric layer. $\phi = \theta/2$, $\theta = kd$ is the phase across the piezoelectric film. k_t^2 is the electromechanical coupling coefficient of the thickness resonance, which is an intrinsic material property and can be obtained by the following equation

$$k_t^2 = \frac{e_{33}^2}{c_{33}^D \varepsilon_{33}^S} \ . \tag{2.16}$$

where material parameters e_{33}, c_{33}^D, and ε_{33}^S denote the piezoelectric constant, the elastic stiffness at constant dielectric displacement, and the dielectric constant at constant strain. More details about these parameters will be presented in the next chapter.

The acoustic input impedance of the piezoelectric layer can be obtained by calculating the acoustic impedance of each layer successively from both sides of the stack in direction towards the piezoelectric layer. For a pure mechanical layer as shown in figure 2.7(b), when Z_1 is loaded at the port 1, the acoustic input impedance looking from port 2 $Z_2 = T_2/v_2$ can be obtained by

$$Z_2 = Z_0 \frac{Z_1 cos(\theta) + jZ_0 sin(\theta)}{Z_0 cos(\theta) + jZ_1 sin(\theta)} \ , \tag{2.17}$$

where $\theta = kd$ is the phase across the mechanical layer, and Z_0 is the specific acoustic impedance of the corresponding mechanical layer.

Mason model is easy to implement when the material properties are known, and it is widely used to analyze the main resonance behavior of the FBARs [3, 44, 45, 57, 61]. The series resonance frequency f_s and the parallel resonance frequency f_p of the multilayer resonator can be predicted quite accurate by Mason model. It has been applied to optimize the effective coupling coefficient of FBARs by adjusting the electrode material and electrode thickness [57, 61, 123]. Another application of Mason model is to optimize the SMR Bragg reflector to be effective for both the longitudinal and the shear waves [68].

However, Mason model is a one-dimensional model, and it only takes the thickness of the layers into consideration. Thus it can not take the lateral spurious modes into consideration. The quality factor deterioration caused by the leakage of the spurious modes can not be predicted by this model.

2.4.1.2 Butterworth Van Dyke (BVD) model

Unlike Mason model, the Butterworth Van Dyke (BVD) model is a phenomenological model, where the FBAR resonator is represented by an equivalent circuit model, as it is shown in figure 2.9.

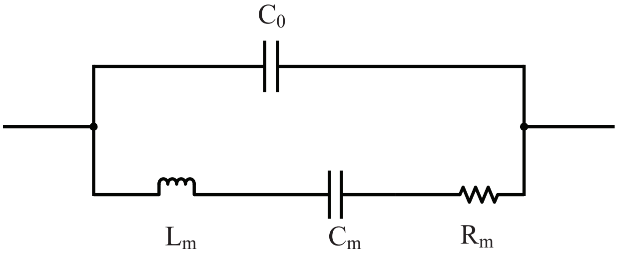

Figure 2.9: Butterworth Van Dyke (BVD) model for resonators.

As it is shown in figure 2.9, the BVD model consists of four basic elements, a motional inductor L_m, a motional capacitor C_m, a resistive loss term R_m, and the parallel connected plate capacitor C_0.

Series electrical impedance Z_s of the motional branch can easily be obtained from the model by

$$Z_s = R_m + j\omega L_m + \frac{1}{j\omega C_m} \ , \tag{2.18}$$

where the series resonance frequency ω_s when $Z_s \to 0$ can be obtained as

$$\omega_s = \frac{1}{\sqrt{L_m C_m}} \ . \tag{2.19}$$

The total impedance Z_p can be obtained by the following equation

$$Z_p = \left(j\omega C_0 + \frac{1}{R_m + j\omega L_m + \frac{1}{j\omega C_m}} \right)^{-1} \ , \tag{2.20}$$

and the parallel resonance frequency ω_p when $Z_p \to \infty$ is

$$\omega_p = \omega_s \sqrt{\left(1 + \frac{C_m}{C_0}\right)} \ . \tag{2.21}$$

Series and parallel resonance quality factors can be obtained by the following equations

$$Q_s = \frac{1}{\omega_s C_m R_m} \ , \tag{2.22}$$

$$Q_p = Q_s \sqrt{1 + \frac{C_m}{C_0}} \ . \tag{2.23}$$

For the BVD-model, the effective electromechanical coupling coefficient k_{eff}^2 can be obtained by [57]

$$k_{eff}^2 = \frac{\pi^2}{8} \frac{C_m}{C_0} \ . \tag{2.24}$$

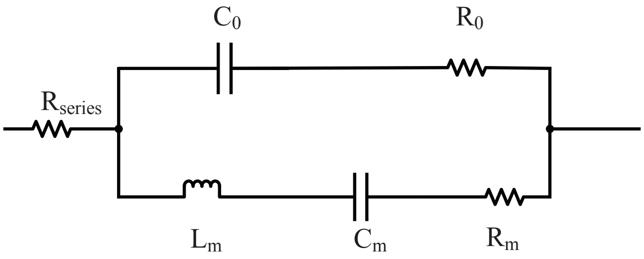

Figure 2.10: Modified Butterworth Van Dyke (mBVD) model for resonators.

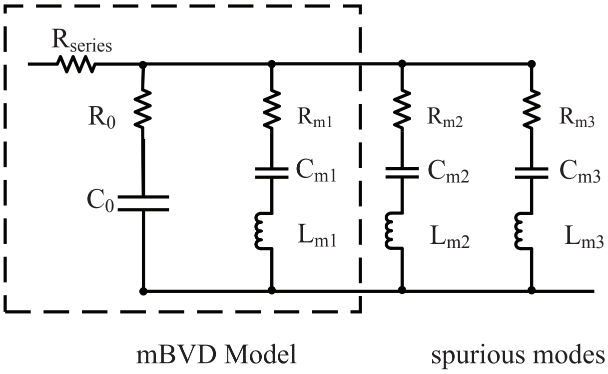

Figure 2.11: mBVD model with additional motional branches to model some of the spurious modes.

The BVD model is widely used as high-level model for the simulation of FBAR devices and design of filters [45, 57, 61]. As it is mentioned before, the BVD model can also be applied to obtain the quality factor Q of the manufactured FBAR resonators [97]. To get a better fit of the BVD model to the experimental results, a modified Butterworth Van Dyke (mBVD) model has been proposed [59]. Figure 2.10 shows the mBVD model for the FBAR resonators. In the mBVD model, two more resistors have been added, R_{series} and R_0. With these two added resistors, the model can fit better to the experiment measurements. And the quality factor at the series resonance frequency Q_s and at the parallel resonance frequency Q_p will be different, depending on the frequency. More motional branches can be added to the mBVD model to account for the spurious modes' resonances, as it is shown in Figure 2.11. However, it can only simulate the influence of the spurious modes. Because it is a phenomenological model, it can not be used to investigate the generation of the spurious modes and design the boundary of FBARs to reduce the spurious modes.

2.4.1.3 Mode Power Coefficient scheme

The mode power coefficient scheme is a method proposed to calculate the power carried by the propagating Rayleigh-Lamb (RL) modes through the so-called mode power coefficient (MPC). A brief derivation of the MPC is given below, and a more detailed description of the scheme can be found in reference [117, 118].

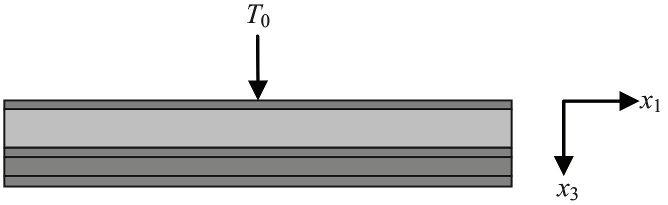

Figure 2.12: A line source $T_0\delta(x_1)$ on top of a multilayer structure.

Suppose plane waves with $\partial/\partial x_2 = 0$ are excited and propagated toward the $\pm x_1$ direction in a multilayer structure shown in Figure 2.12. The layers are homogeneous and assumed to be infinitely wide along the x_1 and x_2 direction. The upper half ($x_3 < 0$) is assumed to be vacuum. The surface displacement $u_n(x_1)$ and stresses $T_m(x_1)$ normal to the surface can be expressed in the Fourier integral form,

$$u_n(x_1) = \frac{1}{2\pi}\int_{-\infty}^{+\infty} u_n(\beta)e^{(-j\beta x_1)}\,d\beta\ , \tag{2.25}$$

$$T_m(x_1) = \frac{1}{2\pi}\int_{-\infty}^{+\infty} T_m(\beta)e^{(-j\beta x_1)}\,d\beta\ . \tag{2.26}$$

Here, β is the wavenumber of the mode toward $+x_1$ direction. The time dependency $exp(j\omega t)$ is omitted for simplicity.

Provided that the structure layers are linear and $\partial/\partial x_2 = 0$, $u_n(\beta)$ and $T_m(\beta)$ are related to each other by

$$-j\omega u_n(\beta) = Y_{nm}(\beta)T_m(\beta)\ , \tag{2.27}$$

from the law of superposition and the orthogonality of the trigonometric functions. In equation (2.27), $Y_{nm}(\beta)$ is the effective acoustic admittance, which was introduced by Hashimoto et al. [35].

When a line source $T_n(x_1) = T_0\delta(x_1)exp(j\omega t)$ is placed on the top surface at $x_3 = 0$, plane waves with $\partial/\partial x_2 = 0$ are excited and propagated along the waveguide. Here, $\delta(x_1)$ is the delta function and ω is the angular frequency. Power $2P$ per unit width supplied by the surface stress is given by

$$2P = -j\frac{\omega}{2}\int_{-\infty}^{+\infty} u_n(x_1)T_n(x_1)^*\,dx_1\ . \tag{2.28}$$

For a lossless waveguide, P is equal to the power per unit width excited to either the $+x_1$ or the $-x_1$ direction. The waveguide eigen modes are complete and orthogonal to each other. Therefore, the power per unit width P toward $+x_1$ direction can be expressed as the sum of the power per unit width carried by the k^{th} eigen mode P_k as

$$P = \sum_{k=1}^{N} P_k \ . \tag{2.29}$$

Substitute $T_n(x_1) = T_0\delta(x_1)$ at $x_3 = 0$ and equation (2.27) into equation (2.28) and apply the Cauchy-Riemann theorem of the complex integral theory, the power per unit width P_k carried by the k^{th} eigen mode can be obtained by the following equation

$$P_k = c_n^k \left| u_n^k(x_1) \right|^2 \ . \tag{2.30}$$

Here, $u_n^k(x_1)$ is the surface displacement associated with the excited k^{th} eigen mode. And c_n^k is defined as the mode power coefficient MPC; it can be obtained by the following equation

$$c_n^k = \frac{-j\omega^2}{4} \frac{\partial Y_{nn}^{-1}(\beta)}{\partial \beta} |_{\beta=\beta_k} \ . \tag{2.31}$$

By applying the MPC scheme, the power carried by the lateral propagating Rayleigh-Lamb modes in an arbitrary multilayer waveguide can be obtained easily from the calculated or measured surface displacements through equation (2.30). This procedure is simpler and more efficient than the conventional technique based on the estimation of total power flow passing through the whole waveguide cross section [11]. Because the conventional technique needs knowledge of the exact field distribution of each mode, it becomes quite complex and fault-prone when the number of waveguide layers is large. Therefore, the MPC scheme is adopted in chapter 4 to calculate the scattering coefficients for multimode excitation and in chapter 5 to evaluate the power carried by each propagating spurious modes.

2.4.2 Laser interferometry

Laser interferometry is widely used to investigate SAW and BAW devices. In laser interferometry, a coherent laser beam is split into two beams, a measurement beam, and a reference beam. The reference beam is reflected by a mirror and remains undisturbed, while the measurement beam is interacting with the object of measurement and affected by a physical property (temperature, displacement, etc.). The disturbed and undisturbed beams are combined again by a beamsplitter after they were reflected by their designated targets. At this point an interference pattern develops and is subsequently detected by a photo detector to detect information about changes of the measurement object.

When investigating SAW and BAW devices by laser probing, usually the surface vertical motion of the device is detected. The detector output is essentially sensitive to both the amplitude and phase of the surface vertical motion. Common interferometer designs are the Michelson and the Mach-Zehnder [20, 26, 29, 40, 75]. To eliminate the low frequency vibration disturbance, Sagnac interferometer was introduced to characterize SAW and BAW devices operating in high frequencies [34, 38, 127]. The obtained data can be used directly to observe the wave propagation in space domain, or they can be transferred to the wavenumber domain for obtaining dispersion curve of the resonator and/or the material parameters by fitting to the dispersion curves.

Laser interferometry has been proved to be an effective method to investigate RF SAW and BAW devices. It can be applied to investigate the influence of the spurious modes and the boundary conditions. However, it is time consuming and expensive to implement.

2.4.3 Numerical method

For complex resonator geometries and for considering second-order effects, such as spurious modes, numerical simulation has been widely used. Finite element method (FEM) is the most commonly used method to investigate SAW [14, 33, 41] and FBAR devices [62, 66, 87, 108].

The FEM algorithm operates on the partial-differential equations (PDE) and solves the equations either in the time domain or in the frequency domain. The structure is first divided into n elements of finite size. Then, these elements again are defined by a certain number of nodes. The degrees of freedom (DOF) of the physical problem (mechanical displacement, electrical potential, $\ldots$) at these nodes are defined to be the basic unknowns $\mathbf{U_{(k)}}$. The DOFs $\mathbf{U_{(k)}}$ are then presented as shape functions of the nodes within one element. The index k represents the number of the node of the element. By using the local material properties, the element forces $\mathbf{F_{(k)}}$ (mechanical force, current, $\ldots$) can be obtained by $\mathbf{F_{(k)}} = \mathbf{M_{(k)}}\mathbf{U_{(k)}}$, where $\mathbf{M_{(k)}}$ is the local stiffness matrix obtained by applying the minimum energy principle on the shape functions. A global matrix is formed for all the elements $\mathbf{F} = \mathbf{MU}$. Finally, boundary conditions are applied and the equations are solved.

FEM scheme can handle complex structures easily and is convenient to investigate the second-order effects of FBAR devices. Therefore, FEM simulation has been widely applied to investigate the spurious modes in FBAR devices [66, 71, 72, 86]. Among these applications, some were focused on optimizing the piston mode resonator [83, 115, 116]. Analysis of acoustic leakage in FBAR devices was also carried out using FEM simulation qualitatively [114, 122] and quantitatively [120]. However, for FEM simulation, a matrix must be inverted. Current linear-algebra technology limits the size of the matrix that can be inverted and, thus, limits the number of unknowns that the FEM can handle. Another drawback of FEM is that non-physical spurious modes are commonly predicted. These spurious modes must be excluded in a post-processing step, which can be a tedious task.

2.4.4 Summary of the methods for FBAR design

The advantages and disadvantages of the reviewed design methods are shown in Table 2.1. According to this table, the FEM simulation is most suitable for investigating the second-order effects of FBAR devices with complex structures. However, the FEM simulation requires matrix inversion, which limits the number of unknowns it can handle. And it is time consuming to simulate a large structure.

Base on this problem, the finite-difference time-domain (FDTD) method was extended to investigate the characteristics of FBAR devices. FDTD method was first derived by K. S. Yee to solve the electromagnetic problems of Maxwells equations [129]. The computation domain for a structure is discretized into cells and the partial derivatives of the Maxwells curl equations are approximated by the second order accuracy central differences. The response of the structure is then computed using the leap-frog time-stepping algorithm by exciting a source into the computation domain. Following Yees seminal concept, Madariaga introduced a first-order finite-difference formulation for elasticity equations, which is widely used today [65]. The FDTD method exhibits several advantages over other numerical methods. Specifically, the formulation of FDTD is simple and straightforward, it is easy to implement with complex structures, and the boundary conditions can be implemented easily. Furthermore, the update of the variables in FDTD is based on the past field values at the nearest neighbor components, which guarantees its accuracy, and the updating of the variables in FDTD does not need a matrix inversion.

The FDTD method is now widely applied to various problems in the field of elasticity. For instance, the FDTD method is applied to simulate the elastic wave propagation in porous media [24, 130], to model elastic waves in boreholes [107], or to investigate the interaction of elastic waves with buried land mines [105]. However, these applications in the field of elasticity only involve the stress filed components and particle velocities. By introducing the piezoelectric effect and the electric field components, the FDTD method has been extended to investigate SAW devices [125].

In this study, the FDTD method has been developed to model FBAR resonators. Due to the different working principle between SAW devices and FBAR resonators, the FDTD model developed in this study is different from the one developed for investigating SAW devices. Firstly, the wave utilized in SAW devices is propagating in the lateral direction, while the wave utilized in FBAR devices is propagating in the

Table 2.1: Summary of the advantages and disadvantages of the methods for FBAR design.

Design method	**Advantage**	**Disadvantage**
Mason model	1. Can be used to analyze resonance and antiresonance frequencies, effective coupling coefficient k_{eff}^2. 2. Can include electrode material and thickness influence.	1. Can not include second-order effects, such as, spurious modes.
BVD model	1. Can be used to calculate quality factor Q and effective coupling coefficient k_{eff}^2 of FBAR resonators. 2. Can be implemented to design filters using FBAR resonators. 3. Can simulate the influences of some of the spurious modes.	1. Can not track the physical principle for the generation of the spurious modes and, thus, can not be used to design the boundary of the FBAR resonators.
MPC Scheme	1. The MPC coefficient is easy to obtain. 2. The power carried by the lateral propagating modes are easy to obtain.	1. Need to know the amplitude of the surface displacement.
Laser interferometry	1. Can handle complex structures. 2. Second-order effects, such as, spurious modes, can be investigated.	1. Time consuming and expensive to implement.
FEM	1. Can handle complex structures. 2. Second-order effects, such as, spurious modes, can be included.	1. Matrix inversion is required. 2. Non-physical spurious modes need to be post-processed.

thickness direction. Because the piezoelectrically stiffened elastic constant is dependent on the wave propagation direction, a new equation was derived for calculating the stiffened elastic constant for FBAR. Secondly, the boundary condition is different from the one used in the FDTD model for SAW devices. Unlike the Rayleigh wave in the SAW devices, which is nondispersive, the Rayleigh-Lamb (RL) waves in the FBAR resonators are dispersive. Besides, several RL modes are propagating in the FBAR devices within the interested frequency range. The development of the perfectly matched layer (PML) for this problem is quite challenging. Instead of using the PML absorbing boundary condition, an extra column has been added to the left and right side of the model to simulate the free boundary condition. The updating equations for the variables on the extra column have been developed in the FDTD model. Thirdly, to do scattering analysis for FBAR resonators, different RL modes have to be excited in the model. The field distribution of the particle velocities for different modes has to be calculated to excite the corresponding mode in the model. In the FDTD model for analyzing SAW devices, a simple Gaussian pulse is applied as the excitation source. The field distribution of the variables for Rayleigh wave is not considered in the FDTD model. Finally, the post processing method for interpreting the data obtained by the FDTD simulation is different from the one used in the FDTD model for SAW devices. Prony's method is adopted to calculate the wavenumber and the phase velocity of the Rayleigh wave in SAW devices. However, it is not suitable to apply Prony's method to analyze the data obtained for FBAR devices. To apply Prony's method, the number of the modes propagating in the structure has to be determined first. Several RL modes are propagating in FBAR resonators and these modes have different cutoff frequency. Therefore, at different frequency the number of the modes propagating in FBAR may be different and it has to be determined by some other method, such as, the analytical method. Besides, due to the resonance of the FBAR resonator, when applying a Gaussian pulse to the structure, the response of the FBAR resonator is not a simple pulse, but with resonance signals. Hence, it is difficult to determine the same signal at different positions. The dispersion characteristic of the RL modes has made this work even more challenging or impossible to be done. Furthermore, because of mode conversion at the discontinuity boundaries, the amplitude of the reflected modes is a combination of several waves and it is different at different positions. The reflected wave is not a simple linear combination of the modes, which is the assumption of the Prony's method. Thus, the 2D-FFT method is applied to calculate the dispersion curve of the RL modes propagating in the FBAR resonator, and to get the amplitude of respective mode in this study.

In the next chapter, the FDTD model for FBAR resonators will be introduced. In chapter 4, the FDTD model will be combined with the MPC scheme to do the scattering analysis for multimode excitation.

Chapter 3

Acoustic waves in solids and in FDTD model

3.1 Introduction

The first part of this chapter describes the fundamental equations governing the elastic wave motion in solids. By combining the equations of wave motion in solids and the quasi-static approximation of the electromagnetic waves, the governing equations for acoustic waves in piezoelectric materials are derived. In this study, the differential equations are solved by the finite-different time-domain method (FDTD). The FDTD spatial and temporal discretizations of the governing equations are demonstrated. The numerical dispersion and stability of the FDTD model are discussed. Different type of excitation sources are discussed for investigating different properties of the structures. The boundary conditions of the numerical model are presented. From the time-domain particle velocity obtained by the FDTD, the 2D-FFT (two-dimensional fast Fourier transform) method is used to obtain the dispersion curve and the amplitudes of respective modes. Finally, the summary of the FDTD model for simulating the FBAR resonators is given.

3.2 Governing equations

3.2.1 Governing equations for non-piezoelectric materials

The equation of motion, or Newtons law, strain-displacement relation and the elastic constitutive relation form a fundamental set of equations which completely describes the acoustic wave motion in a linear medium [10, 30, 95]. In a lossless non-piezoelectric medium, the two basic field equations are the equation of motion

$$\nabla \cdot \mathbf{T} = \rho \frac{\partial^2 \mathbf{u}}{\partial t^2} - \mathbf{F} \ , \tag{3.1}$$

and the strain-displacement relation

$$\mathbf{S} = \nabla_{\mathbf{s}}(\mathbf{u^t}) \ . \tag{3.2}$$

To completely describe the wave motion in a lossless medium, another equation is needed, which is the elastic constitutive equation

$$\mathbf{T} = \mathbf{c} \cdot \mathbf{S} \ . \tag{3.3}$$

Here, $\mathbf{T}$ is the mechanical stress, $\mathbf{S}$ is the mechanical strain, $\mathbf{F}$ is the inner body forces, $\mathbf{u}$ is the particle displacement, ρ is the mass density of the material. And $\mathbf{c}$ is the elastic stiffness constant, which is a $3 \times 3 \times 3 \times 3$ matrix and describes the elastic characteristics of the medium. ∇ is the Nabla operator,

$$\nabla = \frac{\partial}{\partial x_1}\hat{x_1} + \frac{\partial}{\partial x_2}\hat{x_2} + \frac{\partial}{\partial x_3}\hat{x_3} \ . \tag{3.4}$$

In Cartesian coordinates, the displacement vector $\mathbf{u}$ is defines as

$$\mathbf{u} = u_1 \cdot \hat{x_1} + u_2 \cdot \hat{x_2} + u_3 \cdot \hat{x_3} \ , \tag{3.5}$$

and the tensors $\mathbf{T}$ and $\mathbf{S}$ are in matrix notation

$$\mathbf{T} = \begin{bmatrix} T_{11} & T_{12} & T_{13} \\ T_{21} & T_{22} & T_{23} \\ T_{31} & T_{32} & T_{33} \end{bmatrix} \ , \tag{3.6}$$

$$\mathbf{S} = \begin{bmatrix} S_{11} & S_{12} & S_{13} \\ S_{21} & S_{22} & S_{23} \\ S_{31} & S_{32} & S_{33} \end{bmatrix} \ . \tag{3.7}$$

The notation of the tensor elements is such that the first subscript of each element denotes its direction, and the second subscript denotes the normal to the plane to which the component is effective. The stress is defined as the force acting on a unit area in the solid. Thus, the stress component T_{11} represents a force applied in the x_1 direction to a unit area of the $x_2 - x_3$ plane (described by its normal vector in the x_1 direction); the stress component T_{13} represents a force applied in the x_1 direction to a unit area of the $x_1 - x_2$ plane. Figure 3.1 shows the traction forces acting on an infinitesimally small cube in a Cartesian coordinate system. Since body torques only exist in media with permanent electric or magnetic polarization (ferroelectric or ferromagnetic materials), for piezoelectric materials in this project, the stress matrix is symmetric [10], i. e., $T_{12} = T_{21}, T_{13} = T_{31}$ etc. Consequently, the stress tensor $\mathbf{T}$ has only six independent components. Then, the more convenient abbreviated notation [10] is commonly used instead of the double subscript:

$$\begin{bmatrix} T_1 & T_6 & T_5 \\ T_6 & T_2 & T_4 \\ T_5 & T_4 & T_3 \end{bmatrix} = \begin{bmatrix} T_{11} & T_{12} & T_{13} \\ T_{21} & T_{22} & T_{23} \\ T_{31} & T_{32} & T_{33} \end{bmatrix} \ . \tag{3.8}$$

As a result, the stress vector **T** is represented by the following matrix

$$\mathbf{T} = \begin{bmatrix} T_1 \\ T_2 \\ T_3 \\ T_4 \\ T_5 \\ T_6 \end{bmatrix} . \tag{3.9}$$

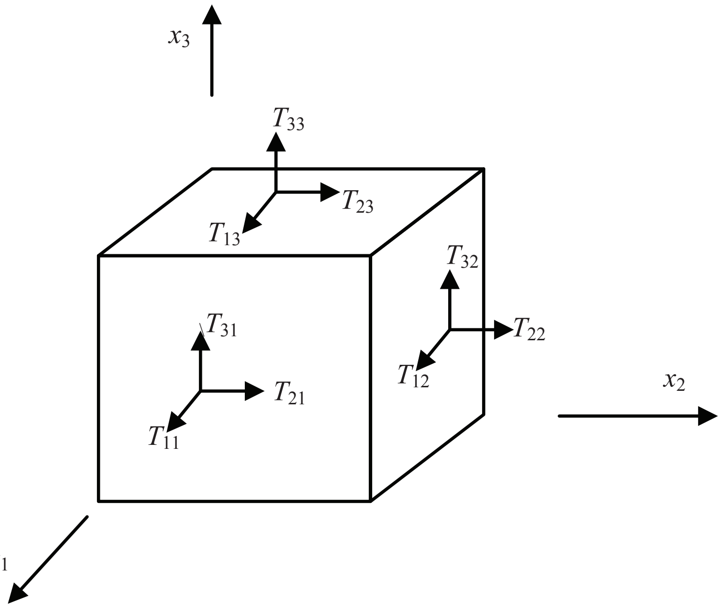

Figure 3.1: Traction forces acting on an infinitesimally small cube.

In equation (3.2), ∇_s is the symmetric part of $\nabla(\mathbf{u^t})$, where ∇ is assumed to be a column vector and $\mathbf{u^t}$ is a row vector. In that case, the vector product $\nabla(\mathbf{u^t})$ represents a matrix

$$\nabla(\mathbf{u^t}) = \begin{bmatrix} \frac{\partial u_1}{\partial x_1} & \frac{\partial u_2}{\partial x_1} & \frac{\partial u_3}{\partial x_1} \\ \frac{\partial u_1}{\partial x_2} & \frac{\partial u_2}{\partial x_2} & \frac{\partial u_3}{\partial x_2} \\ \frac{\partial u_1}{\partial x_3} & \frac{\partial u_2}{\partial x_3} & \frac{\partial u_3}{\partial x_3} \end{bmatrix} , \tag{3.10}$$

and the equation for strain **S** is

$$\mathbf{S} = \nabla_{\mathbf{s}}(\mathbf{u^t}) = \frac{\mathbf{1}}{\mathbf{2}} \left(\nabla(\mathbf{u^t}) + \left(\nabla(\mathbf{u^t})\right)^{\mathbf{t}} \right) , \tag{3.11}$$

where **t** is the transpose of the matrix. It is obvious that the strain tensor **S** is symmetric. Then, similar to equation (3.8), the following abbreviated notation is commonly used

$$\begin{bmatrix} S_1 & S_6 & S_5 \\ S_6 & S_2 & S_4 \\ S_5 & S_4 & S_3 \end{bmatrix} = \begin{bmatrix} S_{11} & 2S_{12} & 2S_{13} \\ 2S_{21} & S_{22} & 2S_{23} \\ 2S_{31} & 2S_{32} & S_{33} \end{bmatrix} . \tag{3.12}$$

Consequently, the strain vector $\mathbf{S}$ can be represented by the following matrix

$$\mathbf{S} = \begin{bmatrix} S_1 \\ S_2 \\ S_3 \\ S_4 \\ S_5 \\ S_6 \end{bmatrix} = \nabla_{Lm}\ \mathbf{u}\ , \tag{3.13}$$

where ∇_{Lm} is the gradient operator ($L = 1$ to 6 and $m = 1$ to 3) that transforms the displacement $\mathbf{u} = [\mathbf{u_1} \quad \mathbf{u_2} \quad \mathbf{u_3}]^{\mathbf{t}}$ into the strain matrix. This gradient operator ∇_{Lm} has a matrix representation

$$\nabla_{Lm} = \begin{bmatrix} \frac{\partial}{\partial x_1} & 0 & 0 \\ 0 & \frac{\partial}{\partial x_2} & 0 \\ 0 & 0 & \frac{\partial}{\partial x_3} \\ 0 & \frac{\partial}{\partial x_3} & \frac{\partial}{\partial x_2} \\ \frac{\partial}{\partial x_3} & 0 & \frac{\partial}{\partial x_1} \\ \frac{\partial}{\partial x_2} & \frac{\partial}{\partial x_1} & 0 \end{bmatrix} . \tag{3.14}$$

3.2.2 Governing equations for piezoelectric materials

For piezoelectric material, the acoustic fields are coupled with the electric fields. Thus, the elastic constitutive equation (3.3) for piezoelectric material is

$$\mathbf{T} = \mathbf{c^E S} - \mathbf{eE}\ , \tag{3.15}$$

and the electric displacement $\mathbf{D}$ can be obtained by the following equation

$$\mathbf{D} = \varepsilon^{\mathbf{S}}\mathbf{E} + \mathbf{eS}\ . \tag{3.16}$$

Here, $\mathbf{E}$ is the electric field, ε^S is the permittivity, c^E is the elastic stiffness constant, and $\mathbf{e}$ is the piezoelectric stress constant. The superscript S and E have been added to ε and c to show that these constants describe dielectric and elastic properties measured under conditions of constant strain and constant electric field, respectively.

As it is mentioned before that the velocity of the elastic waves is 10^3 to 10^5 times slower than that of the electromagnetic waves, the quasi-static approximation was used in our work. According to the quasi-static approximation, the effect of the magnetic field is negligible and the electric field can be derived from a scalar potential Φ

$$\mathbf{E} = -\nabla\Phi\ . \tag{3.17}$$

The governing equations for waves propagating in piezoelectric material shown below can be obtained by combining the Maxwell's equations (3.18-3.19), the equation of motion (3.1), and the constitutive equations (3.15-3.16),

$$-\nabla \times \mathbf{E} = \frac{\partial \mathbf{B}}{\partial t} = 0 \ , \tag{3.18}$$

$$\nabla \times \mathbf{H} = \varepsilon^S \frac{\partial \mathbf{E}}{\partial t} + \frac{\mathbf{e}}{\varepsilon^S} \frac{\partial \mathbf{S}}{\partial t} \ , \tag{3.19}$$

$$\frac{\partial \mathbf{T}}{\partial t} = c^D \frac{\partial \mathbf{S}}{\partial t} - \frac{\mathbf{e}}{\varepsilon^S} \frac{\partial \mathbf{D}}{\partial t} \ , \tag{3.20}$$

$$\nabla \cdot \mathbf{T} = \rho \frac{\partial^2 \mathbf{u}}{\partial t^2} \ . \tag{3.21}$$

Here, the quasi-static approximation is applied and the inner body forces **F** are zero. **B** is the magnetic flux density vector, **H** is the magnetic field vector, c^D is the piezoelectrically stiffened elastic constant, which is different from the elastic stiffness constant c^E. The constant c^D is defined for plane waves and depends on the wave propagation direction, while the constant c^E is measured under a static electric field. The detailed calculation of the constant c^D will be given in the next section.

3.2.2.1 Piezoelectrically stiffened elastic constant

The piezoelectrically stiffened elastic constant c^D can be derived by using the quasi-static approximation [10]. Substitute the strain $\mathbf{S} = \nabla_{Lm}\mathbf{u}$ and the electric field equation (3.17) into the piezoelectric stress equation (3.15), the following equation can be obtained

$$\mathbf{T} = c^E \nabla_{Lm} \mathbf{u} + \mathbf{e} \nabla \Phi \ . \tag{3.22}$$

Hence, the Newton's law equation (3.21) can be written as

$$\nabla \cdot c^E \nabla_{Lm} \mathbf{u} + \nabla \cdot \mathbf{e} \nabla \Phi = \rho \frac{\partial^2 \mathbf{u}}{\partial t^2} \ . \tag{3.23}$$

Similarly, the electric displacement **D** in equation (3.16) can be represented as

$$\mathbf{D} = -\varepsilon^S \nabla \Phi + \mathbf{e} \nabla_{Lm} \mathbf{u} \ , \tag{3.24}$$

and for a source-free medium, this must satisfy the Poisson's equation $\nabla \cdot \mathbf{D} = 0$, so that

$$-\nabla \cdot \varepsilon^S \nabla \Phi + \nabla \cdot \mathbf{e} \nabla_{Lm} \mathbf{u} = 0 \ . \tag{3.25}$$

Equations (3.23) and (3.25) can be expressed in the matrix form as

$$\nabla_{lK} c^E_{KL} \nabla_{Lm} u_m + \nabla_{lK} e_{Km} \nabla_m \Phi = \rho \frac{\partial^2 u_l}{\partial t^2} \ , \tag{3.26}$$

$$\nabla_l \varepsilon^S_{lm} \nabla_m \Phi = \nabla_l e_{lK} \nabla_{Km} u_m \ . \tag{3.27}$$

Here, ∇_{lK} ($l = 1$ to 3 and $K = 1$ to 6) is the transpose of ∇_{Lm} in equation (3.14).

Let us consider a plane wave propagating in a direction $\hat{I}$ in the medium.

$$\hat{I} = \hat{i}l_1 + \hat{j}l_2 + \hat{k}l_3 \ , \tag{3.28}$$

where $\hat{I}$ is a unit vector in the propagation direction, and l_1, l_2, and l_3 are the projections of $\hat{I}$ on the three axes. Then the particle displacement $\mathbf{u}$ is proportional to

$$\mathbf{u} \propto e^{j(\omega t - k\hat{I}\cdot\mathbf{r})} \ , \tag{3.29}$$

where $\mathbf{r} = \hat{i}x_1 + \hat{j}x_2 + \hat{k}x_3$ and k is the wavenumber. Therefore, the derivative of the gradient $\partial\mathbf{u}/\partial x_1$ can be obtained by the following equation

$$\frac{\partial}{\partial x_1} e^{j(\omega t - k\hat{I}\cdot\mathbf{r})} = -jkl_1 e^{j(\omega t - k\hat{I}\cdot\mathbf{r})} = -jkl_1\mathbf{u} \ . \tag{3.30}$$

Similarly, the x_2 and x_3 derivatives of the gradient can be obtained. Thus, the divergence operator ∇_{Lm} can be represented by

$$\nabla_{Lm} = \begin{bmatrix} \frac{\partial}{\partial x_1} & 0 & 0 \\ 0 & \frac{\partial}{\partial x_2} & 0 \\ 0 & 0 & \frac{\partial}{\partial x_3} \\ 0 & \frac{\partial}{\partial x_3} & \frac{\partial}{\partial x_2} \\ \frac{\partial}{\partial x_3} & 0 & \frac{\partial}{\partial x_1} \\ \frac{\partial}{\partial x_2} & \frac{\partial}{\partial x_1} & 0 \end{bmatrix} = -jk \begin{bmatrix} l_1 & 0 & 0 \\ 0 & l_2 & 0 \\ 0 & 0 & l_3 \\ 0 & l_3 & l_2 \\ l_3 & 0 & l_1 \\ l_2 & l_1 & 0 \end{bmatrix} = -jkl_{Lm} \ , \tag{3.31}$$

and the transpose of ∇_{Lm} is

$$\nabla_{lK} = \nabla^t_{Lm} = -jk \begin{bmatrix} l_1 & 0 & 0 & 0 & l_3 & l_2 \\ 0 & l_2 & 0 & l_3 & 0 & l_1 \\ 0 & 0 & l_3 & l_2 & l_1 & 0 \end{bmatrix} \ . \tag{3.32}$$

Consequently, equations (3.26) and (3.27) can be represented by

$$k^2 \left(l_{lK} \ c^E_{KN} \ l_{Nm} \right) u_m + k^2 \left(l_{lK} \ e_{Km} \ l_m \right) \Phi = \rho\omega^2 u_l \ , \tag{3.33}$$

and

$$k^2 \left(l_l \ \varepsilon^S_{lm} \ l_m \right) \Phi = k^2 \left(l_l \ e_{lK} \ l_{Km} \right) u_m \ . \tag{3.34}$$

The factor multiplying Φ on the left-hand side of equation (3.34) is scalar and can be divided out, giving the following equation

$$\Phi = \frac{[l_l \ e_{lN} \ l_{Nm}]}{[l_l \ \varepsilon^S_{lm} \ l_m]} u_m \ . \tag{3.35}$$

Substitute equation (3.35) into equation (3.33), and rearrange some of the terms, the following equation can be obtained

$$k^2 \left(l_{lK} \left(c^E_{KN} + \frac{[e_{Km} \ l_m][l_l \ e_{lN}]}{l_l \ \varepsilon^S_{lm} \ l_m} \right) l_{Nm} \right) u_m = \rho\omega^2 u_l \ . \tag{3.36}$$

This is the Christoffel equation for piezoelectric materials. The piezoelectrically stiffened elastic constant matrix c^D_{KN} can be obtained by

$$c^D_{KN} = c^E_{KN} + \frac{[e_{Km}\ l_m][l_l\ e_{lN}]}{l_l\ \varepsilon^S_{lm}\ l_m}\ . \tag{3.37}$$

The piezoelectrically stiffened elastic constant c^D is dependent on the piezoelectric constant, the permittivity and the wave propagation direction.

3.3 Elastic waves in two-dimensional model

The governing equations for the piezoelectric material and the electrodes in two-dimensional model are developed in this section, which will be discretized into the finite-difference time-domain (FDTD) governing equations in the next section. To develop the two-dimensional governing equations, a schematic of the generic FBAR resonator (shown in Fig.3.2) is considered.

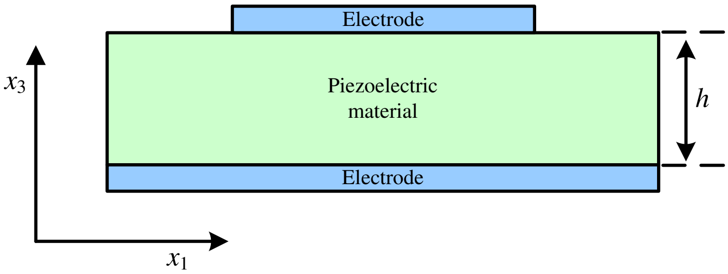

Figure 3.2: Two-dimensional schematic of a generic FBAR resonator.

3.3.1 Governing equations for piezoelectric material

The piezoelectric material considered in this project is AlN, which belongs to the hexagonal system[95]. Therefore, equations (3.15) and (3.16) can be expressed by the matrix equations

$$\begin{bmatrix} T_1 \\ T_2 \\ T_3 \\ T_4 \\ T_5 \\ T_6 \end{bmatrix} = \begin{bmatrix} c_{11}^E & c_{12}^E & c_{13}^E & 0 & 0 & 0 \\ c_{12}^E & c_{11}^E & c_{13}^E & 0 & 0 & 0 \\ c_{13}^E & c_{13}^E & c_{33}^E & 0 & 0 & 0 \\ 0 & 0 & 0 & c_{44}^E & 0 & 0 \\ 0 & 0 & 0 & 0 & c_{44}^E & 0 \\ 0 & 0 & 0 & 0 & 0 & c_{66}^E \end{bmatrix} \begin{bmatrix} S_1 \\ S_2 \\ S_3 \\ S_4 \\ S_5 \\ S_6 \end{bmatrix} - \begin{bmatrix} 0 & 0 & e_{31} \\ 0 & 0 & e_{31} \\ 0 & 0 & e_{33} \\ 0 & e_{15} & 0 \\ e_{15} & 0 & 0 \\ 0 & 0 & 0 \end{bmatrix} \begin{bmatrix} E_1 \\ E_2 \\ E_3 \end{bmatrix} ,(3.38)$$

$$\begin{bmatrix} D_1 \\ D_2 \\ D_3 \end{bmatrix} = \begin{bmatrix} \varepsilon_{11}^S & 0 & 0 \\ 0 & \varepsilon_{11}^S & 0 \\ 0 & 0 & \varepsilon_{33}^S \end{bmatrix} \begin{bmatrix} E_1 \\ E_2 \\ E_3 \end{bmatrix} + \begin{bmatrix} 0 & 0 & 0 & 0 & e_{15} & 0 \\ 0 & 0 & 0 & e_{15} & 0 & 0 \\ e_{31} & e_{31} & e_{33} & 0 & 0 & 0 \end{bmatrix} \begin{bmatrix} S_1 \\ S_2 \\ S_3 \\ S_4 \\ S_5 \\ S_6 \end{bmatrix} .(3.39)$$

The elastic stiffness, mass density, permittivity and piezoelectric constants of AlN are given in Table 3.1. Since AlN belongs to the hexagonal system, the stiffness component c_{66}^E can be obtained by $c_{66}^E = (c_{11}^E - c_{12}^E)/2$.

Table 3.1: Elastic stiffness, mass density, permittivity and piezoelectric constants of AlN

Elastic stiffness (10^{11} N/m^2)					Mass density (kg/m^3)	Permittivity ($\varepsilon_r^S/\varepsilon_o$)		Piezoelectric constant (C/m^2)		
c_{11}^E	c_{12}^E	c_{13}^E	c_{33}^E	c_{44}^E	ρ_{AlN}	ε_{11}^S	ε_{33}^S	e_{15}	e_{31}	e_{33}
3.45	1.25	1.20	3.95	1.18	3512	9	11	-0.48	-0.58	1.55

In this study, the Euler angles of the materials were set at $< 0°, 0°, 0° >$. Hence, the crystalline axes X, Y, and Z coincided with the axes x_1, x_2, and x_3, respectively [19]. Therefore, no coordinate conversion is needed. A 2D FDTD (two-dimensional finite-difference time-domain) model was set up to simulate the FBAR resonators. In this 2D model, only the variables in the $x_1 - x_3$ plane were considered. Therefore, the governing equations of waves propagating in AlN can be obtained by applying the material properties to equations (3.20) and (3.21), and eliminating the strain by equation (3.13),

$$\frac{\partial T_1}{\partial t} = c_{11}^D \frac{\partial^2 u_1}{\partial x_1 \partial t} + c_{13}^D \frac{\partial^2 u_3}{\partial x_3 \partial t} - \frac{e_{31}}{\varepsilon_{33}^S} \frac{\partial D_3}{\partial t} \ , \tag{3.40}$$

$$\frac{\partial T_3}{\partial t} = c_{13}^D \frac{\partial^2 u_1}{\partial x_1 \partial t} + c_{33}^D \frac{\partial^2 u_3}{\partial x_3 \partial t} - \frac{e_{33}}{\varepsilon_{33}^S} \frac{\partial D_3}{\partial t} \ , \tag{3.41}$$

$$\frac{\partial T_5}{\partial t} = c_{44}^D \frac{\partial^2 u_1}{\partial x_3 \partial t} + c_{44}^D \frac{\partial^2 u_3}{\partial x_1 \partial t} - \frac{e_{15}}{\varepsilon_{11}^S} \frac{\partial D_1}{\partial t} \ , \tag{3.42}$$

$$\rho_{AlN} \frac{\partial^2 u_1}{\partial t^2} = \frac{\partial T_1}{\partial x_1} + \frac{\partial T_5}{\partial x_3} \ , \tag{3.43}$$

$$\rho_{AlN} \frac{\partial^2 u_3}{\partial t^2} = \frac{\partial T_5}{\partial x_1} + \frac{\partial T_3}{\partial x_3} \ . \tag{3.44}$$

The values of c^D can be obtained by equation (3.37) derived in Section 3.2.2.1. Since in FBAR the fundamental mode utilized is the thickness resonance mode, in this study the wave vector direction is assumed to be along the x_3-axis. Thus the wave vector in equation (3.28) is

$$\hat{I} = \hat{k} l_3 \ . \tag{3.45}$$

Substituting the values of the piezoelectric constant of AlN (shown in equation (3.38)) into equation (3.37), the second factor in the numerator of the stiffening term can be obtained by

$$[l_l e_{lN}] = \begin{bmatrix} 0 & 0 & 1 \end{bmatrix} \begin{bmatrix} 0 & 0 & 0 & 0 & e_{15} & 0 \\ 0 & 0 & 0 & e_{15} & 0 & 0 \\ e_{31} & e_{31} & e_{33} & 0 & 0 & 0 \end{bmatrix} = \begin{bmatrix} e_{31} & e_{31} & e_{33} & 0 & 0 & 0 \end{bmatrix} \ , \tag{3.46}$$

and the first factor $[e_{Km}\ l_m]$ is the transpose of $[l_l\ e_{lN}]$. Thus,

$$[e_{Km}\ l_m]\,[l_l\ e_{lN}] = \begin{bmatrix} e_{31} \\ e_{31} \\ e_{33} \\ 0 \\ 0 \\ 0 \end{bmatrix} \begin{bmatrix} e_{31} & e_{31} & e_{33} & 0 & 0 & 0 \end{bmatrix} \quad . \tag{3.47}$$

$$= \begin{bmatrix} e_{31}^2 & e_{31}^2 & e_{31}e_{33} & 0 & 0 & 0 \\ e_{31}^2 & e_{31}^2 & e_{31}e_{33} & 0 & 0 & 0 \\ e_{31}e_{33} & e_{31}e_{33} & e_{33}^2 & 0 & 0 & 0 \\ 0 & 0 & 0 & 0 & 0 & 0 \\ 0 & 0 & 0 & 0 & 0 & 0 \\ 0 & 0 & 0 & 0 & 0 & 0 \end{bmatrix}$$

And the denominator is

$$l_l\ \varepsilon_{lm}^S\ l_m = \begin{bmatrix} 0 & 0 & 1 \end{bmatrix} \begin{bmatrix} \varepsilon_{11}^S & 0 & 0 \\ 0 & \varepsilon_{11}^S & 0 \\ 0 & 0 & \varepsilon_{33}^S \end{bmatrix} \begin{bmatrix} 0 \\ 0 \\ 1 \end{bmatrix} = \varepsilon_{33}^S\ . \tag{3.48}$$

Thus, the piezoelectrically stiffened elastic constant matrix $\mathbf{c^D}$ of AlN can be expressed as

$$\left[\mathbf{c^D}\right] = \begin{bmatrix} c_{11}^E + \frac{e_{31}^2}{\varepsilon_{33}^S} & c_{12}^E + \frac{e_{31}^2}{\varepsilon_{33}^S} & c_{13}^E + \frac{e_{31}e_{33}}{\varepsilon_{33}^S} & 0 & 0 & 0 \\ c_{12}^E + \frac{e_{31}^2}{\varepsilon_{33}^S} & c_{11}^E + \frac{e_{31}^2}{\varepsilon_{33}^S} & c_{13}^E + \frac{e_{31}e_{33}}{\varepsilon_{33}^S} & 0 & 0 & 0 \\ c_{13}^E + \frac{e_{31}e_{33}}{\varepsilon_{33}^S} & c_{13}^E + \frac{e_{31}e_{33}}{\varepsilon_{33}^S} & c_{33}^E + \frac{e_{33}^2}{\varepsilon_{33}^S} & 0 & 0 & 0 \\ 0 & 0 & 0 & c_{44}^E & 0 & 0 \\ 0 & 0 & 0 & 0 & c_{44}^E & 0 \\ 0 & 0 & 0 & 0 & 0 & c_{66}^E \end{bmatrix} \quad . \tag{3.49}$$

By rearranging the terms in equation (3.16) and differentiating the variables with respect to t, the detected electric field can be obtained by the following equations,

$$\frac{\partial E_1}{\partial t} = -\frac{e_{15}}{\varepsilon_{11}^S}\left(\frac{\partial^2 u_1}{\partial x_3 \partial t} + \frac{\partial^2 u_3}{\partial x_1 \partial t}\right) + \frac{1}{\varepsilon_{11}^S}\frac{\partial D_1}{\partial t} \ , \tag{3.50}$$

$$\frac{\partial E_3}{\partial t} = -\frac{e_{31}}{\varepsilon_{33}^S}\frac{\partial^2 u_1}{\partial x_1 \partial t} - \frac{e_{33}}{\varepsilon_{33}^S}\frac{\partial^2 u_3}{\partial x_3 \partial t} + \frac{1}{\varepsilon_{33}^S}\frac{\partial D_3}{\partial t} \ . \tag{3.51}$$

The electric potential U_3 along the thickness direction is calculated by

$$U_3 = -\int_h E_3 \, dh \ , \tag{3.52}$$

where h is the thickness of the piezoelectric material between the two electrodes (as shown in Fig. 3.2). The electric impedance Z is calculated by

$$Z = \frac{U(\omega)}{I(\omega)} \ , \tag{3.53}$$

where $U(\omega)$ is the electric potential in frequency domain, and $I(\omega)$ is the electric current in frequency domain.

The governing equations with particle displacement contain second-order derivatives. However, due to the second-order characteristics of the wave equations, the finite-difference equations are complicated and the boundary conditions are difficult to implement. Because of its simplicity, the first-order approach is presently the most popular approach for finite-difference modeling in electromagnetics.

To simplify the governing equations (3.40) - (3.44) and (3.50) - (3.51) from the second-order partial differential equations to the first-order partial differential equations, the particle velocity is introduced for the particle displacement. The particle velocity is the time derivative of the displacement vector:

$$\mathbf{v} = \frac{\partial \mathbf{u}}{\partial \mathbf{t}} \ . \tag{3.54}$$

Replacing $\frac{\partial u_m}{\partial t}$ with v_m (m =1 and 3). The governing equations with only first-order derivatives can be obtained as

$$\frac{\partial T_1}{\partial t} = c_{11}^D \frac{\partial v_1}{\partial x_1} + c_{13}^D \frac{\partial v_3}{\partial x_3} - \frac{e_{31}}{\varepsilon_{33}^S} \frac{\partial D_3}{\partial t} \ , \tag{3.55}$$

$$\frac{\partial T_3}{\partial t} = c_{13}^D \frac{\partial v_1}{\partial x_1} + c_{33}^D \frac{\partial v_3}{\partial x_3} - \frac{e_{33}}{\varepsilon_{33}^S} \frac{\partial D_3}{\partial t} \ , \tag{3.56}$$

$$\frac{\partial T_5}{\partial t} = c_{44}^D \frac{\partial v_1}{\partial x_3} + c_{44}^D \frac{\partial v_3}{\partial x_1} - \frac{e_{15}}{\varepsilon_{11}^S} \frac{\partial D_1}{\partial t} \ , \tag{3.57}$$

$$\rho_{AlN} \frac{\partial v_1}{\partial t} = \frac{\partial T_1}{\partial x_1} + \frac{\partial T_5}{\partial x_3} \ , \tag{3.58}$$

$$\rho_{AlN} \frac{\partial v_3}{\partial t} = \frac{\partial T_5}{\partial x_1} + \frac{\partial T_3}{\partial x_3} \ , \tag{3.59}$$

$$\frac{\partial E_1}{\partial t} = -\frac{e_{15}}{\varepsilon_{11}^S} \left(\frac{\partial v_1}{\partial x_3} + \frac{\partial v_3}{\partial x_1} \right) + \frac{1}{\varepsilon_{11}^S} \frac{\partial D_1}{\partial t} \ , \tag{3.60}$$

$$\frac{\partial E_3}{\partial t} = -\frac{e_{31}}{\varepsilon_{33}^S} \frac{\partial v_1}{\partial x_1} - \frac{e_{33}}{\varepsilon_{33}^S} \frac{\partial v_3}{\partial x_3} + \frac{1}{\varepsilon_{33}^S} \frac{\partial D_3}{\partial t} \ . \tag{3.61}$$

3.3.2 Governing equations for metal

The electrode materials for FBAR resonators, such as the commonly used Al, W, and Ru, are non-piezoelectric materials, which belong to the cubic system [95]. Thus, the piezoelectric constants **e** do not exist for these materials, and the elastic stiffness constants and permittivity need not to be measured under a constant electric field and a constant strain, respectively. Equations (3.15) and (3.16) can be simplified and expressed in the following matrix equations

$$\begin{bmatrix} T_1 \\ T_2 \\ T_3 \\ T_4 \\ T_5 \\ T_6 \end{bmatrix} = \begin{bmatrix} c_{11} & c_{12} & c_{12} & 0 & 0 & 0 \\ c_{12} & c_{11} & c_{12} & 0 & 0 & 0 \\ c_{12} & c_{12} & c_{11} & 0 & 0 & 0 \\ 0 & 0 & 0 & c_{44} & 0 & 0 \\ 0 & 0 & 0 & 0 & c_{44} & 0 \\ 0 & 0 & 0 & 0 & 0 & c_{44} \end{bmatrix} \begin{bmatrix} S_1 \\ S_2 \\ S_3 \\ S_4 \\ S_5 \\ S_6 \end{bmatrix} , \tag{3.62}$$

$$\begin{bmatrix} D_1 \\ D_2 \\ D_3 \end{bmatrix} = \begin{bmatrix} \varepsilon_{11} & 0 & 0 \\ 0 & \varepsilon_{11} & 0 \\ 0 & 0 & \varepsilon_{11} \end{bmatrix} \begin{bmatrix} E_1 \\ E_2 \\ E_3 \end{bmatrix} . \tag{3.63}$$

Here, c_{ij} and ε_{ij} are the elastic stiffness constant and permittivity of non-piezoelectric materials, respectively.

Aluminum is used as the electrodes in this study. The elastic stiffness, mass density and permittivity of Al are given in Table 3.2.

Table 3.2: Elastic stiffness, mass density, and permittivity of Al

Elastic stiffness (10^{10} N/m^2)			Mass density (kg/m^3)	Permittivity ($\varepsilon_r/\varepsilon_o$)
c_{11}	c_{12}	c_{44}	ρ_{Al}	ε_{11}
10.80	6.13	2.85	2700	1

There is no electric field within the metal electrodes. Thus, applying the material properties of Al to equations (3.20) and (3.21), the first-order governing equations of wave propagating in Al can be expressed as

$$\frac{\partial T_1}{\partial t} = c_{11}\frac{\partial v_1}{\partial x_1} + c_{12}\frac{\partial v_3}{\partial x_3} \ , \tag{3.64}$$

$$\frac{\partial T_3}{\partial t} = c_{12}\frac{\partial v_1}{\partial x_1} + c_{33}\frac{\partial v_3}{\partial x_3} \ , \tag{3.65}$$

$$\frac{\partial T_5}{\partial t} = c_{44}\frac{\partial v_1}{\partial x_3} + c_{44}\frac{\partial v_3}{\partial x_1} \ , \tag{3.66}$$

$$\rho_{Al}\frac{\partial v_1}{\partial t} = \frac{\partial T_1}{\partial x_1} + \frac{\partial T_5}{\partial x_3} \ , \tag{3.67}$$

$$\rho_{Al}\frac{\partial v_3}{\partial t} = \frac{\partial T_5}{\partial x_1} + \frac{\partial T_3}{\partial x_3} \ . \tag{3.68}$$

3.4 FDTD spatial and temporal discretizations

As the governing equations (3.55)-(3.61) and (3.64)-(3.68) in the partial differential form cannot be solved analytically, in this study, the numerical finite-difference scheme is used. In the finite-difference scheme, the partial differential equations are commonly discretized using centered finite differences. Let $f(x)$ be one of the continuous function in the system of the governing equations. For a finite difference Δx, the derivative of a function $f = f(x)$ with respect to x at the point x_0 can be approximated by a centered finite difference:

$$\begin{aligned}\frac{\partial f}{\partial x}|_{x=x_0} &= \frac{f(x_0+\Delta x/2) - f(x_0-\Delta x/2)}{\Delta x} - \frac{(\Delta x)^2}{24}\frac{\partial^3 f}{\partial x^3}|_{x=x_0} - \frac{(\Delta x)^4}{384}\frac{\partial^5 f}{\partial x^5}|_{x=x_0} + \cdots \\ &= \frac{f(x_0+\Delta x/2) - f(x_0-\Delta x/2)}{\Delta x} + O\left(\Delta x^2\right)\end{aligned} \tag{3.69}$$

In equation (3.69), the term $O\left(\Delta x^2\right)$ denotes the error term. The smaller the finite difference Δx is, the higher accuracy can be obtained. When the finite difference Δx is sufficiently small, equation (3.69) can be approximated to

$$\frac{\partial f}{\partial x}|_{x=x_0} = \frac{f(x_0 + \Delta x/2) - f(x_0 - \Delta x/2)}{\Delta x} \; . \tag{3.70}$$

A second-order accurate centered finite difference is obtained by equation (3.70).

In the FDTD algorithm, the governing partial differential equations are approximated by the second-order accurate centered finite difference for both the space and time derivatives.

3.4.1 FDTD spatial discretization

When applying the centered finite difference discretization to the governing partial differential equations, a discrete grid of regular rectangular shape arises. The spatial layout of the field variables in the proposed FDTD model is shown in Figure 3.3. In this layout, each field component is surrounded by the field components it is dependent on[84]. One important characteristic of the finite-difference grid is that the particle velocity and the stress components are not allocated at the same points in space. The structure of the finite-difference grid is quite similar to the one used for the electromagnetic finite-difference modeling, which is called the Yee-cell[111]. The main difference between the proposed FDTD model and the electromagnetic FDTD model is that the proposed FDTD model includes the electric and acoustic field components instead of the electric and magnetic field components.

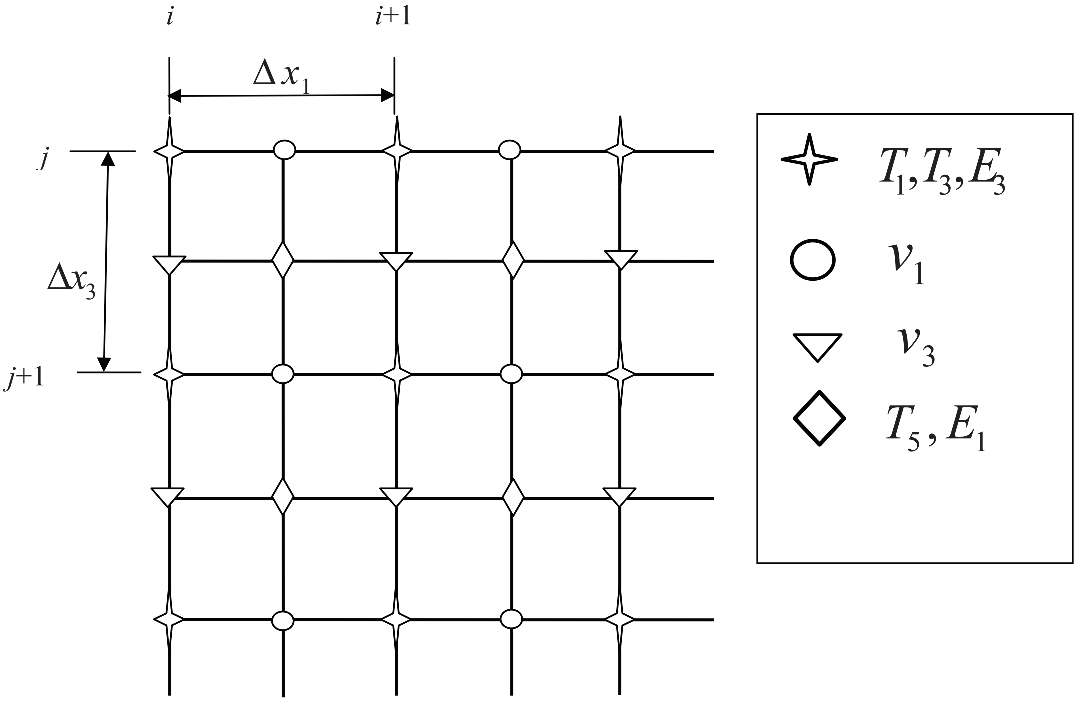

Figure 3.3: Spatial layout of the variables in the FDTD model.

The finite-difference grid can be viewed as being composed of basis cells. Each basis cell is characterized by the space step sizes Δx_1 and Δx_3 in the x_1 and x_3 direction, respectively. The position of the cell component in real space can be identified by $x_1 = i \cdot \Delta x_1$ and $x_3 = j \cdot \Delta x_3$ [84]. The positions of the field components of the (i, j)-th cell in real space are listed in Table 3.3.

Table 3.3: Positions of the field components of the (i, j)-th cell in the finite-difference grid.

Field component	x_1	x_3
T_1	$i\Delta x_1$	$j\Delta x_3$
T_3	$i\Delta x_1$	$j\Delta x_3$
T_5	$\left(i+\frac{1}{2}\right)\Delta x_1$	$\left(j+\frac{1}{2}\right)\Delta x_3$
v_1	$\left(i+\frac{1}{2}\right)\Delta x_1$	$j\Delta x_3$
v_3	$i\Delta x_1$	$\left(j+\frac{1}{2}\right)\Delta x_3$
E_1	$\left(i+\frac{1}{2}\right)\Delta x_1$	$\left(j+\frac{1}{2}\right)\Delta x_3$
E_3	$i\Delta x_1$	$j\Delta x_3$

3.4.2 FDTD temporal discretization

The same centered finite-difference approximation is applied to the field components in time [84]. The time derivative of a function $f = f(t)$ at t_0 can be expressed by introducing a finite difference Δt:

$$\frac{\partial f}{\partial t}\Big|_{t=t_0} = \frac{f(t_0 + \Delta t/2) - f(t_0 - \Delta t/2)}{\Delta t} \ . \tag{3.71}$$

In the temporal discretization, the discrete time is labeled with the index n. Assuming the increment time of the finite-difference algorithm to be Δt, the values of the stress and electric field components are set to be known at the full time step, $t = n\Delta t$, while the values of the particle velocity components are evaluated at the half time step, $t = \left(n + \frac{1}{2}\right)\Delta t$. This time update scheme is the so-called leap-frog scheme[111]. Note that this method is an explicit method. Updating the values of the components only depends on the results at the previous times.

Applying finite differences in both space and time, the partial differential equations are approximately discretized into difference equations. For example, applying the discretization to equation (3.56) yields

$$\frac{\left(T_3\Big|_{i,j}^{n+1} - T_3\Big|_{i,j}^{n}\right)}{\Delta t} = \left[\frac{c_{13}^D}{\Delta x_1}\left(v_1\Big|_{i+\frac{1}{2},j}^{n+\frac{1}{2}} - v_1\Big|_{i-\frac{1}{2},j}^{n+\frac{1}{2}}\right) + \frac{c_{33}^D}{\Delta x_3}\left(v_3\Big|_{i,j+\frac{1}{2}}^{n+\frac{1}{2}} - v_3\Big|_{i,j-\frac{1}{2}}^{n+\frac{1}{2}}\right)\right] \ .$$

$$- \frac{e_{33}}{\varepsilon_{33}^S}\frac{D_3\Big|_{i,j}^{n+1} - D_3\Big|_{i,j}^{n}}{\Delta t} \tag{3.72}$$

By rearranging the terms, the FDTD equation for the longitudinal stress T_3 at the incremented time $t = (n+1)\Delta t$ can be obtained as

$$
\begin{aligned}
T_3\Big|_{i,j}^{n+1} = T_3\Big|_{i,j}^{n} + \Delta t \left[\frac{c_{13}^D}{\Delta x_1}\left(v_1\Big|_{i+\frac{1}{2},j}^{n+\frac{1}{2}} - v_1\Big|_{i-\frac{1}{2},j}^{n+\frac{1}{2}}\right) + \frac{c_{33}^D}{\Delta x_3}\left(v_3\Big|_{i,j+\frac{1}{2}}^{n+\frac{1}{2}} - v_3\Big|_{i,j-\frac{1}{2}}^{n+\frac{1}{2}}\right)\right] & . \\
- \frac{e_{33}}{\varepsilon_{33}^S}\left(D_3\Big|_{i,j}^{n+1} - D_3\Big|_{i,j}^{n}\right) &
\end{aligned}
\tag{3.73}
$$

The symbol $T_3\Big|_{i,j}^{n+1}$ denotes the numerical value of the stress component T_3 at the position $x_1 = i\Delta x_1$ and $x_3 = j\Delta x_3$ at the time $t = (n+1)\Delta t$. According to equation (3.73), $T_3\Big|_{i,j}^{n+1}$ can be evaluated by the stress component at the previous time step $T_3\Big|_{i,j}^{n}$ and the adjacent particle velocities at the previous half time step. The effect of the external electric field is also included by including the difference between the current field value $D_3\Big|_{i,j}^{n+1}$ and the previous field value $D_3\Big|_{i,j}^{n}$.

3.4.3 Governing equations of piezoelectric material in FDTD model

By applying the finite-difference scheme in space and time as it is stated in Section 3.4.2, the discrete governing equations of AlN in the FDTD model can be obtained. Firstly, for the stress components in AlN, equations (3.55) - (3.57) are discretized as

$$
\begin{aligned}
T_1\Big|_{i,j}^{n+1} = T_1\Big|_{i,j}^{n} + \Delta t \left[\frac{c_{11}^D}{\Delta x_1}\left(v_1\Big|_{i+\frac{1}{2},j}^{n+\frac{1}{2}} - v_1\Big|_{i-\frac{1}{2},j}^{n+\frac{1}{2}}\right) + \frac{c_{13}^D}{\Delta x_3}\left(v_3\Big|_{i,j+\frac{1}{2}}^{n+\frac{1}{2}} - v_3\Big|_{i,j-\frac{1}{2}}^{n+\frac{1}{2}}\right)\right] & , \\
- \frac{e_{31}}{\varepsilon_{33}^S}\left(D_3\Big|_{i,j}^{n+1} - D_3\Big|_{i,j}^{n}\right) &
\end{aligned}
\tag{3.74}
$$

$$
\begin{aligned}
T_3\Big|_{i,j}^{n+1} = T_3\Big|_{i,j}^{n} + \Delta t \left[\frac{c_{13}^D}{\Delta x_1}\left(v_1\Big|_{i+\frac{1}{2},j}^{n+\frac{1}{2}} - v_1\Big|_{i-\frac{1}{2},j}^{n+\frac{1}{2}}\right) + \frac{c_{33}^D}{\Delta x_3}\left(v_3\Big|_{i,j+\frac{1}{2}}^{n+\frac{1}{2}} - v_3\Big|_{i,j-\frac{1}{2}}^{n+\frac{1}{2}}\right)\right] & , \\
- \frac{e_{33}}{\varepsilon_{33}^S}\left(D_3\Big|_{i,j}^{n+1} - D_3\Big|_{i,j}^{n}\right) &
\end{aligned}
\tag{3.75}
$$

$$
\begin{aligned}
T_5\Big|_{i+\frac{1}{2},j+\frac{1}{2}}^{n+1} = {} & T_5\Big|_{i+\frac{1}{2},j+\frac{1}{2}}^{n} \\
& + \Delta t \left[\frac{c_{44}^D}{\Delta x_3}\left(v_1\Big|_{i+\frac{1}{2},j+1}^{n+\frac{1}{2}} - v_1\Big|_{i+\frac{1}{2},j}^{n+\frac{1}{2}}\right) + \frac{c_{44}^D}{\Delta x_1}\left(v_3\Big|_{i+1,j+\frac{1}{2}}^{n+\frac{1}{2}} - v_3\Big|_{i,j+\frac{1}{2}}^{n+\frac{1}{2}}\right)\right] . \\
& - \frac{e_{15}}{\varepsilon_{11}^S}\left(D_1\Big|_{i+\frac{1}{2},j+\frac{1}{2}}^{n+1} - D_1\Big|_{i+\frac{1}{2},j+\frac{1}{2}}^{n}\right)
\end{aligned}
\tag{3.76}
$$

Secondly, for the particle velocity components in AlN, equations (3.58) and (3.59) are discretized as

$$v_1\Big|_{i+\frac{1}{2},j}^{n+\frac{1}{2}} = v_1\Big|_{i+\frac{1}{2},j}^{n-\frac{1}{2}} + \frac{\Delta t}{\rho_{AlN}}\left[\frac{1}{\Delta x_1}\left(T_1\Big|_{i+1,j}^{n} - T_1\Big|_{i,j}^{n}\right) + \frac{1}{\Delta x_3}\left(T_5\Big|_{i+\frac{1}{2},j+\frac{1}{2}}^{n} - T_5\Big|_{i+\frac{1}{2},j-\frac{1}{2}}^{n}\right)\right], \tag{3.77}$$

$$v_3\Big|_{i,j+\frac{1}{2}}^{n+\frac{1}{2}} = v_3\Big|_{i,j+\frac{1}{2}}^{n-\frac{1}{2}} + \frac{\Delta t}{\rho_{AlN}}\left[\frac{1}{\Delta x_1}\left(T_5\Big|_{i+\frac{1}{2},j+\frac{1}{2}}^{n} - T_5\Big|_{i-\frac{1}{2},j+\frac{1}{2}}^{n}\right) + \frac{1}{\Delta x_3}\left(T_3\Big|_{i,j+1}^{n} - T_3\Big|_{i,j}^{n}\right)\right]. \tag{3.78}$$

Finally, for the electric components in AlN, equations (3.60) and (3.61) are discretized as

$$\begin{aligned} E_1\Big|_{i+\frac{1}{2},j+\frac{1}{2}}^{n+1} &= E_1\Big|_{i+\frac{1}{2},j+\frac{1}{2}}^{n} \\ &- \frac{e_{15}\Delta t}{\varepsilon_{11}^S}\left[\frac{1}{\Delta x_3}\left(v_1\Big|_{i+\frac{1}{2},j+1}^{n+\frac{1}{2}} - v_1\Big|_{i+\frac{1}{2},j}^{n+\frac{1}{2}}\right) + \frac{1}{\Delta x_1}\left(v_3\Big|_{i+1,j+\frac{1}{2}}^{n+\frac{1}{2}} - v_3\Big|_{i,j+\frac{1}{2}}^{n+\frac{1}{2}}\right)\right], \\ &+ \frac{1}{\varepsilon_{11}^S}\left(D_1\Big|_{i+\frac{1}{2},j+\frac{1}{2}}^{n+1} - D_1\Big|_{i+\frac{1}{2},j+\frac{1}{2}}^{n}\right) \end{aligned} \tag{3.79}$$

$$\begin{aligned} E_3\Big|_{i,j}^{n+1} &= E_3\Big|_{i,j}^{n} - \frac{e_{31}\Delta t}{\varepsilon_{11}^S\Delta x_1}\left(v_1\Big|_{i+\frac{1}{2},j}^{n+\frac{1}{2}} - v_1\Big|_{i-\frac{1}{2},j}^{n+\frac{1}{2}}\right) - \frac{e_{33}\Delta t}{\varepsilon_{33}^S\Delta x_3}\left(v_3\Big|_{i,j+\frac{1}{2}}^{n+\frac{1}{2}} - v_3\Big|_{i,j-\frac{1}{2}}^{n+\frac{1}{2}}\right) \\ &. \\ &+ \frac{1}{\varepsilon_{33}^S}\left(D_3\Big|_{i,j}^{n+1} - D_3\Big|_{i,j}^{n}\right) \end{aligned} \tag{3.80}$$

3.4.4 Governing equations of metal in FDTD model

Similarly, by applying the finite-difference scheme in space and time as it is stated in Section 3.4.2, the discrete governing equations of Al in the FDTD model can be obtained. Note that the commonly used W and Ru will have the same governing equations as Al, because they all belong to the cubic system. For the stress and particle velocity components in Al, equations (3.64) - (3.68) are discretized as

$$T_1\Big|_{i,j}^{n+1} = T_1\Big|_{i,j}^{n} + \Delta t\left[\frac{c_{11}}{\Delta x_1}\left(v_1\Big|_{i+\frac{1}{2},j}^{n+\frac{1}{2}} - v_1\Big|_{i-\frac{1}{2},j}^{n+\frac{1}{2}}\right) + \frac{c_{12}}{\Delta x_3}\left(v_3\Big|_{i,j+\frac{1}{2}}^{n+\frac{1}{2}} - v_3\Big|_{i,j-\frac{1}{2}}^{n+\frac{1}{2}}\right)\right], \tag{3.81}$$

$$T_3\Big|_{i,j}^{n+1} = T_3\Big|_{i,j}^{n} + \Delta t\left[\frac{c_{12}}{\Delta x_1}\left(v_1\Big|_{i+\frac{1}{2},j}^{n+\frac{1}{2}} - v_1\Big|_{i-\frac{1}{2},j}^{n+\frac{1}{2}}\right) + \frac{c_{33}}{\Delta x_3}\left(v_3\Big|_{i,j+\frac{1}{2}}^{n+\frac{1}{2}} - v_3\Big|_{i,j-\frac{1}{2}}^{n+\frac{1}{2}}\right)\right], \tag{3.82}$$

$$T_5\Big|_{i+\frac{1}{2},j+\frac{1}{2}}^{n+1} = T_5\Big|_{i+\frac{1}{2},j+\frac{1}{2}}^{n}$$

$$+\Delta t\left[\frac{c_{44}}{\Delta x_3}\left(v_1\Big|_{i+\frac{1}{2},j+1}^{n+\frac{1}{2}} - v_1\Big|_{i+\frac{1}{2},j}^{n+\frac{1}{2}}\right) + \frac{c_{44}}{\Delta x_1}\left(v_3\Big|_{i+1,j+\frac{1}{2}}^{n+\frac{1}{2}} - v_3\Big|_{i,j+\frac{1}{2}}^{n+\frac{1}{2}}\right)\right],$$

$$v_1\Big|_{i+\frac{1}{2},j}^{n+\frac{1}{2}} = v_1\Big|_{i+\frac{1}{2},j}^{n-\frac{1}{2}} + \frac{\Delta t}{\rho_{Al}}\left[\frac{1}{\Delta x_1}\left(T_1\big|_{i+1,j}^{n} - T_1\big|_{i,j}^{n}\right) + \frac{1}{\Delta x_3}\left(T_5\Big|_{i+\frac{1}{2},j+\frac{1}{2}}^{n} - T_5\Big|_{i+\frac{1}{2},j-\frac{1}{2}}^{n}\right)\right], \tag{3.83}$$

$$v_3\Big|_{i,j+\frac{1}{2}}^{n+\frac{1}{2}} = v_3\Big|_{i,j+\frac{1}{2}}^{n-\frac{1}{2}} + \frac{\Delta t}{\rho_{Al}}\left[\frac{1}{\Delta x_1}\left(T_5\Big|_{i+\frac{1}{2},j+\frac{1}{2}}^{n} - T_5\Big|_{i-\frac{1}{2},j+\frac{1}{2}}^{n}\right) + \frac{1}{\Delta x_3}\left(T_3\big|_{i,j+1}^{n} - T_3\big|_{i,j}^{n}\right)\right]. \tag{3.84}$$

3.5 Numerical analysis of the FDTD algorithm: dispersion and stability

The FDTD algorithm provides a good approximation to the real physical behavior of the fields. However, the finite-difference approximation of derivatives of continuous functions unavoidably introduces an error to the solution. To reduce the numerical error to an acceptable extent, the numerical dispersion and stability of the FDTD scheme are discussed in this section. The restrictions of the spatial step sizes Δx_1 and Δx_3 and the time step size Δt are investigated, respectively.

3.5.1 Numerical dispersion

Numerical dispersion is an undesired nonphysical effect inherently present in the FDTD algorithm. The finite-difference approximation of derivatives of continuous functions unavoidably introduces an error to the solution. This means that the wave propagation velocity of the numerical solution will generally differ from the actual wave velocity, and vary with frequency, the spatial grid size, and the wave propagation direction. The differences of phase velocities numerically obtained by the FDTD method from the actual phase velocities is referred to as numerical dispersion, which exposes itself as a distortion of the waveform.

In practice, in order to reduce this numerical dispersion to an acceptable extent, the space step size should not exceed one twentieth of the minimum wavelength excited within the model. That is

$$\Delta x_1, \Delta x_3 < \frac{\lambda_{min}}{20}, \tag{3.85}$$

and

$$\lambda_{min} = \frac{v_{min}}{f_{max}} \ , \tag{3.86}$$

where f_{max} is the maximum frequency of the excited source, and v_{min} is the minimum phase velocity of the acoustic wave propagating in the structure.

3.5.2 Numerical stability

Numerical instability is an undesired possibility that the numerically calculated results can spuriously increase without limit as time-marching continues. The FDTD algorithm samples the acoustic and electric fields at discrete points both in time and space. The sampling step sizes (Δt in time, Δx_1, and Δx_3 in space) must satisfy certain restrictions to guarantee the stability of the solution. Specifically, to ensure the stability of the FDTD scheme, the time increment step size Δt should be chosen to satisfy the Courant condition [111]:

$$v_{max}\Delta t\sqrt{\frac{1}{\Delta x_1^2} + \frac{1}{\Delta x_3^2}} \leq 1 \ , \tag{3.87}$$

where v_{max} is the maximum phase velocity of the acoustic wave propagating in the structure. If a square cell with $\Delta x_1 = \Delta x_3$ is chosen, equation (3.87) is simplified to

$$v_{max}\frac{\Delta t}{\Delta x_1} \leq \frac{1}{\sqrt{2}} \ . \tag{3.88}$$

Note that the Courant condition only provides a relationship between the spatial grid size and the time step. Satisfaction of the Courant condition does not guarantee the numerical accuracy of the solution. One must still comply with the sampling theory requirements with respect to the highest excited frequency in the model. Usually, when the spatial grid size is chosen according to the numerical dispersion requirements as it is stated in Section 3.5.1, the time step size chosen to satisfy the Courant condition will implicity comply with the sampling theory requirements.

3.6 Excitation source

In this section, three types of source waveforms will be discussed, the Gaussian pulse waveform, the toneburst waveform, and the sinusoidal waveform. These three types of waveforms will be applied to different FDTD simulations in this study.

3.6.1 Gaussian pulse waveform

Gaussian pulse waveform is suitable for wideband analysis. The pulse characteristic is dependent on the frequency range of the simulation[111]. The Gaussian pulse in time domain is expressed as:

$$g(t) = exp\left(-\frac{4\pi(t-t_0)^2}{\tau^2}\right) \ . \tag{3.89}$$

In our analysis, τ and t_0 equal to $\frac{2}{f_{max}}$. For example, the Gaussian pulse with the maximum simulation frequency of 2 GHz is shown in Figure 3.4. The frequency domain characteristic is obtained by FFT (fast Fourier transform). This waveform was applied as the excitation source of the electric displacement ($\mathbf{D}$) to calculate the dispersion characteristic of FBAR.

3.6.2 Toneburst waveform

The toneburst waveform is suitable for narrowband analysis. Generally, the toneburst used in this study is a sinusoidal wave of several cycles multiplied by a window function $h(t)$. The window function is used to smooth the turn-on and turn-off procedure of the source and reduce the influence of the sidelobes. The time domain expression of the toneburst wave is

$$g(t) = sin(\omega_0 t) \cdot h(t) \quad (0 \leq t \leq t_1) \ , \tag{3.90}$$

where ω_0 is the center frequency of the interested frequency range, $h(t)$ is a window function and t_1 stands for the duration of the wave.

A sinusoidal wave of five cycles modified by a Hanning window at the frequency of 1.315 GHz is shown in Figure 3.5 as an example. The toneburst waveform was used as the excitation source for multimode excitation scattering analysis in Chaper 4.

3.6.3 Sinusoidal waveform

A sine or cosine function is a single-frequency waveform, which is suitable for the steady state analysis. The time domain expression of the sinusoidal wave is simply

$$g(t) = sin(\omega_0 t) \ . \tag{3.91}$$

A sinusoidal wave at the frequency of 1.331 GHz is shown in Figure 3.6 as an example. Here, only part of the sine wave is shown for a clear view. In FDTD simulation, the sinusoidal waveform is excited for a limited duration, and the turn-on and turn-off of the wave will add other frequency components to the frequency spectrum. Thus, the frequency domain characteristic of the sinusoidal waveform is not a single line at the frequency of ω_0, as it is shown in Figure 3.6(b). The sinusoidal waveform excitation was used to observe the steady state response of FBAR resonators in Chapter 5. To observe the steady state response, the simulation should be run long enough such that the transient response due to the turn on of the sources die out and only the sinusoidal response persists.

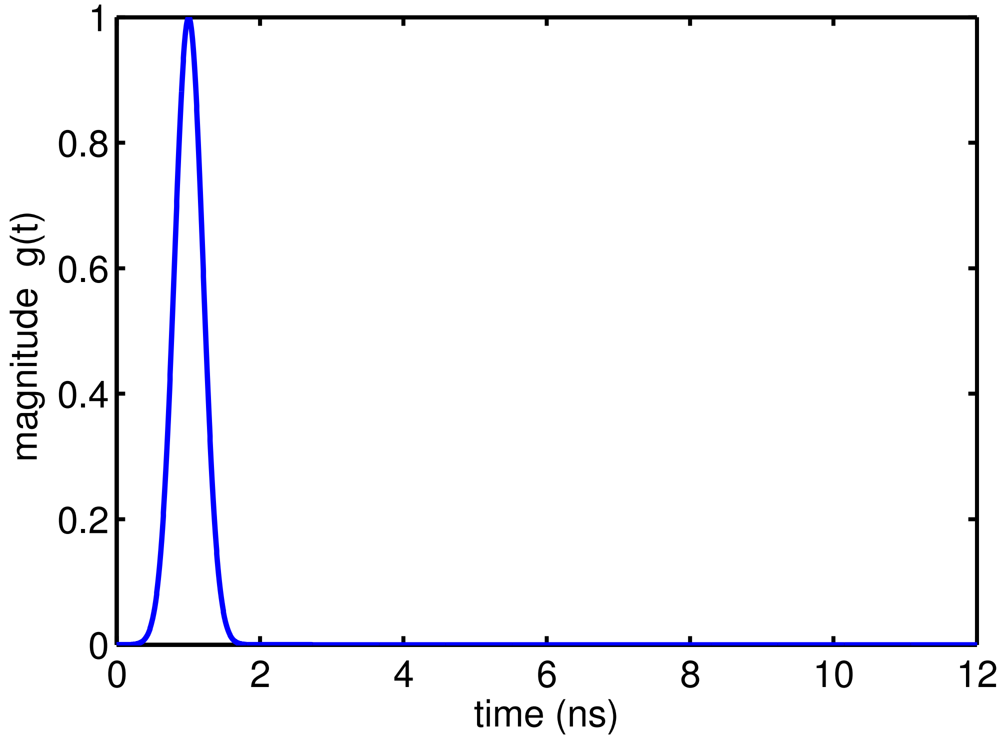

(a)

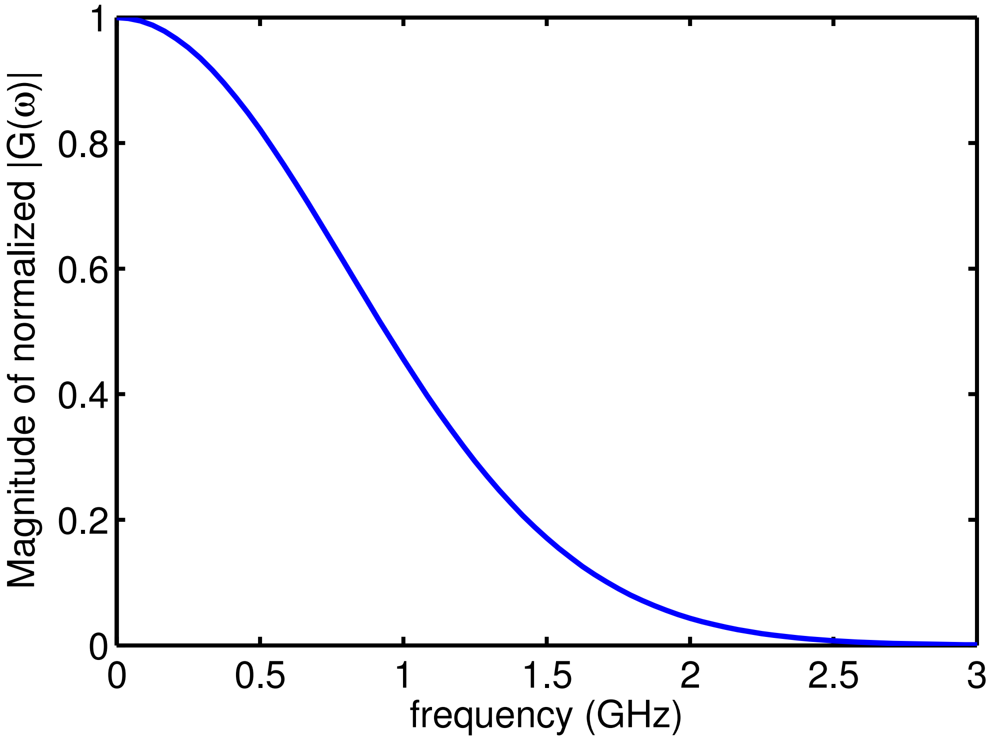

(b)

Figure 3.4: Gaussian pulse waveform with maximum frequency of 2GHz: (a) in the time domain, (b) in the frequency domain.

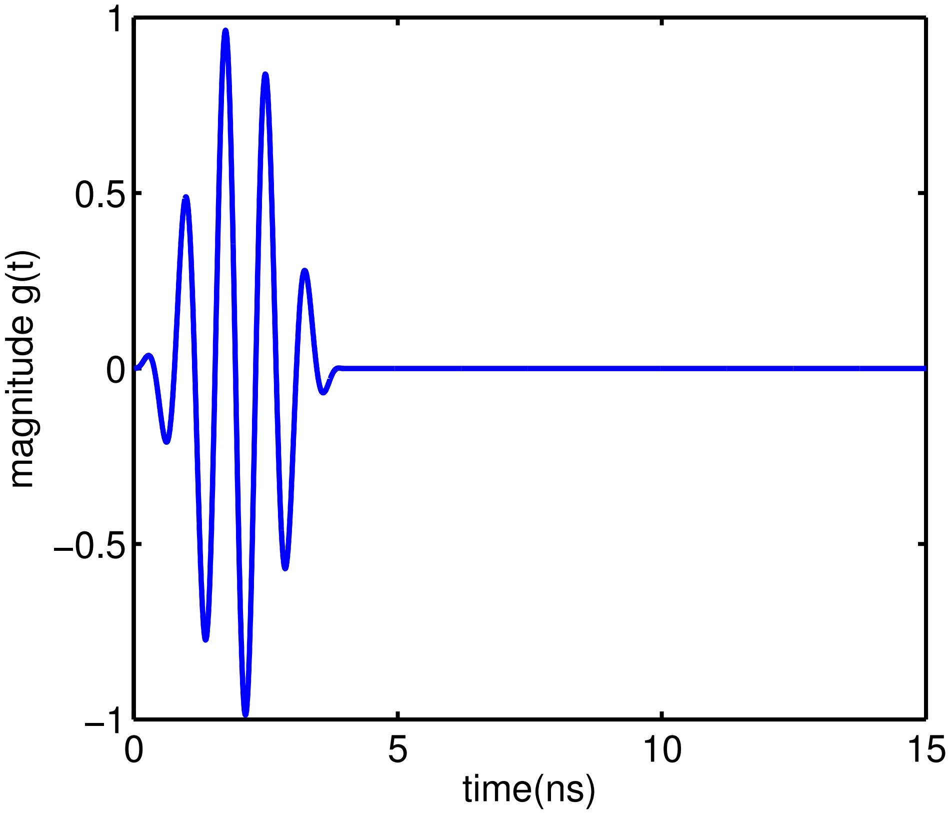

(a)

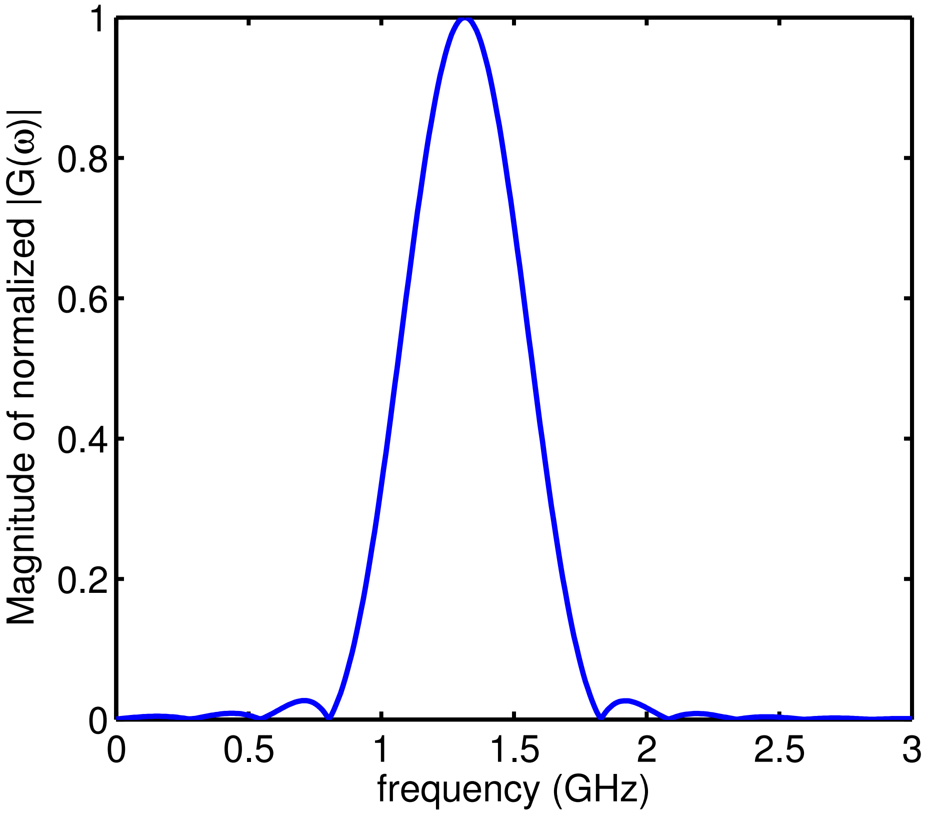

(b)

Figure 3.5: Toneburst waveform of five cycles at 1.315 GHz: (a) in the time domain, (b) in the frequency domain.

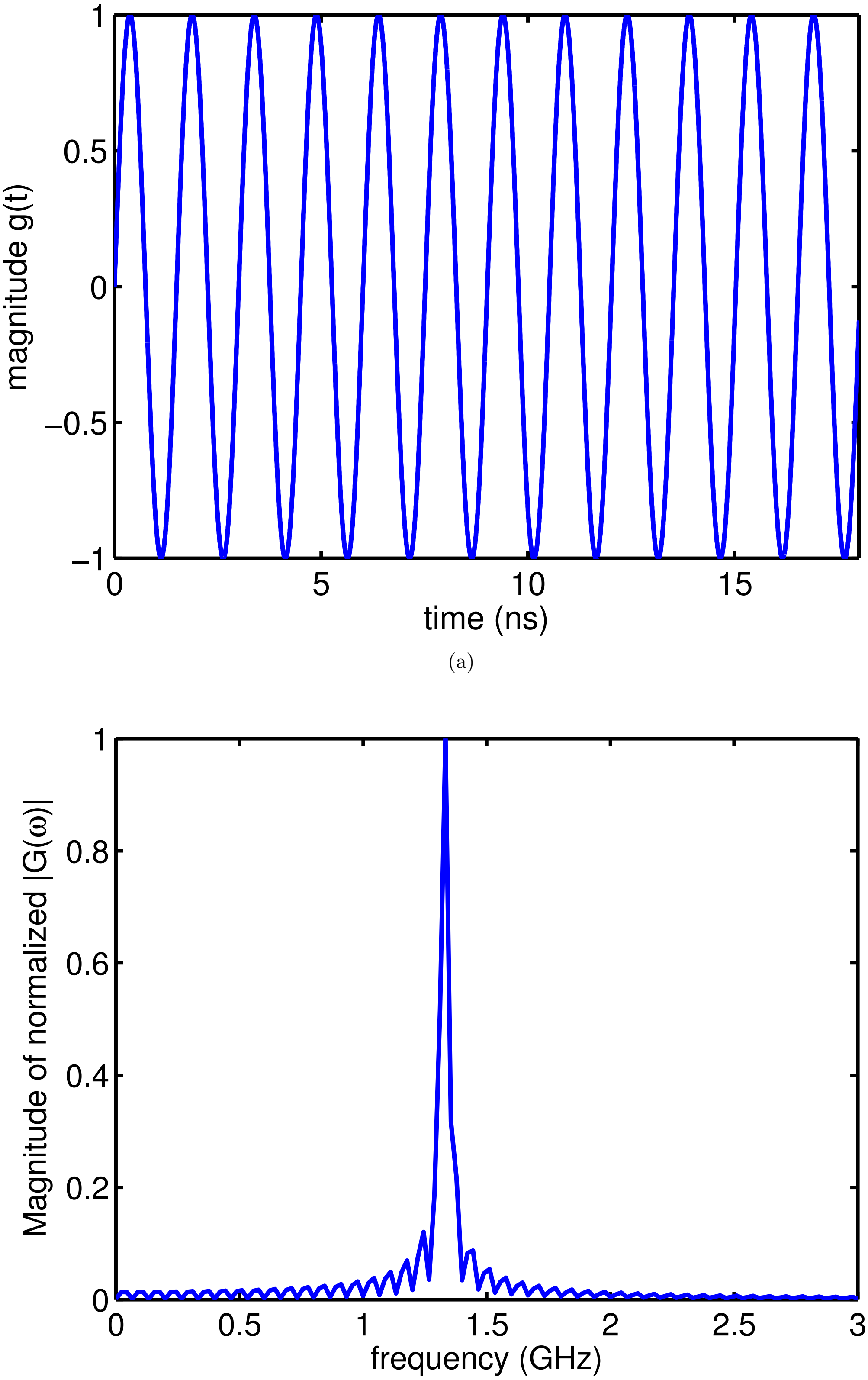

(a)

(b)

Figure 3.6: Sinusoidal waveform at 1.331 GHz: (a) in the time domain, (b) in the frequency domain.

3.7 Boundary conditions

When implementing the FDTD scheme, the boundary conditions should be treated in a special manner. Two kinds of boundary conditions are discussed in this section: the external boundaries (air and medium interfaces), and the internal boundaries (boundaries within the medium caused by a change in material properties). Here, only the stress and particle velocity components are considered, because the electric field intensity is only used to observe the electric response, and it does not affect the wave propagation.

3.7.1 Free surface boundary condition

The numerical model of the FBARs (free-standing bulk acoustic resonators) is bounded at its top and bottom face by a free surface. A free surface is the interface between a medium and air. In air, all elastic fields vanish. Consequently, due to the continuity of the normal stress, all normal stress components on the interface between the air and the material should be zero [104]:

$$T_3(x_1, x_3 = 0 \ \text{ or } \ h) = 0 \ , \tag{3.92}$$

$$T_5(x_1, x_3 = 0 \ \text{ or } \ h) = 0 \ , \tag{3.93}$$

where h is the total thickness of the model.

Since in the numerical simulation the stress component T_5 is not located on the interface (shown in Fig. 3.3), condition (3.93) should be treated in a special way by adding an extra row above and below the model (Fig. 3.7). With this extra row, the shear stress T_5 at $x_3 = 0$ is averaged on the interface and the average is set to be zero:

$$\frac{\left(T_5\Big|_{i,-\frac{1}{2}}^{n} + T_5\Big|_{i,\frac{1}{2}}^{n}\right)}{2} = 0 \ . \tag{3.94}$$

$T_5\Big|_{i,\frac{1}{2}}^{n}$ is located within the model, so it is calculated using the normal update equations. Based on equation (3.94), the transverse stresses on the extra row $T_5\Big|_{i,-\frac{1}{2}}^{n}$ can be obtained by the following equation:

$$T_5\Big|_{i,-\frac{1}{2}}^{n} = -T_5\Big|_{i,\frac{1}{2}}^{n} \ . \tag{3.95}$$

Consequently, the velocity on the interface $v_1\Big|_{i,0}^{n+\frac{1}{2}}$ can be evaluated using the normal governing equations by the values of the transverse stress components on the extra row $T_5\Big|_{i,-\frac{1}{2}}^{n}$. Similarly, the same approach can be applied to the bottom surface.

The particle velocity components on the extra row $v_3\Big|_{i,-\frac{1}{2}}^{n+\frac{1}{2}}$ can be used to calculate the longitudinal stresses on the surface $T_1\Big|_{i,0}^{n+1}$. However, the velocity components on the extra row $v_3\Big|_{i,-\frac{1}{2}}^{n+\frac{1}{2}}$ cannot be calculated by the normal governing equations. They should

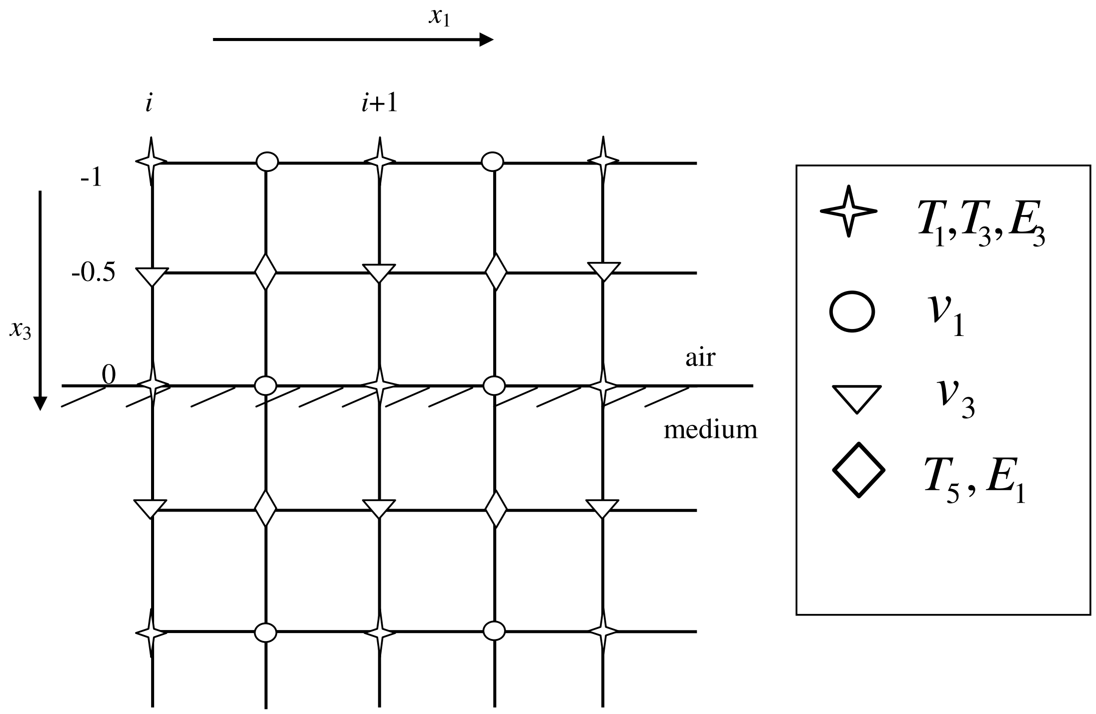

Figure 3.7: FDTD grid with an extra row inserted on the top interface.

be treated in a special manner. The update equation for the velocity components on the extra row $v_3\Big|_{i,-\frac{1}{2}}^{n+\frac{1}{2}}$ is obtained by setting $T_3\Big|_{i,0}^{n}$ on the top interface to zero. Without external excitation, by implementing the stress free condition of T_3 on the top interface, the following equation can be obtained from equation (3.75):

$$0 = 0 + \Delta t \left[\frac{c_{13}^D}{\Delta x_1} \left(v_1 \Big|_{i+\frac{1}{2},0}^{n+\frac{1}{2}} - v_1 \Big|_{i-\frac{1}{2},0}^{n+\frac{1}{2}} \right) + \frac{c_{33}^D}{\Delta x_3} \left(v_3 \Big|_{i,\frac{1}{2}}^{n+\frac{1}{2}} - v_3 \Big|_{i,-\frac{1}{2}}^{n+\frac{1}{2}} \right) \right] . \tag{3.96}$$

By rearranging the terms of equation (3.96), the update equation for particle velocity v_3 on the extra row is obtained:

$$v_3 \Big|_{i,-\frac{1}{2}}^{n+\frac{1}{2}} = v_3 \Big|_{i,\frac{1}{2}}^{n+\frac{1}{2}} + \frac{c_{13}^D \Delta x_3}{c_{33}^D \Delta x_1} \left(v_1 \Big|_{i+\frac{1}{2},0}^{n+\frac{1}{2}} - v_1 \Big|_{i-\frac{1}{2},0}^{n+\frac{1}{2}} \right) . \tag{3.97}$$

Now, the stress free boundary condition is satisfied on the top surface and all the field components on the surface are determined.

In a similar way, the update equation for particle velocity v_3 on the bottom extra row is as below:

$$v_3 \Big|_{i,j+\frac{1}{2}}^{n+\frac{1}{2}} = v_3 \Big|_{i,j-\frac{1}{2}}^{n+\frac{1}{2}} - \frac{c_{13}^D \Delta x_3}{c_{33}^D \Delta x_1} \left(v_1 \Big|_{i+\frac{1}{2},j}^{n+\frac{1}{2}} - v_1 \Big|_{i-\frac{1}{2},j}^{n+\frac{1}{2}} \right) . \tag{3.98}$$

Similarly, the free surface also exist on the left and right air and medium interfaces. The stress free condition on the left or right boundary is applied by setting stress fields

T_1 and T_5 to zero:

$$T_1(x_1 = 0 \;\text{ or }\; L, x_3) = 0 \;, \tag{3.99}$$

$$T_5(x_1 = 0 \;\text{ or }\; L, x_3) = 0 \;, \tag{3.100}$$

where L is the length of the model.

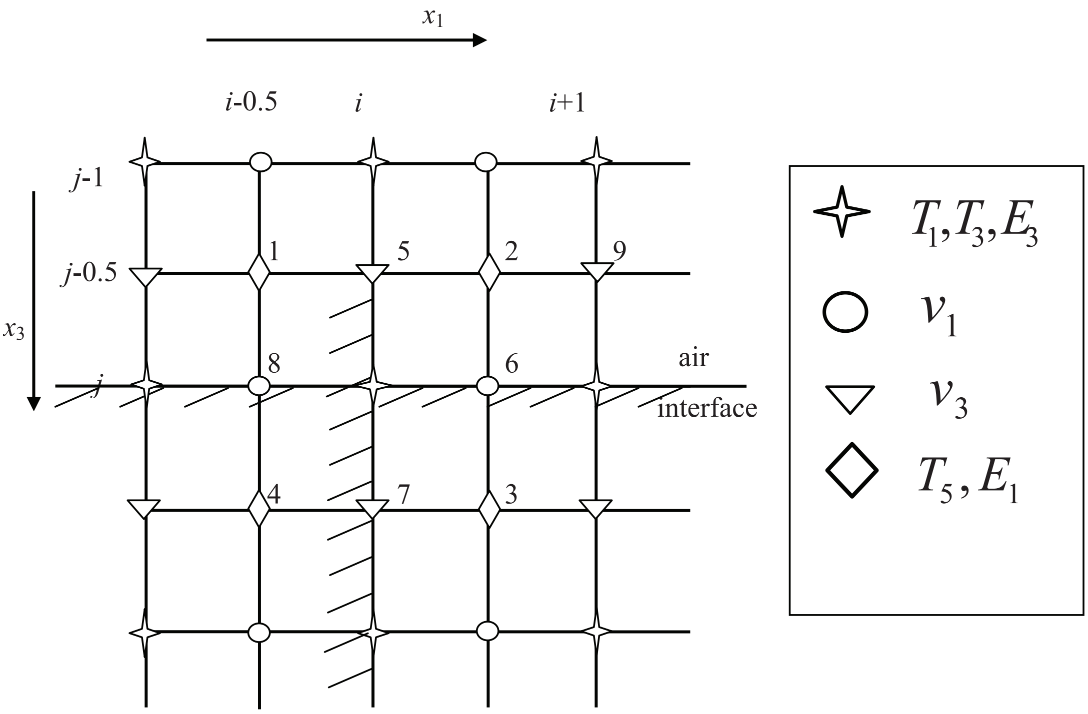

Figure 3.8: FDTD grid with an extra row inserted on the top interface and an extra column inserted on the left boundary.

Since T_5 is not located on the left or right boundary (shown in Fig. 3.3), an extra column should also be added on the left side and right side of the model. Condition (3.100) should be treated in a special way by adding an extra column on the left and right side of the model (Fig. 3.8). With this extra column, the shear stress T_5 is averaged on the interface and the average is set to be zero:

$$\frac{T_5\Big|^{n}_{i-\frac{1}{2},j-\frac{1}{2}} + T_5\Big|^{n}_{i+\frac{1}{2},j-\frac{1}{2}}}{2} = 0 \;. \tag{3.101}$$

For $i \neq 0$, $T_5\Big|^{n}_{i-\frac{1}{2},j-\frac{1}{2}}$ is calculated by equation (3.101). $T_5\Big|^{n}_{i+\frac{1}{2},j-\frac{1}{2}}$ is located inside the module, so it is calculated using the normal update equations. However, for $i = 0$, T_5 is at the intersection of the extra row and extra column, and equation (3.101) is not valid any more. Thus, $T_5\Big|^{n}_{-\frac{1}{2},-\frac{1}{2}}$ is calculated by averaging the two nearest point around it (in Fig. 3.8 T_5 at point 1 is calculated by averaging the values of T_5 on point 2 and 4). The shear stress components T_5 at the other intersections are treated in a similar way. The stress free condition T_1 equal to zero is used to derive the update equation for v_1 on the extra column. Without external excitation, by implementing the stress free condition of T_1 on the left interface, the following equation can be obtained from equation (3.74):

$$0 = 0 + \Delta t \left[\frac{c_{11}^D}{\Delta x_1} \left(v_1 \Big|_{\frac{1}{2},j}^{n+\frac{1}{2}} - v_1 \Big|_{-\frac{1}{2},j}^{n+\frac{1}{2}} \right) + \frac{c_{13}^D}{\Delta x_3} \left(v_3 \Big|_{0,j+\frac{1}{2}}^{n+\frac{1}{2}} - v_3 \Big|_{0,j-\frac{1}{2}}^{n+\frac{1}{2}} \right) \right] . \tag{3.102}$$

Consequently, the update equation for v_1 on the left extra column is obtained by rearranging the terms of equation (3.102):

$$v_1 \Big|_{-\frac{1}{2},j}^{n+\frac{1}{2}} = v_1 \Big|_{\frac{1}{2},j}^{n+\frac{1}{2}} + \frac{c_{13}^D \Delta x_1}{c_{11}^D \Delta x_3} \left(v_3 \Big|_{0,j+\frac{1}{2}}^{n+\frac{1}{2}} - v_3 \Big|_{0,j-\frac{1}{2}}^{n+\frac{1}{2}} \right) . \tag{3.103}$$

In a similar way, the update equation for particle velocity v_1 on the right extra column is as below:

$$v_1 \Big|_{i+\frac{1}{2},j}^{n+\frac{1}{2}} = v_1 \Big|_{i-\frac{1}{2},j}^{n+\frac{1}{2}} - \frac{c_{13}^D \Delta x_1}{c_{11}^D \Delta x_3} \left(v_3 \Big|_{i,j+\frac{1}{2}}^{n+\frac{1}{2}} - v_3 \Big|_{i,j-\frac{1}{2}}^{n+\frac{1}{2}} \right) . \tag{3.104}$$

From equation (3.97) and (3.103), the particle velocity v_3 on the extra row at point 5 (Fig. 3.8) is calculated by v_3 at point 7 and v_1 at points 6 and 8, whereas the particle velocity v_1 on the extra column at point 8 is calculated by v_1 at point 6 and v_3 at points 5 and 7. v_3 on the extra row at point 5 and v_1 on the extra column at point 8 can not be calculated unless one of them is calculated by another method. In this project, v_3 on the extra row at point 5 is calculated by averaging the two nearest points around it (in Fig. 3.8 v_3 at point 5 is calculated by averaging the values of v_3 at point 7 and 9). v_3 on the other corner of the structure are calculated in a similar way. The parameters used on the extra row and extra column are the same as the parameters used in the adjacent material. Finally, the stress free boundary condition is satisfied and all the field components on the surface are determined.

3.7.2 Interface boundary condition

The interface boundary conditions are applied at the interfaces between two different materials. Figure 3.9 shows a cross section of the FDTD grid at an interface between two materials. To minimize the number of the field components that are located on the interface, the boundary is placed such that it always passes through the shear stress components, as it is shown in Fig. 3.9. Thus, the normal particle velocity components are always placed on the interface. To ensure that the Courant condition is a sufficient stability condition, the material properties such as the elastic stiffness constants and material mass densities are averaged at the interface boundary [104].

As shown in Figure 3.9, the interface boundaries contain the shear stress components (T_5) and the particle velocity components (v_1 and v_3). However, the longitudinal stress components (T_1 and T_3) will never lie on the boundary. Thus, the longitudinal elastic stiffness constants do not have to be averaged. At an interface between two materials, the

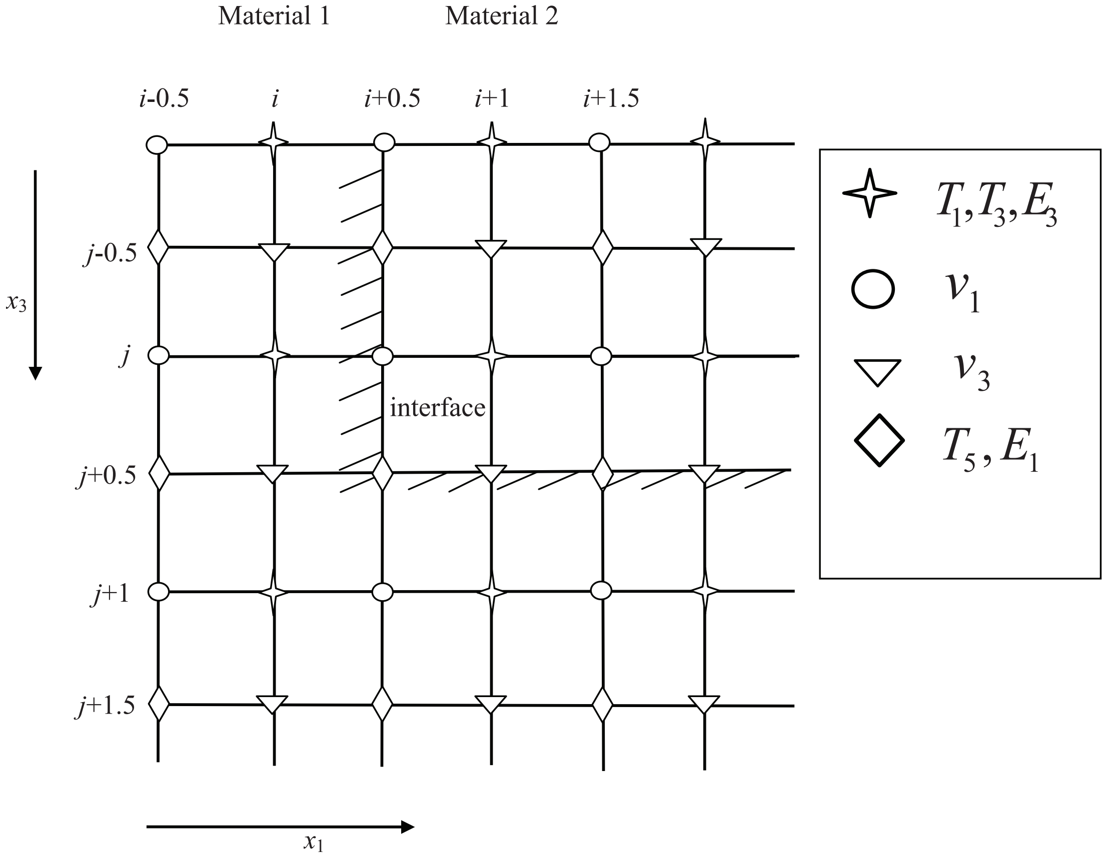

Figure 3.9: Finite-difference grid at the interface between two materials.

mass density of the material is averaged (Eq. 3.105) and the inverse of the shear elastic stiffness constant is averaged (Eq. 3.106).

$$\rho_{avg} = \frac{\rho_{material\ 1} + \rho_{material\ 2}}{2} \ , \tag{3.105}$$

$$c_{avg} = \frac{2}{\frac{1}{c_{material\ 1}} + \frac{1}{c_{material\ 2}}} \ , \tag{3.106}$$

where $\rho_{material\ 1}$ and $\rho_{material\ 2}$ are the mass densities in the material 1 and the material 2, respectively. $c_{material\ 1}$ and $c_{material\ 2}$ are the shear elastic stiffness constants in the material 1 and the material 2, respectively. Then, this boundary condition is applied to the discrete finite-difference grids. For instance, the material mass density used to calculate $v_3\,|_{i+1,j+0.5}$ on the interface in Fig. 3.9 is:

$$\rho_{avg}\,|_{i+1,j+0.5} = \frac{\rho\,|_{i+1,j-0.5} + \rho\,|_{i+1,j+1.5}}{2} \ . \tag{3.107}$$

And, the averaged shear elastic stiffness constants used for calculating the shear stress component $T_5\,|_{i+0.5,j-0.5}$ on the interface in Fig. 3.9 are:

$$c_{avg}\,|_{i+0.5,j-0.5} = 2\left(\frac{1}{c\,|_{i-0.5,j-0.5}} + \frac{1}{c\,|_{i+1.5,j-0.5}}\right)^{-1} \ . \tag{3.108}$$

For the shear stress components at the corner of the interface, the shear elastic stiffness constants must be averaged among all the four adjacent cells. For example, the averaged shear elastic stiffness constants used for calculating the shear stress component $T_5\,|_{i+0.5,j+0.5}$ (shown in Fig. 3.9) are

$$c_{avg}\,|_{i+0.5,j+0.5} = 4\left(\frac{1}{c\,|_{i-0.5,j+0.5}} + \frac{1}{c\,|_{i+0.5,j+1.5}} + \frac{1}{c\,|_{i+1.5,j+0.5}} + \frac{1}{c\,|_{i+0.5,j-0.5}}\right)^{-1}, \tag{3.109}$$

where $c\,|_{i+1.5,j+0.5}$ and $c\,|_{i+0.5,j-0.5}$ are located on the interface of two materials and can be obtained in a similar way as equation (3.108).

Following this averaging method, all material properties located at the interface of different materials can be determined.

In practice, a viscous acoustic damping material, such as a viscoelastic material, such as polyimide, can be added at the boundary to absorb the outgoing acoustic waves. The substrate on which the piezoelectric layer is deposited will influence the quality of the piezoelectric layer. Some metals lead to better c-axis-oriented crystal structure than others, because of crystallographic compatibility between them and the AlN layer. Molybdenum (Mo), tungsten (W), aluminum (Al) and platinum (Pt) are some of the materials commonly used in AlN-based FBAR fabrication. Additional post-processing technique such as annealing of the piezoelectric-deposited wafer may be applied to improve the crystals quality and smooth the interface between the metal and piezoelectric layer [18].

3.8 2D-FFT method

FBAR resonators utilize the fundamental longitudinal mode along the thickness direction. However, Rayleigh-Lamb modes are also excited and propagate along the lateral direction. The purpose of this study is to investigate these spurious modes within the FBAR resonators. The two-dimensional Fourier transformation (2D FFT) method is applied to extract the dispersion curve of these Rayleigh-Lamb modes, and obtain the amplitudes of each mode at a specified frequency.

The 2D FFT method was proposed to measure the amplitudes and velocities of Lamb waves when many propagating modes are present in nondestructive testing (NDT) applications [7, 8]. Assuming a harmonic acoustic wave propagating in a plate along x_1 direction, the particle velocity on the surface $v(x_1, t)$ may be expressed as

$$v(x_1, t) = A(\omega)e^{j(\omega t - \beta x_1 - \theta)}\ , \tag{3.110}$$

where $A(\omega)$ is a frequency dependent amplitude constant, ω is the angular frequency, β is the wavenumber, and θ denotes the phase. Applying the 2D FFT analysis to the particle velocity on the surface $v(x_1, t)$ is composed of two steps: firstly, a temporal Fourier transform is applied to transform the data from the time to frequency domain; then a spatial Fourier transform is applied to transform the data to the frequency-wavenumber domain. Theoretically, applying 2D FFT analysis to equation (3.110) giving

$$V(\beta, f) = \int_{-\infty}^{+\infty} \int_{-\infty}^{+\infty} v(x_1, t) e^{-j(\omega t + \beta x_1)} dx_1 \; dt \; . \tag{3.111}$$

The discrete two-dimensional Fourier transform can be defined in a similar way to the one-dimensional discrete Fourier transform (DFT) given in standard texts (for example [80]). A two-dimensional array of amplitudes at discrete frequencies and wavenumbers can be obtained by applying the discrete 2D FFT transform to the data gained experimentally or numerically. As in the one-dimensional case, the sampling rate of data in time and in space must be sufficiently high to avoid aliasing. Window functions such as the Hanning window may be applied to reduce the influence of the sidelobes, and zeros may be padded to the end of the signal to smooth the FFT result. Details of the fast Fourier transform algorithm, aliasing, leakage, zero padding and other effects associated with discrete Fourier transform can be found in standard texts (for example [85]).

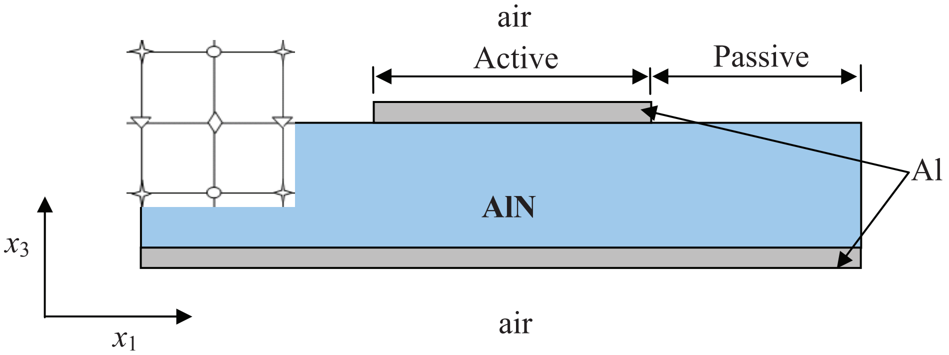

Figure 3.10: 2D FDTD model of FBAR resonator for dispersion analysis.

A Gaussian pulse with maximum frequency of 2 GHz as shown in section 3.6.1 is applied as the excitation source for a FBAR resonator (shown in Fig. 3.10). Here, Gaussian pulse is applied as the electric displacement D_3 in the thickness direction within the active region, the electric displacement D_1 in the lateral direction is assumed to be negligible. The particle velocity components $v_1(x_1, t)$ on the top surface at the passive region calculated by the FDTD method are recorded. Then 2D FFT algorithm is applied to these recorded data to get the dispersion curve of the Rayleigh-Lamb modes propagating in the passive region, as shown in Fig. 3.11(a). The dispersion characteristic of the passive region is also obtained by the effective acoustic impedance, as shown in Fig. 3.11(b). It can be observed that the dispersion curve obtained by FDTD simulation and 2D FFT extraction is in good agreement with the one obtained by the effective acoustic impedance. The amplitude of each mode can be obtained for a specified frequency. Thus, the FDTD algorithm presented in this chapter can be used to investigate the spurious modes in FBAR resonators.

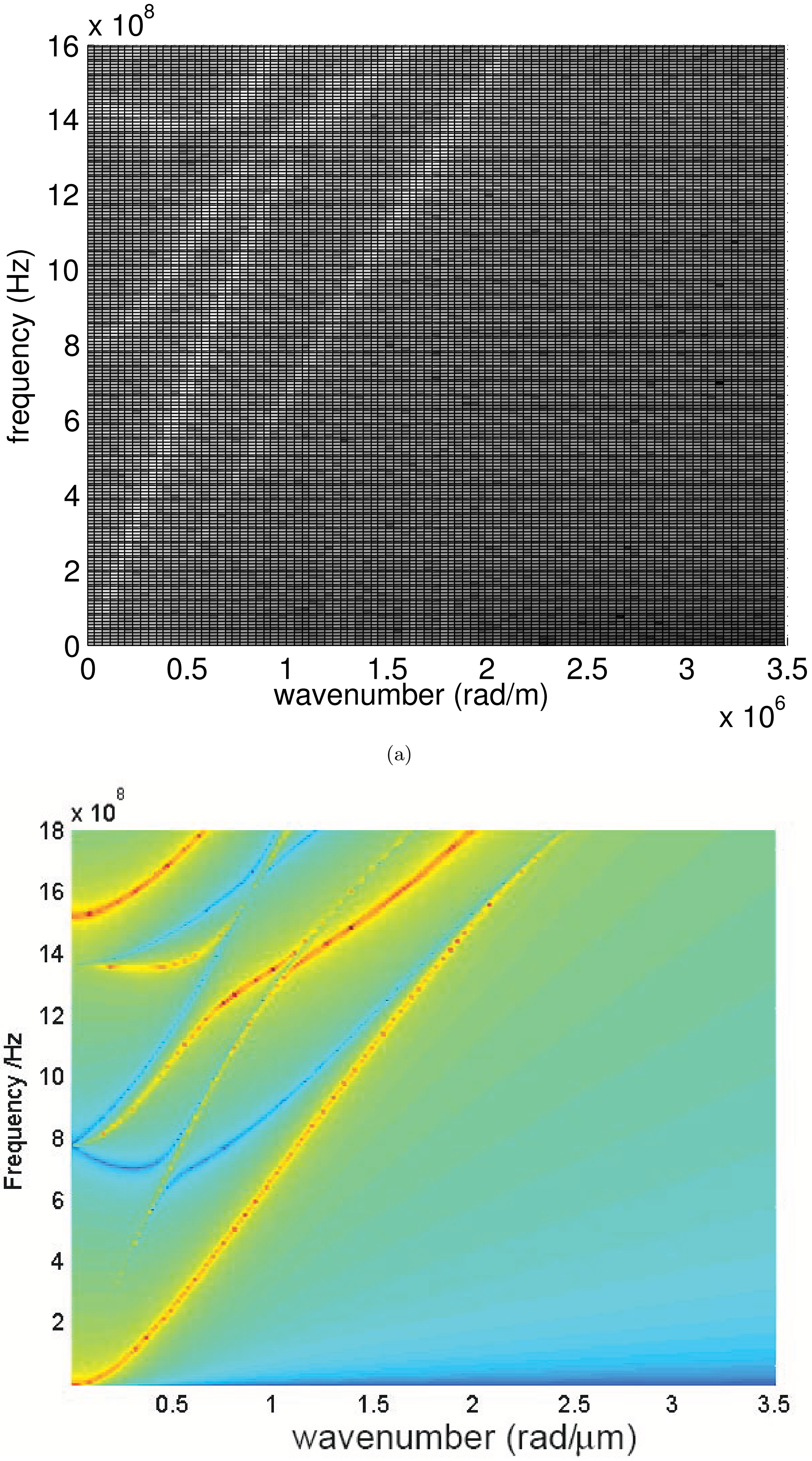

(a)

(b)

Figure 3.11: Dispersion curve for FBAR resonator passive region (AlN/Al with thickness of $3\mu m/0.6\mu m$: (a) obtained by 2D-FFT method, (b) obtained by the effective acoustic impedance (This graph is courtesy of F. Thalmayr, Sand 9, Inc..).

3.9 Summary

The proposed FDTD scheme for modeling FBAR resonators is summarized in Figure 3.12. The initial value of the stress, particle velocity, and electric field components is zero. At $t = 0$, a source, electrical source or mechanical source, is applied to the model. Then the stress field components are calculated at t and the free surface boundary condition is set. The electric field components are calculated at t as well. After a half time step, the particle velocity components are calculated at $t = t + 1/2$. If the iteration time t does not exceed the upper limit of the iteration time t_{max}, the procedures are iterated. The proposed FDTD model will be used to do the scattering analysis for multimode excitation in Chapter 4 and investigate the FBAR resonator proposed in Chapter 5.

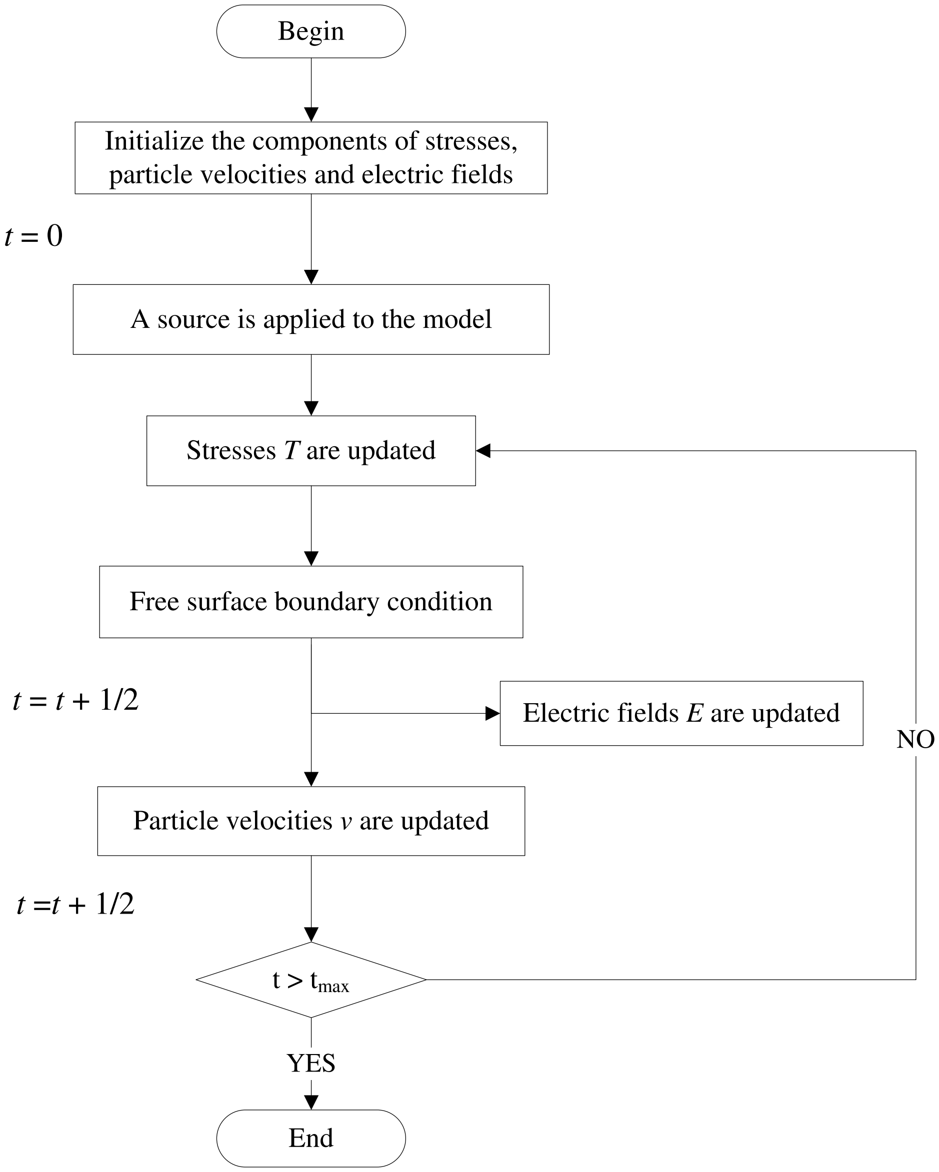

Figure 3.12: The proposed FDTD procedure for modeling the FBAR.

Chapter 4

Wave scattering analysis for multimode excitation

4.1 Introduction

In this Chapter, the wave scattering analysis for the nondestructive testing (NDT) and film bulk acoustic resonators (FBAR) is reviewed. The limitations of the existing wave scattering schemes are pointed out. The derivation of the scattering analysis for multimode excitation is presented. After checking the validity of the proposed method, the multimode wave scattering analysis is applied to two generic free-standing bulk acoustic resonator (FBAR) structures.

4.1.1 Nondestructive testing

A common application of acoustic wave scattering analysis is the ultrasonic nondestructive testing (NDT) to detect cracks, defects and delamination in plates and other more complex structures. The standard ultrasonic testing method uses bulk stress waves. In pulse excitation method, a bulk wave pulse is excited in the test medium. When the bulk wave pulse interacts with a defect, it is partially or totally back scattered, depending on the defect properties. By measuring the time of flight and amplitude of the reflected wave, the location of the defect and the acoustic impedance mismatch can be determined. The disadvantages of using bulk waves are: firstly, the investigation of thin plates and detection of defects on or very close to an interface are limited by the finite pulse bandwidth of the bulk wave, and secondly, using bulk waves is essentially one-dimensional, that is the area interrogated is along a line joining the two transducers (shown in Fig. 4.1). This one-dimensional characteristic has limited bulk wave application in testing large structures. More details about the standard ultrasonic NDT can be found in standard text books [17].

To solve the difficulties of bulk wave testing, Worlton proposed to use Lamb waves for fast nondestructive testing of plate-like structures [126]. Since then there has been an increasing interest in the applications of Lamb waves and other guided waves in NDT.

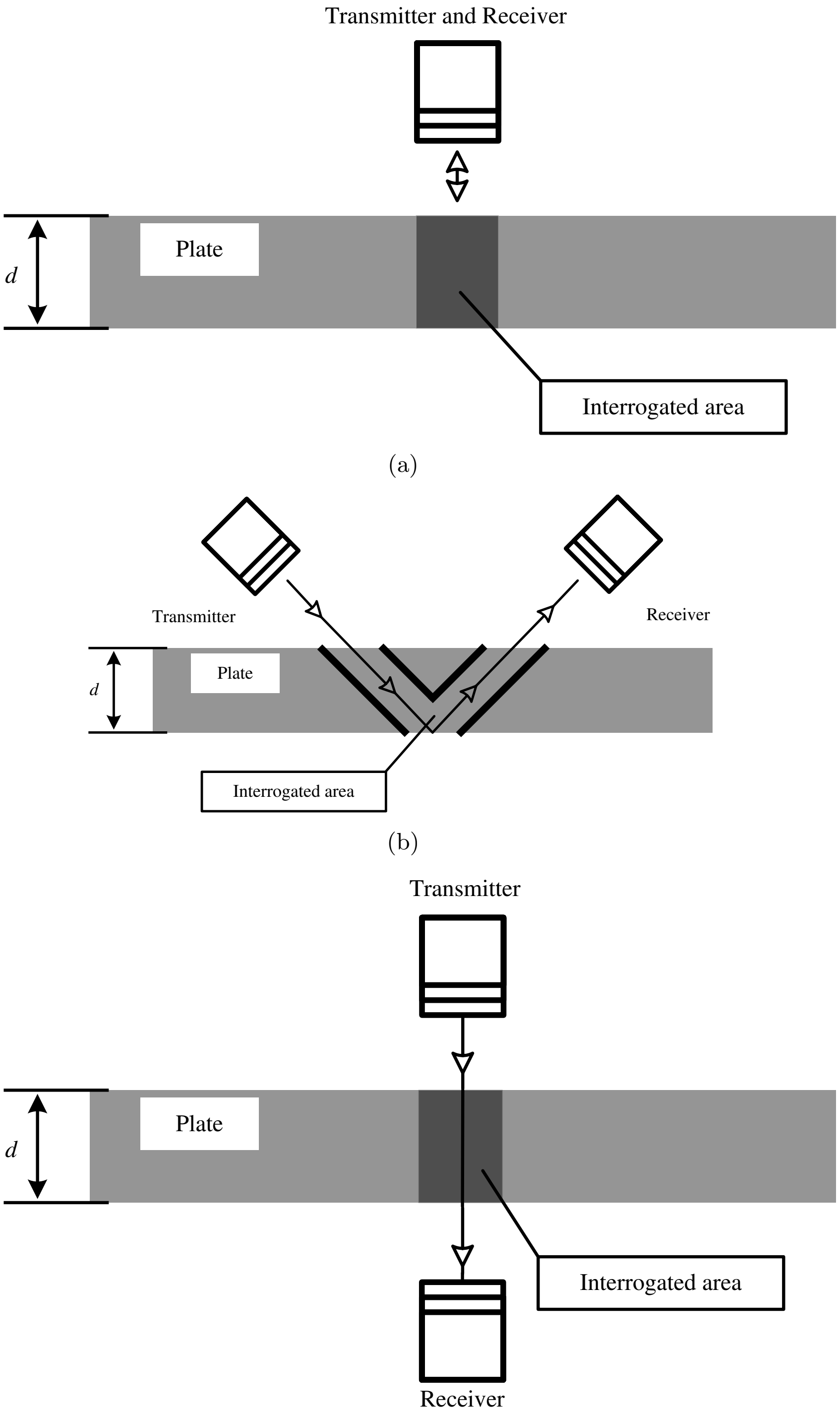

(a)

(b)

(c)

Figure 4.1: Schematic representation of nondestructive testing using bulk waves (a) pulse-echo mode, (b) pitch-catch mode, and (c) through-transmission mode.

Figure 4.2 shows a typical setup for investigation of a plate by Lamb waves. Due to the characteristics of Lamb waves, they produce stresses throughout the thickness of the plate. Therefore, the whole thickness of the plate is interacted with the Lamb waves. This property has enabled the possibility to detect defects that are located at or very near interfaces, or at other internal locations [39]. Lamb waves have also been applied to determine the elastic and viscoelastic properties of materials [13, 89]. Furthermore, because Lamb waves are essentially two-dimensional waves, exciting a specific Lamb wave into the plate, the Lamb wave can interrogate a two-dimensional area between the transmitting transducer and the receiving transducer (Fig. 4.2). Thus, Lamb waves has been widely use for coarse, fast inspection on large plates or plate-like structures [12, 22, 67, 94].

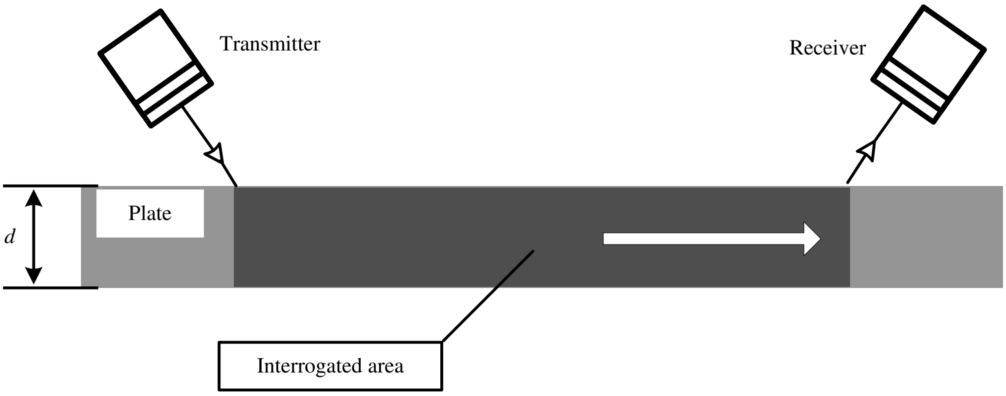

Figure 4.2: Schematic representation of nondestructive testing using Lamb waves.

4.1.2 Wave scattering in FBAR

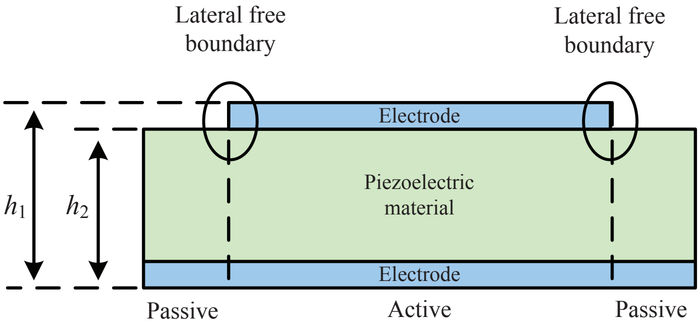

Figure 4.3: Sketch of a thin film resonator with lateral free boundaries.

For FBARs and other thin film resonating devices, the electrode thickness is typically in the order of several hundred nm, and the thickness of the whole device is usually in the order of a few μm. Therefore, the step height $h_1 - h_2$ of the lateral boundaries is significant comparing with the overall device thickness h_1(shown in Fig. 4.3). Consequently, the dispersion curves of the active and passive area are quite different for these devices. For example, the dispersion characteristics of a FBAR resonator with the combination of Al/AlN/Al (with thickness of $0.3\mu m/3\mu m/0.3\mu m$) for different regions are shown in Figure 4.4. Here, modes A_n are the propagating antisymmetric Lamb modes, and S_n are the propagating symmetric Lamb modes in the active region. Because the passive region is not symmetric, the modes propagating in this region do not show symmetric nor antisymmetric behavior. These modes are referred as pseudo symmetric (pS_n) and pseudo antisymmetric (pA_n) modes respectively, in analogy to the Lamb mode nomenclature. To get a clear view, the dispersion curves for S_1 and pS_1 mode of the active and passive area are plotted together in Fig. 4.4(c). The field distribution of each mode are also with significant differences in different sections of the resonator. Moreover, the lateral boundary conditions cannot be fulfilled by a single mode.

To satisfy the boundary conditions, a finite number of forward and backward propagating and an infinite amount of evanescent modes have be to considered. Therefore, scattering analysis has to be conducted to investigate these forward and backward scattering modes at the lateral boundaries. Note that the evanescent modes only exist in the vicinity of the discontinuity boundaries. By applying the scattering analysis to FBARs, energy conversion paths, power transfer below the cut-off frequency, and mechanical excitation of modes can be explained [117]. Scattering analysis can be applied for further improvement of FBAR device analysis and design with regard to border regions. The purpose of this chapter is to propose a more efficient scattering analysis scheme, aiming to investigate the lateral spurious modes and improve the quality factor of FBAR.

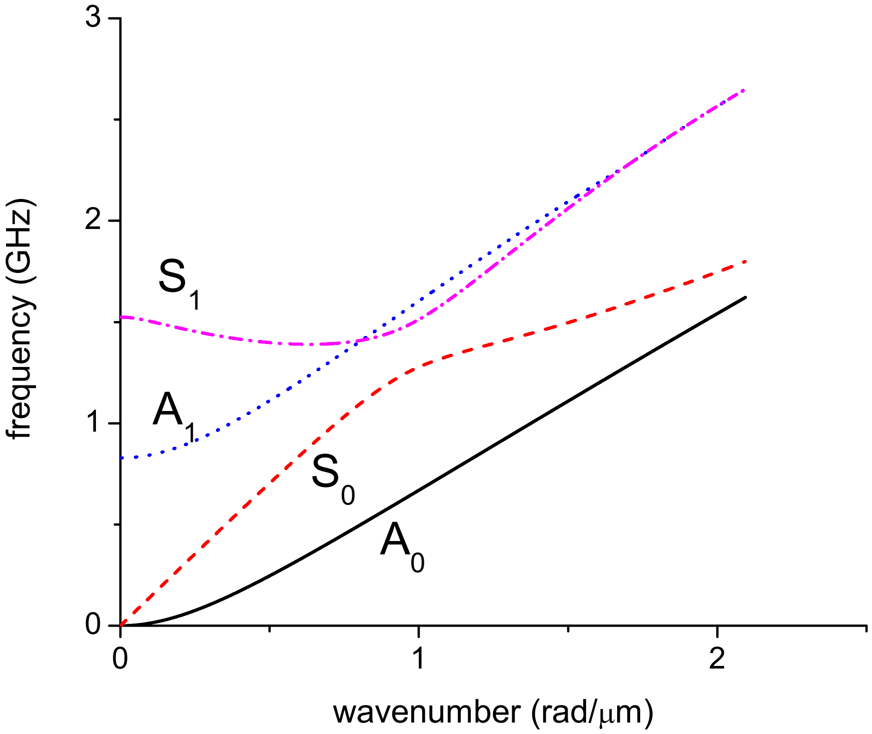
3
2
1
0
frequency (GHz)
0
1
2
wavenumber (rad/μm)
S1
A1
S0
A0

(a)

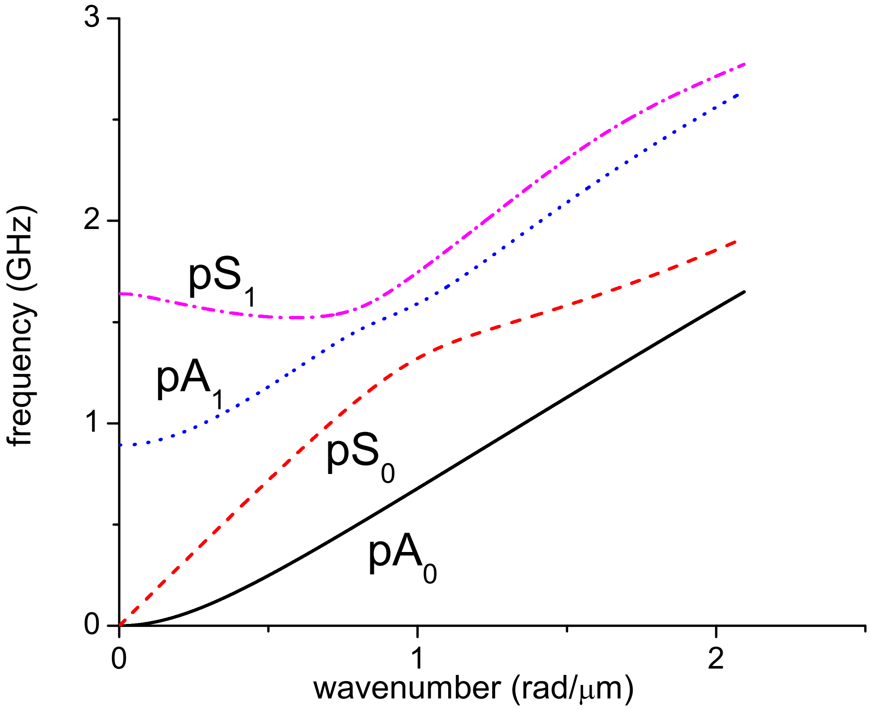
3
2
1
0
frequency (GHz)
0
1
2
wavenumber (rad/μm)
pS1
pA1
pS0
pA0

(b)

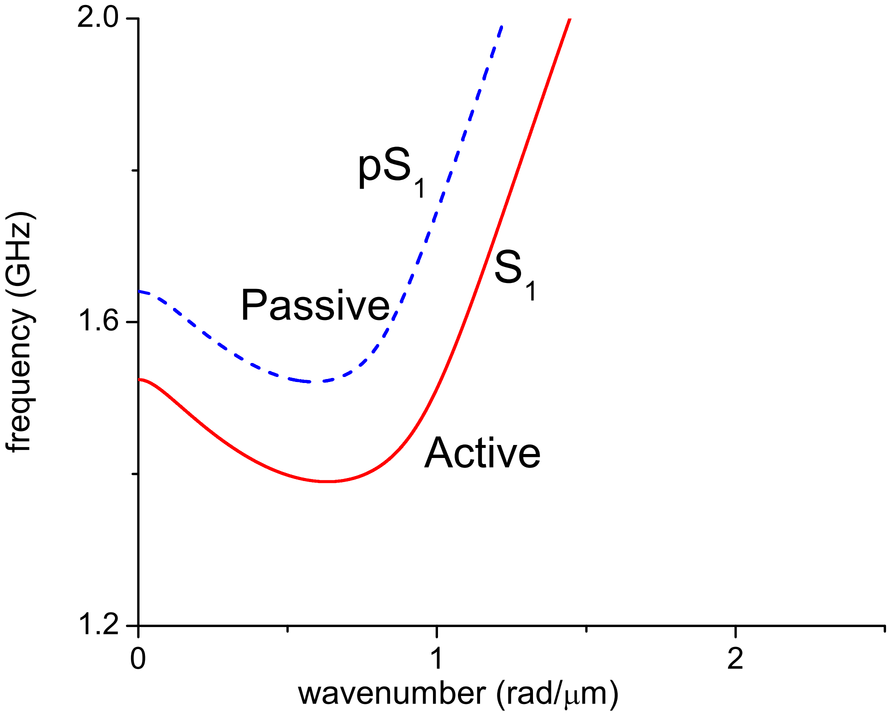

(c)

Figure 4.4: Dispersion curves of a FBAR with the combination of Al/AlN/Al (with thickness of $0.3\mu m/3\mu m/0.3\mu m$) (a) Active area, (b) Passive area, (c) Active area vs passive area for S_1 and pS_1 mode.

4.2 Methods for scattering analysis

Three methods for wave scattering analysis will be reviewed in this section: Torvik's method, time domain FEM simulation (TD-FEM), and frequency domain FEM simulation (FD-FEM). The limitations of these methods will be pointed out, and serve as the motivation for proposing the scattering analysis for multimode excitation in the next section.

4.2.1 Torvik's method

A semi-analytical method has been proposed by Torvik [121] for analyzing the backscattering of Lamb waves from the free edge of a plate. In Torvik's analysis, it has been assumed that the propagating modes in the semi-infinite plate and in an infinite extended plate are identical. A harmonic Lamb wave at frequency ω_o is excited and propagating in the x_1 direction (shown in Fig. 4.5) and it is completely reflected at the plate free edge ($x_1 = 0$). Because this model is two-dimensional, shear stresses in addition to the longitudinal stresses are present. Unlike the longitudinal stress, shear stress reflecting from a free edge does not change its sign. Therefore, a single reflection mode can not fulfill the boundary conditions of zero traction on the free edge. This implies that wave conversion happens and the reflected waves include finite propagating

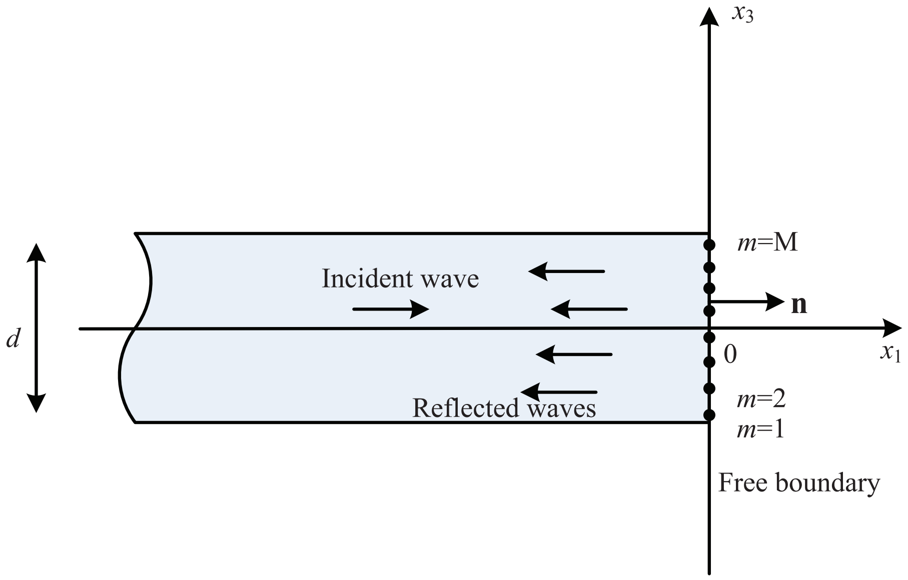

Figure 4.5: Lamb wave reflection at the plate free edge.

and an infinite evanescent eigenmodes. In other words, the traction free boundary condition should be satisfied by the incident and reflected waves:

$$\mathbf{T}_{inc} \cdot \mathbf{n} \cdot A_{inc} + \sum_{k} \mathbf{T}_{ref,\ k} \cdot \mathbf{n} \cdot A_{ref,\ k} = 0\ . \tag{4.1}$$

Here, $\mathbf{T}_{inc}$ is the stress vector of the incident wave; $\mathbf{T}_{ref,\ k}$ is the stress vector of the k^{th} reflected wave. A_{inc} is the amplitude of the incident wave, and $A_{ref,\ k}$ is the amplitude of the k^{th} reflected wave. And $\mathbf{n}$ is the normal vector on the edge. The reflection coefficients in amplitude can be obtained by the following equation:

$$r_k = \frac{A_{ref,\ k}}{A_{inc}}\ , \tag{4.2}$$

where r_k is the reflection coefficient of the k^{th} reflected mode in amplitude. The Lamb wave power reflection coefficients R_k can also be obtained by the following equation:

$$R_k = \frac{P_{ref,\ k}}{P_{inc}}\ , \tag{4.3}$$

where P_{inc} is the power of the incident wave, and $P_{ref,\ k}$ is the power of the k^{th} reflected mode. The power can be obtained by multiplying the calculated or measured displacement amplitude square with the mode power coefficient as described in section 2.4.1.3 [118]. Or it can be obtained by relating the calculated or measured displacement amplitude to power through the coefficient ζ as described in [78]. The calculation of the coefficient ζ needs the knowledge of the exact field distribution of the respective mode [77]. Thus, it is difficult to calculate and fault-prone for multilayer structures. The mode power coefficients on the other hand are easy to calculate, and therefore, are adopted in this study.

In order to obtain the reflection coefficients, the amplitudes of respective mode have to be determined. The free boundary is discretized into $m = 1 \ldots M$ collocated points, which represent the whole field on the free edge (shown in Fig. 4.5). In the waveguide $k = 1 \ldots N$ propagating and evanescent eigenmodes are assumed to be present. Then, equation 4.1 can be written in discretized form as

$$\mathbf{T}_{inc}(m) \cdot \mathbf{n} \cdot A_{inc} + \sum_k \mathbf{T}_{ref,\ k}(m) \cdot \mathbf{n} \cdot A_{ref,\ k} = 0 \ , (m = 1 \ldots M) \ , \tag{4.4}$$

where $\mathbf{T}_{inc}(m)$ is the stress vector of the incident mode at location m, and $\mathbf{T}_{ref,\ k}(m)$ is the stress vector of the k^{th} reflected mode at location m. Equation (4.4) can be written in matrix form as

$$\mathbf{T}_{inc}(m) \cdot \mathbf{n} \cdot A_{inc} + \mathbf{M} \cdot \mathbf{A}_{ref} = 0 \ , \tag{4.5}$$

where $\mathbf{A}_{ref}$ is the vector including all the N reflected mode amplitudes and $\mathbf{M}$ is a $2M \times N$ matrix. $\mathbf{n}$ is perpendicular to axis x_3 in this case, thus $\mathbf{T}_{ref,\ k}(m) \cdot \mathbf{n}$ is a $2 \times N$ matrix

$$\begin{bmatrix} T_1^{ref,1}(m) & T_1^{ref,2}(m) & \cdots & T_1^{ref,N}(m) \\ T_5^{ref,1}(m) & T_5^{ref,2}(m) & \cdots & T_5^{ref,N}(m) \end{bmatrix} , \tag{4.6}$$

$T_1^{ref,k}(m)$ is the longitudinal stress component and $T_5^{ref,k}(m)$ is the shear stress component of the k^{th} reflected mode at location m. For the general case when $\mathbf{n}$ is not perpendicular to one of the axis, $\mathbf{M}$ is a $3M \times N$ matrix. Then, the unknown reflected mode amplitudes can be calculated by

$$\mathbf{A}_{ref} = -\left(\mathbf{M}^t\mathbf{M}\right)^{-1}\mathbf{M}^t\mathbf{T}_{inc}(m) \cdot \mathbf{n} \cdot A_{inc} \ , \tag{4.7}$$

where the exponents t and -1 mean respectively transpose and inverse of a matrix. Note that the value of N and M should be sufficient big to ensure the accuracy of this method.

Torvik's method is only applicable to single mode excitation. Moreover, the implementation of Torvik's method requires the knowledge of the imaginary or complex wavenumbers β of the evanescent modes at a given frequency, which are difficult to calculate. The field distribution of respective mode also has to be calculated precisely, which has increased the difficulty to carry out this method even more. Thus, pure numerical method using FEM simulation has been proposed, which will be reviewed in the next two sections.

4.2.2 Time domain FEM simulation

The most common method to perform scattering analysis is the time-domain FEM simulation (TD-FEM). A schematic of the TD-FEM method is shown in Fig. 4.6. A two-dimensional model is set up to model the waveguide and the scattering boundary. The waveguide and the scattering boundary are discretized into elements, which are defined by a certain number of nodes. The number of nodes should be large enough, that is a minimum of 20 nodes per wavelength is usually required. A single mode at a frequency ω_o is excited at the left end of the plate. A transient analysis is set up, and a large number of time steps is simulated. For $0 < t < t_1$, a finite acoustic burst of the desired incident mode is excited at the left end of the plate by imposing its theoretical longitudinal and shear displacements $u_1(x_3, t)exp(j\omega_o t)$ and $u_3(x_3, t)exp(j\omega_o t)$ on the FEM DOF (Fig. 4.6(a)). The incident mode is propagating forward and scattered at the right edge for $t_2 < t < t_3$ as shown in Fig. 4.6(b). For $t > t_3$, only the reflected waves are propagating in the plate. The surface displacements $u(x_1, t)$ are monitored and recorded during this process. Consequently, a two-dimensional fast Fourier transform (2D FFT) is applied to these recorded displacements

$$u(\beta, \omega) = \int_{-\infty}^{+\infty} \int_{-\infty}^{+\infty} u(x_1, t)e^{-j(\omega t + \beta x_1)} dx_1 \; dt \; . \tag{4.8}$$

The dispersion characteristic of the plate can be obtained by $u(\beta, \omega)$. Surface amplitude $A_{ref,k}$ of the k^{th} reflected mode can be obtained by $A_{ref,k} = |u(\beta_k, \omega_o)|$. It can be compared directly to the amplitude of the incident mode or related to the respective mode power as described in chapter 2.

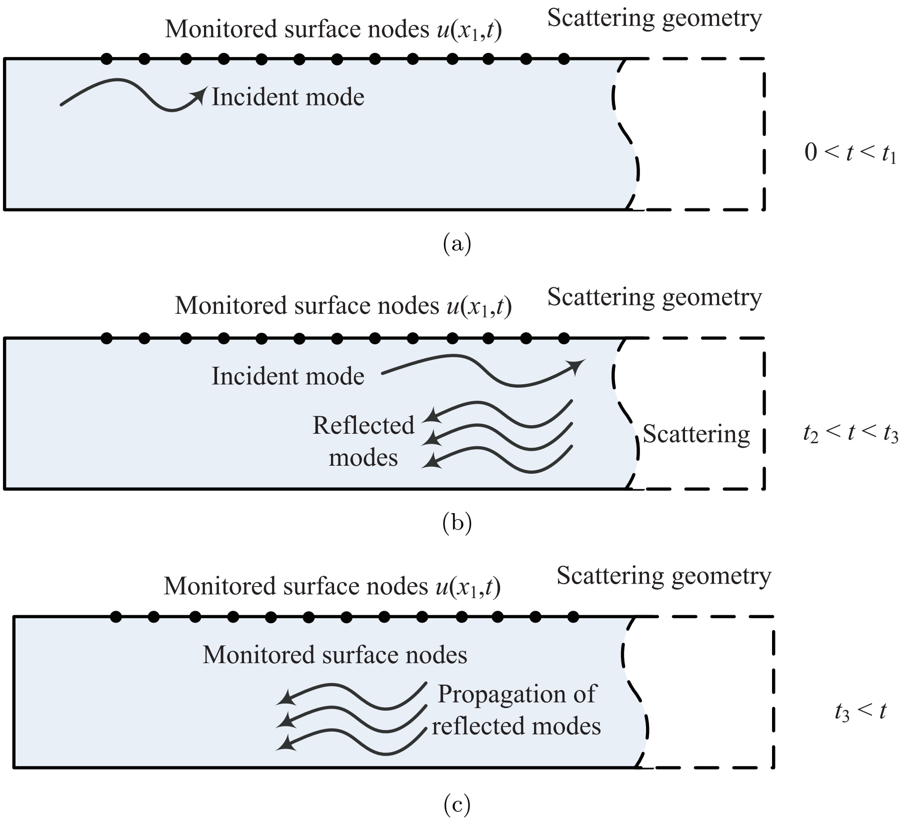

Figure 4.6: Schematic of different time steps in the time-domain FEM analysis for wave scattering (a) Lamb wave burst to excite the incident mode, (b) reflection of the incident mode at the right boundary, and (c) propagation of the reflected waves.

It should be noted that in addition to the amplitude $A_{ref,k}$ of the k^{th} reflected mode at the frequency of ω_o, the amplitudes of the reflected modes at other frequencies can also be obtained by this method. However, these values are not utilized by this method, because this method is only applicable to single mode excitation at the frequency of ω_o. It is a waste of resources. To use the resources more efficiently, frequency domain FEM simulation was proposed [119], which will be reviewed in the next section.

4.2.3 Frequency domain FEM simulation

To get rid of the redundant data obtained by time-domain FEM (TD-FEM) analysis, Thalmayr et. al. have proposed a frequency-domain FEM (FD-FEM) analysis method for single mode incident wave scattering [119]. Fig. 4.7 shows a schematic setup of the FD-FEM analysis for wave scattering. Similar to TD-FEM analysis, first, a two-dimensional model of the waveguide and the scattering boundary is set up. A single mode at a frequency ω_o is excited at the left end of the plate by imposing its theoretical longitudinal and shear displacements $u_1(x_3, \omega_o)exp(j\omega_o t)$ and $u_3(x_3, \omega_o)exp(j\omega_o t)$ on the FEM DOF (Fig. 4.7). To isolate the injected wave from the backscattered waves, TD-FEM analysis can separate these waves by time or by the 2D-FFT method. Besides, this isolation can be achieved by implementing an appropriated injection damping mechanism (IDM) in the FD-FEM analysis model (shown in Fig. 4.7). The IDM should be designed properly. Both the forward propagating injected wave and the backward propagating backscattered waves are strongly damped within the IDM. Meanwhile, a sufficient amount of energy of the injected wave arrives at the left end of the undamped or regular waveguide. Then, the surface displacements $u(x_1, \omega_o)$ are monitored and recorded. Finally, a one-dimensional fast Fourier transform (1D FFT) is applied to these recorded displacements

$$u(\beta, \omega_o) = \int_{-\infty}^{+\infty} u(x_1, \omega_o) e^{-j\beta x_1} dx_1 \ . \tag{4.9}$$

Surface amplitude $A_{ref,k}$ of the k^{th} reflected mode can be obtained by $A_{ref,k} = |u(\beta_k, \omega_o)|$. It can be compared directly to the amplitude of the incident mode or related to the respective mode power as described in chapter 2.

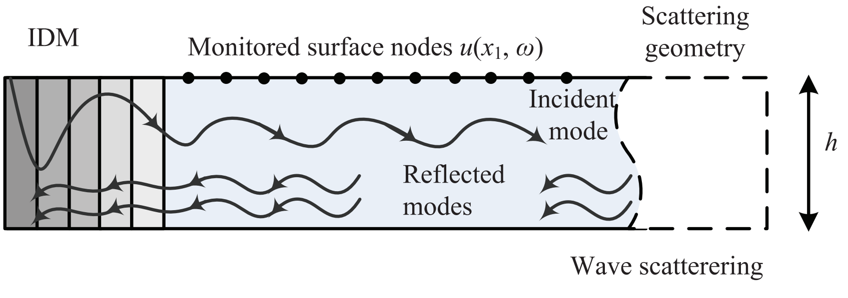

Figure 4.7: Schematic of the frequency-domain FEM setup for the analysis of wave scattering.

To eliminate the influence of the evanescent modes, the displacements are recorded in a sufficient distance from the scattering boundary. This FD-FEM analysis method is more efficient than the TD-FEM analysis in terms of the time consumption[119]. However, it can only be applicable to single mode excitation wave scattering analysis. Therefore, a more efficient wave scattering analysis method has been proposed to utilize the data obtained by 2D FFT method for multimode excitation wave scattering, which will be presented in the next section.

4.3 Scattering analysis for multimode excitation

All the wave scattering analysis methods reviewed in section 4.2 have the same problem: they can only be applied to single mode excitation wave scattering analysis. However, experimentally excitation via transducers of finite dimensions inevitably excites multiple modes at any particular frequency. Therefore, a more efficient wave scattering analysis method for multimode excitation is proposed, which will be described in this section.

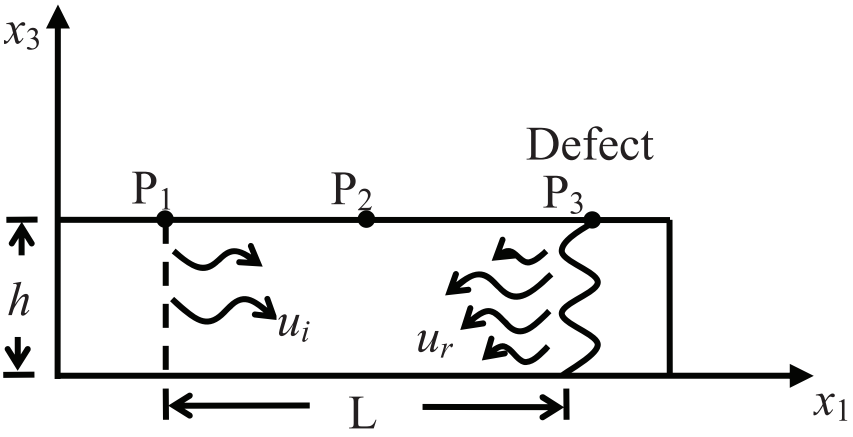

Figure 4.8: Schematic of the model setup for the analysis of multimode excitation wave scattering.

A pulse-echo setup for multimode excitation wave scattering analysis using guided Lamb waves is depicted in Figure 4.8. Lamb waves are excited by a multimode transducer such as a Nd:YAG laser at P_1 and the scattered Lamb waves are examined by another transducer at P_2. The plate can be a single-layer plate or multi-layer composite laminates with neglectable losses. For the sake of illustration, P_2 is assumed to be lie between P_1 and the defect, which is located at P_3. In this setup, both incident waves and scattered waves are measured by the transducer at P_2.

Suppose a toneburst with center angular frequency ω_o is excited by the transducer at P_1. It is assumed that the bandwidth of the toneburst is narrow so that the temporal function of the toneburst can be represented by $e^{j\omega_o t}$. In practice, the method can be used for wideband signals provided that both the transmitting and receiving transducers are broadband devices. The excited toneburst consists of N Lamb wave modes with displacement distribution $\Psi_n(x_3)$ and amplitude a_n:

$$u_i(x_3,t) = \sum_{n=0}^{N-1} a_n \Psi_n(x_3) e^{j\omega_o t} \qquad (t \geq 0)\ . \tag{4.10}$$

Due to the dispersive property of Lamb waves, the excited Lamb wave modes propagate along the plate with phase velocity $v_n = \omega_o/\beta_n$ $(n = 1, 2, ..., N-1)$ where β_n is the wavenumber of the n^{th} Lamb wave mode. The wavenumbers can be analytically determined by finding the root of the dispersion equation derived from the Navier's displacement equation [90] or numerical methods such as the finite element method (FEM) [8]. The displacement expression along the direction x_1 can be written as

$$u_i(x_1,x_3,t) = \sum_{n=0}^{N-1} a_n \Psi_n(x_3) e^{j(\omega_o t - \beta_n x_1)} \qquad (t \geq 0)\ . \tag{4.11}$$

Due to the difference in phase velocity, the incident Lamb wave modes scattered by the defect at different time t_n where $t_n = L/v_n$ and L is the separation between the measurement point and the defect. The distance L can be accurately estimated by measuring the time-of-flight (t_{TOF}) of the fastest reflected Lamb wave mode:

$$L = t_{TOF} \times \mathbf{Max}[v_n]/2\ . \tag{4.12}$$

At the defect, each incident Lamb wave mode is scattered into N propagating Lamb wave modes $\Psi_n(x_3)$ as well as evanescent modes $\Phi_k(x_3)$. The reflected wave of the n^{th} incident Lamb wave mode can be written as

$$u_{rn}(x_1,x_3,t) = \sum_{m=0}^{N-1} a_{mn} \Psi_m(x_3) e^{j(\omega_o t + \beta_m x_1)} + \sum_{k}^{\infty} b_k \Phi_k(x_3) e^{(j\omega_o t + \alpha_k x_1)} \quad (t \geq t_n)\ , \tag{4.13}$$

where a_{mn} is the amplitude of the m^{th} Lamb wave mode converted from the n^{th} Lamb wave mode, α_k and b_k are, respectively, the attenuation constant and amplitude of the k^{th} evanescent mode. The evanescent modes only exist in the vicinity around the defect and do not carrying power along the structure. Hereafter, only the N propagating modes are considered.

Combining all the scattered Lamb wave modes, the scattered waves consists of $N \times N$ components:

$$u_r(x_1, x_3, t) = \sum_{n=0}^{N-1} u_{rn}(x_1, x_3, t) \ . \tag{4.14}$$

In general, the scattered Lamb wave modes overlap in time-domain so that it is difficult to determine the $N \times N$ unknown mode conversion coefficients a_{mn}.

Alleyne et. al. [8, 9] have used the two-dimensional Fourier transform (2D FFT) to analyse the scattering of defects by various Lamb wave modes. The method presented here is an extension of the 2D FFT method. By applying the spatial Fourier transform to the measured incident and scattered Lamb waves at P_2, we have the spectrum with $2N$ components located at the wavenumber $k_x = \pm\beta_0, \beta_1, ..., \beta_{N-1}$. The components correspond to the N incident Lamb wave modes and N scattered Lamb wave modes. The expression of the incident and scattered waves in wavenumber domain are:

$$U_i(k_x, x_3, t) = \sum_{n=0}^{N-1} a_n \Psi_n(x_3) \delta(k_x + \beta_n) e^{j\omega_o t} \ , \tag{4.15}$$

$$U_r(k_x, x_3, t) = \sum_{n=0}^{N-1} \sum_{m=0}^{N-1} a_{mn} \Psi_m(x_3) \delta(k_x - \beta_m) e^{j\omega_o (t - t_n)} \ . \tag{4.16}$$

In practice, the displacements on the surface ($x_3 = h$) of the structure are measured. The amplitude of the n^{th} incident Lamb wave mode and n^{th} scattered Lamb wave mode on the surface of the structure in wavenumber domain are:

$$A_{in} = a_n \Psi_n(h) e^{j\omega_o t} \qquad \textbf{at } k_x = -\beta_n \ , \tag{4.17}$$

$$A_{rn} = \sum_{m=0}^{N-1} a_{nm} \Psi_n(h) e^{j\omega_o (t - t_m)} \qquad \textbf{at } k_x = \beta_n \ . \tag{4.18}$$

Figure 4.9 shows a typical spectrum of a structure which supports three propagating Lamb wave modes.

Combining the Eq. (4.17) and Eq. (4.18), we can express the amplitude of the scattered Lamb wave modes in terms of the incident Lamb wave modes:

$$A_{rn} = \sum_{m=0}^{N-1} r_{nm} A_{im} e^{-j\omega_o t_m} \ , \tag{4.19}$$

$$r_{nm} = \frac{a_{nm} \Psi_n(h)}{a_m \Psi_m(h)} \ , \tag{4.20}$$

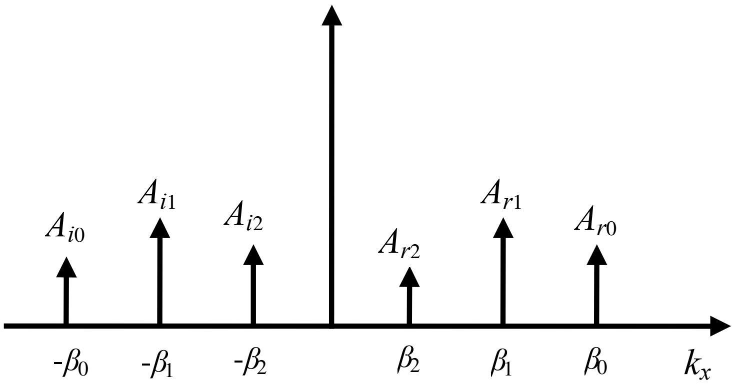

Figure 4.9: Spectrum of a typical Lamb wave measured by the transducer at P_2. Three Lamb modes are supported by the structure at the measuring frequency.

where r_{nm} is the complex mode amplitude conversion coefficient from mode m to mode n.

As the A_{rn} is the vector sum of all Lamb waves converted from all the incident Lamb wave modes, in order to extract the mode conversion coefficient of each mode. The above measurement is repeated with another $(N-1)$ different excitations. Finally, we can set up a matrix equation.

$$\mathbf{A_r} = \mathbf{r}\mathbf{T}\mathbf{A_i} \ , \tag{4.21}$$

$$\mathbf{A_r} = \begin{bmatrix} A^1_{r0} & A^2_{r0} & \cdots & A^N_{r0} \\ A^1_{r1} & A^2_{r1} & \cdots & A^N_{r1} \\ \vdots & \vdots & \ddots & \vdots \\ A^1_{r,N-1} & A^2_{r,N-1} & \cdots & A^N_{r,N-1} \end{bmatrix} , \tag{4.22}$$

$$\mathbf{A_i} = \begin{bmatrix} A^1_{i0} & A^2_{i0} & \cdots & A^N_{i0} \\ A^1_{i1} & A^2_{i1} & \cdots & A^N_{i1} \\ \vdots & \vdots & \ddots & \vdots \\ A^1_{i,N-1} & A^2_{i,N-1} & \cdots & A^N_{i,N-1} \end{bmatrix} , \tag{4.23}$$

$$\mathbf{T} = \begin{bmatrix} e^{-j\omega_o t_0} & 0 & \cdots & 0 \\ 0 & e^{-j\omega_o t_1} & \cdots & 0 \\ \vdots & \vdots & \ddots & \vdots \\ 0 & 0 & \cdots & e^{-j\omega_o t_{N-1}} \end{bmatrix} , \tag{4.24}$$

$$\mathbf{r} = \begin{bmatrix} r_{00} & r_{01} & \cdots & r_{0,N-1} \\ r_{10} & r_{11} & \cdots & r_{1,N-1} \\ \vdots & \vdots & \ddots & \vdots \\ r_{N-1,0} & r_{N-1,1} & \cdots & r_{N-1,N-1} \end{bmatrix} , \tag{4.25}$$

where the superscript p in A^p_{in} and A^p_{rn} is used to denote the p^{th} measured spectral components of the Lamb wave modes. The complex mode amplitude conversion coefficient r_{nm} on surface can be determined by solving Eq. (4.21) with N different excitations.

The complex mode amplitude conversion coefficient r_{nm} on surface can be further related to the power scattering coefficients s_{nm} by the mode power coefficients c_n [118]. The incident power of the m^{th} Lamb wave mode expressed in terms of the mode power coefficient c_m is

$$P_m = c_m |a_m \Psi_m(h)|^2 , \tag{4.26}$$

and the power of the Lamb wave converted from mode m to mode n can be expressed as

$$P_{nm} = c_n |a_{nm} \Psi_n(h)|^2 . \tag{4.27}$$

The power scattering coefficient s_{nm} is defined as

$$s_{nm} = \frac{P_{nm}}{P_m} . \tag{4.28}$$

Combining equations (4.20) and (4.26 - 4.28) together, we have

$$s_{nm} = \frac{c_n}{c_m} |r_{nm}|^2 . \tag{4.29}$$

The phase factor $e^{-j\omega_o t_m}$ in matrix $\mathbf{T}$ only affects the phase of the complex mode amplitude conversion coefficient r_{nm}. Omitting $e^{-j\omega_o t_m}$ in matrix $\mathbf{T}$ will not influence the value of the power scattering coefficient s_{nm}. This is reasonable since the power scattering coefficient s_{nm} is only related to the scattering boundary. This was confirmed by the validation example in the next section.

4.4 Validation of the scattering analysis for multimode excitation

In this section, the reflection of the two lowest antisymmetric modes A_0 and A_1 at the free edge of a plate is considered to verify the validity of the proposed scheme presented in section 4.3. The thickness of the plate is 1.0 mm. The free edge (P_3) and the observation point (P_2) are, respectively, 100 mm and 65 mm away from the excitation point (P_1). The plate is stainless steel with density $\rho = 7800$ kg/m^3, Young's modules $E = 200.43$ GPa, and Poisson ratio $v = 0.29$.

A two-dimensional finite-difference time-domain (FDTD) model (developed in chapter 3) is set up to simulate the propagation of the Lamb waves. Both the temporal-derivatives and spatial-derivatives in the equation of motion, which relates the particle velocity and the stress, are approximated by second-order centred finite differences as described in chapter 3. The particle velocity is adopted in the FDTD simulation in order to simplify the formulation. As mentioned in chapter 3, the particle velocity is related to the particle displacement u by $v = \partial u/\partial t$ in time-domain and $V = j\omega_o U$ in frequency-domain. The zero traction condition is enforced on the boundaries. As it is mentioned in section 3.5, to reduce the artificial numerical dispersion effects to an acceptable extent, the spatial step size Δx_1 and Δx_3 are set to both 5×10^{-5} m, which is approximately equal to one twentieth of the smallest wavelength of the toneburst. To ensure the stability of the simulation, the time increment interval is chosen to be 6×10^{-9} s in order to satisfy the Courant stability condition [111].

A five-cycle Lamb wave toneburst (demonstrated in section 3.6.2) composed of A_0 and A_1 modes is numerically launched by imposing their theoretical particle velocity components [8] $\mathbf{v}(x_3)$ at P_1

$$\mathbf{v}(x_3) = K_1\mathbf{v}^0(x_3) + K_2\mathbf{v}^1(x_3)\ , \tag{4.30}$$

where $\mathbf{v}^i(x_3)$ is the particle velocity of the A_i mode, and K_i are arbitrary constants, which are set to 1 and 5 in this simulation. The number of cycles of the toneburst should be chosen such that the toneburst covers the frequency range of interest. It is better not to choose a too large number to reduce the simulation time. In this case, the bandwidth of the toneburst covers the frequency-thickness product range of $2.5\text{MHz} \cdot \text{mm} < F < 3.5\text{MHz}\cdot\text{mm}$. Within this frequency-thickness product range, only these two antisymmetric modes are above their cutoff frequencies.

Figure 4.10 shows the normalized time history and its wavenumber spectrum at frequency 2.6 MHz of the incident Lamb wave collected at 30 mm away from the excitation point P_1. Because of dispersive property of Lamb waves, the A_0 and A_1 modes cannot be distinguished in time-domain. On the other hand, the wavenumber spectrum shows that the incident Lamb wave consists of two modes with phase constant 2.45 rad/mm and 5.91 rad/mm, which are corresponding to the A_1 mode and A_0 mode, respectively.

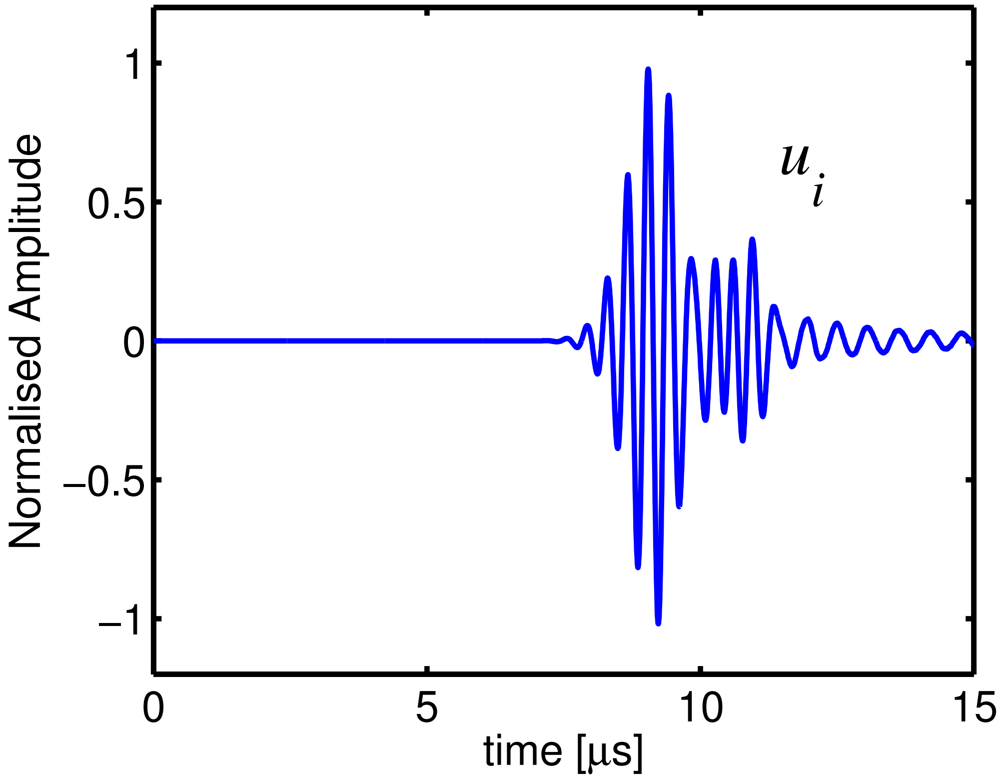

(a)

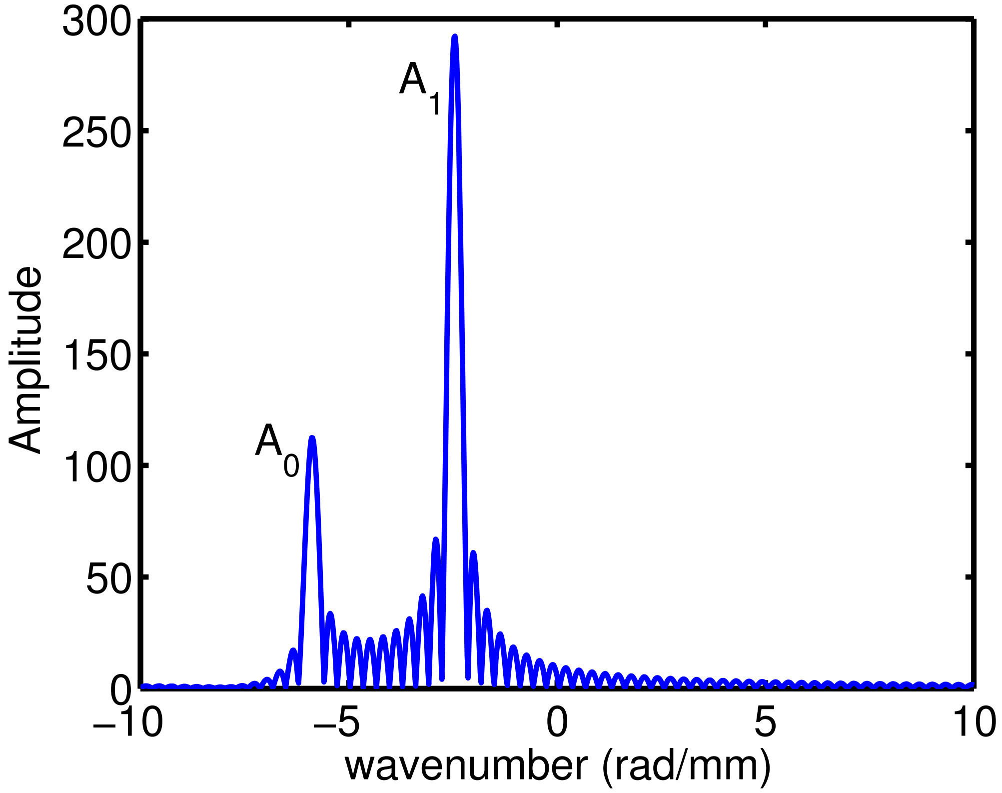

(b)

Figure 4.10: Incident Lamb waves at $x_1 = 30$mm when the input A_0 and A_1 modes are excited at $x_1 = 0$. (a) Time history, (b) Wavenumber spectrum at frequency = 2.6 MHz.

Figure 4.11(a) shows the normalized time history of the Lamb wave collected at P_2. The duration of the simulation is long enough to include the incident Lamb wave and the reflected Lamb waves from the free end of the plate. The incident Lamb wave consists of two overlapping tonebursts while the reflected wave contains more than two overlapping tonebursts because of the mode conversion at the free edge [78, 121]. Figure 4.11(b) shows the wavenumber spectrum at frequency 2.6 MHz of the Lamb wave collected at P_2. It can be observed that the reflected wave consists of mode A_0 and mode A_1 only but more than two tonebursts are observed in time domain. It is because the reflection boundary is symmetric, no mode conversion from antisymmetric to symmetric modes can occur. Besides, the incident mode A_0 and A_1 have different phase velocity so that they arrive at the boundary at different time. After the reflection from the boundary, there are four tonebursts travelling in the plate. They are A_1 mode converted from the incident A_1 mode, A_0 mode converted from the incident A_1 mode, A_1 mode converted from the incident A_0 mode, and A_0 mode converted from the incident A_0 mode. Since the two reflected A_1 mode converted from the incident A_0 mode and the incident A_1 mode have the same wavenumber at a given frequency, these two waves cannot be distinguished from both time-domain history and the wavenumber-domain spectrum. To distinguish these two waves, the simulation is repeated with the constants $K_1 = 0.3$ and $K_2 = 11$ for the amplitude of the two incident Lamb wave modes. The amplitudes of the two incident modes are determined by the K_i values. Therefore, the second set of two K_i values should not be proportional to the first set of values to make sure that the matrix $\mathbf{A_i}$ is invertible in Eq. (4.21) to get the conversion coefficient $\mathbf{r}$. If K_1 is larger than K_2 for the first set of values, it is better to chose K_1 smaller than K_2 for the second set of values to reduce the numerical error, and vice versa. The complex amplitude of the incident modes (A_{i0} and A_{i1}) and reflected modes (A_{r0} and A_{r1}) can be obtained by applying 2D FFT to the time sequence of the equally allocated monitoring points on the top surface. With the two wavenumber spectra obtained from the simulations, the complex mode amplitude conversion coefficients r_{nm} are determined by solving the matrix equation (Eq. (4.21)).

Fig. 4.12 shows the amplitude of the conversion coefficients r_{nm} for A_0 and A_1 modes reflecting from the free edge. The result shows that all the coefficients of a multimode incident Lamb wave can be resolved. It can also be observed that the amplitude of the conversion coefficient r_{10} is much larger than that of r_{01} for the specified frequency-thickness range. This implies that mode A_0 is more sensitive to the free boundary condition than mode A_1. As it is mentioned in section 4.1.1, Lamb waves are commonly used in nondestructive testing (NDT) applications. Because of this kind of phenomenon, i.e. each mode is sensitive to different types of defects, most previous work exciting a pure

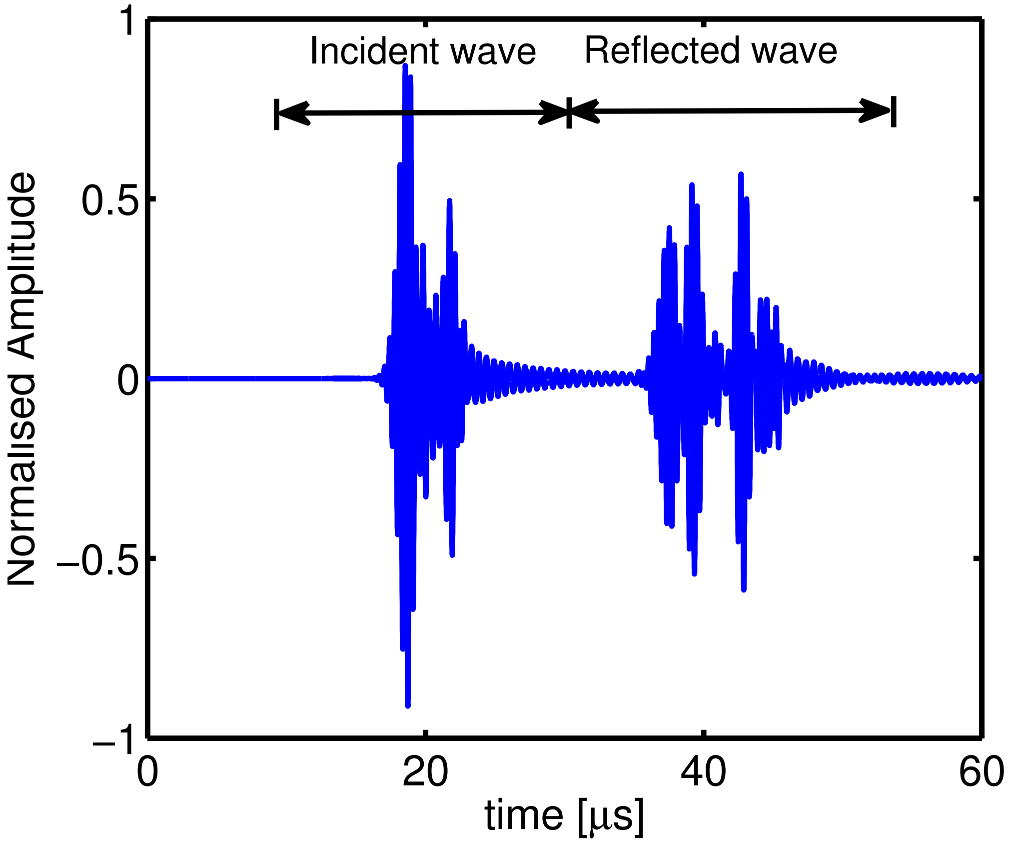

(a)

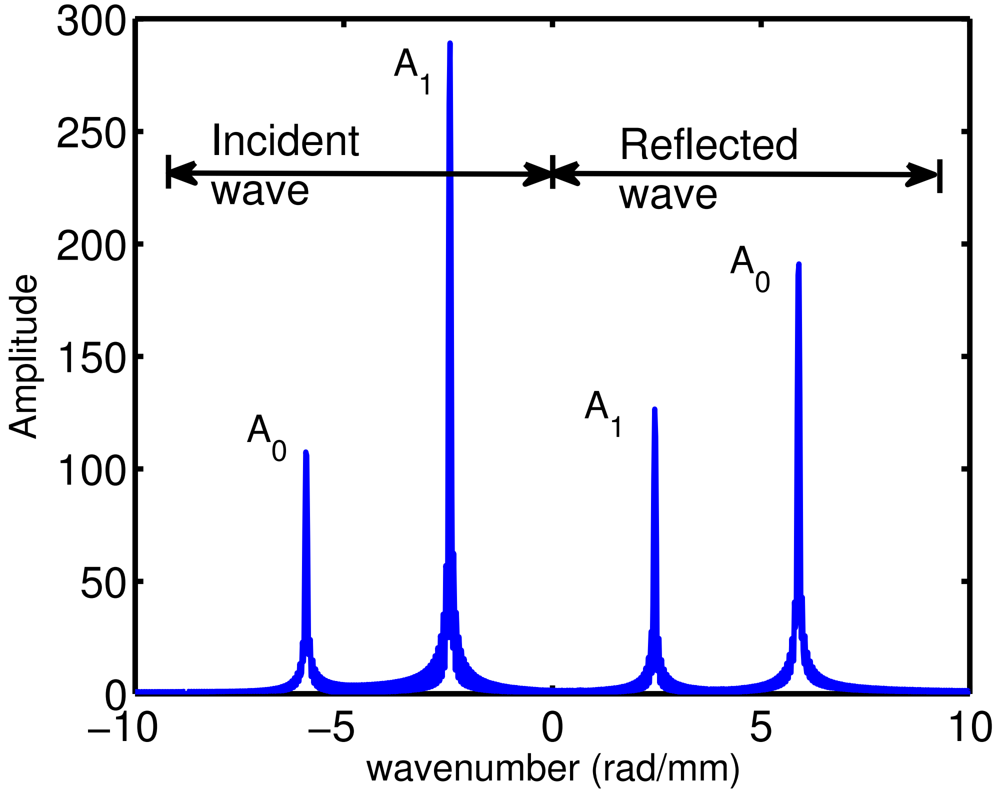

(b)

Figure 4.11: Scattered Lamb waves at P_2. (a) Time history, (b) Frequency spectrum.

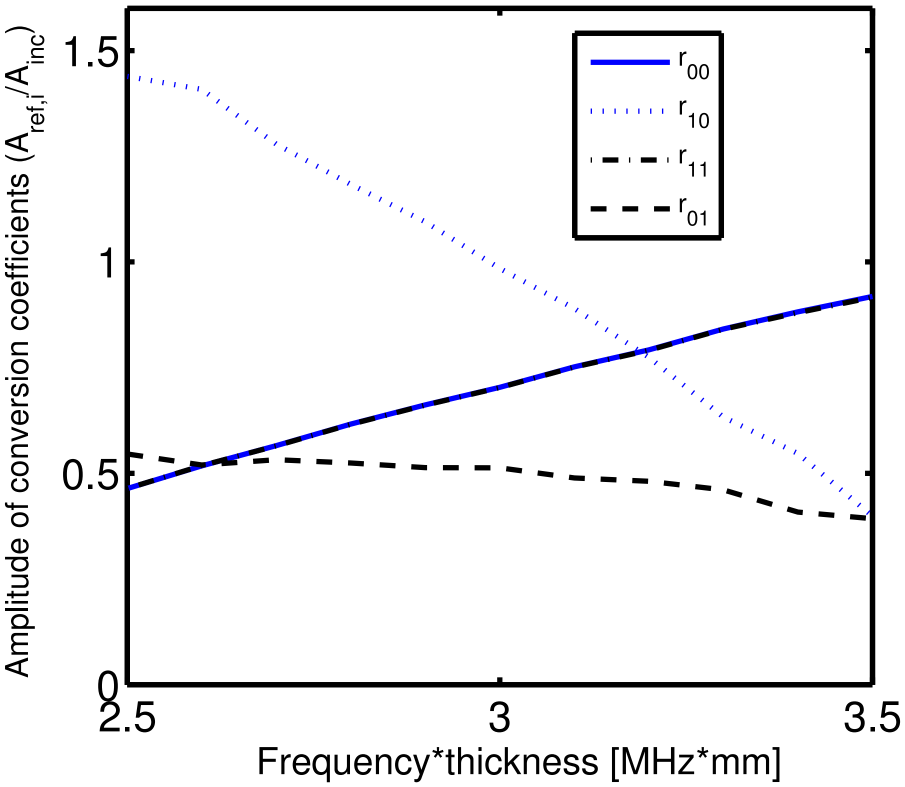

Figure 4.12: Amplitude of the conversion coefficients r_{nm} for A_0 and A_1 modes reflecting from the free edge.

Lamb wave mode for testing rely on partial knowledge of the defect[25, 31, 43, 69, 76, 110]. If multimode excited Lamb waves can be applied in NDT applications, various defects can be detected simultaneously and the testing process will become more robust. Moreover, the resolution of a NDT generally depends on the guided wavelength of the Lamb mode. Therefore, in order to detect small defects, Lamb mode with higher phase velocity operated at higher frequency-thickness product should be used. However, for large frequency-thickness product, structures support a large number of propagating Lamb wave modes. Therefore, it is challenging to excite a pure Lamb wave mode for large frequency-thickness product, that is multimode Lamb wave modes will inevitably be present. The scheme proposed in this chapter has provided a simple way to extract and interpret the multimode Lamb wave modes scattering information and thus, make the application of Lamb wave modes in NDT simpler.

In order to compare with the results obtained by other methods [119, 121] the power scattering coefficients s_{mn} are calculated by Eq. (4.29). The mode power coefficients c_n are calculated by the effective acoustic admittance as described in section 2.4.1.3. The mode power coefficients c_n for mode A_0 and A_1 are shown in Fig. 4.13. Figure 4.14 shows the power scattering coefficients calculated by the proposed method. The result shows that all the coefficients of a multimode incident Lamb wave can be resolved. It is also observed that $s_{10} = s_{01}$, which is consistent with the reciprocal property of the free space boundary. Besides, $s_{00} = s_{11}$ because of the conservation of energy ($s_{11} + s_{01} = s_{00} + s_{10} = 1$). The accuracy of the results is also validated by comparing with the results obtained by single mode excitation FEM scheme [119] in Fig. 4.15. It is observed that our obtained results are in good agreement with the one obtained by FEM method. Before doing the scattering analysis, the energy differences between the incident modes and reflected modes are also calculated to check the computation accuracy, which are shown in Table 4.1 and Table 4.2 for the first set of data and the second set of data, respectively. $P_{A_n,inc}$ (n=0, 1) is the power of the incident mode A_n, and P_{inc} is the total incident power calculated by $P_{inc} = P_{A_0,inc} + P_{A_1,inc}$. $P_{A_n,ref}$ (n=0, 1) is the power of the reflected mode A_n, and P_{ref} is the total reflected power calculated by $P_{ref} = P_{A_0,ref} + P_{A_1,ref}$. Energy difference between the incident modes and the reflected modes P_{dif} is calculated by $P_{dif} = (P_{ref} - P_{inc})/P_{inc}$. It is observed that the energy difference is smaller than 0.25% at all frequencies. The accuracy of the results can be improved by increasing the simulation time and elongating the structure to allocate more monitoring points on the surface to improve the frequency and wavenumber resolution, respectively.

A similar problem was analyzed by time-domain FEM (TD-FEM) method [78] and frequency-domain FEM (FD-FEM) method [119]. The calculation time to obtain a single set of scattering parameters was reported to be 24 hours by the use of the TD-FEM method, and less than 20 seconds by the use of FD-FEM method with a Pentium Core 2 Duo personal computer [119]. The simulation time for the structure mentioned in this work is around 4 hours by a computer with Intel Xeon 3.33 GHz CPU and 16 GB of RAM. Merely regarding the simulation time, FD-FEM method is superior to the TD-FEM method and the FDTD scattering analysis scheme proposed in this work. However, the scattering analysis scheme proposed in this work can be applied to obtain the scattering parameters for multimode excitation for a frequency range, while the FD-FEM method can only obtain the response at a single frequency for each simulation. Therefore, the proposed multimode scattering analysis scheme is especially useful when the scattering parameters need to be calculated over a wide frequency range or in practice where a single mode excitation is challenging or impossible. In addition, the simulation time of the proposed FDTD method can be reduced by parallelization, and an almost linear speed-up with the number of processors can be achieved [104].

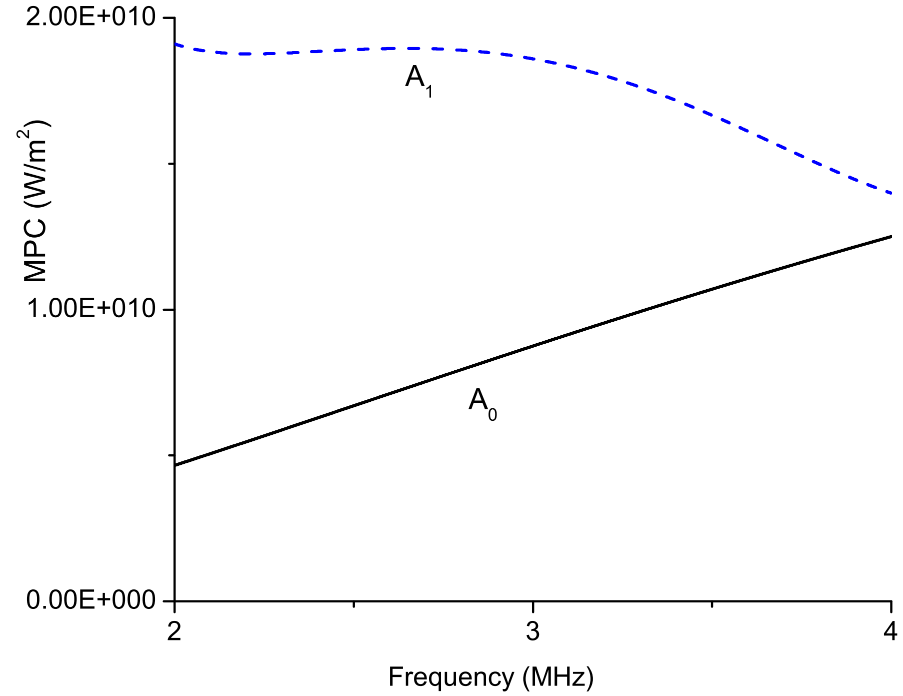

Figure 4.13: Mode power coefficient c_n for A_0 and A_1 modes propagating in steel plate.

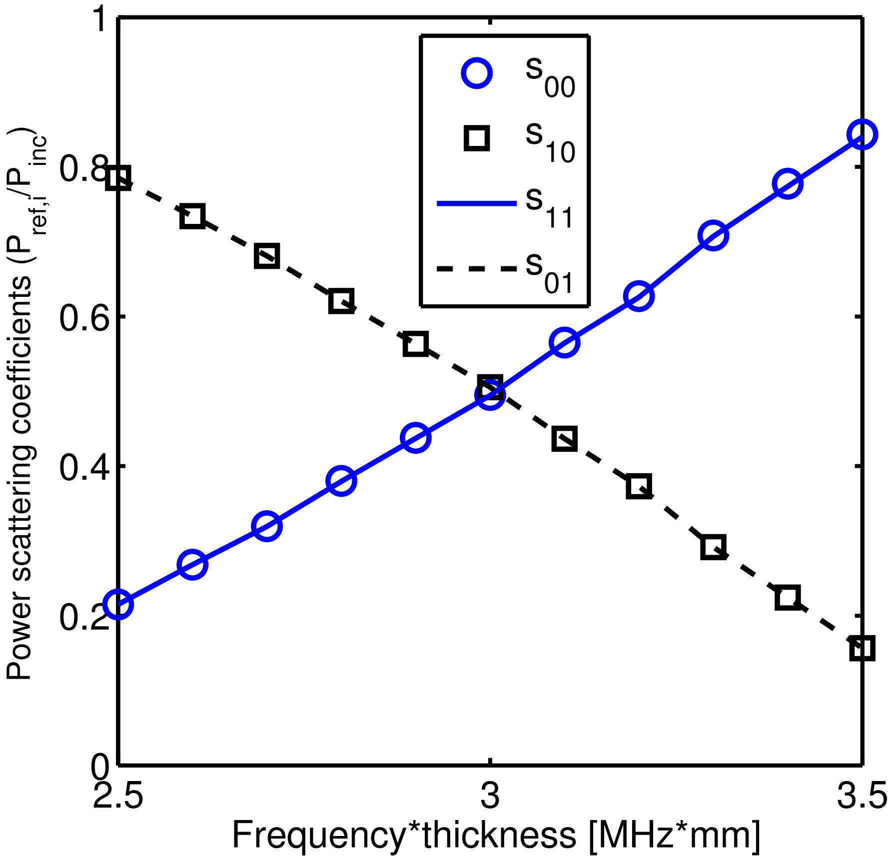

Figure 4.14: Power scattering coefficients s_{nm} for A_0 and A_1 modes reflecting from the free edge.

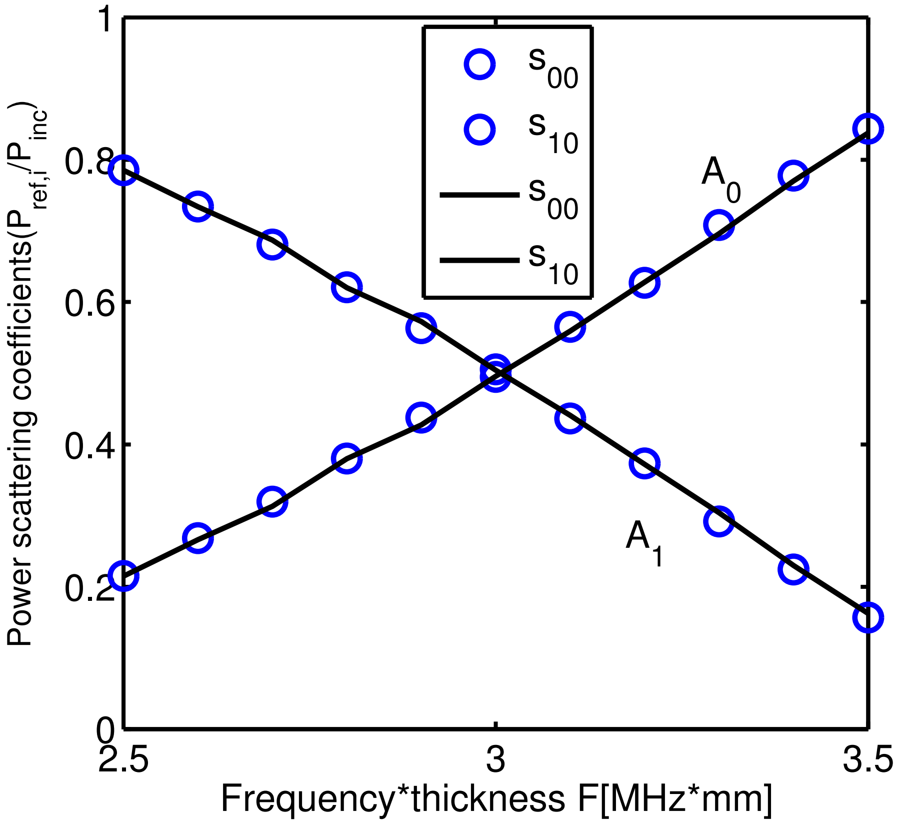

Figure 4.15: Power scattering coefficients s_{nm} for mode A_0 reflecting from the free edge; ◯ obtained by FDTD simulation, solid lines are obtained by FEM method[119].

Table 4.1: Energy difference between the incident modes and the reflected modes for the first set of data.

frequency (MHz)	$P_{A_0,inc}$ 10^{-8}W	$P_{A_1,inc}$ 10^{-8}W	P_{inc} 10^{-8}W	$P_{A_0,ref}$ 10^{-8}W	$P_{A_1,ref}$ 10^{-8}W	P_{ref} 10^{-8}W	P_{dif} (%)
2.5	17.40	1.38	18.78	4.81	13.97	18.78	0.03
2.6	18.53	1.61	20.14	6.15	14.03	20.19	0.24
2.7	20.49	1.64	22.14	7.66	14.48	22.14	0.03
2.8	19.12	1.47	20.59	8.17	12.44	20.61	0.07
2.9	16.40	1.23	17.63	7.87	9.78	17.65	0.10
3.0	13.18	0.94	14.12	7.00	7.12	14.12	0.04
3.1	9.31	0.67	9.99	5.55	4.45	10.00	0.13
3.2	6.16	0.40	6.56	4.01	2.55	6.56	0.03
3.3	3.08	0.19	3.27	2.24	1.04	3.27	0.00
3.4	1.36	0.08	1.44	1.07	0.37	1.44	0.14
3.5	0.49	0.02	0.51	0.42	0.10	0.51	0.01

Table 4.2: Energy difference between the incident modes and the reflected modes for the second set of data.

frequency (MHz)	$P_{A_0,inc}$ 10^{-8}W	$P_{A_1,inc}$ 10^{-8}W	P_{inc} 10^{-8}W	$P_{A_0,ref}$ 10^{-8}W	$P_{A_1,ref}$ 10^{-8}W	P_{ref} 10^{-8}W	P_{dif} (%)
2.5	1.57	4.21	5.79	3.65	2.14	5.79	0.03
2.6	1.72	4.98	6.70	4.12	2.60	6.72	0.24
2.7	1.88	5.34	7.22	4.24	2.99	7.22	0.03
2.8	1.80	5.03	6.82	3.81	3.02	6.83	0.05
2.9	1.56	4.37	5.94	3.15	2.79	5.94	0.08
3.0	1.27	3.45	4.72	2.37	2.35	4.72	0.01
3.1	0.92	2.50	3.42	1.61	1.81	3.42	0.11
3.2	0.62	1.60	2.21	0.98	1.23	2.21	-0.05
3.3	0.32	0.75	1.07	0.44	0.62	1.07	-0.07
3.4	0.14	0.35	0.49	0.19	0.30	0.49	-0.04
3.5	0.05	0.11	0.16	0.06	0.10	0.16	-0.16

4.5 Multimode wave scattering analysis in generic FBAR model

The proposed multimode scattering analysis scheme is applied to study two generic FBAR resonators in this section. For simplicity, firstly, the generic FBAR resonator with symmetric electrodes on top and bottom is set up to analyze the scattering phenomena of two lowest antisymmetric Lamb modes scattering on the discontinuities. Following that, a practical FBAR structure with bottom electrode extended to the whole structure is investigated. The power scattering coefficients of these two generic FBAR structures are compared and a new structure with frame-like airgap on bottom electrode was proposed based on the scattering analysis of these two structures, which will be investigated in the next chapter.

4.5.1 Generic FBAR model with symmetric electrodes

The generic FBAR resonator with symmetric electrodes on top and bottom (shown in Fig. 4.16) is set up to analyze the scattering phenomena of two lowest antisymmetric Lamb modes scattering on the discontinuities in this section. The FBAR resonator is composed of a piezoelectric AlN layer with $3\mu m$ thickness sandwiched between two Al electrodes with $0.6\mu m$ in thickness. The scattering boundary (P_3) and the observation point in the active region (P_2) are, respectively, 150 μm and 95 μm away from the excitation point (P_1). The observation point in the passive region (P_4) and the outer boundary (G) are, respectively, 50 μm and 500 μm away from the scattering boundary (P_3). The material properties used in this study was presented in section 3.3.

A two-dimensional finite-difference time-domain (FDTD) model (developed in chapter 3) is set up to simulate the propagation of the Lamb waves. Both the temporal-derivatives

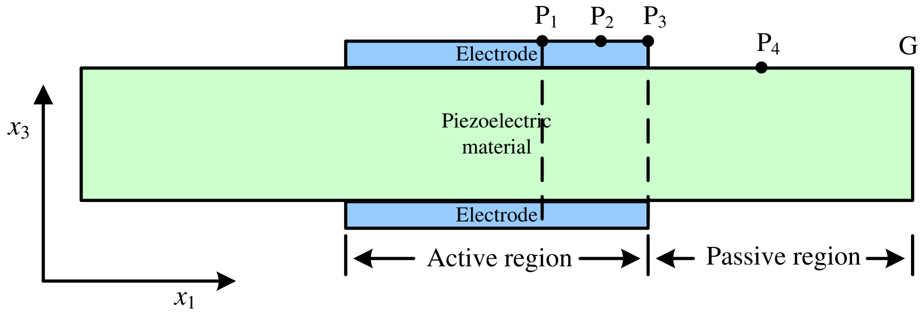

Figure 4.16: Schematic of a generic FBAR resonator with symmetric electrodes for Lamb wave scattering analysis.

and spatial-derivatives in the wave propagation governing equations, which relates the particle velocity and the stress, are approximated by second-order centred finite differences as described in section 3.4. The particle velocity is adopted in the FDTD simulation in order to simplify the formulation. As mentioned in chapter 3, the particle velocity is related to the particle displacement u by $v = \partial u/\partial t$ in time-domain and $V = j\omega_o U$ in frequency-domain. The zero traction condition is enforced on the boundaries and the structure is long enough to eliminate the scattering from the outer boundary (G as shown in Fig. 4.16). As it is mentioned in section 3.5, to reduce the artificial numerical dispersion effects to an acceptable extent, the spatial step size Δx_1 and Δx_3 are set to both 5×10^{-8} m, which is approximately equal to one twentieth of the smallest wavelength of the toneburst. To ensure the stability of the simulation, the time increment interval is chosen to be 3×10^{-12} s in order to satisfy the Courant stability condition [111].

A eight-cycle Lamb wave toneburst (demonstrated in section 3.6.2) composed of A_0 and A_1 modes is numerically launched by imposing their theoretical particle velocity components [11]$\mathbf{v}(x_3)$ at P_1

$$\mathbf{v}(x_3) = K_1\mathbf{v}^0(x_3) + K_2\mathbf{v}^1(x_3) \ , \tag{4.31}$$

where $\mathbf{v}^i(x_3)$ is the particle velocity of the A_i mode, and K_i are arbitrary constants, which are set to 7 and 1 in this simulation. The bandwidth of the toneburst covers the frequency range of 1 GHz $< f <$ 1.6 GHz. The resonance frequency f_s of the FBAR resonator is approximately 1.298 GHz and the antiresonance frequency f_a is approximately 1.331 GHz. For simplicity, only the frequency range 1.300 GHz $< f <$ 1.330 GHz is considered in this simulation. The dispersion characteristics of the active region and the passive region of the FBAR resonator are shown in Fig. 4.17. It can be observed from Fig. 4.17 that within the interested frequency range, only modes A_0, A_1, S_0 and S_1 are above their cutoff frequencies in the active region, and only modes A_0, A_1 and S_0 are above their cutoff frequencies in the passive region. When the incident wave arrives at the scattering boundary at P_3, mode conversion happens, and the converted waves are partially reflected back into the active region, while others are propagating forward into the passive region. Since the scattering boundary at P_3 is symmetric, no mode conversion from antisymmetric to symmetric modes can occur. Therefore, within the investigated frequency range, only modes A_0 and A_1 are propagating in both active and passive regions of the structure.

Figure 4.18 shows the normalized time history and its wavenumber spectrum at frequency 1.315 GHz of the incident Lamb wave collected at 50 μm away from the excitation point P_1. Because of dispersive property of Lamb waves, the A_0 and A_1 modes cannot be distinguished in time-domain. On the other hand, the wavenumber spectrum shows that the incident Lamb wave consists of two modes with phase constant 0.98 rad/μm and 1.79 rad/μm, which are corresponding to the A_1 mode and A_0 mode, respectively.

The reflected waves propagating back into the active region are examined first. Figure 4.19(a) shows the normalized time history of the Lamb wave collected at P_2. The duration of the simulation is long enough to include the incident Lamb wave and the reflected Lamb waves from the discontinuity at P_3. The incident Lamb wave consists of two overlapping tonebursts while the reflected wave contains more than two overlapping tonebursts because of the mode conversion at the boundary (P_3). Figure 4.19(b) shows the wavenumber spectrum at frequency 1.315 GHz of the Lamb wave collected at P_2. It can be observed that the reflected wave consists of mode A_0 and mode A_1 only but more than two tonebursts are observed in time domain. As it is mentioned before, because the scattering boundary is symmetric, no mode conversion from antisymmetric to symmetric modes can occur. Besides, the incident mode A_0 and A_1 have different phase velocity so that they arrive at the boundary at different time. Therefore, after the reflection from the boundary, there are four tonebursts travelling in the active region. They are A_1 mode converted from the incident A_1 mode, A_0 mode converted from the incident A_1 mode, A_1 mode converted from the incident A_0 mode, and A_0 mode converted from the incident A_0 mode. Since the two reflected A_1 mode converted from the incident A_0 mode and the incident A_1 mode have the same wavenumber at a given frequency, these two waves cannot be distinguished from both time-domain history and the wavenumber-domain spectrum. To distinguish these two waves, the simulation is repeated with the constants $K_1 = 0.1$ and $K_2 = 17$ for the amplitude of the two incident Lamb wave modes. The complex amplitude of the incident modes (A_{i0} and A_{i1}) and reflected modes (A_{r0} and A_{r1}) can be obtained by applying 2D FFT to the time sequence of the equally allocated monitoring points on the top surface of the active region. With the two wavenumber spectra obtained from the simulations, the complex mode amplitude conversion coefficients of the reflected modes r^r_{nm} are determined

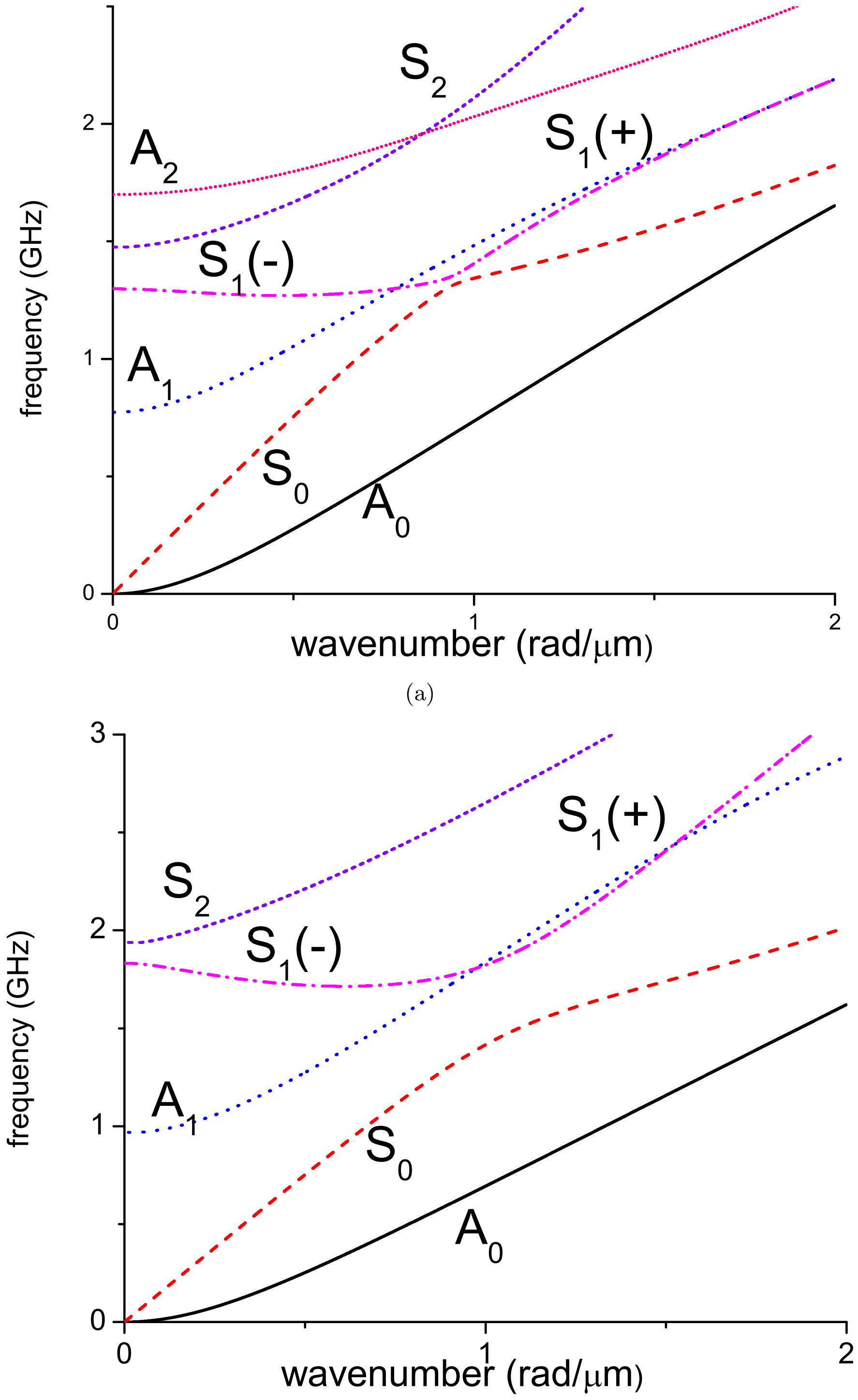

(a)

(b)

Figure 4.17: Dispersion characteristics of FBAR resonator with symmetric electrodes. (a) Active region, (b) Passive region.

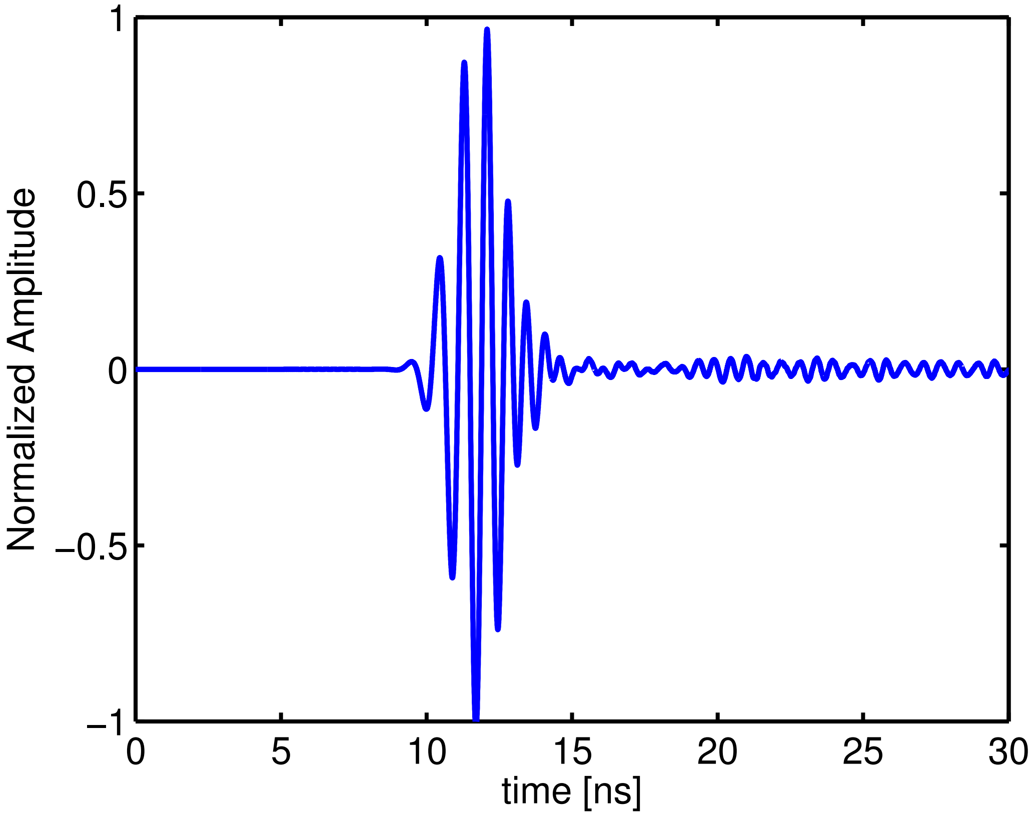

(a)

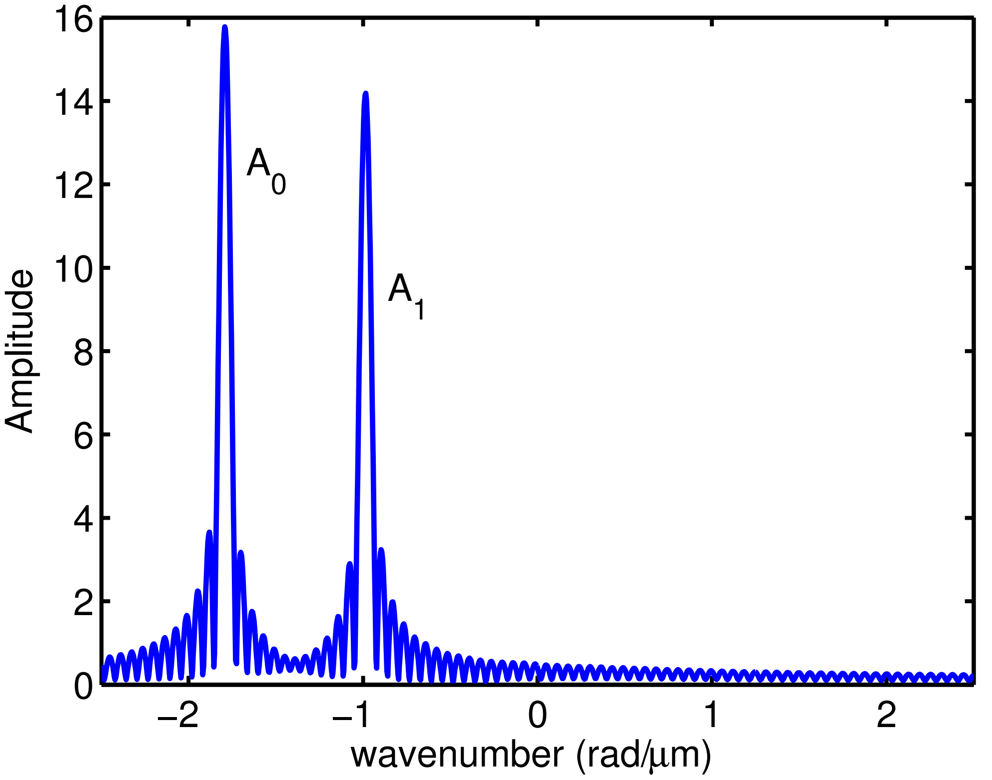

(b)

Figure 4.18: Incident Lamb waves at $x_1 = 50\mu$m when the input A_0 and A_1 modes are excited at $x_1 = 0$. (a) Time history, (b) Wavenumber spectrum at frequency = 1.315 GHz.

by solving the matrix equation (Eq. (4.21)).

Finally, the power scattering coefficients of the reflected modes s^r_{mn} are calculated by Eq. (4.29). The mode power coefficients c_n are calculated by the effective acoustic admittance as described in section 2.4.1.3. The mode power coefficients c_n for mode A_0 and A_1 in the active region are shown in Fig. 4.20. Table 4.3 shows the power scattering coefficients of the reflected waves calculated by the proposed method. s^r_{mn} is the power reflection coefficient of mode A_n converted into A_m, and $s^r_{A_n}$ is the total power reflection coefficient for mode A_n calculated by $s^r_{A_n} = s^r_{0n} + s^r_{1n}$ (n = 0,1). Figure 4.21 shows the the power scattering coefficients of the reflected waves for the interested frequency range. It is observed that the power reflection coefficients of mode A_0 and A_1 are increasing with the increase of the frequency. Within the investigated frequency range, less than 40% energy of mode A_0 and less than 50% energy of mode A_1 are reflecting back into the active region. The majority energy of mode A_0 and A_1 is lost for the investigated structure.

Table 4.3: Power scattering coefficients of the reflected waves s^r_{mn} for FBAR with symmetric electrodes.

frequency (GHz)	s^r_{00}	s^r_{10}	$s^r_{A_0}$	s^r_{01}	s^r_{11}	$s^r_{A_1}$
1.300	0.112	0.238	0.350	0.234	0.189	0.423
1.305	0.112	0.245	0.357	0.239	0.189	0.428
1.310	0.116	0.252	0.367	0.245	0.190	0.435
1.315	0.120	0.251	0.371	0.248	0.193	0.441
1.320	0.118	0.261	0.379	0.255	0.194	0.449
1.325	0.125	0.265	0.390	0.259	0.195	0.454
1.330	0.123	0.268	0.391	0.262	0.199	0.461

Following the same procedure, the power scattering coefficients of the transmitted modes s^t_{mn} can be calculated by Eq. (4.29). Figure 4.22(a) shows the normalized time history of the Lamb wave collected at P_4. It is observed that no reflecting waves from the outer boundary are present. Figure 4.22(b) shows the wavenumber spectrum at frequency 1.315 GHz of the Lamb wave collected at P_4. It is confirmed that the transmitted wave consists of forward propagating mode A_0 and mode A_1 only. The complex amplitude of the transmitted modes (A_{t0} and A_{t1}) can be calculated by applying 2D FFT to the time sequence of the equally allocated monitoring points on the top surface of the passive region. The complex amplitude of the transmitted modes (A_{t0} and A_{t1}) are used instead of the reflected modes (A_{r0} and A_{r1}) in the matrix (Eq. (4.22)) to calculate the complex mode amplitude conversion coefficients of the transmitted modes r^t_{nm} by solving the matrix equation (Eq. (4.21)). The mode power coefficients c_n for mode A_0 and A_1 in the passive region are shown in Fig. 4.23. Table 4.4 shows the power scattering coefficients of the transmitted waves calculated by the

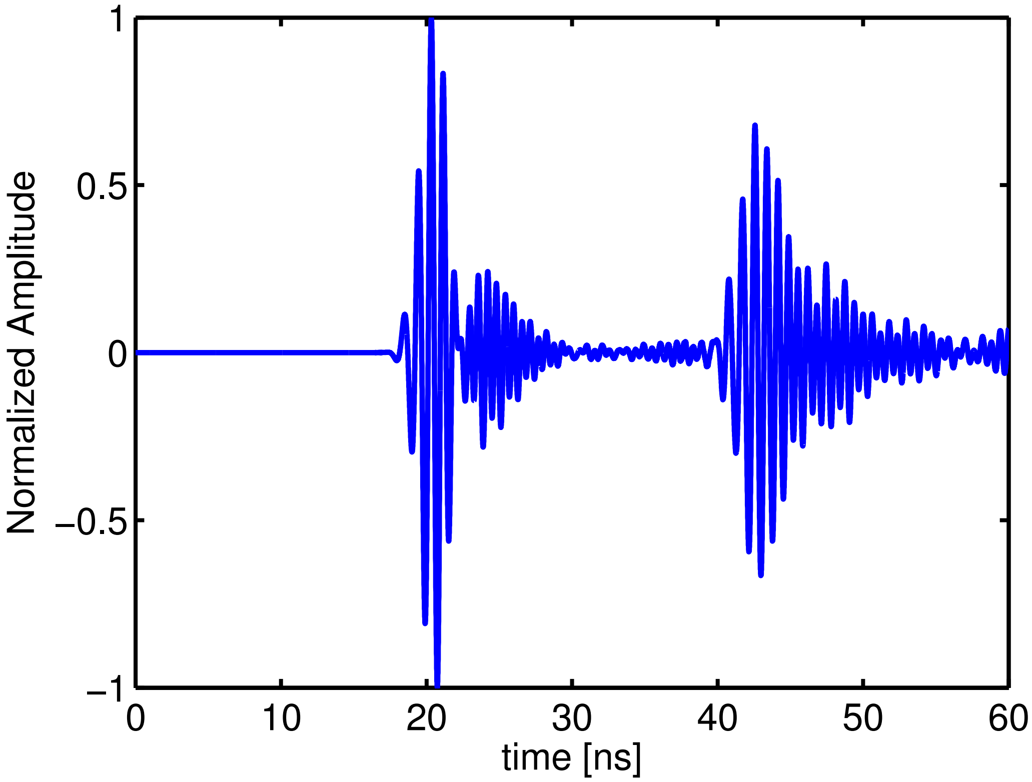

(a)

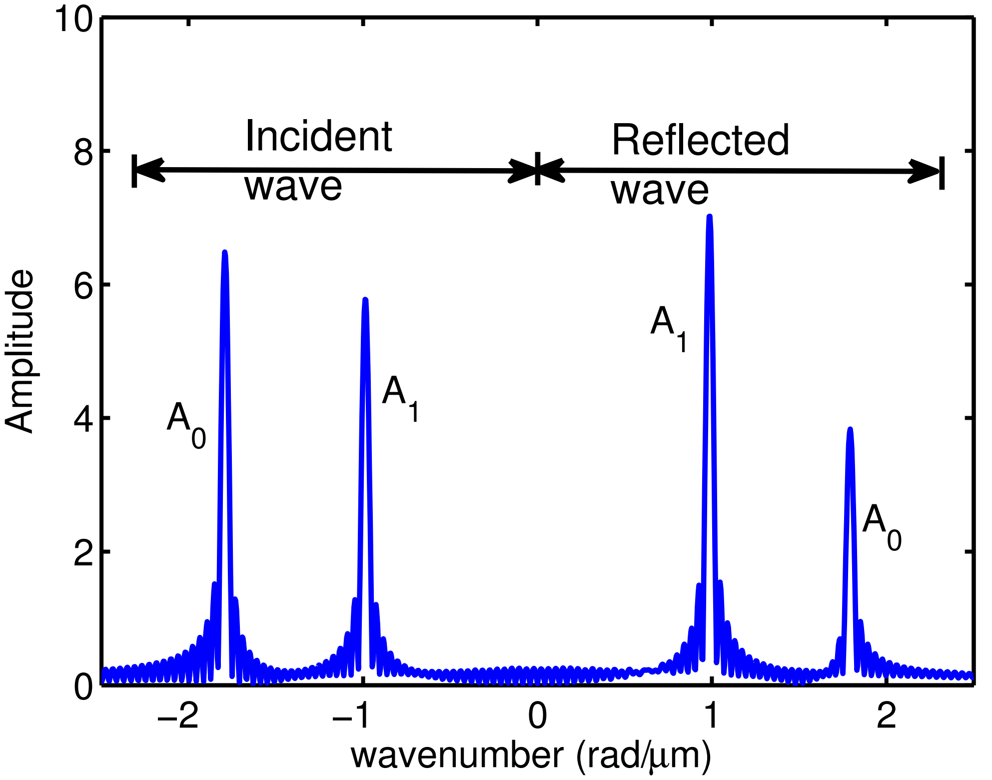

(b)

Figure 4.19: Scattered Lamb waves at P_2 for FBAR with symmetric electrodes. (a) Time history, (b) Frequency spectrum.

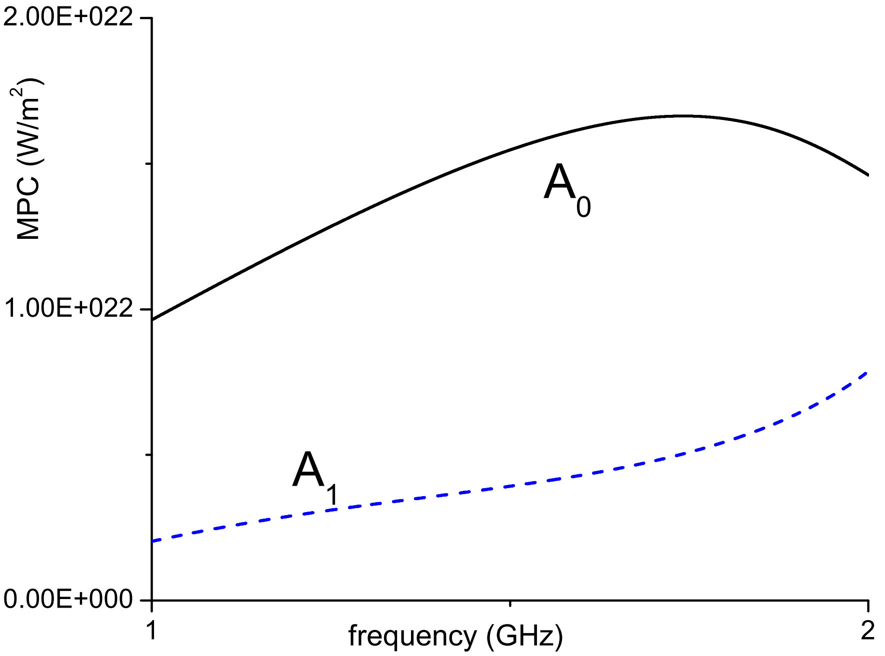

Figure 4.20: Mode power coefficient c_n for A_0 and A_1 modes propagating in active region for FBAR with symmetric electrodes.

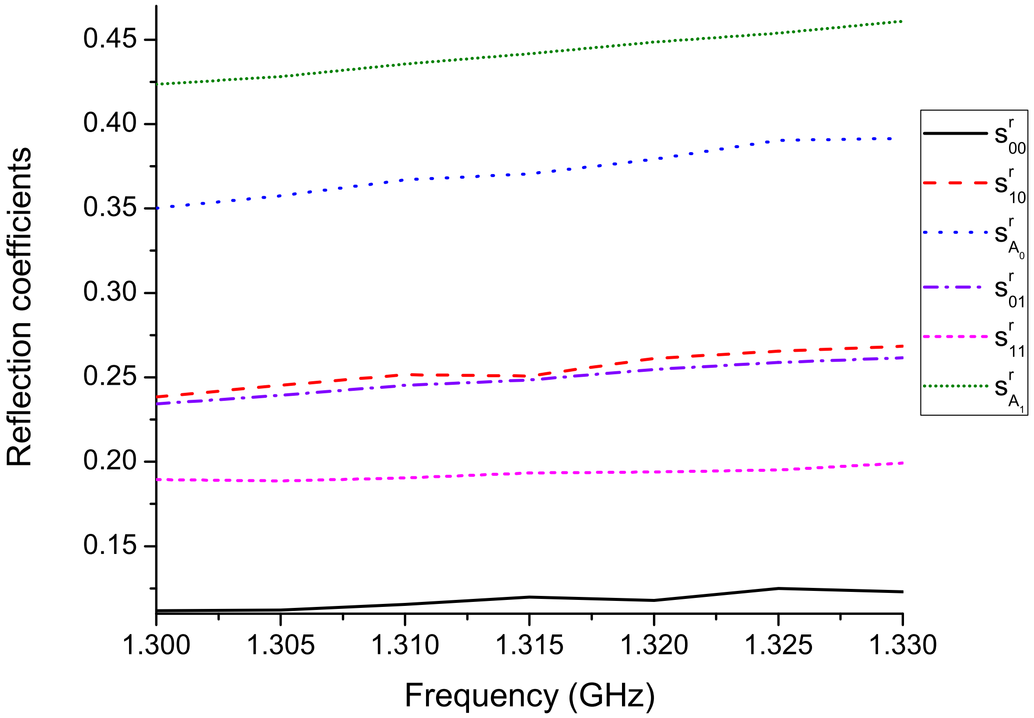

Figure 4.21: The power scattering coefficients s^r_{nm} for A_0 and A_1 modes reflecting from the symmetric boundary at P_3.

proposed method. s^t_{mn} is the power transmission coefficient of mode A_n converted into A_m, and $s^t_{A_n}$ is the total power transmission coefficient for mode A_n calculated by $s^t_{A_n} = s^t_{0n} + s^t_{1n}$ (n = 0,1). Figure 4.24 shows the the power scattering coefficients of the transmitted waves for the interested frequency range. It is observed that the power transmission coefficients of mode A_0 and A_1 are generally decreasing with the increase of the frequency. Within the investigated frequency range, more than 60% energy of mode A_0 and more than 50% energy of mode A_1 are propagating into the passive region, causing energy leakage in FBAR resonators.

Table 4.4: Power scattering coefficients of the transmitted waves s^t_{mn} for FBAR with symmetric electrodes.

frequency (GHz)	s^t_{00}	s^t_{10}	$s^t_{A_0}$	s^t_{01}	s^t_{11}	$s^t_{A_1}$
1.300	0.517	0.135	0.652	0.159	0.397	0.556
1.305	0.512	0.141	0.653	0.165	0.392	0.557
1.310	0.498	0.144	0.642	0.169	0.379	0.548
1.315	0.497	0.155	0.652	0.177	0.384	0.561
1.320	0.460	0.157	0.617	0.172	0.364	0.536
1.325	0.471	0.166	0.637	0.186	0.361	0.547
1.330	0.453	0.165	0.618	0.185	0.333	0.518

To ensure the time convergence of the simulation, two different time steps $59,000$ and $60,000$ were used respectively. The differences of amplitudes of the incident modes, reflected modes and transmitted modes calculated by using these two different time steps are less than 0.004% for all points. The energy differences between the incident modes and the converted modes are also calculated to check the computation accuracy, which are shown in Table 4.5 and Table 4.6 for the first set of data and the second set of data, respectively. $P_{A_n,inc}$ (n=0, 1) is the power of the incident mode A_n, and P_{inc} is the total incident power calculated by $P_{inc} = P_{A_0,inc} + P_{A_1,inc}$. $P_{A_n,ref}$ (n=0, 1) is the power of the reflected mode A_n, $P_{A_n,tra}$ (n=0, 1) is the power of the transmitted mode A_n, and P_{conv} is the total converted power calculated by $P_{conv} = P_{A_0,ref} + P_{A_1,ref} + P_{A_0,tra} + P_{A_1,tra}$. Energy difference between the incident modes and the converted modes P_{dif} is calculated by $P_{dif} = (P_{conv} - P_{inc})/P_{inc}$. It is observed that the energy difference is smaller than 5% for all points. Energy conservation is also checked by combining Table 4.3 and Table 4.4, shown in Table 4.7. $s^r_{A_n}$ (n=0, 1) is the total power reflection coefficient for mode A_n (shown in Table 4.3). $s^t_{A_n}$ (n=0, 1) is the total power transmission coefficient for mode A_n (shown in Table 4.4). And $s^{total}_{A_n}$ (n=0, 1) is the total power scattering coefficient for mode A_n, calculated by $s^{total}_{A_n} = s^r_{A_n} + s^t_{A_n}$. By energy conservation, $s^{total}_{A_n}$ should be equal to 1. It is observed that the error is less than 3% at all frequencies. The accuracy of the results can be improved by increasing the simulation time and elongating the structure to

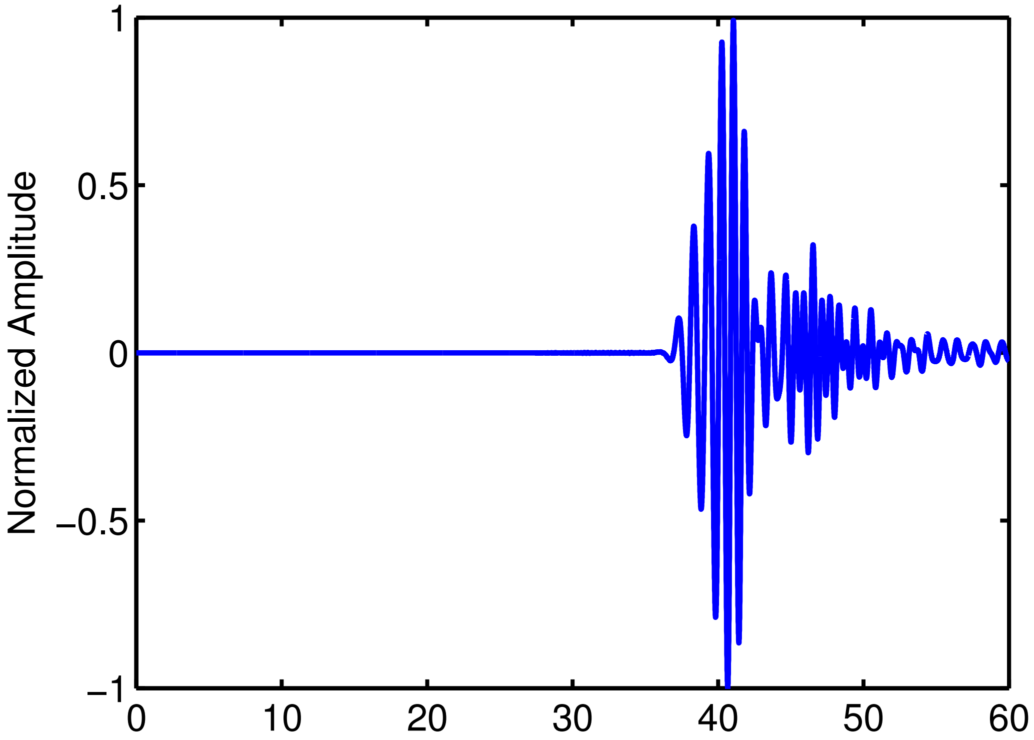

(a)

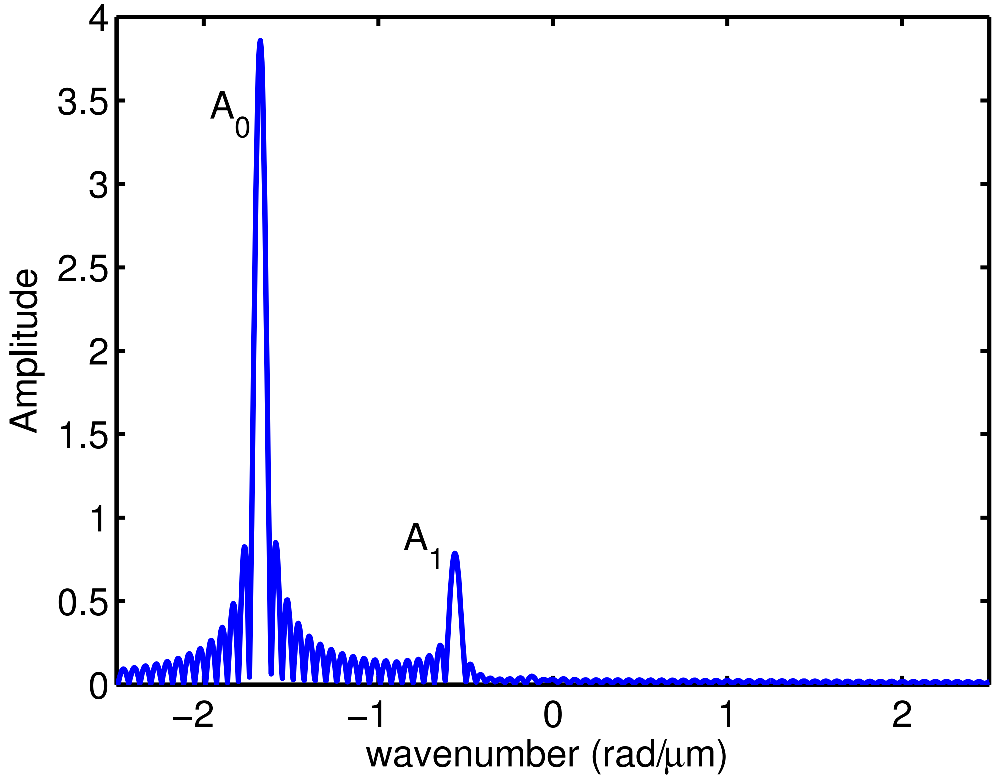

(b)

Figure 4.22: Transmitted Lamb waves at P_4 for FBAR with symmetric electrodes. (a) Time history, (b) Frequency spectrum.

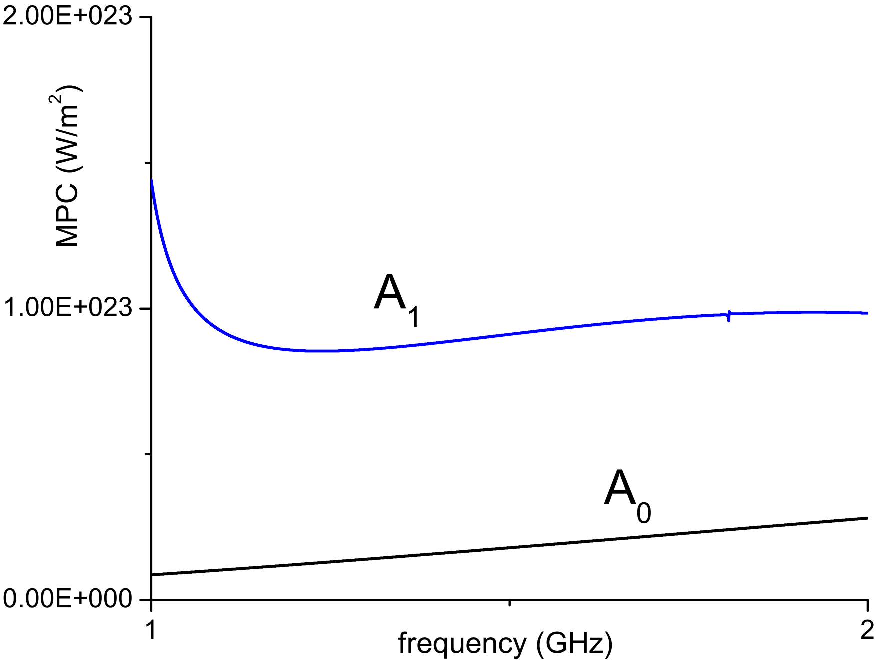

Figure 4.23: Mode power coefficient c_n for A_0 and A_1 modes propagating in passive region for FBAR with symmetric electrodes.

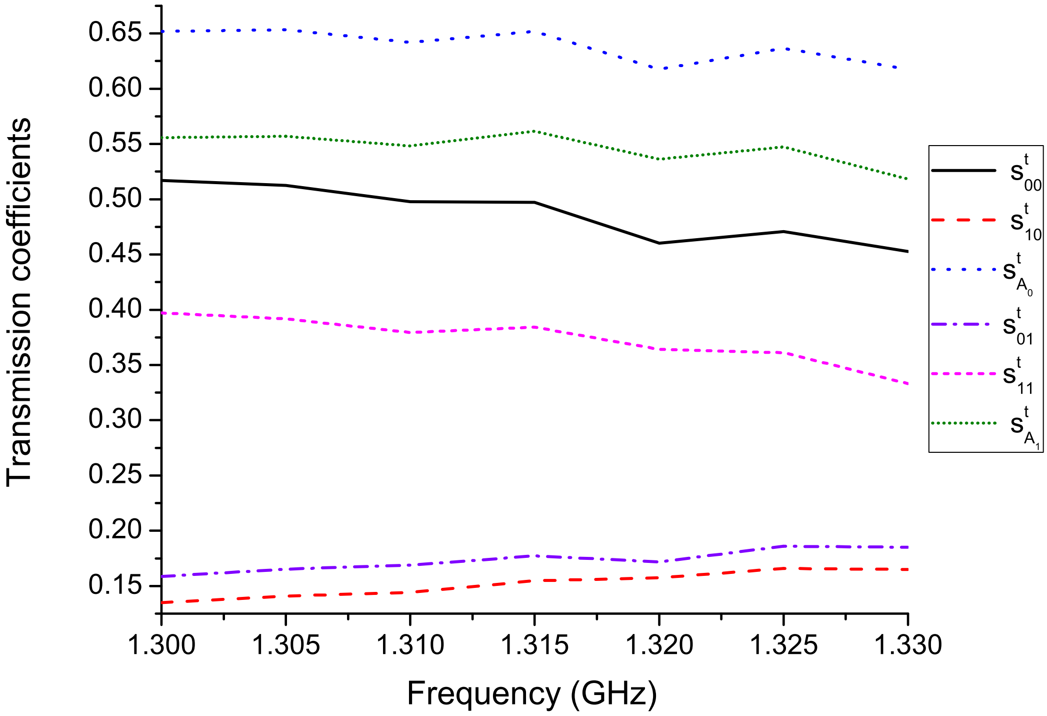

Figure 4.24: The power scattering coefficients s^t_{nm} for A_0 and A_1 modes transmitted into the passive region.

allocate more monitoring points on the surface to improve the frequency and wavenumber resolution, respectively.

Table 4.5: Energy difference between the incident modes and the converted modes for the first set of data.

frequency (GHz)	$P_{A_0,inc}$ $10^{-8}W$	$P_{A_1,inc}$ $10^{-8}W$	P_{inc} $10^{-8}W$	$P_{A_0,ref}$ $10^{-8}W$	$P_{A_1,ref}$ $10^{-8}W$	$P_{A_0,tra}$ $10^{-8}W$	$P_{A_1,tra}$ $10^{-8}W$	P_{conv} $10^{-8}W$	P_{dif}
1.300	79.31	22.90	102.21	6.02	7.25	69.02	22.98	105.28	0.030
1.305	77.29	22.69	99.98	6.97	8.57	67.53	21.08	103.97	0.040
1.310	79.06	23.26	102.32	9.00	10.27	67.04	19.67	105.99	0.036
1.315	76.59	22.57	99.17	10.08	11.39	64.52	18.11	104.10	0.050
1.320	77.97	23.32	101.29	12.08	14.13	60.21	16.34	102.76	0.015
1.325	75.45	22.66	98.11	13.94	15.69	58.56	14.49	102.68	0.047
1.330	75.81	22.98	98.79	15.40	18.29	54.94	12.42	101.06	0.023

Table 4.6: Energy difference between the incident modes and the converted modes for the second set of data.

frequency (GHz)	$P_{A_0,inc}$ $10^{-8}W$	$P_{A_1,inc}$ $10^{-8}W$	P_{inc} $10^{-8}W$	$P_{A_0,ref}$ $10^{-8}W$	$P_{A_1,ref}$ $10^{-8}W$	$P_{A_0,tra}$ $10^{-8}W$	$P_{A_1,tra}$ $10^{-8}W$	P_{conv} $10^{-8}W$	P_{dif}
1.300	0.31	4.23	4.55	1.33	1.36	0.19	1.48	4.36	-0.040
1.305	0.30	4.05	4.35	1.27	1.29	0.19	1.44	4.19	-0.037
1.310	0.30	4.01	4.31	1.26	1.27	0.19	1.43	4.15	-0.036
1.315	0.28	3.79	4.07	1.18	1.19	0.20	1.41	3.99	-0.020
1.320	0.27	3.76	4.04	1.16	1.16	0.22	1.37	3.92	-0.030
1.325	0.26	3.55	3.81	1.08	1.07	0.26	1.33	3.74	-0.018
1.330	0.25	3.49	3.74	1.04	1.02	0.29	1.25	3.60	-0.035

Table 4.7: Power scattering coefficients of the converted modes for FBAR with symmetric electrodes.

frequency (GHz)	$s^r_{A_0}$	$s^t_{A_0}$	$s^{total}_{A_0}$	$s^r_{A_1}$	$s^t_{A_1}$	$s^{total}_{A_1}$
1.300	0.350	0.652	1.002	0.424	0.556	0.980
1.305	0.357	0.653	1.010	0.428	0.557	0.985
1.310	0.367	0.642	1.009	0.436	0.548	0.984
1.315	0.371	0.652	1.023	0.442	0.561	1.003
1.320	0.379	0.617	0.996	0.449	0.536	0.985
1.325	0.390	0.636	1.026	0.454	0.547	1.001
1.330	0.392	0.618	1.010	0.461	0.518	0.979

4.5.2 Generic FBAR model with asymmetric electrodes

A practical generic FBAR resonator with asymmetric electrodes (bottom electrode is extended to the whole structure as shown in Fig. 4.25) is set up to analyze the scattering phenomena of the two lowest antisymmetric Lamb modes at the discontinuities in this section. The FBAR resonator is again composed of a piezoelectric AlN layer with $3\mu m$ thickness sandwiched between two Al electrodes with $0.6\mu m$ in thickness. The scattering boundary (P_3) and the observation point in the active region (P_2) are, respectively, 300

μm and 210 μm away from the excitation point (P_1). The observation point in the passive region (P_4) and the outer boundary (G) are, respectively, 25 μm and 600 μm away from the scattering boundary (P_3). The material properties used in this study was presented in section 3.3.

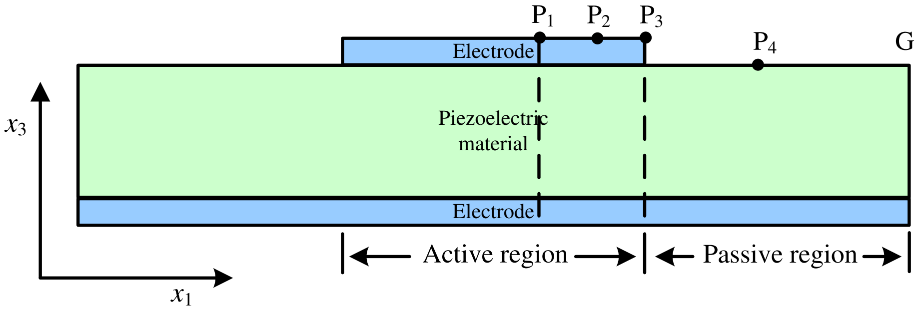

Figure 4.25: Schematic of a generic FBAR resonator with asymmetric electrodes for Lamb wave scattering analysis.

Similarly, a two-dimensional finite-difference time-domain (FDTD) model (developed in chapter 3) is set up to simulate the propagation of the Lamb waves. The spatial step size and temporal step size are chosen to be the same used to analyze the FBAR resonator with symmetric electrodes in section 4.5.1.

A eight-cycle Lamb wave toneburst (demonstrated in section 3.6.2) composed of A_0 and A_1 modes is numerically launched by imposing their theoretical particle velocity components $\mathbf{v}(x_3)$ [11] at P_1 as described by Eq. (4.31). The constants K_1 and K_2 are set to 0.14 and 23 in this simulation. The bandwidth of the toneburst again covers the frequency range of 1 GHz $< f <$ 1.6 GHz. The dispersion characteristic of the active region is the same as the one for the FBAR resonator with symmetric electrodes (shown in Fig. 4.17(a)). The dispersion characteristic of the passive region is shown in Fig. 4.26. Because the passive layer is not symmetric, the modes propagating in this region do not show symmetric nor antisymmetric behavior. These modes are referred as pseudo symmetric (pS_n) and pseudo antisymmetric (pA_n) modes respectively, in analogy to the Lamb mode nomenclature. Again, only the frequency range 1.300 GHz $< f <$ 1.330 GHz is considered in this simulation. When the incident wave arrives at the scattering boundary P_3, mode conversion happens, and the converted waves are partially reflected back into the active region, while others are propagating forward into the passive region. Since the scattering boundary at P_3 is asymmetric, mode conversion from antisymmetric to symmetric modes occurs. Therefore, it can be observed from Fig. 4.17(a) and Fig. 4.26 that within the investigated frequency range, A_0, A_1, S_0 and $S_1(+)$ are propagating in the active region, while pA_0, pA_1 and pS_0 are propagating in the passive region.

Figure 4.27 shows the normalized time history and its wavenumber spectrum at

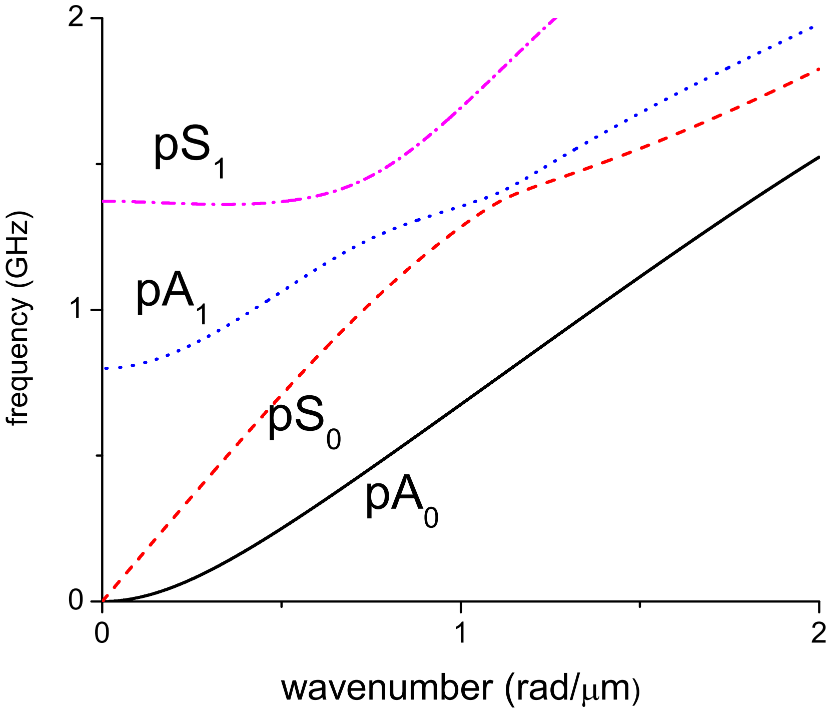

Figure 4.26: Dispersion characteristic of FBAR resonator with asymmetric electrodes in the passive region.

frequency 1.315 GHz of the incident Lamb wave collected at 50 μm away from the excitation point P_1. Because of dispersive property of Lamb waves, the A_0 and A_1 modes cannot be distinguished in time-domain. On the other hand, the wavenumber spectrum shows that the incident Lamb wave consists of two modes with phase constant 0.98 rad/μm and 1.79 rad/μm, which are corresponding to the A_1 mode and A_0 mode, respectively.

The reflected waves propagating back into the active region are examined first. Figure 4.28(a) shows the normalized time history of the Lamb wave collected at P_2. The duration of the simulation is long enough to include the incident Lamb wave and the reflected Lamb waves from the discontinuity at P_3. The incident Lamb wave consists of two overlapping tonebursts while the reflected wave contains more than two overlapping tonebursts because of the mode conversion at the boundary (P_3). Figure 4.28(b) shows the wavenumber spectrum at frequency 1.315 GHz of the Lamb wave collected at P_2. It can be observed that the reflected wave consists of four modes, mode A_0, A_1, S_0 and S_1. Each backward reflected mode is a combination of the mode converted from the incident mode A_0 and A_1. Take the reflected mode A_1 as an example, since the two reflected A_1 mode converted from the incident A_0 mode and the incident A_1 mode have the same wavenumber at a given frequency, these two waves cannot be distinguished from both time-domain history and the wavenumber-domain spectrum. To distinguish these two waves, the simulation is repeated with the constants $K_1 = 7$ and $K_2 = 1$ for the amplitude of the two incident Lamb wave

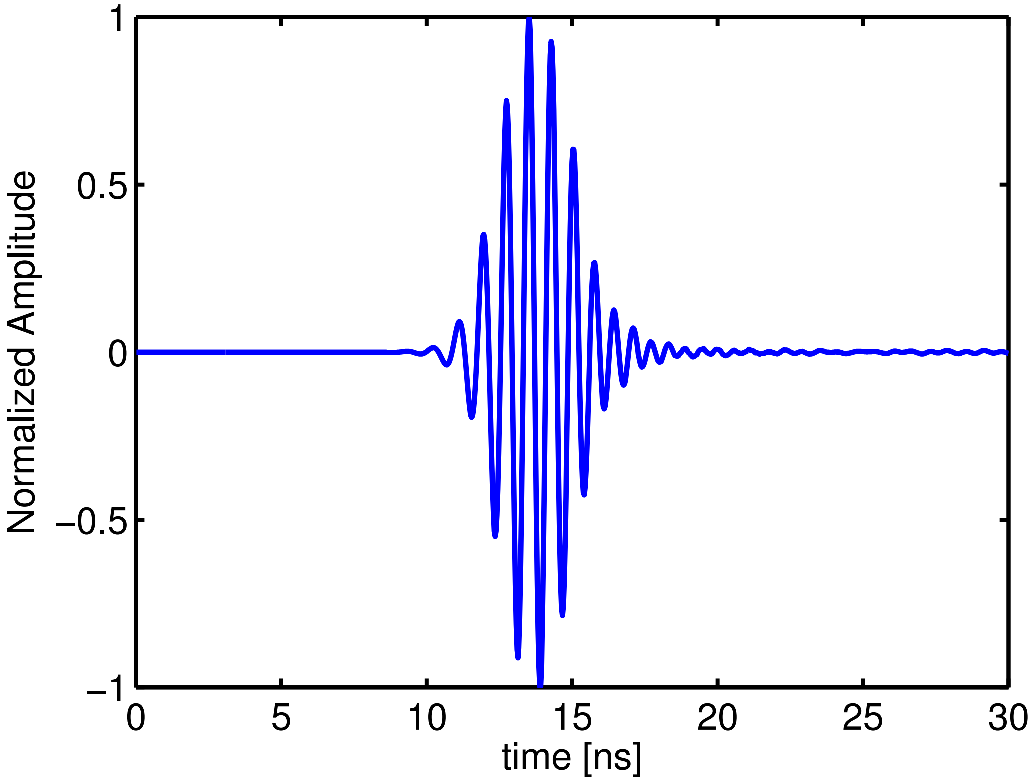

(a)

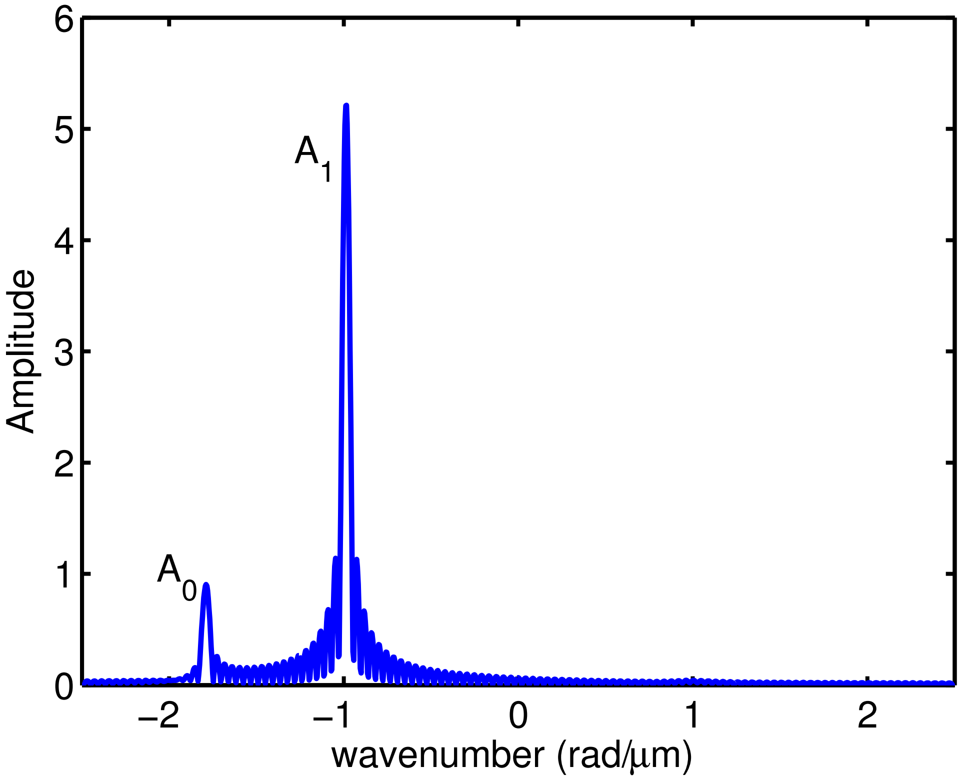

(b)

Figure 4.27: Incident Lamb waves at $x_1 = 50\mu$m when the input A_0 and A_1 modes are excited at $x_1 = 0$. (a) Time history, (b) Wavenumber spectrum at frequency = 1.315 GHz.

modes. The complex amplitude of the incident modes (A_{i0} and A_{i1}) and reflected modes (A_{r0}, A_{r1}, S_{r0}, and S_{r1}) can be obtained by applying 2D FFT to the time sequence of the equally allocated monitoring points on the top surface of the active region. With the two wavenumber spectra obtained from the simulations, the complex mode amplitude conversion coefficients of the reflected antisymmetric modes r^{ra}_{nm} and symmetric modes r^{rs}_{nm} are determined by solving the matrix equation (Eq. (4.21)). Two set of matrix equations are obtained, one with the reflected antisymmetric modes A_0 and A_1, and the other one with the reflected symmetric modes S_0 and S_1.

Finally, the power scattering coefficients of the reflected antisymmetric modes s^{ra}_{mn} and symmetric modes s^{rs}_{mn} are calculated by Eq. (4.29). The mode power coefficients c_n are calculated by the effective acoustic admittance as described in section 2.4.1.3. The mode power coefficients c_n for mode A_0, A_1, S_0 and S_1 in the active region are shown in Fig. 4.29. Table 4.8 shows the power scattering coefficients of the reflected waves calculated by the proposed method. s^{ra}_{mn} is the power reflection coefficient of mode A_n converted into mode A_m, and s^{rs}_{mn} is the power reflection coefficient of mode A_n converted into mode S_m. $s^{r}_{A_n}$ is the total power reflection coefficient for mode A_n calculated by $s^{r}_{A_n} = s^{ra}_{0n} + s^{ra}_{1n} + s^{rs}_{0n} + s^{rs}_{1n}$ (n = 0,1). Figure 4.30 shows the the power scattering coefficients of the reflected waves for the interested frequency range. It is observed that the power reflection coefficients of mode A_0 and A_1 are increasing with the increase of the frequency. Within the investigated frequency range, less than 34% energy of mode A_0 and less than 44% energy of mode A_1 are reflecting back into the active region. The majority energy of mode A_0 and A_1 is lost into the passive region. It is also observed that mode A_0 is mainly converted into modes S_1 and A_1, while mode A_1 is mainly converted into modes S_0 and A_0. By reciprocity, if the incident mode is S_1, most of its energy will be converted into A_0, and if the incident mode is S_0, most of its energy will be converted into A_1.

Table 4.8: Power scattering coefficients of the reflected waves s^{ra}_{mn} and s^{rs}_{mn} for FBAR with asymmetric electrodes.

frequency (GHz)	s^{ra}_{00}	s^{ra}_{10}	s^{rs}_{00}	s^{rs}_{10}	$s^{r}_{A_0}$	s^{ra}_{01}	s^{ra}_{11}	s^{rs}_{01}	s^{rs}_{11}	$s^{r}_{A_1}$
1.300	0.005	0.093	0.025	0.126	0.249	0.088	0.010	0.211	0.049	0.359
1.305	0.004	0.090	0.020	0.130	0.243	0.094	0.008	0.212	0.052	0.366
1.310	0.005	0.099	0.012	0.139	0.254	0.107	0.013	0.220	0.039	0.380
1.315	0.007	0.106	0.017	0.140	0.269	0.102	0.013	0.221	0.042	0.378
1.320	0.010	0.125	0.014	0.141	0.290	0.122	0.012	0.222	0.048	0.404
1.325	0.036	0.129	0.028	0.141	0.333	0.125	0.023	0.222	0.052	0.421
1.330	0.043	0.112	0.034	0.140	0.330	0.116	0.050	0.211	0.053	0.430

Following the same procedure, the power scattering coefficients of the transmitted antisymmetric modes s^{ta}_{mn} and symmetric modes s^{ts}_{mn} can be calculated by Eq. (4.29).

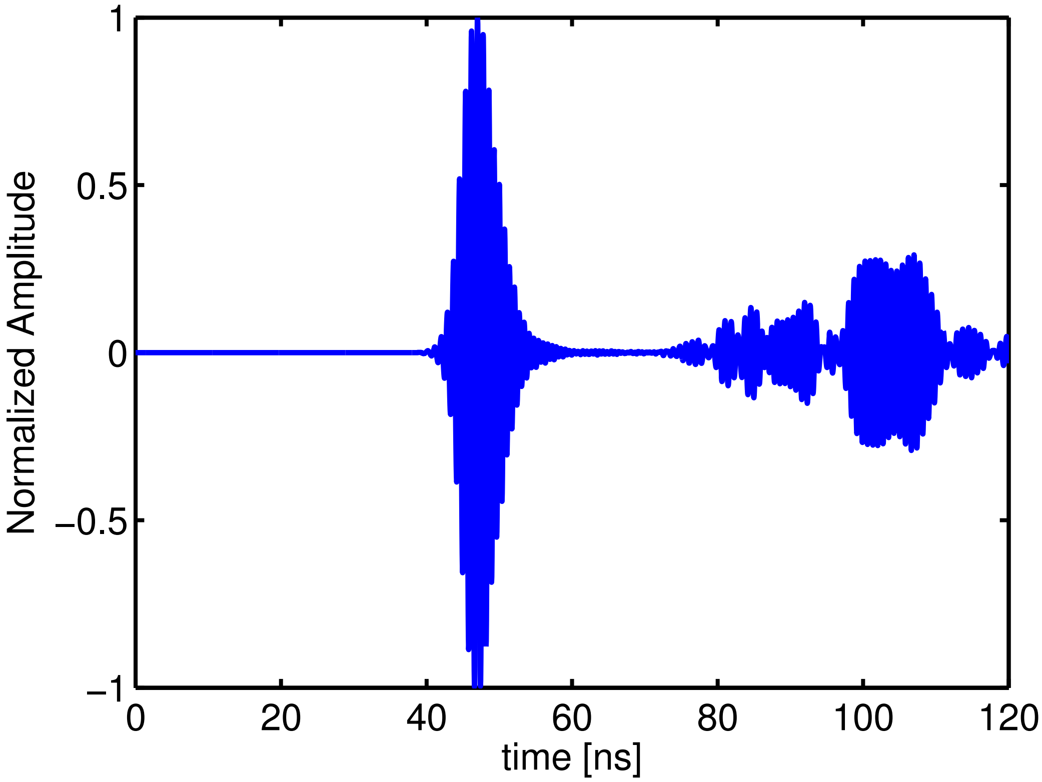

(a)

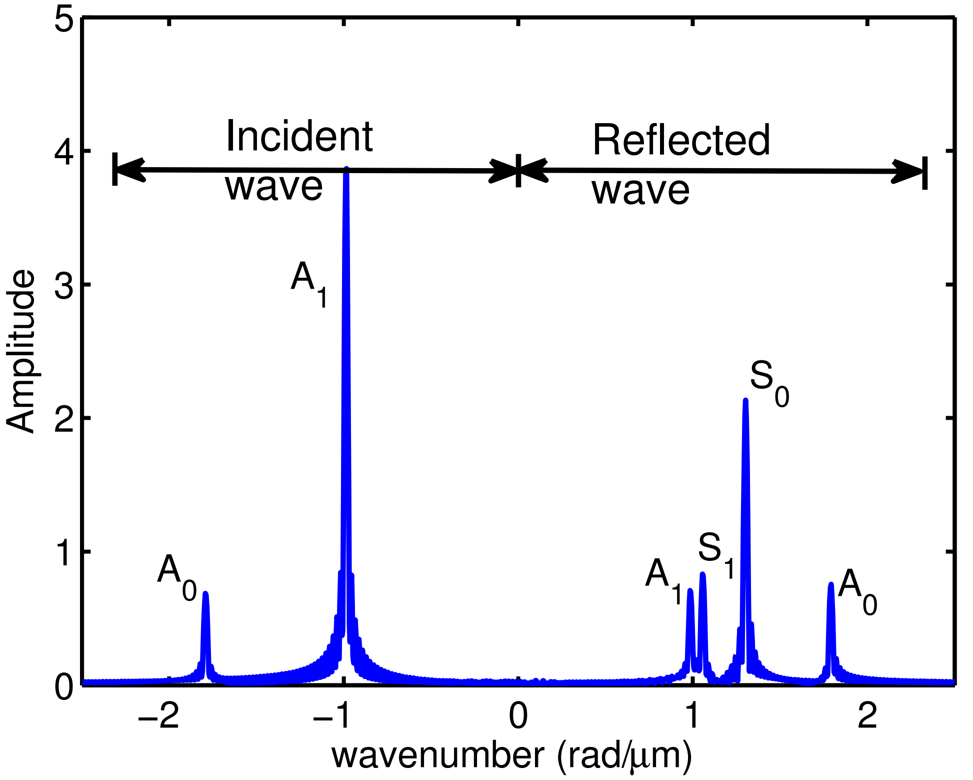

(b)

Figure 4.28: Scattered Lamb waves at P_2 for FBAR with asymmetric electrodes. (a) Time history, (b) Frequency spectrum.

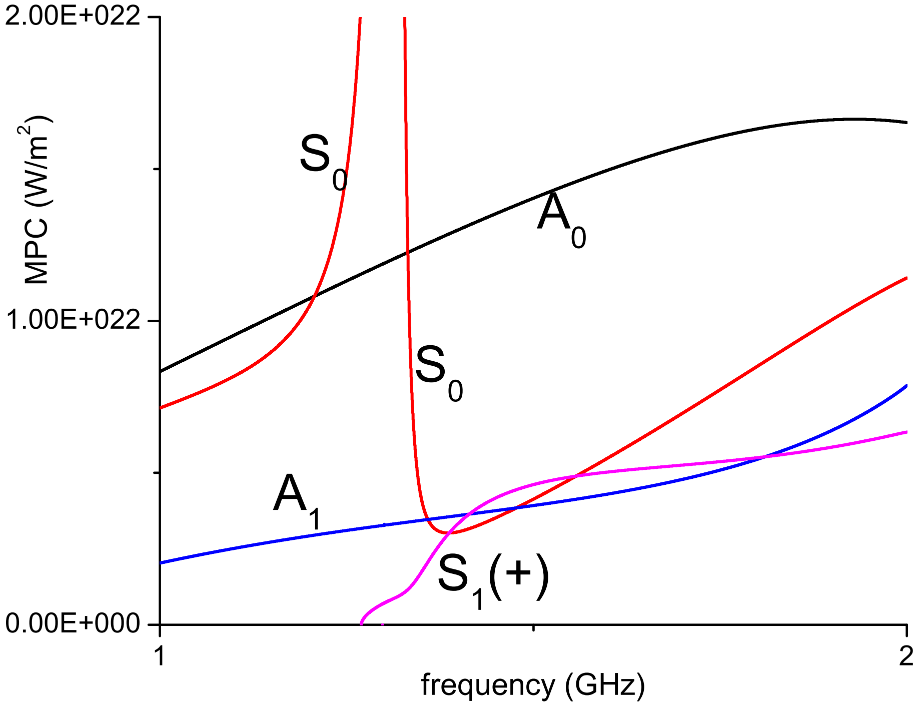

Figure 4.29: Mode power coefficient c_n for A_0, A_1, S_0 and S_1 modes propagating active region for FBAR with asymmetric electrodes.

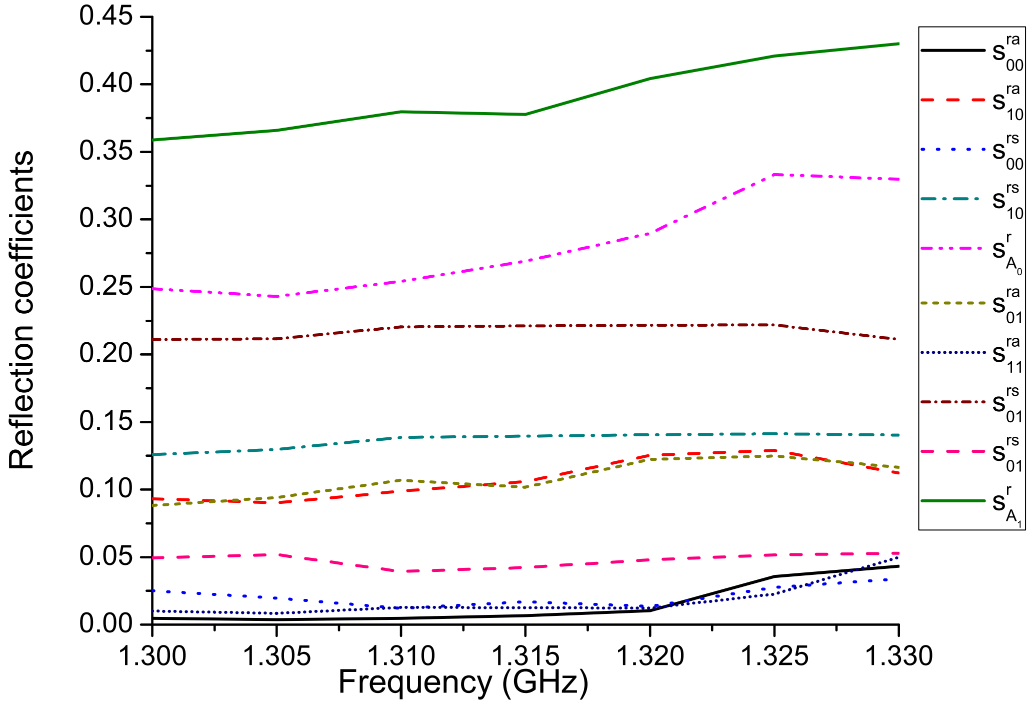

Figure 4.30: The power scattering coefficients s^{ra}_{mn} and s^{rs}_{mn} for A_0 and A_1 modes reflecting from the asymmetric boundary at P_3.

Figure 4.31(a) shows the normalized time history of the Lamb wave collected at P_4. It is observed that no reflecting waves from the outer boundary are present. Figure 4.31(b) shows the wavenumber spectrum at frequency 1.315 GHz of the Lamb wave collected at P_4. It is confirmed that the transmitted wave consists of forward propagating mode pA_0, pA_1 and pS_0 only. The complex amplitude of the transmitted modes (A_{t0}, A_{t1}, and S_{t0}) can be calculated by applying 2D FFT to the time sequence of the equally allocated monitoring points on the top surface of the passive region. The complex amplitude of the transmitted modes (A_{t0}, A_{t1} and S_{t0}) are used instead of the reflected modes (A_{r0} and A_{r1}) in the matrix (Eq. (4.22)) to calculate the complex mode amplitude conversion coefficients of the transmitted modes r^{ta}_{nm} and r^{ts}_{nm} by solving the matrix equation (Eq. (4.21)). The mode power coefficients c_n for mode pA_0, pA_1 and pS_0 in the passive region are shown in Fig. 4.32. Table 4.9 shows the power scattering coefficients of the transmitted waves calculated by the proposed method. s^{ta}_{mn} is the power transmission coefficient of mode A_n converted into mode A_m, and s^{ts}_{mn} is the power transmission coefficient of mode A_n converted into mode S_m. $s^t_{A_n}$ is the total power transmission coefficient for mode A_n calculated by $s^t_{A_n} = s^{ta}_{0n} + s^{ta}_{1n} + s^{ts}_{0n}$ (n = 0,1). Figure 4.33 shows the the power scattering coefficients of the transmitted waves for the interested frequency range. It is observed that the power transmission coefficients of mode A_0 and A_1 are decreasing with the increase of the frequency. Within the investigated frequency range, more than 66% energy of mode A_0 and more than 56% energy of mode A_1 are propagating into the passive region, causing energy leakage in FBAR resonators.

Table 4.9: Power scattering coefficients of the transmitted waves s^{ta}_{mn} and s^{ts}_{mn} for FBAR with asymmetric electrodes.

frequency (GHz)	s^{ta}_{00}	s^{ta}_{10}	s^{ts}_{00}	$s^t_{A_0}$	s^{ta}_{01}	s^{ta}_{11}	s^{ts}_{01}	$s^t_{A_1}$
1.300	0.738	0.013	0.002	0.753	0.014	0.460	0.149	0.624
1.305	0.730	0.015	0.004	0.749	0.015	0.458	0.148	0.620
1.310	0.726	0.015	0.004	0.745	0.017	0.448	0.149	0.613
1.315	0.722	0.017	0.002	0.740	0.018	0.444	0.174	0.637
1.320	0.718	0.029	0.002	0.749	0.022	0.419	0.176	0.618
1.325	0.653	0.031	0.002	0.687	0.028	0.349	0.202	0.579
1.330	0.644	0.024	0.001	0.669	0.024	0.340	0.196	0.560

To ensure the time convergence of the simulation, two different time steps $59,000$ and $60,000$ were used respectively. The differences of amplitudes of the incident modes, reflected modes and transmitted modes calculated by using these two different time steps are less than 2% for all points. The energy differences between the incident modes and the converted modes are also calculated to check the computation accuracy, which are shown in Table 4.10 and Table 4.11 for the first set of data and the second set of data, respectively.

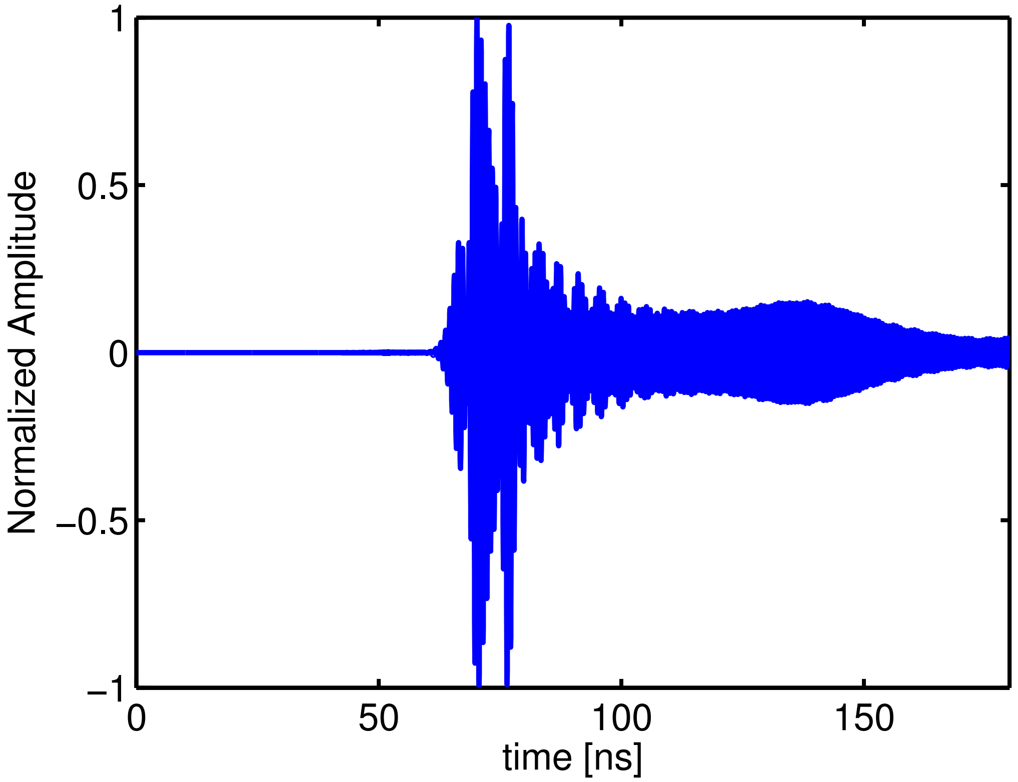

(a)

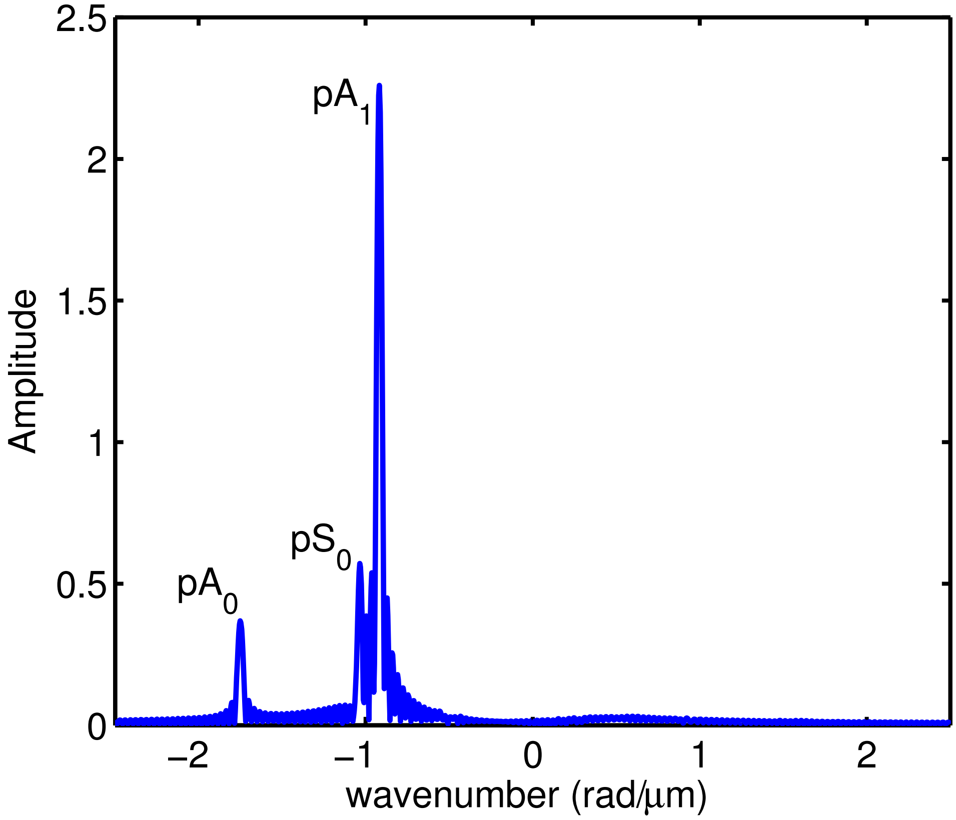

(b)

Figure 4.31: Transmitted Lamb waves at P_4 for FBAR with asymmetric electrodes. (a) Time history, (b) Frequency spectrum.

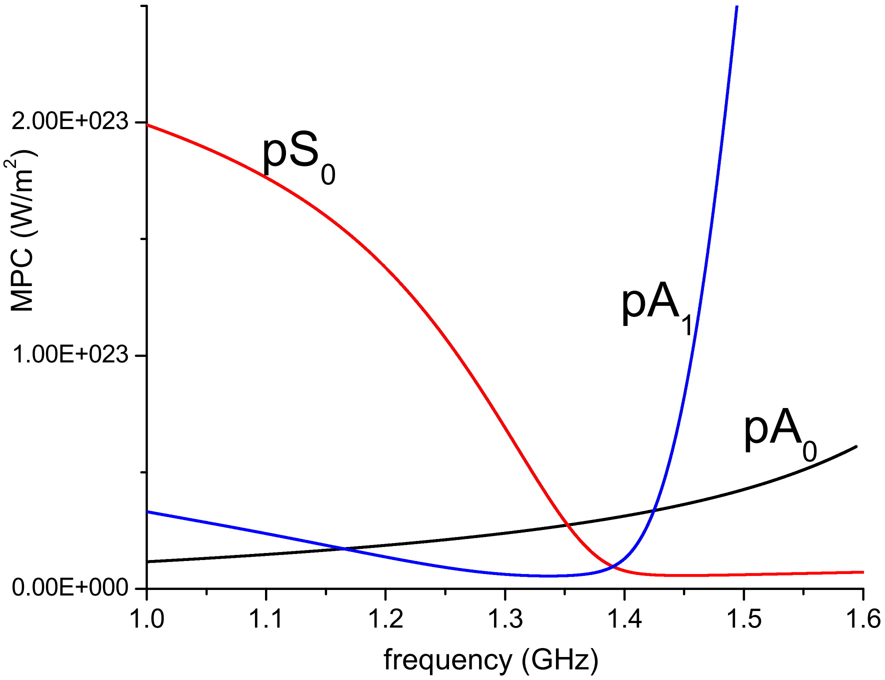

Figure 4.32: Mode power coefficient c_n for pA_0, pA_1 and pS_0 modes propagating in passive region for FBAR with asymmetric electrodes.

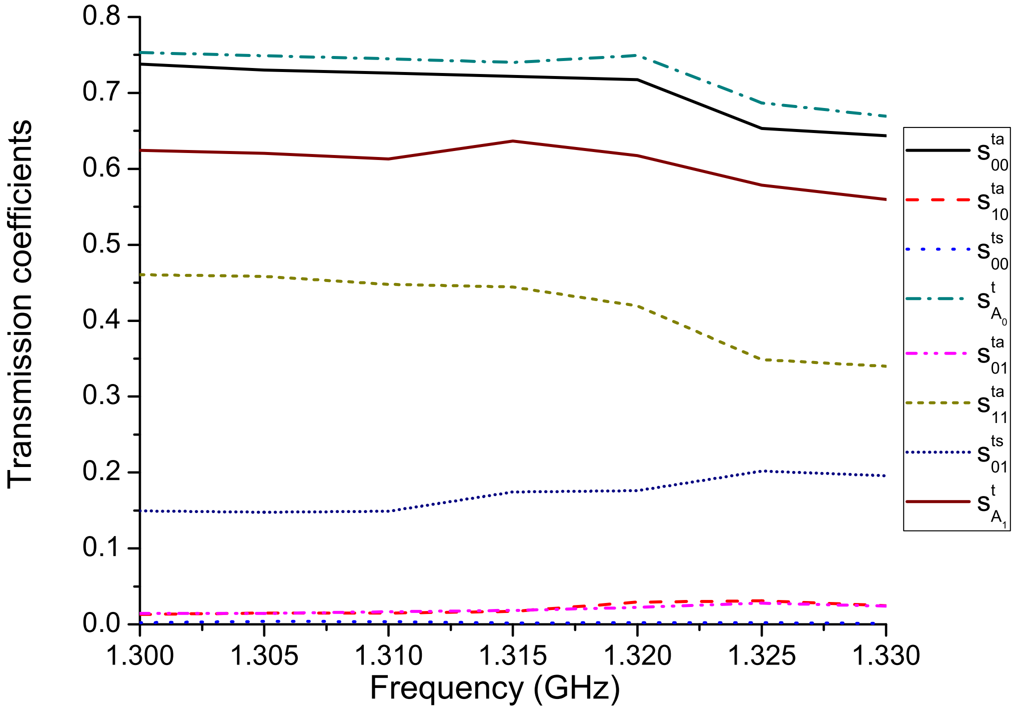

Figure 4.33: The power scattering coefficients s^{ta}_{mn} and s^{ts}_{mn} for A_0 and A_1 modes transmitted into the passive region.

$P_{A_n,inc}$ (n=0, 1) is the power of the incident mode A_n, and P_{inc} is the total incident power calculated by $P_{inc} = P_{A_0,inc} + P_{A_1,inc}$. $P_{A_n,ref}$ (n=0, 1) is the power of the reflected mode A_n, and $P_{S_n,ref}$ (n=0, 1) is the power of the reflected mode S_n. $P_{pA_n,tra}$ (n=0, 1) is the power of the transmitted mode pA_n, and $P_{pS_0,tra}$ is the power of the transmitted mode pS_0. P_{conv} is the total converted power calculated by $P_{conv} = P_{A_0,ref} + P_{A_1,ref} + P_{S_0,ref} + P_{S_1,ref} + P_{pA_0,tra} + P_{pA_1,tra} + P_{pS_0,tra}$. Energy difference between the incident modes and the converted modes P_{dif} is calculated by $P_{dif} = (P_{conv} - P_{inc})/P_{inc}$. It is observed that the energy difference is smaller than 5% at all frequencies. Energy conservation is also checked by combining Table 4.8 and Table 4.9, shown in Table 4.12. $s^r_{A_n}$ (n=0, 1) is the total power reflection coefficient for mode A_n (shown in Table 4.8). $s^t_{A_n}$ (n=0, 1) is the total power transmission coefficient for mode A_n (shown in Table 4.9). And $s^{total}_{A_n}$ (n=0, 1) is the total power scattering coefficient for mode A_n, calculated by $s^{total}_{A_n} = s^r_{A_n} + s^t_{A_n}$. By energy conservation, $s^{total}_{A_n}$ should be equal to 1. It is observed that the error is less than 4% at all frequencies. The accuracy of the results can be improved by increasing the simulation time and elongating the structure to allocate more monitoring points on the surface to improve the frequency and wavenumber resolution, respectively.

Comparing Table 4.4 with Table 4.9, it is observed that with symmetric electrodes, less energy is propagating into the passive region for both mode A_0 and A_1. Therefore, less energy is lost and the quality factor Q is higher for FBAR with symmetric electrodes than the one with asymmetric electrodes. But, a FBAR resonator with symmetric electrodes is not suitable for practical application. A more practical FBAR structure with frame-like airgap on bottom electrode is proposed and will be investigated in the next chapter.

Table 4.10: Energy difference between the incident modes and the converted modes for the first set of data.

frequency (GHz)	$P_{A_0,inc}$ $10^{-8}W$	$P_{A_1,inc}$ $10^{-8}W$	P_{inc} $10^{-8}W$	$P_{A_0,ref}$ $10^{-8}W$	$P_{A_1,ref}$ $10^{-8}W$	$P_{S_0,ref}$ $10^{-8}W$	$P_{S_1,ref}$ $10^{-8}W$	$P_{A_0,tra}$ $10^{-8}W$	$P_{A_1,tra}$ $10^{-8}W$	$P_{S_0,tra}$ $10^{-8}W$	P_{conv} $10^{-8}W$	P_{dif}
1.300	0.62	8.23	8.86	0.75	0.28	2.48	0.80	0.19	3.47	1.23	9.20	0.039
1.305	0.63	7.78	8.41	0.72	0.24	2.53	0.87	0.23	2.99	1.19	8.76	0.042
1.310	0.61	7.86	8.47	0.72	0.27	2.62	0.71	0.27	2.94	1.20	8.73	0.031
1.315	0.59	7.57	8.16	0.75	0.30	2.78	0.72	0.34	2.37	1.29	8.55	0.048
1.320	0.59	8.04	8.63	0.87	0.33	3.19	0.81	0.43	1.65	1.31	8.59	-0.004
1.325	0.56	8.46	9.02	0.95	0.48	3.44	0.98	0.65	0.98	1.47	8.96	-0.007
1.330	0.57	8.64	9.20	0.48	0.91	2.29	1.35	0.74	2.23	1.63	9.65	0.048

Table 4.11: Energy difference between the incident modes and the converted modes for the second set of data.

frequency (GHz)	$P_{A_0,inc}$ $10^{-8}W$	$P_{A_1,inc}$ $10^{-8}W$	P_{inc} $10^{-8}W$	$P_{A_0,ref}$ $10^{-8}W$	$P_{A_1,ref}$ $10^{-8}W$	$P_{S_0,ref}$ $10^{-8}W$	$P_{S_1,ref}$ $10^{-8}W$	$P_{A_0,tra}$ $10^{-8}W$	$P_{A_1,tra}$ $10^{-8}W$	$P_{S_0,tra}$ $10^{-8}W$	P_{conv} $10^{-8}W$	P_{dif}
1.300	78.27	23.46	101.73	1.60	5.00	1.32	4.46	66.82	17.24	2.31	98.74	-0.029
1.305	78.14	22.55	100.69	2.01	5.13	2.08	4.70	65.54	15.26	2.27	96.99	-0.037
1.310	78.23	23.03	101.26	2.84	5.72	3.33	5.74	64.04	15.47	2.35	99.50	-0.017
1.315	77.93	22.42	100.35	3.79	5.57	5.30	5.84	60.97	13.15	2.83	97.44	-0.029
1.320	78.49	23.58	102.07	6.03	6.77	9.51	6.30	58.19	10.35	2.77	99.93	-0.021
1.325	77.40	22.69	100.09	12.21	7.55	21.72	5.14	45.60	4.76	4.67	101.66	0.016
1.330	76.17	22.86	99.03	10.97	1.92	24.58	1.27	50.93	1.53	6.59	97.80	-0.012

Table 4.12: Power scattering coefficients of the converted modes for FBAR with asymmetric electrodes.

frequency (GHz)	$s^r_{A_0}$	$s^t_{A_0}$	$s^{total}_{A_0}$	$s^r_{A_1}$	$s^t_{A_1}$	$s^{total}_{A_1}$
1.300	0.249	0.753	1.002	0.359	0.624	0.983
1.305	0.243	0.749	0.992	0.366	0.620	0.986
1.310	0.254	0.745	0.999	0.380	0.613	0.993
1.315	0.269	0.740	1.009	0.378	0.637	1.014
1.320	0.290	0.749	1.039	0.404	0.618	1.022
1.325	0.333	0.687	1.020	0.421	0.579	1.000
1.330	0.330	0.669	0.999	0.430	0.560	0.990

Chapter 5

FBAR with frame-like airgap on bottom electrode for suppression of spurious modes

5.1 Introduction

Based on the scattering analysis of the two generic free-standing bulk acoustic resonator (FBAR) structures in Chapter 4, a new structure of FBAR resonator with frame-like airgap on bottom electrode is proposed to suppress the spurious modes and improve the quality factor [128]. The proposed FBAR structure is presented first. Following that, the time domain analysis developed in Chapter 3 is carried out for the proposed structure. Furthermore, the frequency domain analysis is conducted to provide a more profound understanding for the phenomenon. Finally, some discussions on the simulation results are given.

The proposed FBAR structure is shown in Fig. 5.1. In this structure, a frame-like airgap is formed on the bottom electrode of FBAR. The airgap is put aligned to the top electrode, where the discontinuity lies. The spurious waves are generated at the discontinuity boundary. Therefore, the airgap allocated at the discontinuity boundary is applied to change the boundary condition and suppress the spurious waves. The piezoelectric material used in this investigation is AlN and the electrode metal is Al. The material properties used in this simulation is presented in section 3.3.

A two-dimensional finite-difference time-domain (FDTD) model (developed in chapter 3) was set up to simulate the structure. The zero traction condition was enforced on the boundaries and the structure was long enough to eliminate the scattering from the outer boundary. As it is mentioned in section 3.5, to reduce the artificial numerical dispersion effects to an acceptable extent, the spatial step size Δx_1 and Δx_3 were both set to 5×10^{-8} m, which was approximately equal to one twentieth of the smallest wavelength of the excitation source. To ensure the stability of the simulation, the time increment interval

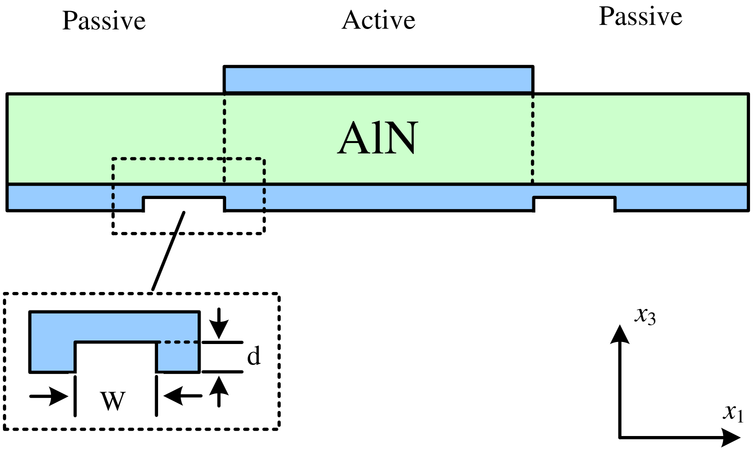

Figure 5.1: The proposed FBAR resonator with frame-like airgap to suppress the spurious modes.

was chosen to be 3×10^{-12} s in order to satisfy the Courant stability condition [111].

Firstly, time domain analysis is carried out in the next section. A sinusoidal wave at antiresonance frequency of the structure is used as the excitation source in the FDTD simulation. The displacements are extracted to analyze the proposed structure. Furthermore, the frequency domain analysis is conducted to provide a more profound understanding for the phenomenon in section 5.3. A Gaussian pulse is applied as the excitation source in this case. The power of each spurious mode is calculated and analyzed for the proposed structure.

5.2 Time domain analysis for the proposed structure

In this section, a sinusoidal wave (demonstrated in section 3.6.3) at antiresonance frequency of the structure was used as the excitation source in the FDTD simulation. The thickness of the piezoelectric layer was 3 μm and the thicknesses of the top and bottom electrode layer were both 0.6 μm. The width of the top electrode was 100 μm and the width of the whole structure was 500 μm. The displacements on the top layer and bottom layer of the piezoelectric material as shown in Fig. 5.2 were observed. Due to the spatial discretization of the FDTD algorithm, the particle velocity v_3 (thus the particle displacement u_3) does not lie on the top or bottom interface between the electrode and the piezoelectric material. Thus, the top layer is the first layer below the interface of the top electrode and the piezoelectric material and the bottom layer is the first layer above the interface of the bottom electrode and the piezoelectric material. The displacements were extracted at the time instant when the resonator was in a steady resonant state. The structure was large enough that there are no reflection waves from the outer boundary.

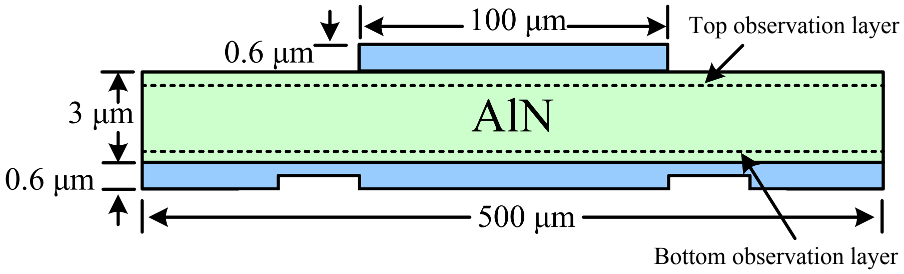

Figure 5.2: Observation displacement layers in the time domain analysis.

The displacement u_3 along the top observation layer at $t = 18$ ns is shown in Fig. 5.3. The depth of the airgap was 0.6 μm in this case, which is corresponding to totally removing the bottom electrode in the airgap region. Because of symmetry, only the right passive region of the structure is shown in Fig. 5.3(b). Fig. 5.3(c) shows the displacement distribution in the active region, or the overlap of the top electrode and bottom electrode region. In the ideal case, no spurious wave generated in the structure, the displacement inside the active region should be a flat line. In Fig. 5.3, it is observed that the amplitude of the ripples of the proposed structure is much smaller than that of the structure without airgap on the bottom electrode. The ripples are generated by resonance of the plate waves in the transverse direction [46], which are the sources of the spurious modes. So, the smaller amplitude of the ripples means less lateral spurious waves and less energy is leaked. Energy trapping is also observed in Fig. 5.3. The displacement u_3 along the bottom layer is displayed in Fig. 5.4. Similar phenomenon is observed in Fig. 5.4. Therefore, only the displacements on the top layer are considered in the rest of this chapter. A different time instant is chosen for Fig. 5.4 to show that the amplitude of ripples is reduced at different time instants.

The influence of the airgap width and depth on the spurious wave suppression are investigated in the next two subsections.

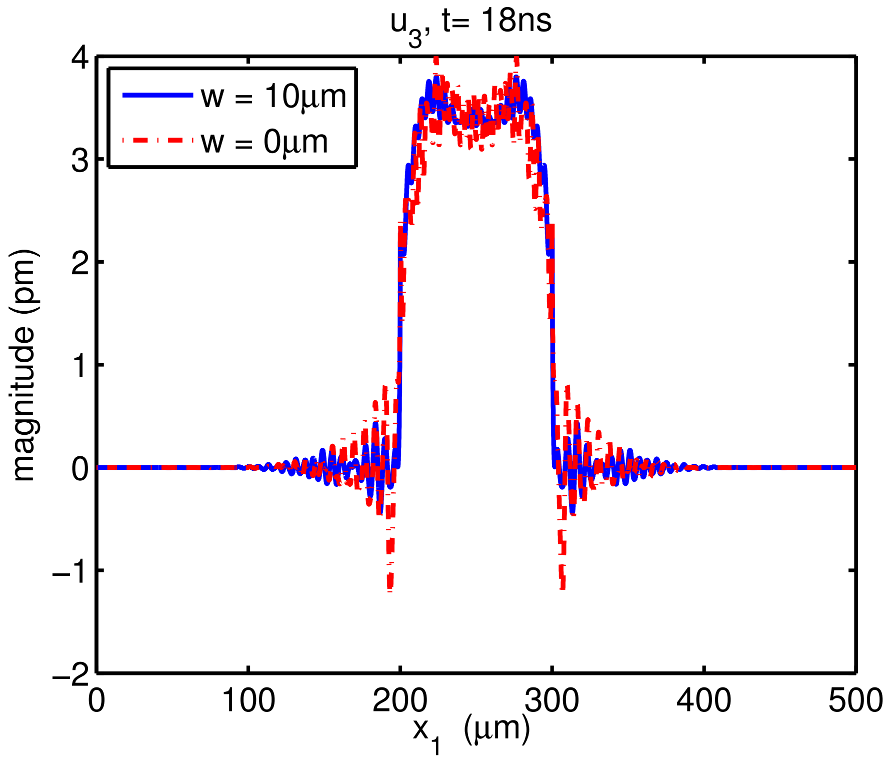
u_3, t= 18ns
w = 10μm
w = 0μm
magnitude (pm)
4
3
2
1
0
−1
−2
0
100
200
300
400
500
x_1 (μm)

(a)

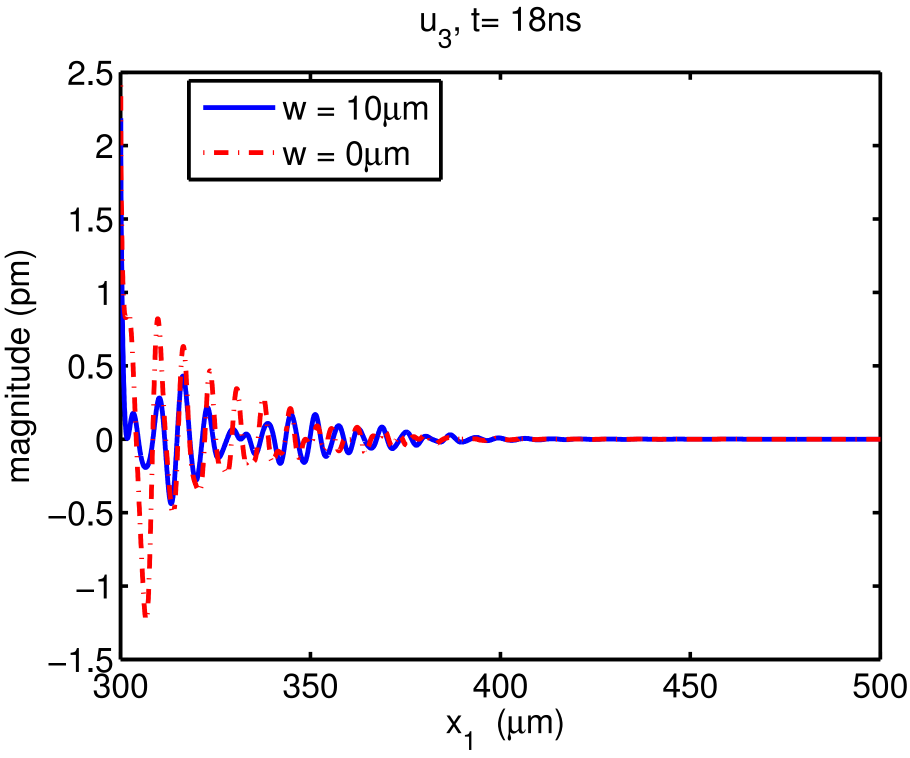
u_3, t= 18ns
w = 10μm
w = 0μm
magnitude (pm)
2.5
2
1.5
1
0.5
0
−0.5
−1
−1.5
300
350
400
450
500
x_1 (μm)

(b)

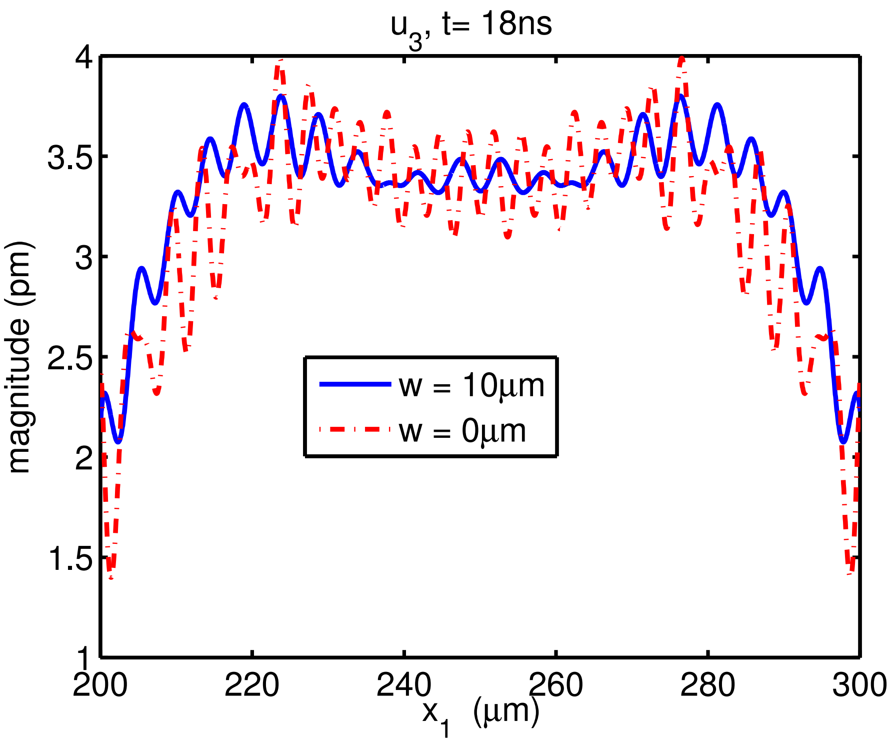

(c)

Figure 5.3: Displacement u_3 along the top observation layer for FBAR resonator with (w = 10 μm) and without (w = 0 μm) airgap on the bottom electrode (a) The whole structure, (b) The right passive region of the structure, (c) Active region.

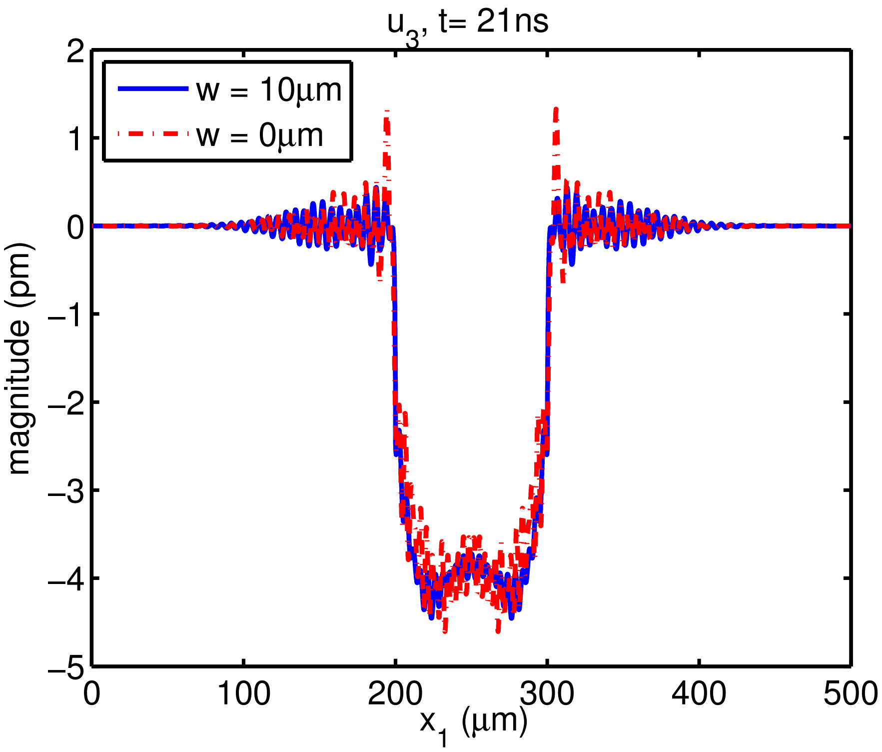

Figure 5.4: Displacement u_3 along the bottom observation layer for FBAR resonator with (w = 10 μm) and without (w = 0 μm) airgap on the bottom electrode.

5.2.1 FBAR with different bottom electrode airgap width

The effect of the bottom electrode airgap width on the spurious wave suppression is examined in this section. To reduce the simulation time, the width of the whole structure was reduced to 300 μm. The airgap depth was fixed to 0.6 μm as shown in Fig. 5.5. The width of the airgap was varied from 0.5 μm to 12 μm with a step of 0.5 μm. A sinusoidal wave at antiresonance frequency of the structure was used as the excitation source for all the cases.

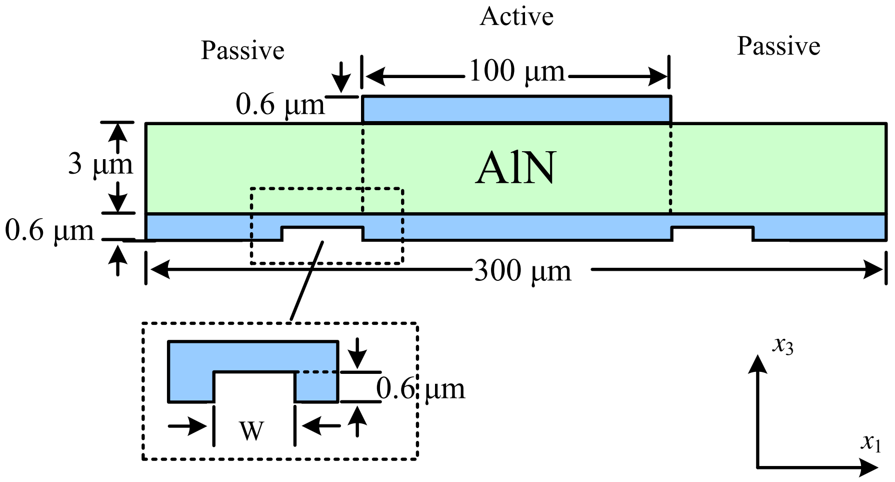

Figure 5.5: The FBAR resonator with airgap on the bottom electrode for time domain analysis on the effect of the airgap width.

Figure 5.6 shows the comparison of displacements of FBAR with bottom electrode airgap width of 0.5 μm and 3 μm. It is quite obvious that the amplitude of the ripples of the structure with 0.5 μm airgap width is much larger than that of the structure with 3 μm airgap width in both active and passive regions. Figure 5.7 shows the comparison of displacements of FBAR with bottom electrode airgap width of 2 μm and 7 μm. It can be observed that the amplitude of the ripples does not have too much difference for these two different airgap widths.

As the amplitude of the ripples in the passive region is proportional to the leakage power, the sum of the square of the displacement amplitude along the top observation layer in the passive region ($P_i = \sum(u_i(x_{1j}))^2$) were calculated and compared for different airgap width. Due to symmetry, only the right passive region was investigated. Figure 5.8 shows the sum of the square of the displacement amplitude in the right passive region for different airgap width. It is observed that the sum decreases quickly from the width of 0 μm (without airgap) to the width of 2 μm. When the width is larger than 2 μm, the sum shows a quasi-periodic behavior, and the difference between different width is relatively small. For the active region, similar phenomenon can be observed for the displacement amplitude. However, it is difficult to compare them in the way for the passive region,

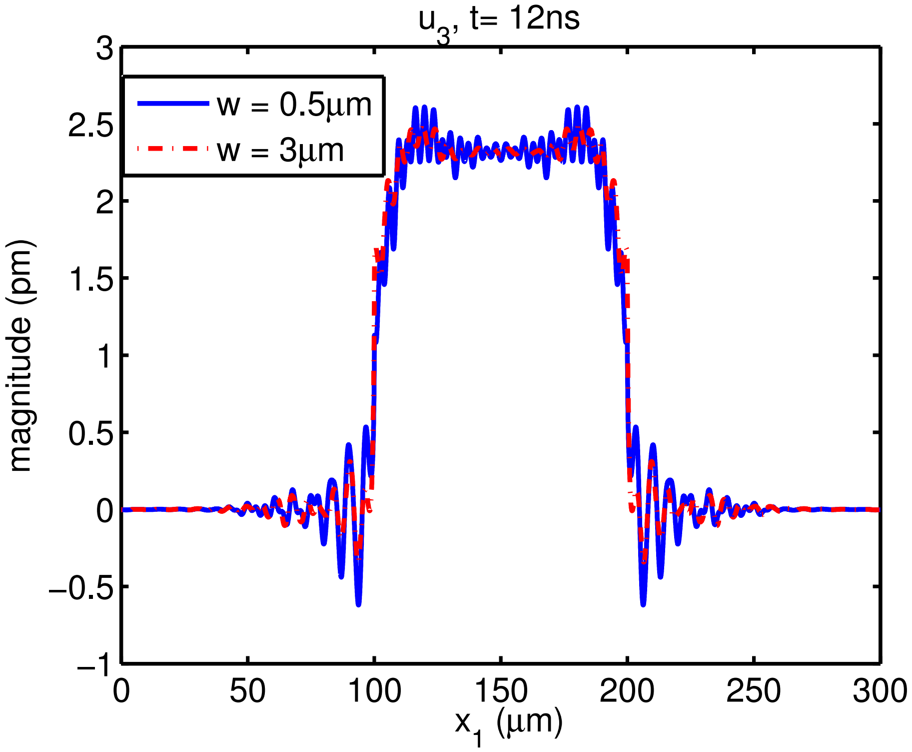
u_3, t= 12ns
w = 0.5µm
w = 3µm
magnitude (pm)
3
2.5
2
1.5
1
0.5
0
−0.5
−1
0
50
100
150
200
250
300
x_1 (µm)

(a)

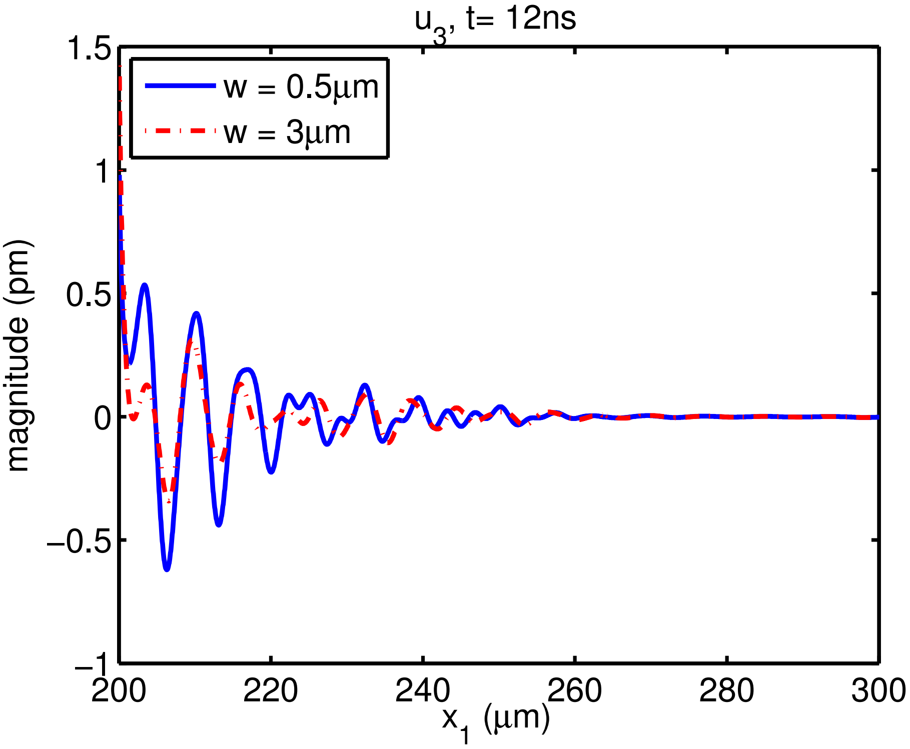
u_3, t= 12ns
w = 0.5µm
w = 3µm
magnitude (pm)
1.5
1
0.5
0
−0.5
−1
200
220
240
260
280
300
x_1 (µm)

(b)

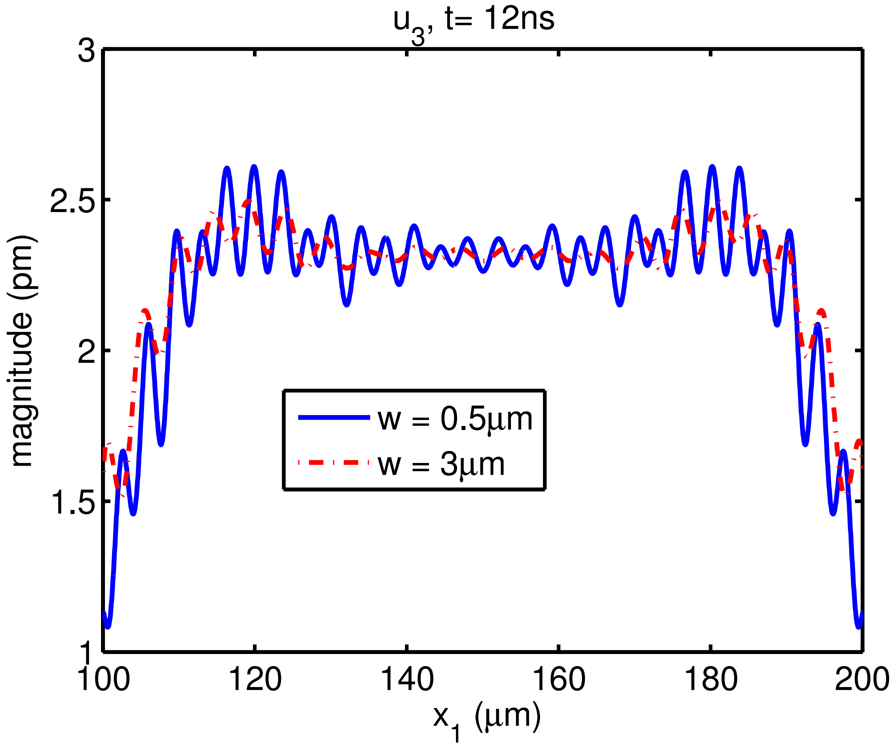

(c)

Figure 5.6: Displacement u_3 along the top observation layer of the piezoelectric material for different airgap width (a) The whole structure, (b) The right passive region of the structure, (c) Active region.

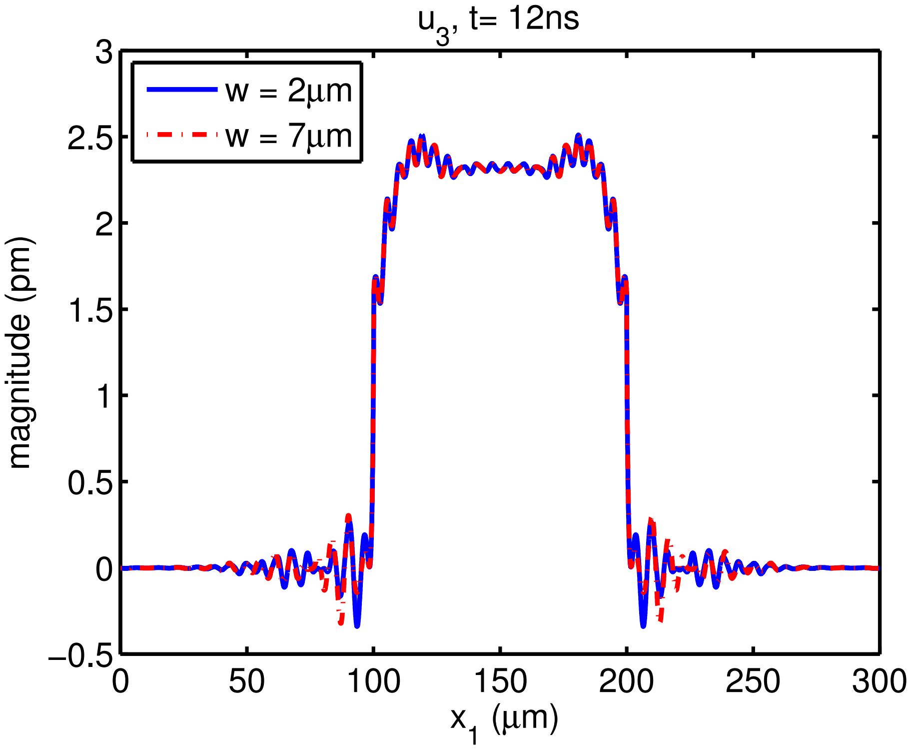

Figure 5.7: Displacement u_3 along the top observation layer of the piezoelectric material for different airgap width.

because it is difficult to separate the spurious waves from the desired longitudinal waves. More detailed analysis is conducted in the frequency domain in section 5.3.1.

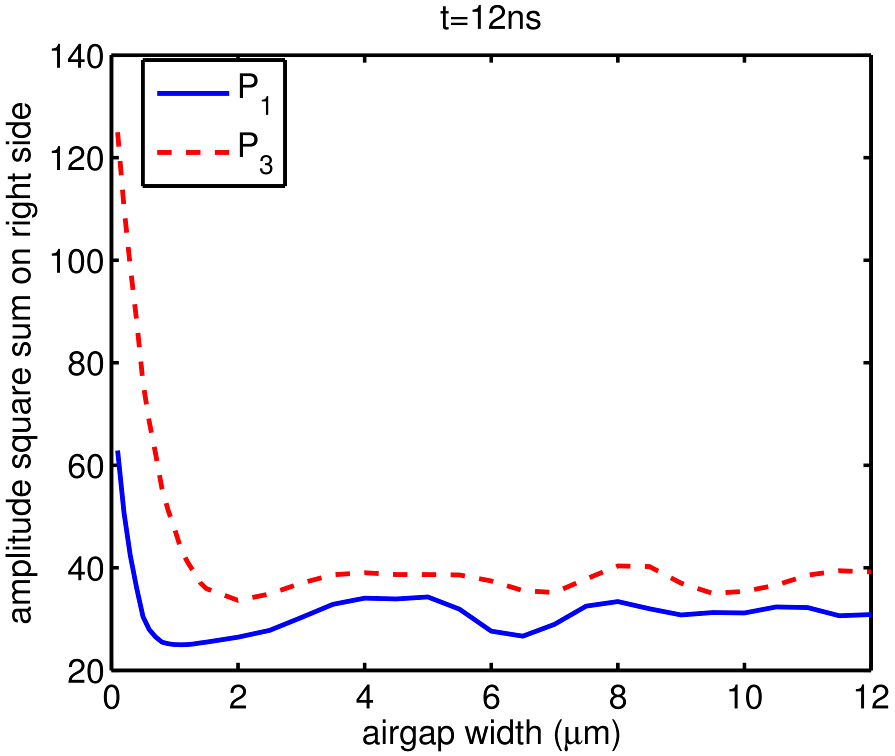

Figure 5.8: Sum of the square of the displacement amplitude in the right passive region for different airgap width.

5.2.2 FBAR with different bottom electrode airgap depth

The effect of the bottom electrode airgap depth on the spurious wave suppression is investigated in this section. The width of the whole structure used in this case was again 300 μm. The airgap width was fixed to 3 μm as shown in Fig. 5.9. The depth of the airgap was increased from 0 to 0.6 μm with a step of 0.1 μm. A sinusoidal wave at antiresonance frequency of the structure was used as the excitation source for all the cases.

It is observed in Fig. 5.10 that the amplitude of ripples of structure with 0.1 μm airgap depth is much larger than that of structure with 0.6 μm airgap depth. The sum of the square of the displacement amplitude along the top observation layer in the right passive region ($P_i = \sum(u_i(x_{1j}))^2$) were also calculated and compared for different airgap depth (shown in Fig. 5.11). It is observed that as the depth of the airgap increases, the sum decreases quickly. Structure with 0.6 μm airgap depth has the best performance, which is corresponding to totally removing the bottom electrode in the airgap region. This is undesirable because the structure cannot connect to other devices after removing the bottom electrode in the airgap region. Fortunately, 0.1 μm difference of the depth will

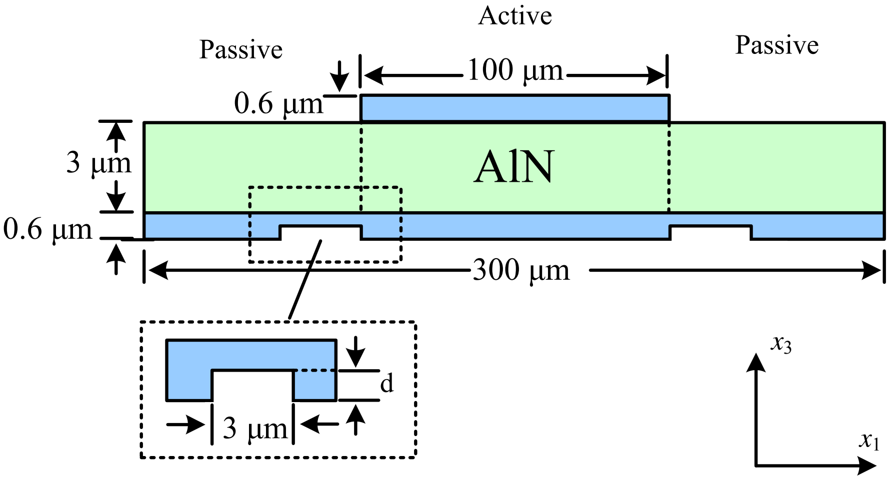

Figure 5.9: The FBAR resonator with airgap on the bottom electrode for time domain analysis on the effect of the airgap depth.

not affect the performance too much, which is shown in Fig. 5.12. More detailed analysis is conducted in the frequency domain in section 5.3.2.

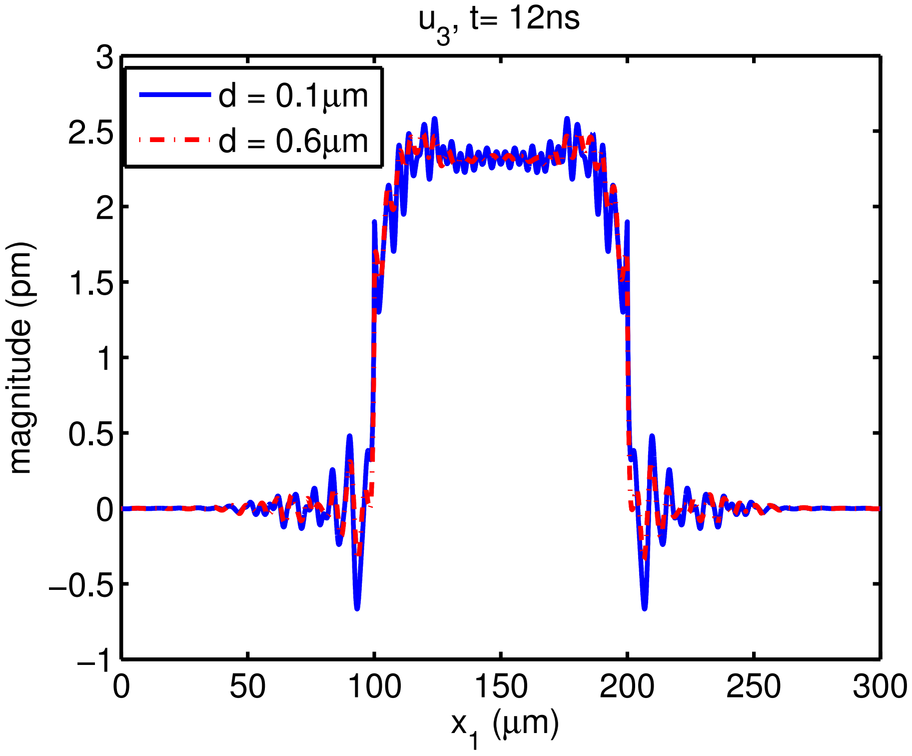
u_3, t= 12ns
d = 0.1µm
d = 0.6µm
magnitude (pm)
x_1 (µm)
3
2.5
2
1.5
1
0.5
0
−0.5
−1
0
50
100
150
200
250
300

(a)

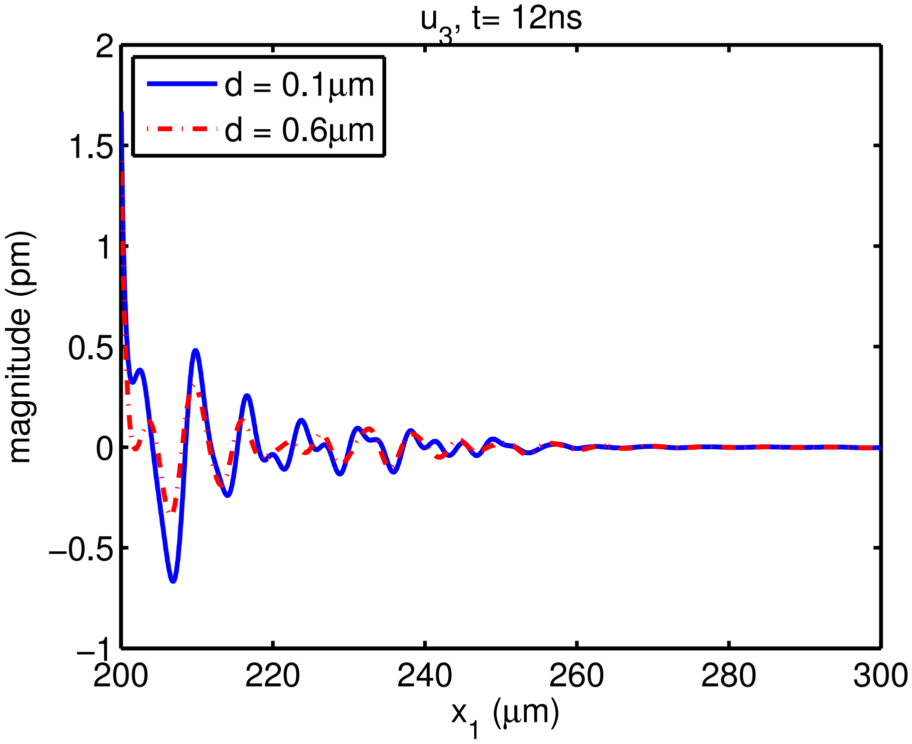
u_3, t= 12ns
d = 0.1µm
d = 0.6µm
magnitude (pm)
x_1 (µm)
2
1.5
1
0.5
0
−0.5
−1
200
220
240
260
280
300

(b)

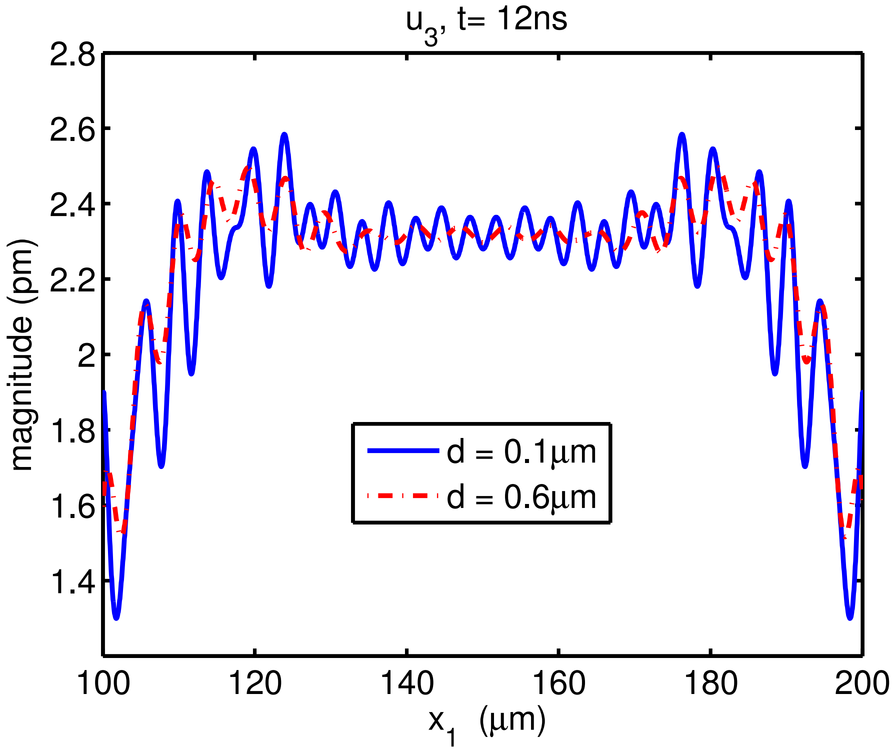

(c)

Figure 5.10: Displacement u_3 along the top observation layer of the piezoelectric material for different airgap depth (a) The whole structure, (b) The right passive region of the structure, (c) Active region.

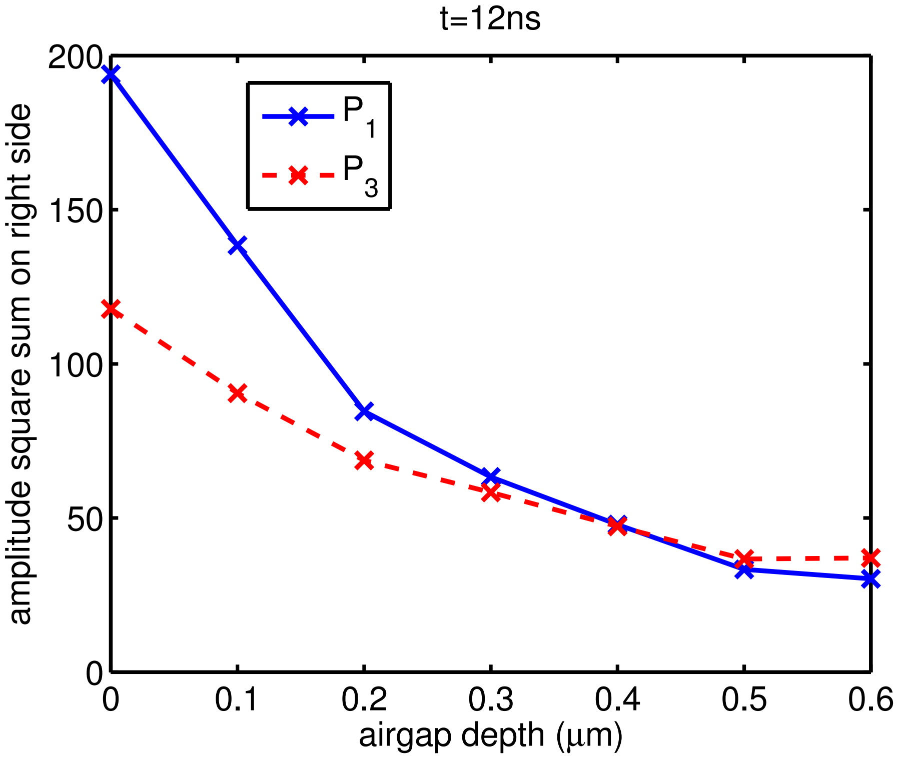

Figure 5.11: Sum of the square of the displacement amplitude in the right passive region for different airgap depth.

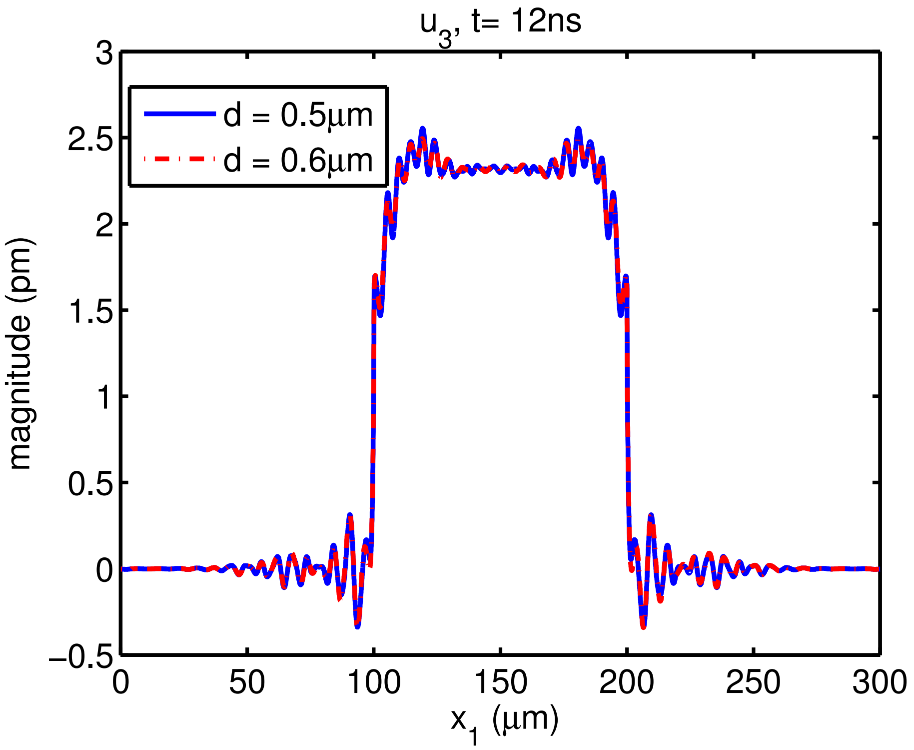

Figure 5.12: Displacement u_3 along the top observation layer of the piezoelectric material for different airgap depth.

5.3 Frequency domain analysis for the proposed structure

In this section, the frequency domain analysis is conducted to provide a more profound understanding for the observed phenomenon in time domain. A Gaussian pulse with maximum frequency of 2 GHz (demonstrated in section 3.6.1) was used as the excitation source. The particle velocities $v_n(x_1, t)$ (n=1,3) on the top surface in the active region and the passive region were calculated and recorded by the FDTD model. The power of each propagating Lamb mode was calculated by Eq. (2.30). The amplitude of the particle displacement used in Eq. (2.30) were obtained by applying 2D FFT to the recorded particle velocities $v_n(x_1, t)$ (n=1,3) on the top surface in the active region and the passive region, respectively. Since the particle velocity is related to the particle displacement u by $v = \partial u/\partial t$ in time domain, the amplitude of the particle displacement in frequency domain can be calculated by $U(\omega_o) = V(\omega_o)/j\omega_o$.

The proposed structure has the same configuration in the active region as the one investigated in section 4.5.1 and 4.5.2. Therefore, the dispersion characteristic in the active region is the same as the one shown in Fig. 4.17(a). For the passive region, only a small part of the bottom electrode was cut out. Excluding this small part, the remaining part in the passive region has the same layer configuration as the one investigated in section 4.5.2. Thus, the dispersion characteristic in the passive region is the same as the one shown in Fig. 4.26. The resonance frequency f_s of the investigated FBAR resonator was approximately 1.298 GHz and the antiresonance frequency f_a was approximately 1.331 GHz. For simplicity, only the frequency range 1.300 GHz $< f <$ 1.330 GHz was considered. Within this frequency range, Lamb modes A_0, A_1, S_0 and $S_1(+)$ are propagating in the active region, and pA_0, pA_1 and pS_0 are propagating in the passive region. These Lamb modes are the unwanted spurious modes. The mode power coefficients used to calculate the power of each mode are the same as the one used in section 4.5.2 (shown in Fig. 4.29 and Fig. 4.32).

The influence of the airgap width and depth on the spurious wave suppression is investigated in the next two subsections. Furthermore, the power of the spurious modes at different frequency is also investigated for a specified airgap width and depth.

5.3.1 Power of the spurious modes for different airgap width

The effect of the airgap width on the spurious wave suppression is examined in this section. The top electrode width was extended to 192 μm to improve the spatial resolution in the active region, and the whole structure width was extended to 1400 μm to avoid the outer boundary reflection. The airgap depth was fixed to 0.5 μm as shown in Fig. 5.13. The width of the airgap was varied from 1 μm to 12 μm with a step of 1 μm. The power of the propagating Lamb modes was compared for different gap width in the active region and the passive region. Due to the symmetry of the structure, only the modes propagating in the right passive region were analyzed. The amplitude of the longitudinal mode was also compared for different airgap width.

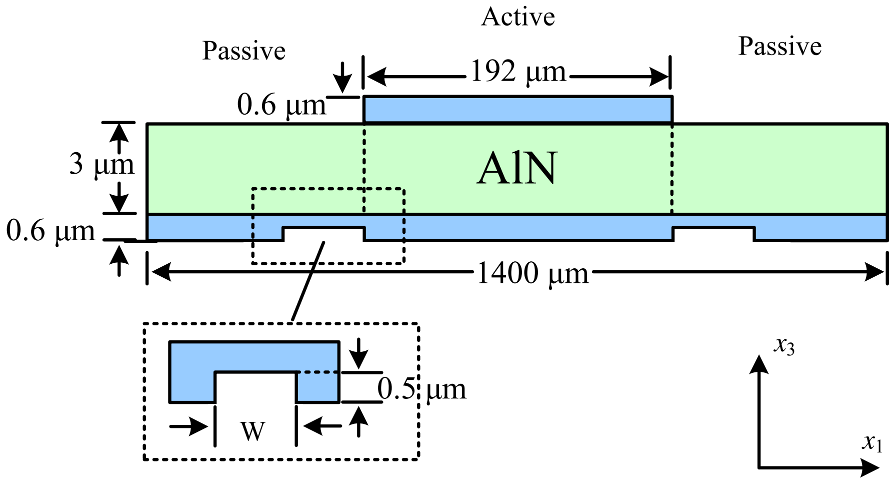

Figure 5.13: The FBAR resonator with airgap on the bottom electrode for frequency domain analysis on the effect of airgap width.

Figure 5.14 shows the power of the propagating Lamb modes in the active region at 1.33 GHz, which is near the antiresonance frequency. It is observed that the power of mode A_0 and A_1 decreases quickly from the width of 0 μm (without airgap) to the width of 2 μm. When the width is larger than 2 μm, the power shows a quasi-periodic behavior, and the difference between different width is relatively small. The power for mode S_0 and S_1 decreases quickly from the width of 0 μm (without airgap) to the width of 1 μm. When the width is larger than 1 μm, the power also shows a quasi-periodic behavior. It can also be observed that the power of mode S_0 and S_1 is larger than that of mode A_0 and A_1 for airgap width larger than 2 μm. Similar phenomenon was also observed at other frequencies within the investigated frequency range. For example, the power of different propagating Lamb modes in the active region at 1.3 GHz, which is near the resonance frequency, is plotted in Fig. 5.15.

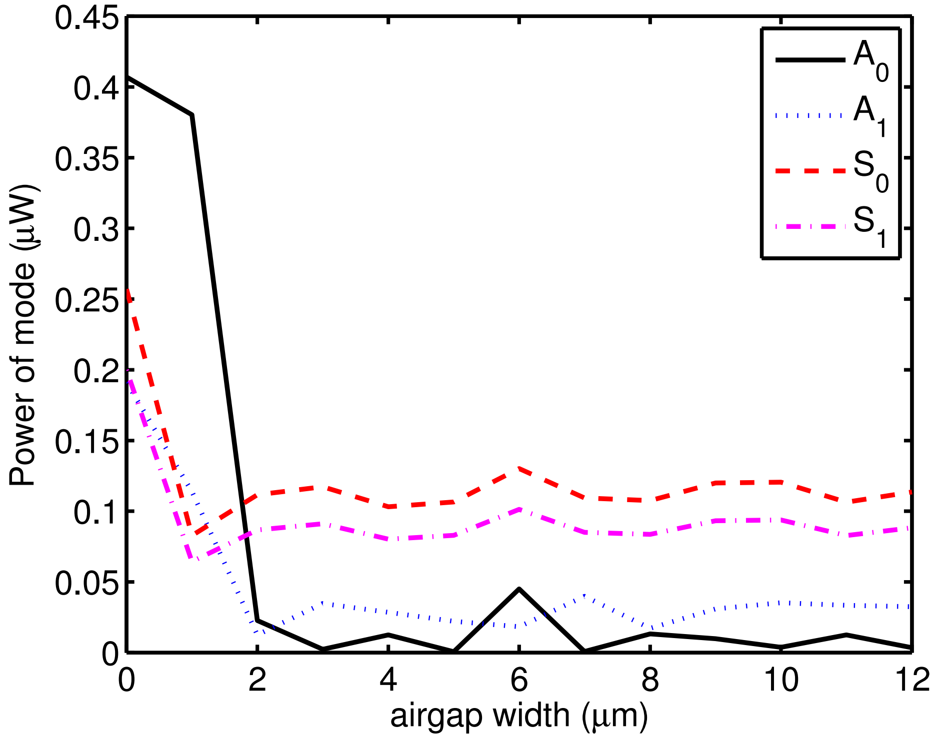

Figure 5.14: Power of Lamb modes in the active region at 1.33 GHz for different airgap width.

The total power of Lamb modes in the active region at 1.33 GHz is also shown in Fig. 5.16. It is observed that the total power of the spurious modes decreases quickly from the width of 0 μm (without airgap) to the width of 2 μm. When the width is larger than 2 μm, the total power shows a quasi-periodic behavior, and the difference between different width is relatively small. Similar phenomenon was also observed at other frequencies within the investigated frequency range. For example, the total power of the spurious modes in the active region at 1.3 GHz, which is near the resonance frequency, is plotted in Fig. 5.17.

Figure 5.18 shows the power of the propagating Lamb modes in the passive region at 1.33 GHz, which is near the antiresonance frequency. It is observed that the power

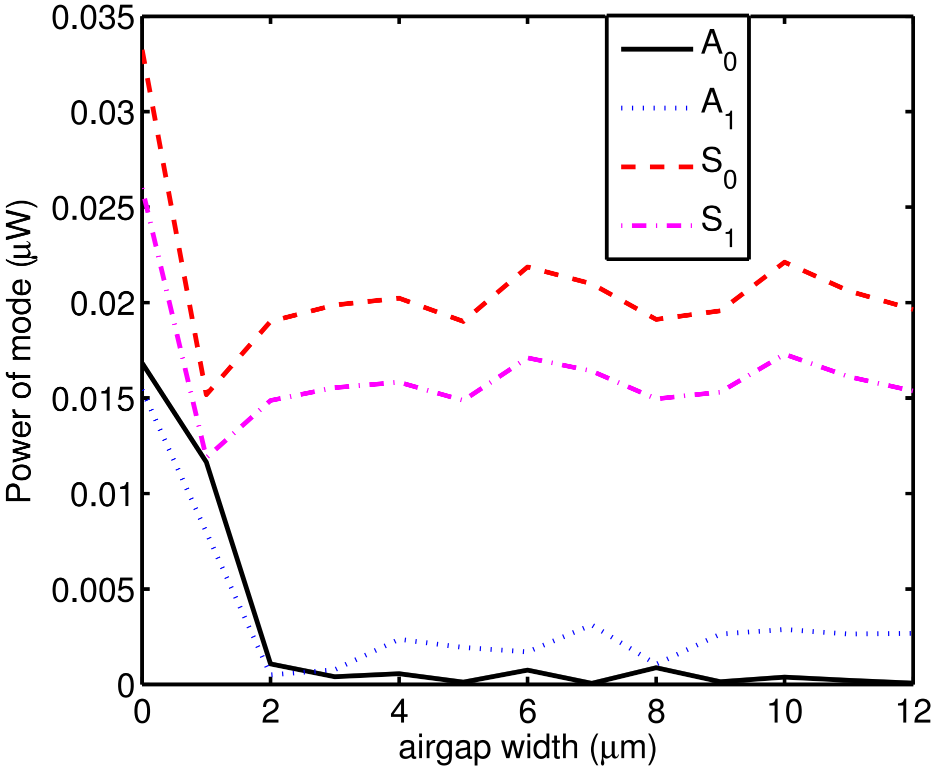

Figure 5.15: Power of Lamb modes in the active region at 1.3 GHz for different airgap width.

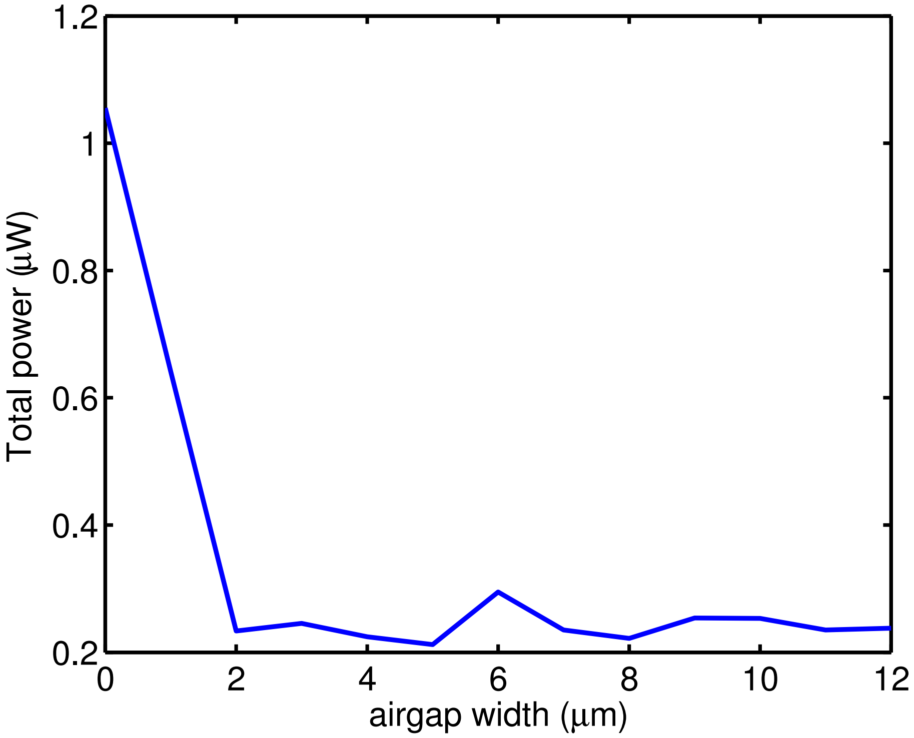

Figure 5.16: The total power of Lamb modes in the active region at 1.33 GHz for different airgap width.

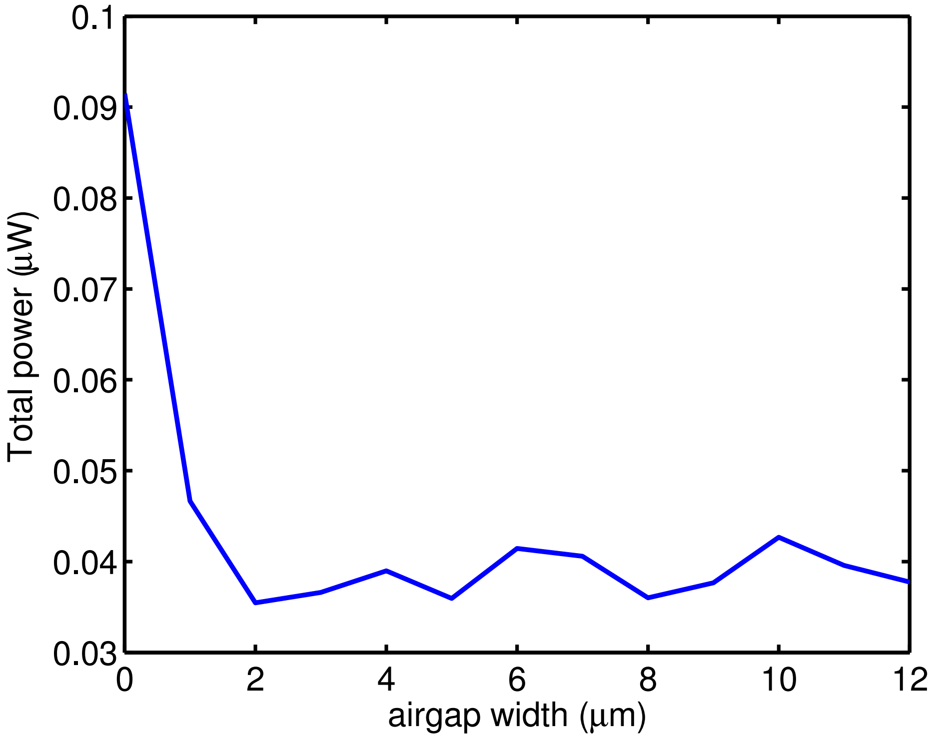

Figure 5.17: The total power of Lamb modes in the active region at 1.3 GHz for different airgap width.

of mode pA_0 and pA_1 decreases quickly from the width of 0 μm (without airgap) to the width of 2 μm. When the width is larger than 2 μm, the power difference between different width is relatively small. On the other hand, the power for mode pS_0 increases quickly from the width of 0 μm (without airgap) to the width of 2 μm. When the width is larger than 2 μm, the power difference for different width is relatively small. It can also be observed that the power of mode pS_0 is much smaller than that of mode pA_0 and pA_1 when the width is smaller than 2 μm, and it is a little bit larger than that of mode pA_0 and pA_1 when the width is larger than 2 μm. This has resulted in quick reduction of total leakage power from the width of 0 μm to the width of 2 μm, which is shown in Fig. 5.19. It is also observed that the total leakage power shows a quasi-periodic behavior, and the difference for different width is relatively small, when the width is larger than 2 μm. Similar phenomenon was also observed at other frequencies within the investigated frequency range, with the exception at 1.3 GHz. At 1.3 GHz, similar to the mode pA_0 and pA_1, the power of mode pS_0 decreases quickly as the width increases from 0 μm to 2 μm, shown in Fig. 5.20. For the total leakage power, the same phenomenon is observed for the whole investigated frequency range. For example, the total leakage power at 1.3 GHz, which is near the resonance frequency, is plotted in Fig. 5.21.

From Fig. 5.16, Fig. 5.17, Fig. 5.19, and Fig. 5.21, it is observed that the total

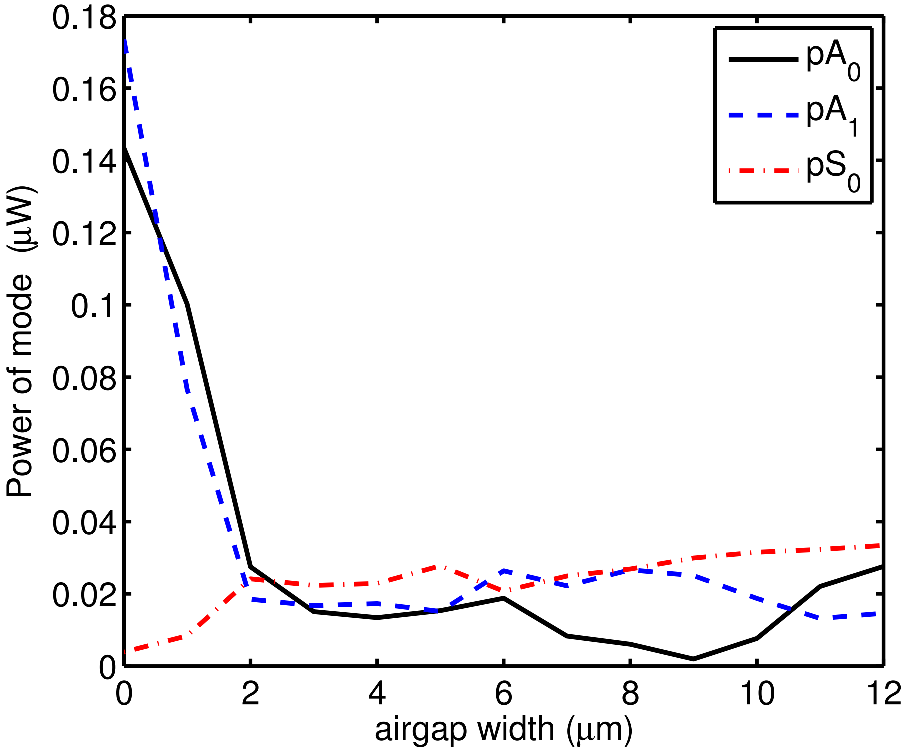

Figure 5.18: Power of Lamb modes in the passive region at 1.33 GHz for different airgap width.

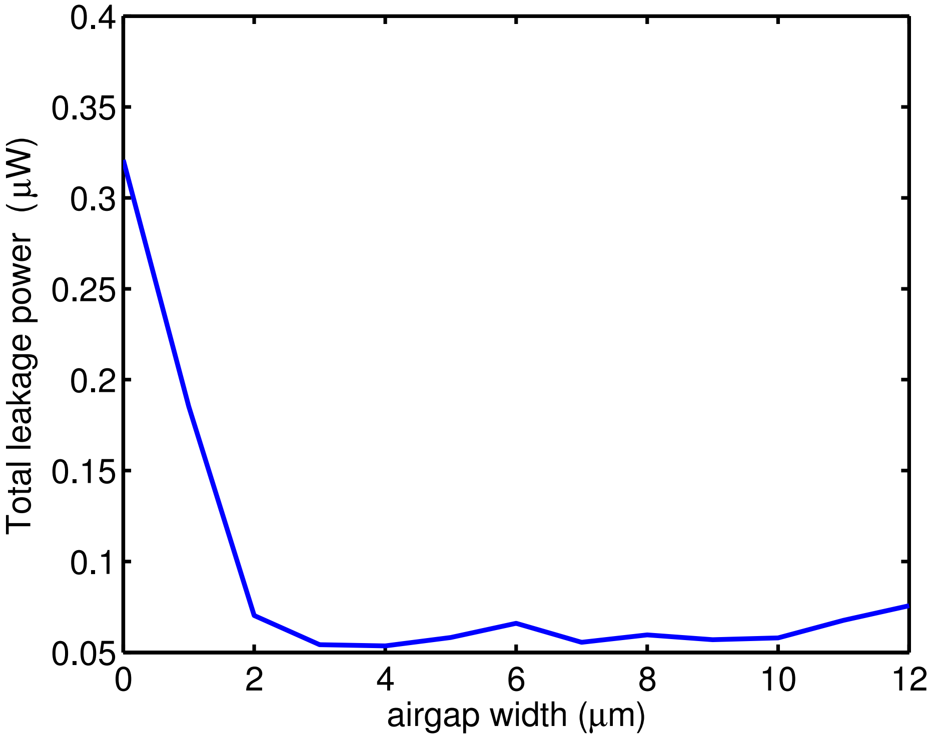

Figure 5.19: The total leakage power of Lamb modes in the passive region at 1.33 GHz for different airgap width.

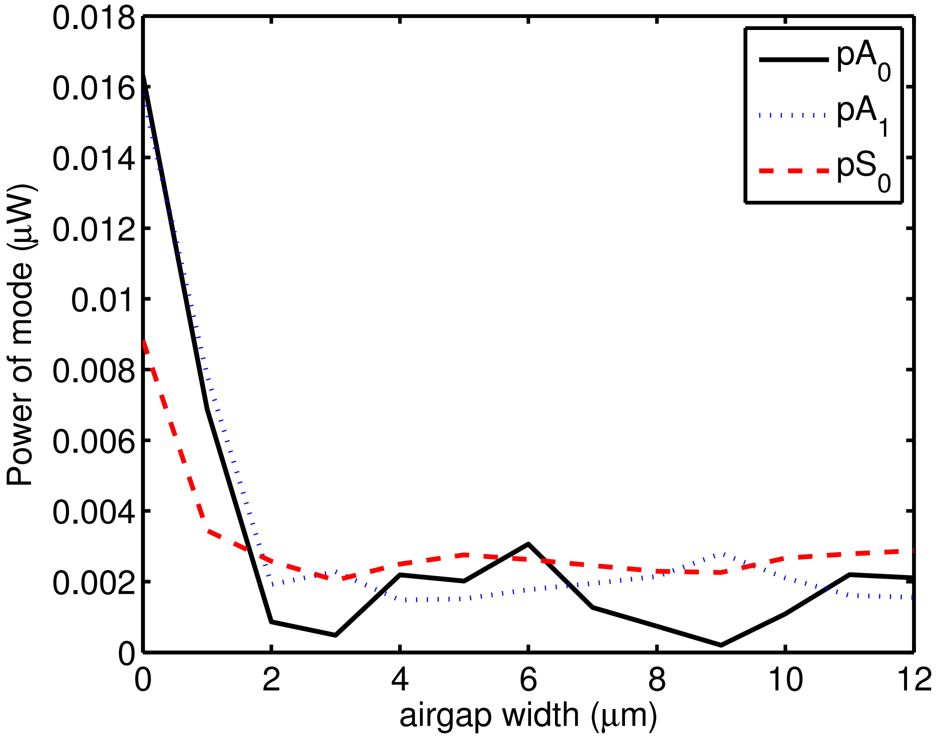

Figure 5.20: Power of Lamb modes in the passive region at 1.3 GHz for different airgap width.

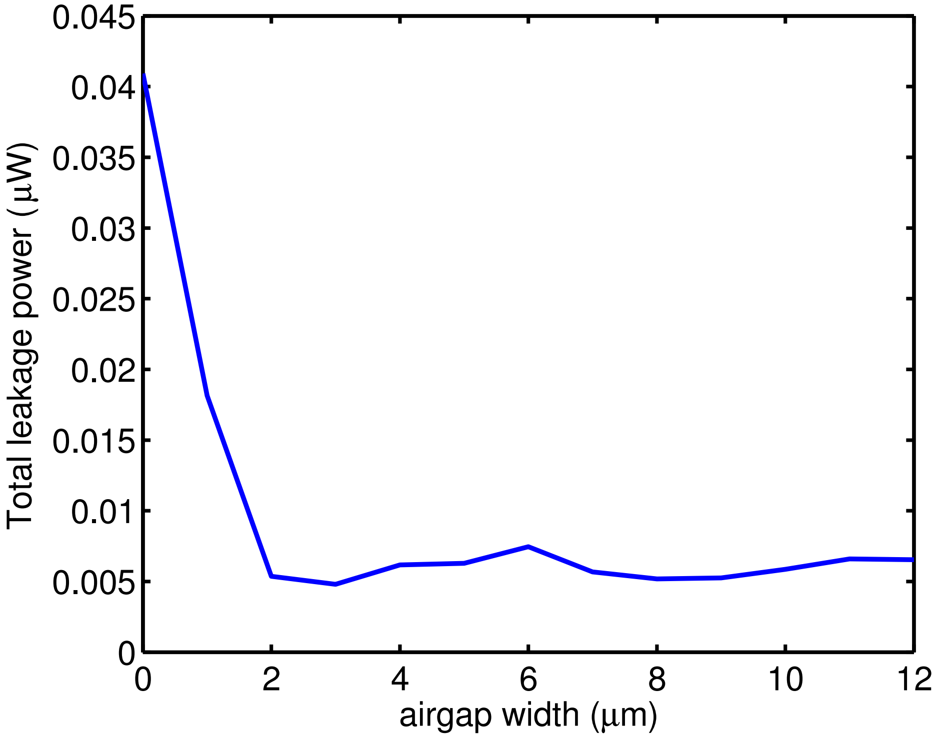

Figure 5.21: The total leakage power of Lamb modes in the passive region at 1.3 GHz for different airgap width.

spurious modes power in both active region and passive region decreases quickly as the width increases from 0 μm to 2 μm. When the width is larger than 2 μm, the power shows a quasi-periodic behavior, and the difference for different width is relatively small. This is in good agreement with results obtained by time domain analysis (shown in Fig. 5.8). Since the excitation source was the same for all cases, reduction in spurious modes power in the active region and leakage power in the passive region means that more power has been stored in the main longitudinal mode within the investigated frequency range. Because the mode power coefficient for the longitudinal mode is not easy to calculate, and it should be the same for all cases, the amplitude of the longitudinal mode at 1.33 GHz was compared for different gap width, shown in Fig. 5.22. It is observed that the amplitude of the longitudinal mode increases quickly as the gap width increases from 0 μm to 2 μm. When the width is larger than 2 μm, the amplitude shows a quasi-periodic behavior, and the difference for different width is relatively small. This result is consistent with the reduction of spurious mode power as shown in Fig. 5.16, Fig. 5.17, Fig. 5.19, and Fig. 5.21. Similar phenomenon was also observed at other frequencies within the investigated frequency range.

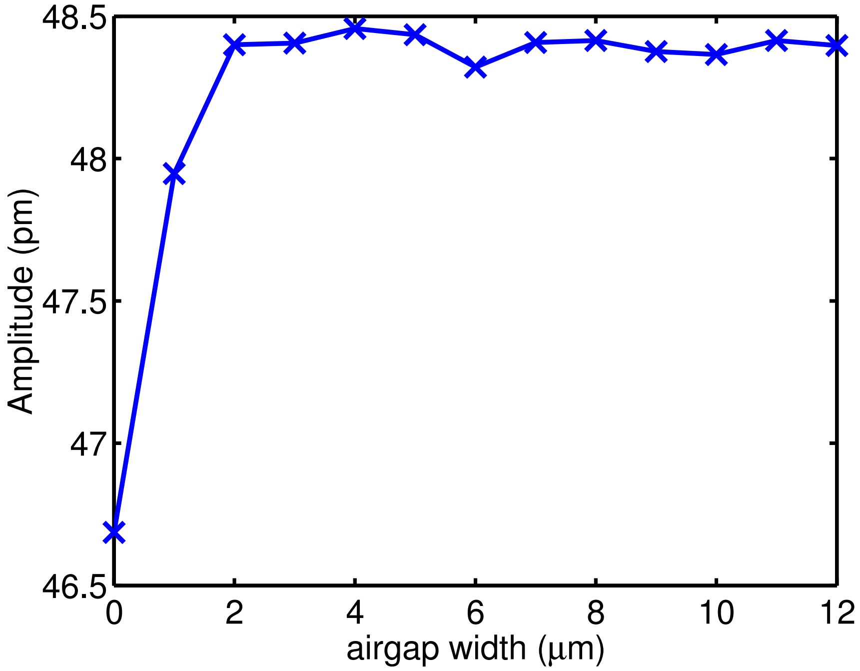

Figure 5.22: Amplitude of the longitudinal mode at 1.33 GHz for different airgap width.

5.3.2 Power of the spurious modes for different airgap depth

Following the same procedure, the effect of the airgap depth on the spurious wave suppression is examined in this section. The dimension of the structure was the same as the one used in the previous subsection. The airgap width was fixed to 8 μm as shown in

Fig. 5.23. The depth of the airgap was varied from 0 μm to 0.6 μm with a step of 0.1 μm. A Gaussian pulse with maximum frequency of 2 GHz was used as the excitation source for all cases. The power of the propagating Lamb modes in the active region and the passive region was compared for different airgap depth. Due to the symmetry of the structure, only the modes propagating in the right passive region were analyzed. The amplitude of the longitudinal mode was also compared for different airgap depth.

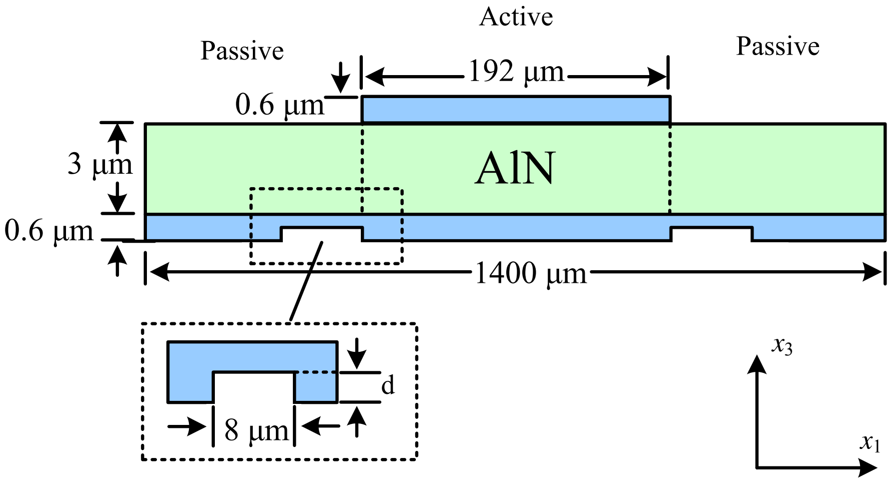

Figure 5.23: The FBAR resonator with airgap on the bottom electrode for frequency domain analysis on the effect of the airgap depth.

Figure 5.24 shows the power of the propagating Lamb modes in the active region at 1.33 GHz, which is near the antiresonance frequency. It is observed that the power of mode A_0, S_0, and S_1 decreases quickly from the depth of 0 μm (without airgap) to the depth of 0.6 μm. However, the power of mode A_1 increases as the depth increases from 0 μm to 0.1 μm, then it decreases as the depth increases. It can also be observed that the power of mode S_0 and S_1 is larger than that of mode A_0 and A_1 with the depth larger than 0.2 μm. Similar phenomenon was also observed at other frequencies within the investigated frequency range. For example, the power of propagating Lamb modes in the active region at 1.3 GHz for different airgap depth is plotted in Fig. 5.25.

The total power of the propagating Lamb modes in the active region at 1.33 GHz is also shown in Fig. 5.26. It is observed that the total power decreases quickly from the depth of 0 μm (without airgap) to the depth of 0.6 μm. Similar phenomenon was also observed at other frequencies within the investigated frequency range. For example, the total power of the propagating Lamb modes in the active region at 1.3 GHz is plotted in Fig. 5.27.

Figure 5.28 shows the power of the propagating Lamb modes for different airgap depth in the passive region at 1.33 GHz, which is near the antiresonance frequency. It is observed that the power of mode pA_0 and pA_1 decreases quickly from the depth of 0 μm (without

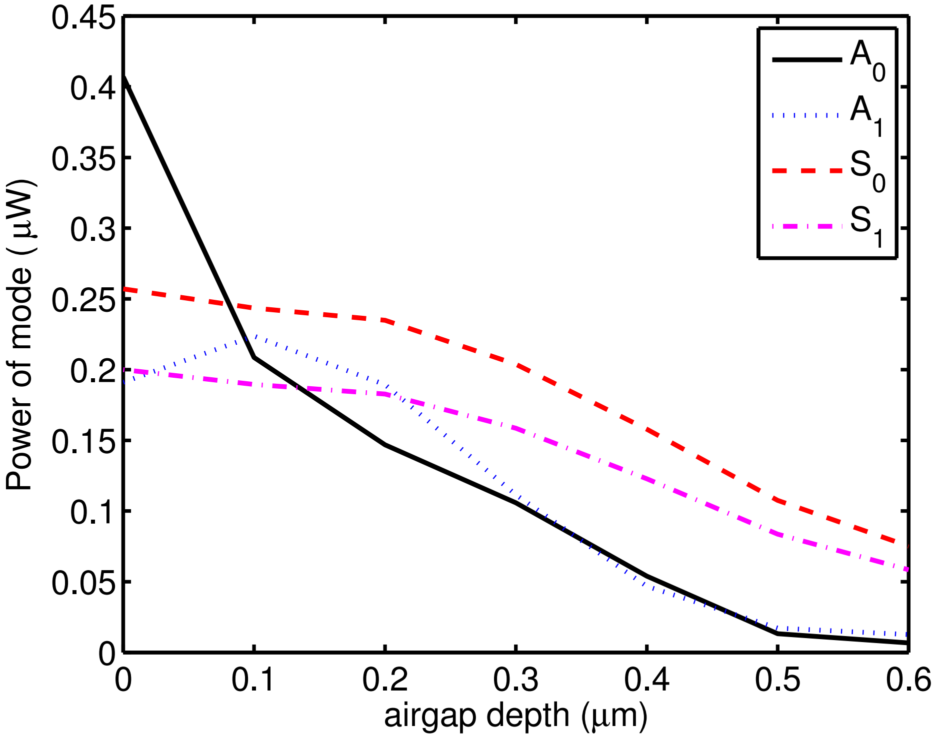

Figure 5.24: Power of Lamb modes in the active region at 1.33 GHz for different airgap depth.

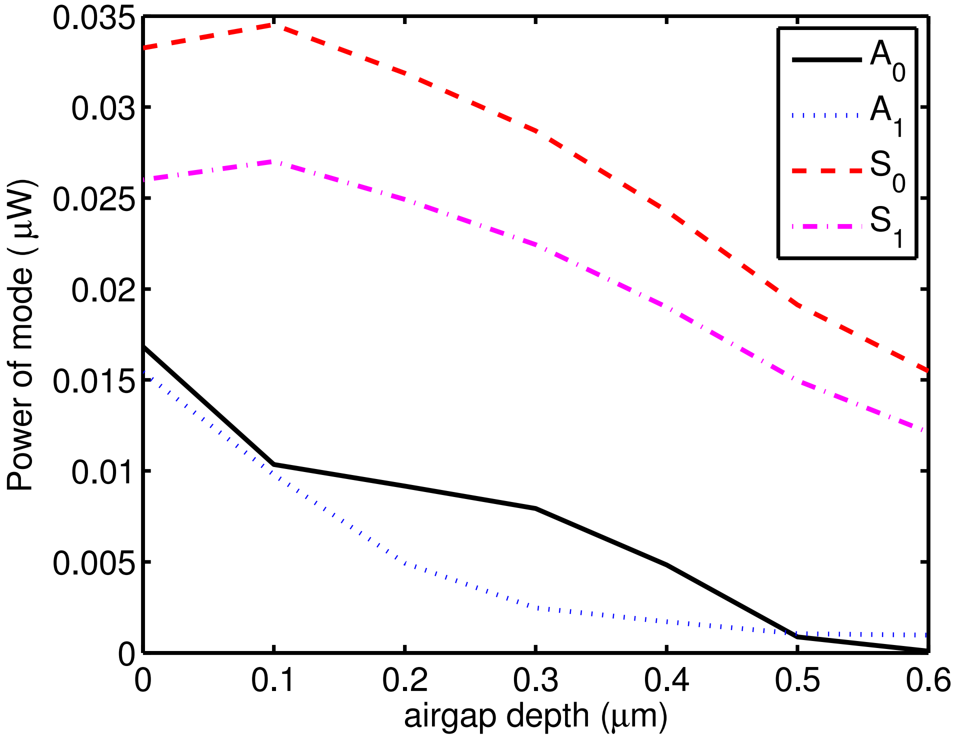

Figure 5.25: Power of Lamb modes in the active region at 1.3 GHz for different airgap depth.

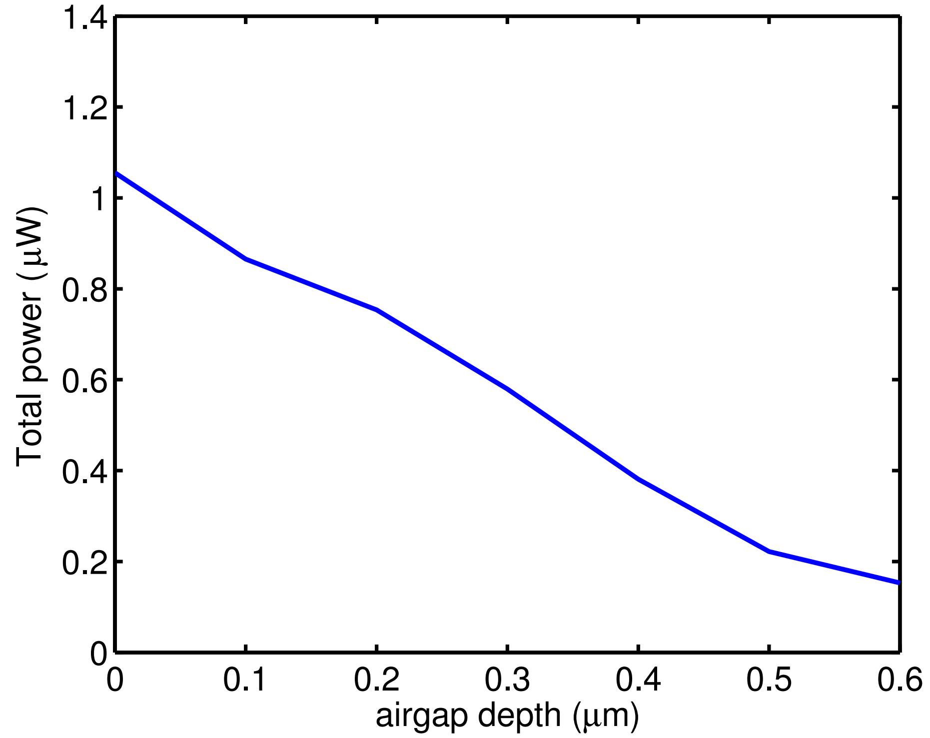

Figure 5.26: The total power of Lamb modes in the active region at 1.33 GHz for different airgap depth.

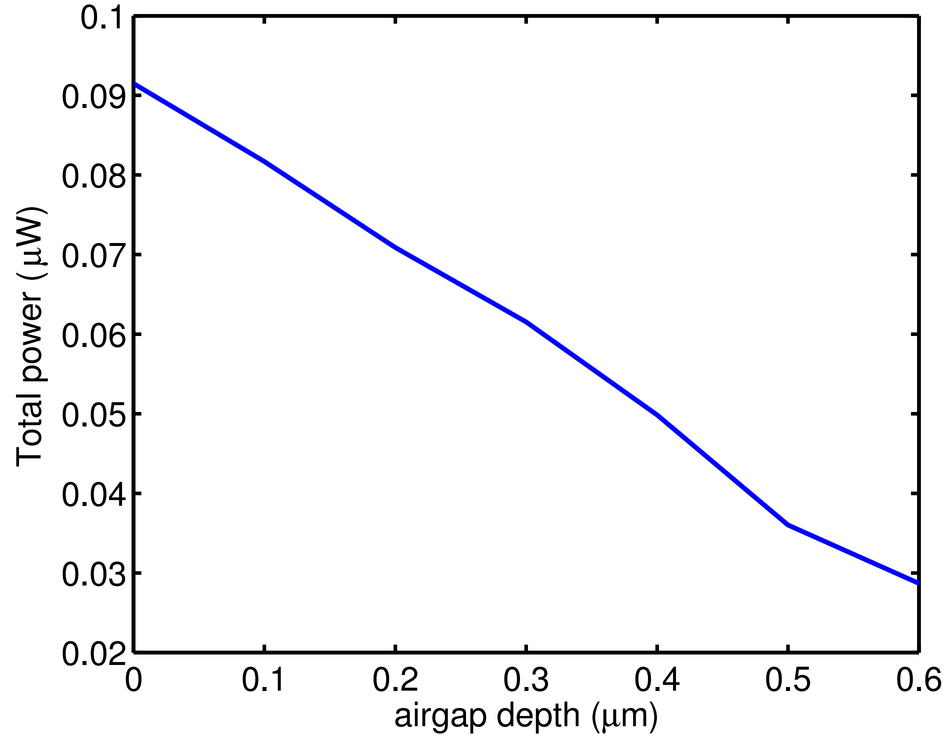

Figure 5.27: The total power of Lamb modes in the active region at 1.3 GHz for different airgap depth.

airgap) to the depth of 0.6 μm. On the other hand, the power of mode pS_0 increases quickly from the depth of 0 μm (without airgap) to the depth of 0.6 μm. It can also be observed that the power of mode pS_0 is much smaller than that of mode pA_0 and pA_1 when the depth is less than 0.4 μm, and it is close to that of mode pA_0 and pA_1 when the depth is larger than 0.4 μm. This has resulted in quick reduction of total leakage power from the depth of 0 μm to the depth of 0.6 μm, which is shown in Fig. 5.29. Similar phenomenon was also observed at other frequencies within the investigated frequency range, with the exception at 1.3 GHz. At 1.3 GHz, similar to the mode pA_0 and pA_1, the power of mode pS_0 decreases quickly as the depth increases from 0 μm to 0.6 μm, shown in Fig. 5.30. For the total leakage power, the same phenomenon is observed for the whole investigated frequency range. For example, the total leakage power at 1.3 GHz, which is near the resonance frequency, is shown in Fig. 5.31.

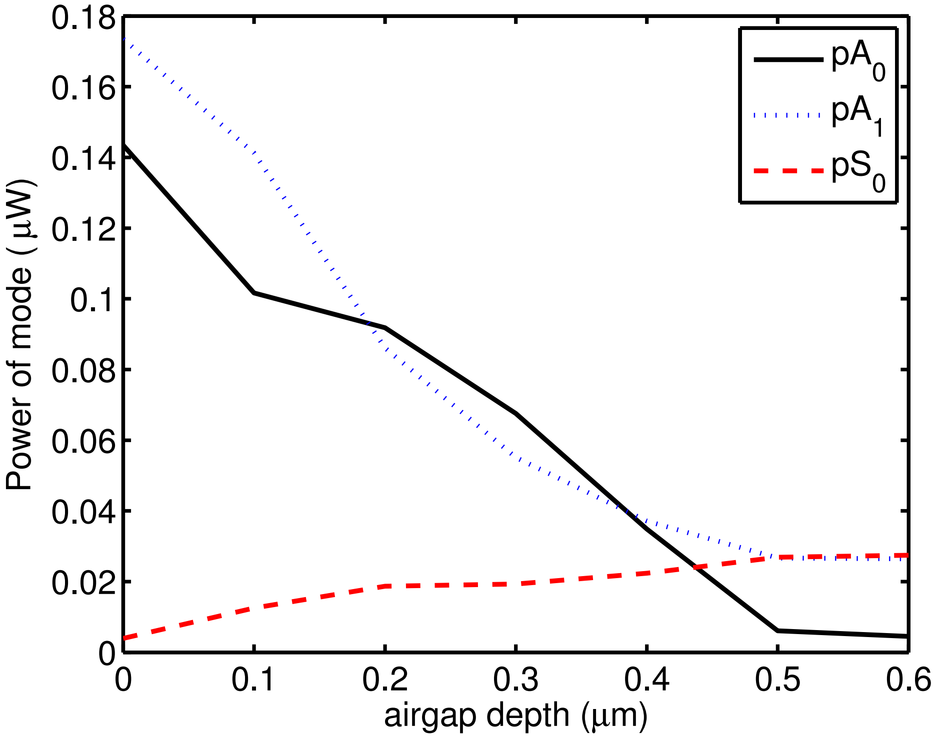

Figure 5.28: Power of Lamb modes in the passive region at 1.33 GHz for different airgap depth.

From Fig. 5.26, Fig. 5.27, Fig. 5.29, and Fig. 5.31, it is observed that the total spurious modes power in both active region and passive region decreases quickly as the depth increases from 0 μm to 0.6 μm. The difference between the depth of 0.5 μm and the depth of 0.6 μm is relatively small. This is in good agreement with results obtained by time domain analysis (shown in Fig. 5.11). Since the excitation source was the same for all cases, reduction in spurious modes power in the active region and leakage power

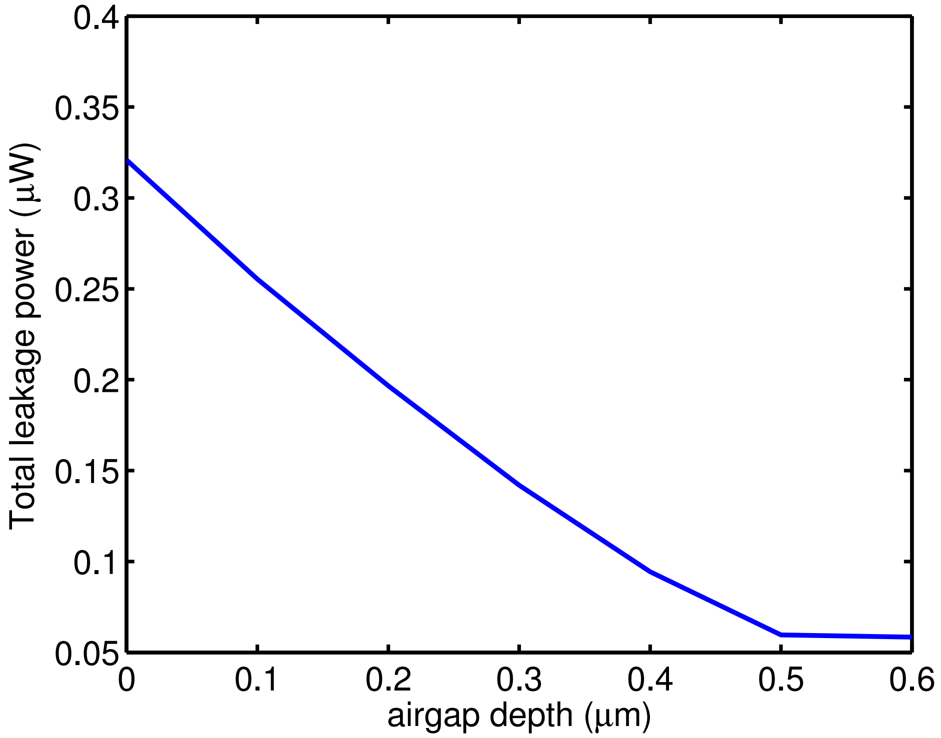

Figure 5.29: The total leakage power of Lamb modes in the passive region at 1.33 GHz for different airgap depth.

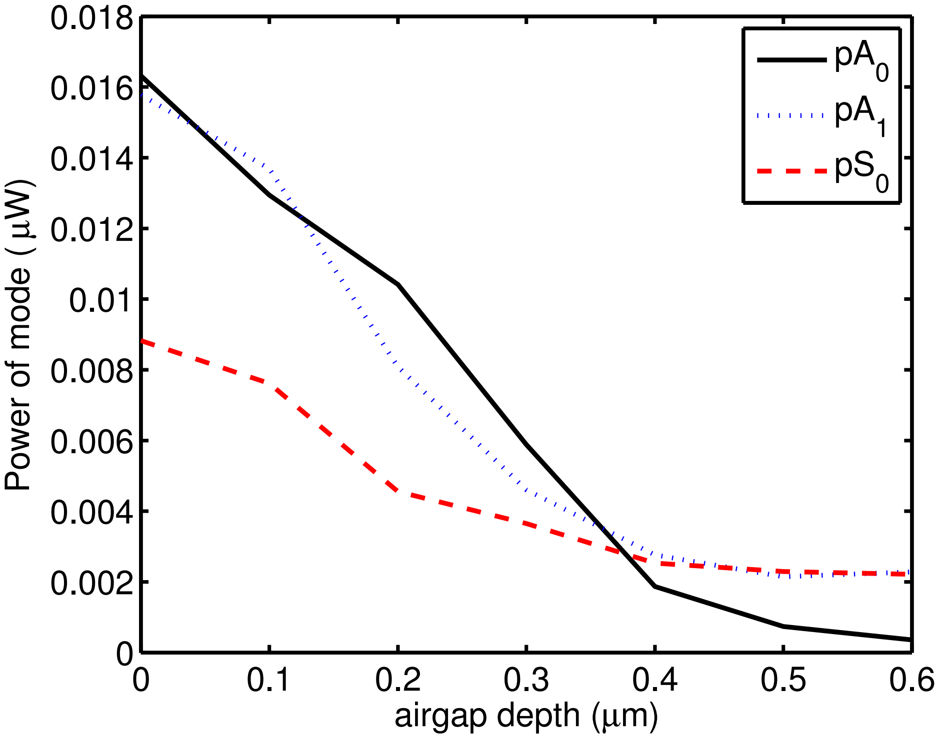

Figure 5.30: Power of Lamb modes in the passive region at 1.3 GHz for different airgap depth.

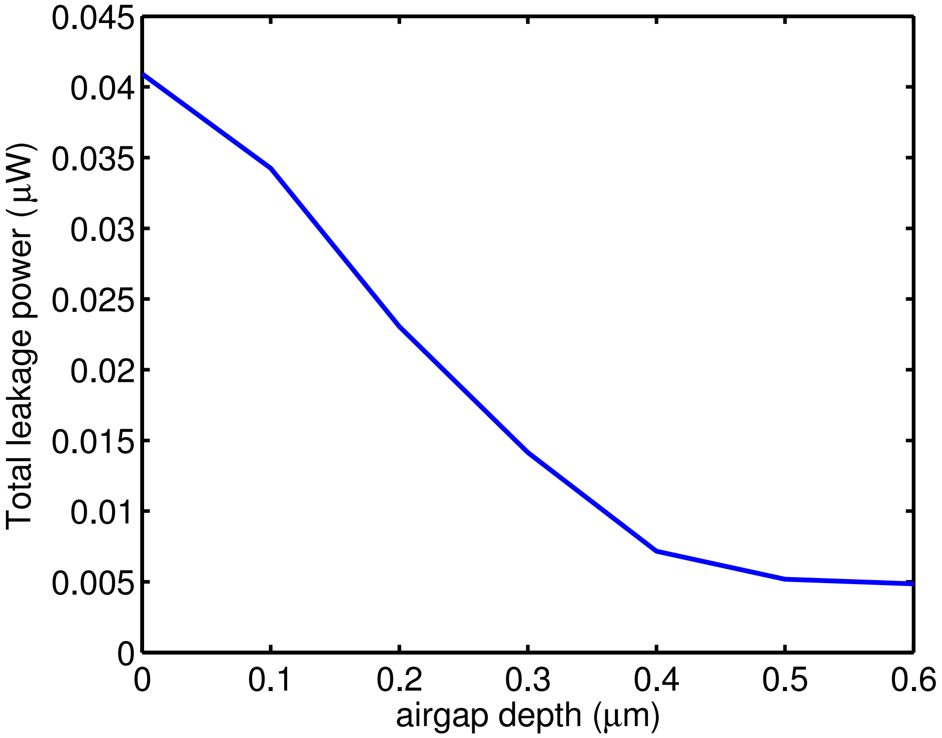

Figure 5.31: The total leakage power of Lamb modes in the passive region at 1.3 GHz for different airgap depth.

in the passive region means that more power has been stored in the main longitudinal mode within the investigated frequency range. Because the mode power coefficient for the longitudinal mode is not easy to calculate, and it should be the same for all cases, the amplitude of the longitudinal mode at 1.33 GHz was compared for different airgap depth, shown in Fig. 5.32. It is observed that the amplitude of the longitudinal mode increases as the gap depth increases from 0 μm to 0.6 μm. This result is consistent with the reduction of spurious mode power as shown in Fig. 5.26, Fig. 5.27, Fig. 5.29, and Fig. 5.31. Similar phenomenon was also observed at other frequencies within the investigated frequency range.

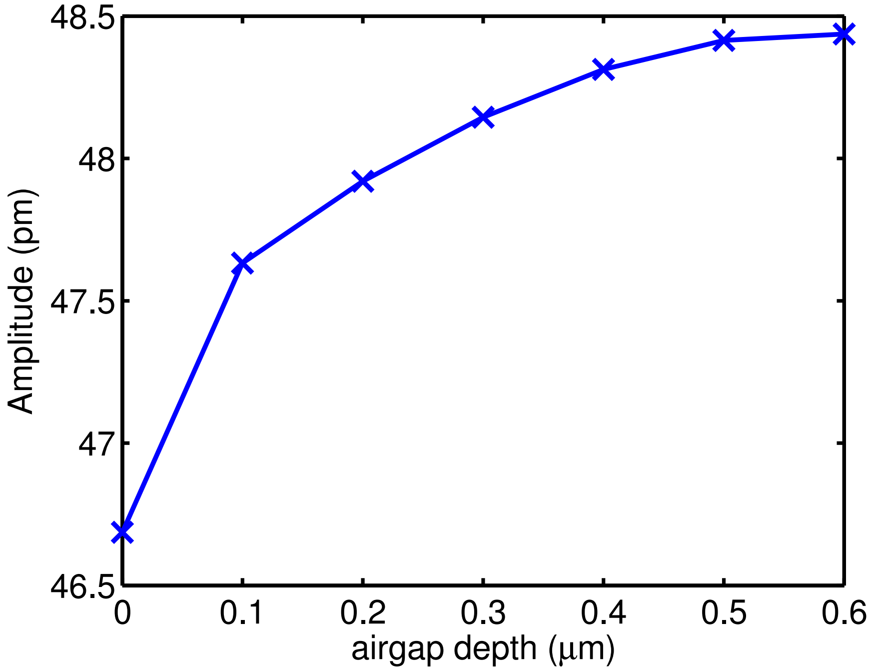

Figure 5.32: Amplitude of the longitudinal mode at 1.33 GHz for different airgap depth.

5.3.3 Power of the spurious modes at different frequency

In this section, the power of the spurious modes at different frequency is investigated. The dimension of the structure was the same as the one used in the previous two subsections. The airgap width was fixed to 3 μm and the depth was fixed to 0.5 μm. The power of the propagating Lamb modes was compared at different frequency in both the active region and the passive region. Due to the symmetry of the structure, only the modes propagating in the right passive region were analyzed. The amplitude of the longitudinal mode was also calculated at different frequency.

Figure 5.33 shows the power of the propagating Lamb modes in the active region at different frequency. It is observed that within the investigated frequency range the spurious modes power of the proposed FBAR resonator is lower than that of the one without the airgap on the bottom electrode. It is also observed that the power of mode S_0 and S_1 is generally higher than that of mode A_0 and A_1 (shown in Fig. 5.34). To get a clear view on whether the introduction of the frame-like airgap on the bottom electrode can suppress the spurious wave generation or not, the total power of the spurious modes was also compared with the one without airgap on the bottom electrode as shown in Fig. 5.35. It can be observed that the proposed FBAR resonator can reduce the total power by more than 4 dB throughout the investigated frequency range.

Figure 5.36 shows the power of the propagating Lamb modes in the passive region at different frequency. It is observed that the power of the spurious mode pA_0 and pA_1

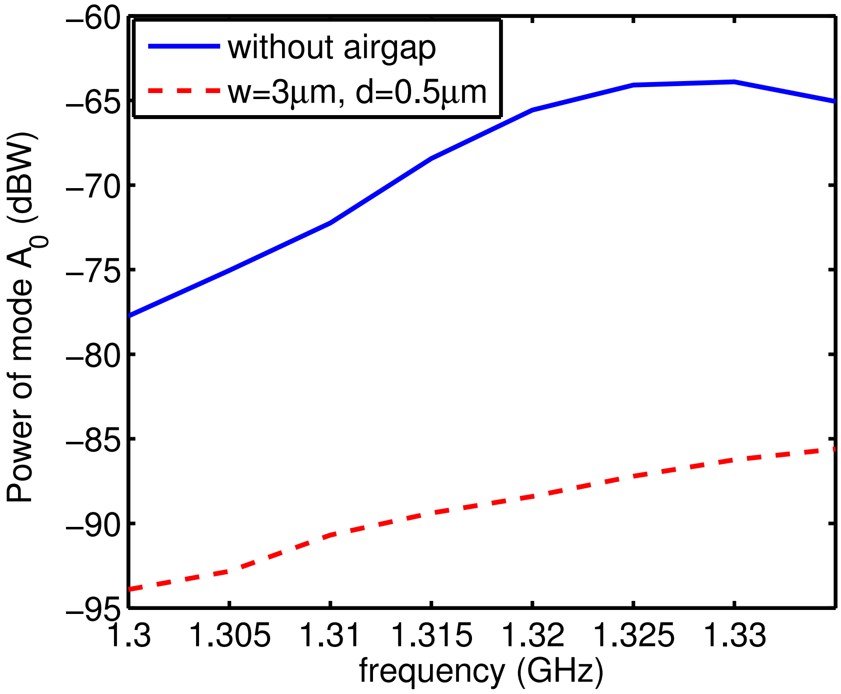
−60
−65
−70
−75
−80
−85
−90
−95
Power of mode A_0 (dBW)
1.3
1.305
1.31
1.315
1.32
1.325
1.33
frequency (GHz)
without airgap
w=3µm, d=0.5µm

(a)

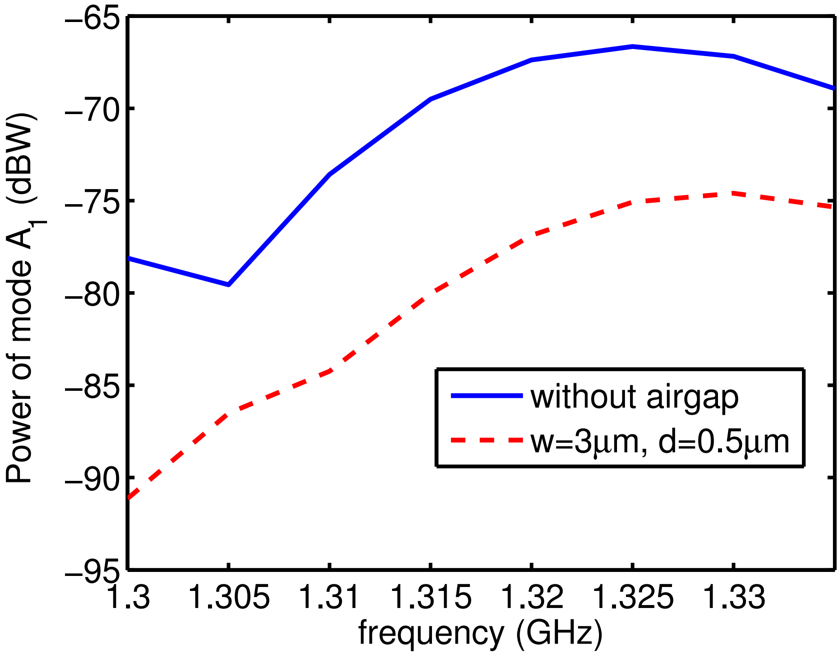
−65
−70
−75
−80
−85
−90
−95
Power of mode A_1 (dBW)
1.3
1.305
1.31
1.315
1.32
1.325
1.33
frequency (GHz)
without airgap
w=3µm, d=0.5µm

(b)

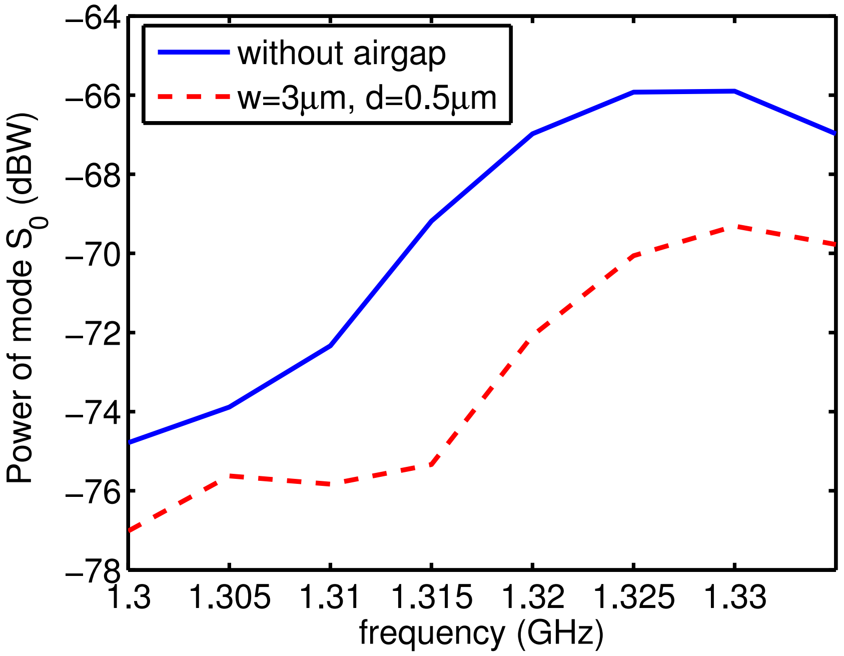

(c)

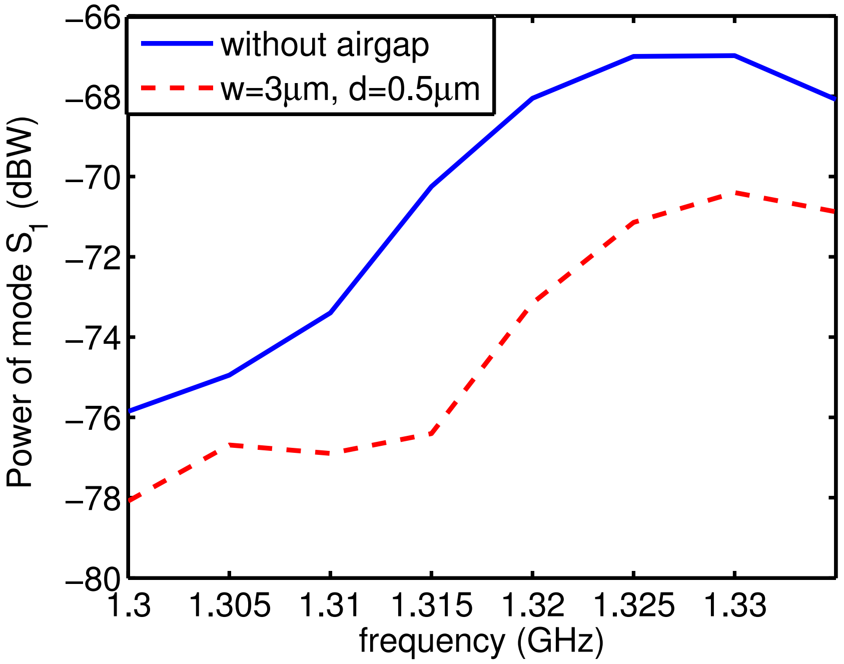

(d)

Figure 5.33: Power of Lamb modes in the active region of FBAR resonator with and without airgap on the bottom electrode at different frequency (a) mode A_0, (b) mode A_1, (c) mode S_0, and (d) mode S_1.

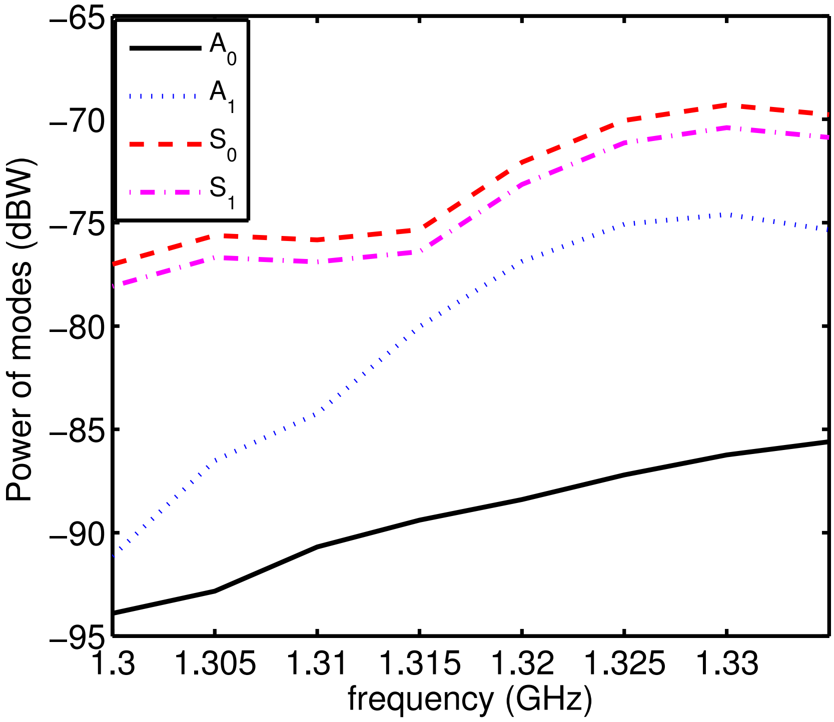

Figure 5.34: Power of Lamb modes in the active region of FBAR resonator with an airgap (w = $3\mu m$, d = $0.5\mu m$) on the bottom electrode at different frequency.

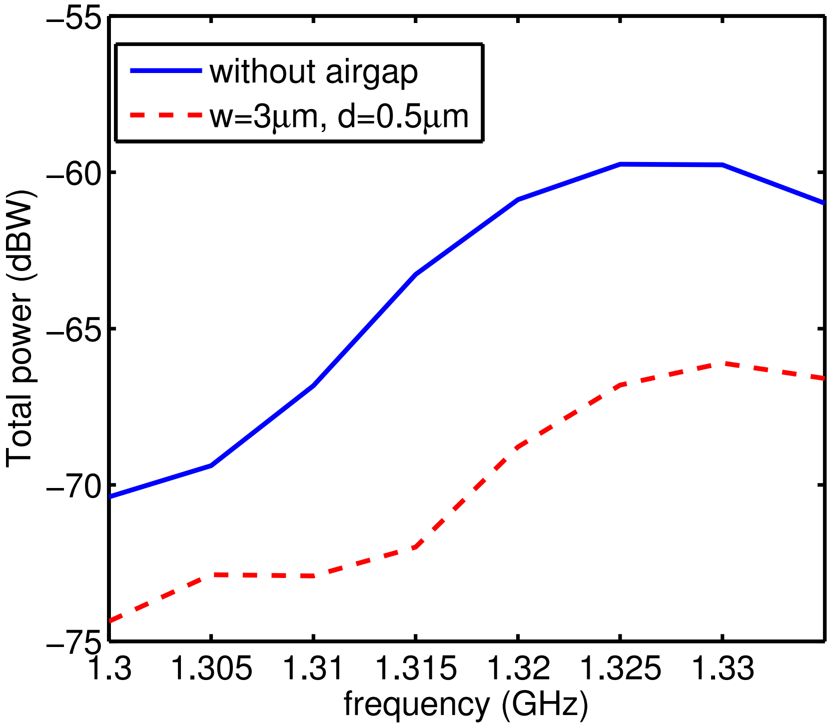

Figure 5.35: Total power of Lamb modes in the active region of FBAR resonator with and without airgap on the bottom electrode.

is lower than that of the one without the airgap on the bottom electrode within the investigated frequency range. However, the power of mode pS_0 is higher than that of the one without frame on the bottom electrode (shown in Fig. 5.36(c)). It is also observed that the power of mode pS_0 is generally higher than that of mode pA_0 and pA_1 as shown in Fig. 5.37. To get a clear view on whether the application of the frame-like airgap on the bottom electrode can suppress the energy leakage or not, the total leakage power is plotted in Fig. 5.38. It can be observed that the proposed FBAR resonator can reduce the total leakage power by more than 6 dB throughout the investigated frequency range.

From Fig. 5.35 and Fig. 5.38, it is observed that both the total power of the spurious modes within the active region, and the total leakage power of the spurious modes in the passive region are significantly reduced by etching an airgap on the bottom electrode of FBAR. Since the same input power was applied to these two structures, the reduction of the power of spurious modes in the active region and the leakage power in the passive region means that more power has been stored in the main longitudinal mode within the investigated frequency range. Because the mode power coefficient for the longitudinal mode is not easy to calculate, and it should be the same for these two structures, only the amplitude of the longitudinal mode is plotted in Fig. 5.39. It is observed that the amplitude of the longitudinal mode is generally larger than that of the one without airgap on the bottom electrode. This result is consistent with the reduction of spurious mode power as shown in Fig. 5.35 and Fig. 5.38.

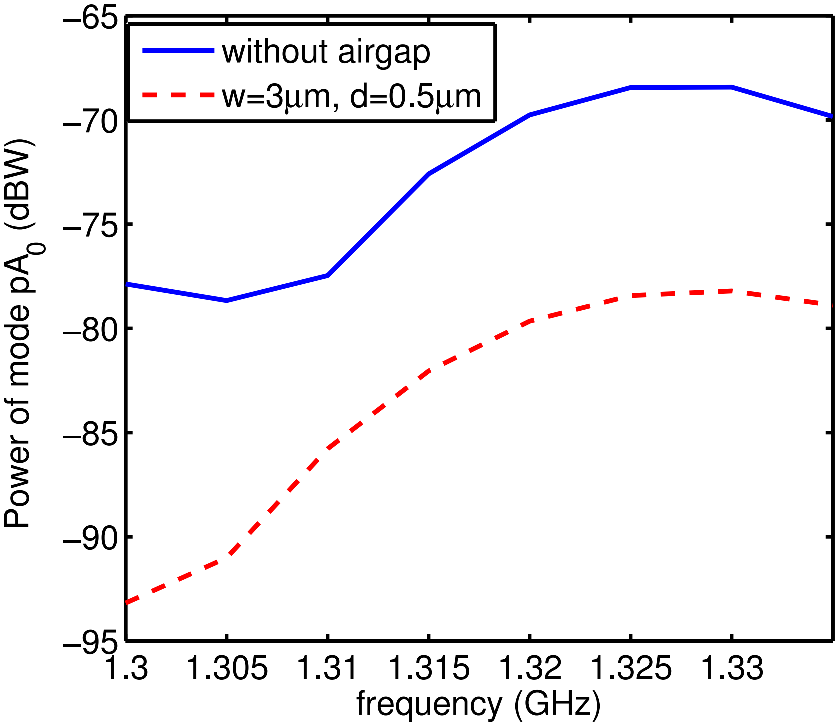
−65
−70
−75
−80
−85
−90
−95
1.3
1.305
1.31
1.315
1.32
1.325
1.33
frequency (GHz)
Power of mode pA_0 (dBW)
without airgap
w=3μm, d=0.5μm

(a)

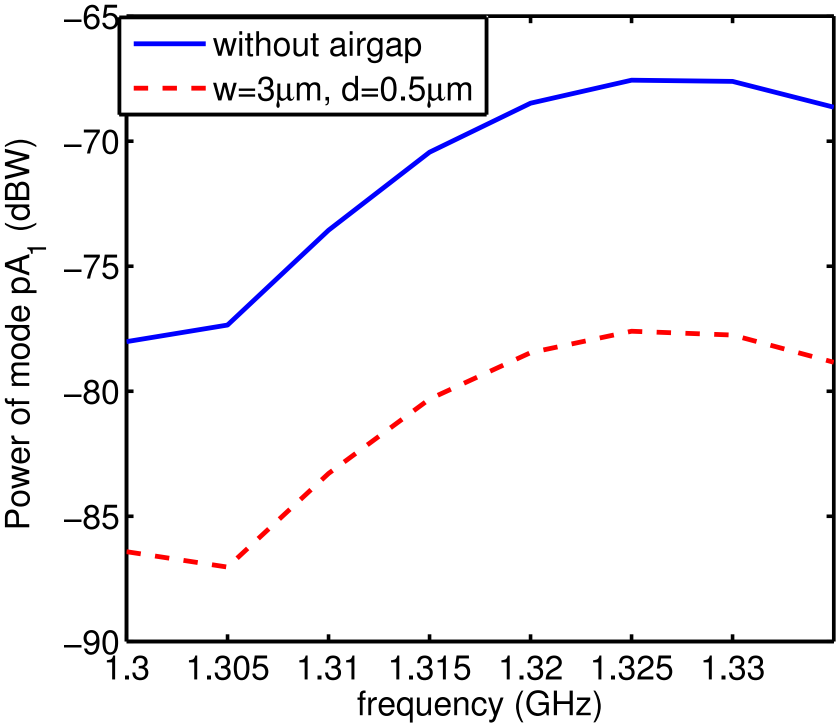
−65
−70
−75
−80
−85
−90
1.3
1.305
1.31
1.315
1.32
1.325
1.33
frequency (GHz)
Power of mode pA_1 (dBW)
without airgap
w=3μm, d=0.5μm

(b)

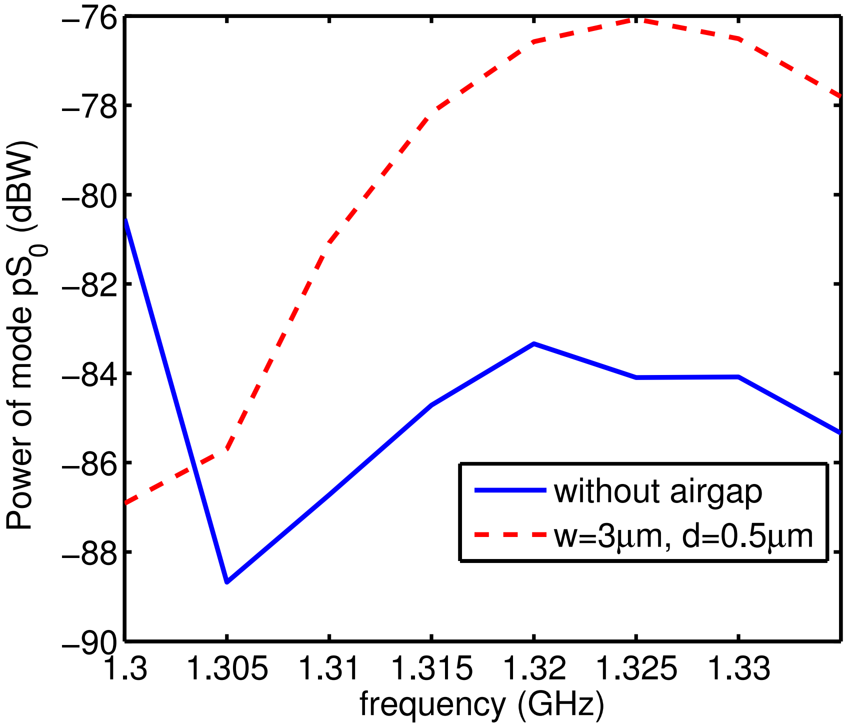

(c)

Figure 5.36: Power of Lamb modes in the passive region of FBAR resonator with and without airgap on the bottom electrode at different frequency (a) mode pA_0, (b) mode pA_1, and (c) mode pS_0.

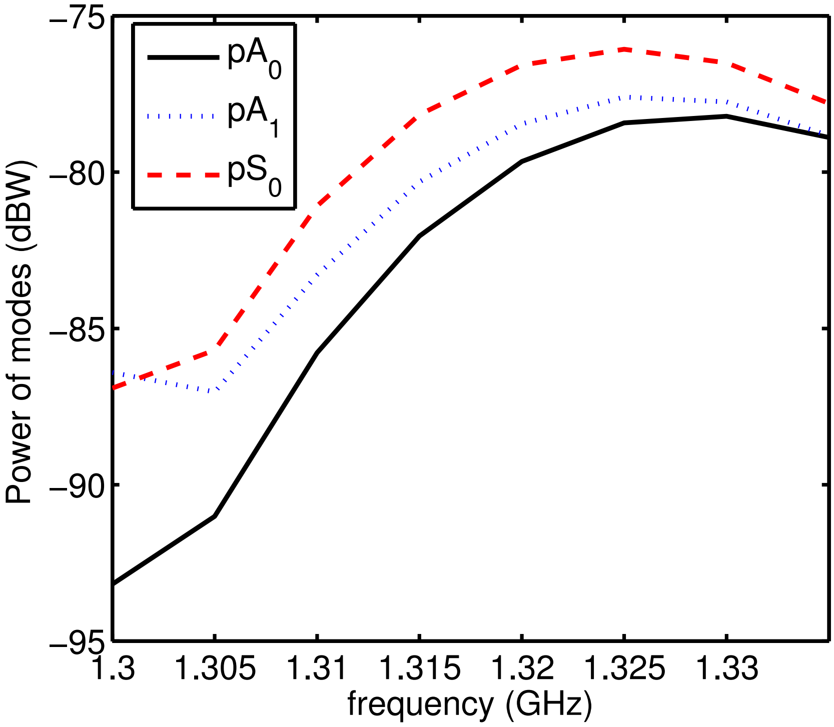

Figure 5.37: Power of Lamb modes in the passive region of FBAR resonator with an airgap (w = $3\mu m$, d = $0.5\mu m$) on the bottom electrode at different frequency.

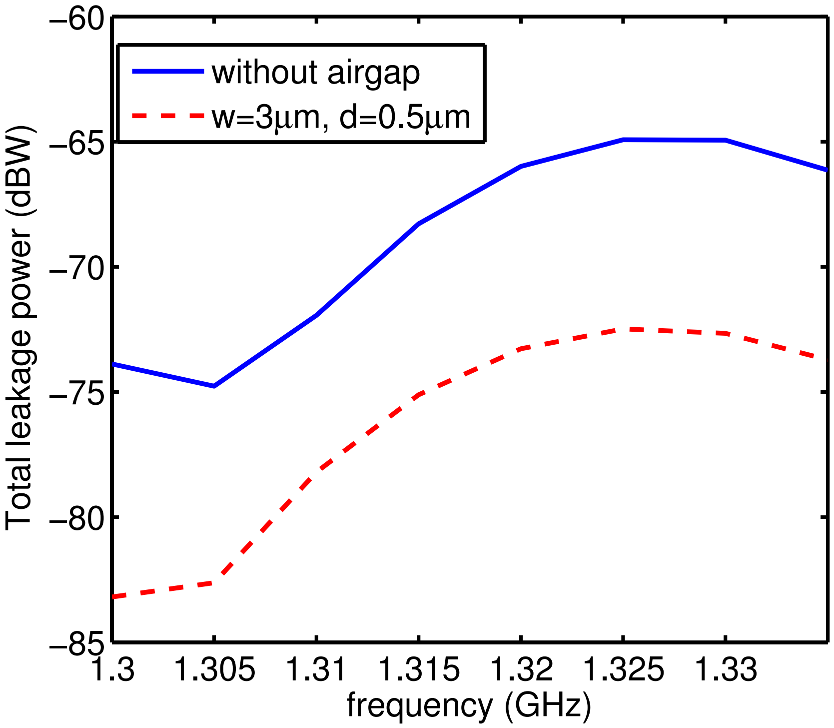

Figure 5.38: Total leakage power of Lamb modes in the passive region of FBAR resonator with and without airgap on the bottom electrode.

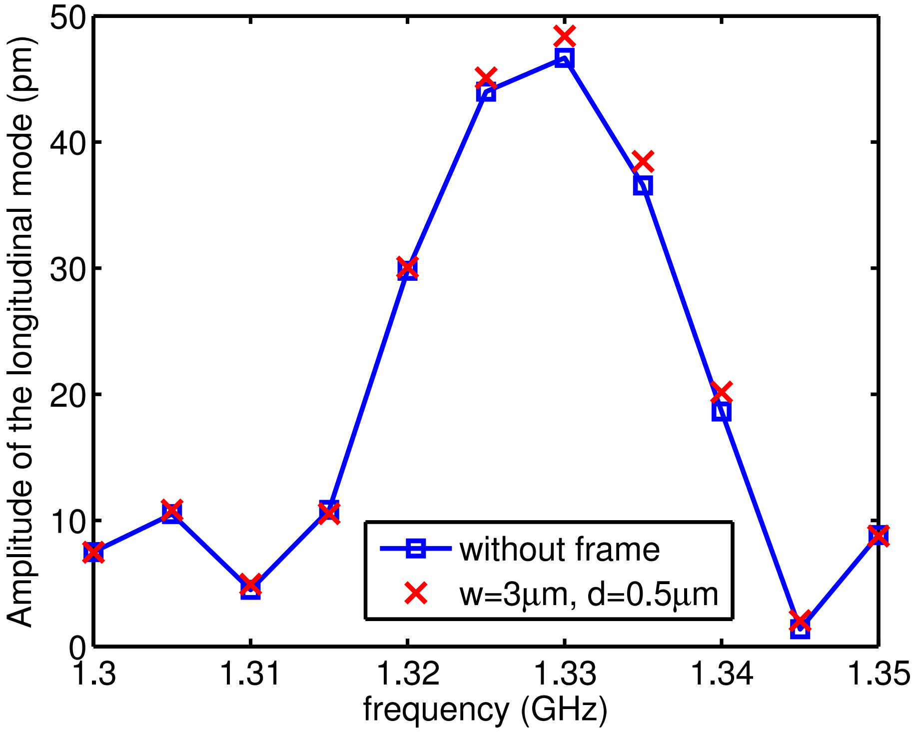

Figure 5.39: Amplitude of the longitudinal mode for FBAR resonator with and without airgap on the bottom electrode at different frequency.

5.4 Discussion

A free-standing bulk acoustic resonator (FBAR) with airgap on bottom electrode was proposed to suppress the spurious waves in this section. It was observed in time domain that, with proper width and depth of the airgap, the amplitude of the ripples of the proposed FBAR resonator in both the active region and the passive region was significantly reduced. By introducing an airgap on the bottom electrode, the impedance difference between the active region and the peripheral region is increased. Thus, more energy has been trapped in the active region, which is consistent with the scattering analysis results obtained in chapter 4. Besides, the peripheral region with an airgap on the bottom electrode has a higher cut-off frequency than the active region. Due to its type II dispersion characteristic, for the fundamental thickness extensional mode, the corresponding wavenumber in the peripheral region is real, which satisfies the continuity conditions. Therefore, less spurious waves are excited. More detailed analysis was carried out in the frequency domain. The frequency domain investigation has confirmed that the power of each propagating Lamb mode in the active region was reduced when the frame-like airgap was introduced on the bottom electrode. Consequently, the total power of the spurious modes in the active region was reduced by the application of airgap on the bottom electrode. However, not all the leakage power of the spurious modes in the passive region was reduced. The leakage power of mode pA_0 and pA_1 was reduced, while the leakage power of mode pS_0 was increased. Fortunately, the reduction of the power of mode pA_0 and pA_1 was larger than the increase of the power of mode pS_0. Thus, the total leakage power of the Lamb modes in the passive region was reduced with the application of airgap on the bottom electrode. The amplitude of the longitudinal mode, or the thickness extensional mode (the mode utilized in the FBAR resonator), was generally larger than that of the one without airgap on the bottom electrode. Therefore, it is confirmed that with an airgap on the bottom electrode, the excitation of the spurious modes in the active region can be suppressed, and the leaking of energy in the passive region can also be reduced. Consequently, the quality factor of the resonator is enhanced.

Chapter 6

Conclusion and outlook

Several achievements on improving the analysis and design of film bulk acoustic resonator (FBAR) can be claimed by this study:

The finite-difference time-domain (FDTD) scheme was developed in chapter 3 to model the FBAR resonator. The partial derivatives of the equations of motion and the quasi-static Maxwell's equations were discretized to centered finite differences. The free surface boundary condition was applied to the interface between the medium and air. At the interface between different materials, the material properties such as the elastic stiffness constants and the material mass density were averaged to ensure the stability under Courant condition. A wideband Gaussian pulse was applied as the excitation source, and the particle velocities were calculated and recorded. These data were processed by 2D FFT method to get the dispersion curve of the Rayleigh-Lamb modes propagating in the FBAR resonator. Compared with the dispersion curve obtained by the effective acoustic impedance, it was confirmed that the FDTD algorithm and the 2D FFT method can efficiently investigate the effects of various waves excited inside FBAR devices.

Wave scattering analysis for multimode excitation was derived in chapter 4. The theoretical background of the new scheme was presented. To validate the proposed scheme, the reflection of simultaneously excited antisymmetric Lamb wave modes at the free edge of a steel plate was simulated using the FDTD method. By using the mode power coefficients, the power of the Lamb modes was determined from the displacements on the surface of the plate. The mode conversion coefficients obtained were in good agreement with the one calculated by taking multiple measurements with single Lamb wave mode excitation using the finite element method (FEM). The proposed scheme was then applied to two generic free-standing bulk acoustic resonator (FBAR) structures. From the results of these two structures, it was observed that the structure with symmetric electrodes has less energy leaked into the passive region. The proposed scheme can be used to enhance the performance of FBAR devices by modifying their boundaries. It also provides a simple way to detect various defects simultaneously in nondestructive testing (NDT) applications.

Based on the scattering analysis of the two generic FBAR structures in chapter 4, a new FBAR resonator with frame-like airgap on bottom electrode was proposed to suppress the spurious modes and improve the quality factor in chapter 5. Both time domain and frequency domain analysis were carried out to investigate the spurious waves in the proposed structure. From both time domain and frequency domain results, it was observed that with an airgap on the bottom electrode the excitation of spurious modes in the active region was suppressed, and the energy leaked into the passive region was also reduced. Therefore, the proposed structure can reduce the ripples of its impedance and enhance its quality factor as well.

This dissertation provides the basis for the development of FBAR resonator model using the finite-difference time-domain method and the multimode wave scattering analysis. Some future work may be conducted, such as:

1) Absorbing boundary conditions, such as perfectly matched layer (PML), may be developed to emulate the infinite region or the acoustic wave absorbers. With PML added to the outer boundary, the dimension of the model can be reduced. Consequently, the memory size and the simulation time can be reduced.

2) Parallelization of the FDTD model can be conducted to further reduce the simulation time. An almost linear speed-up with the number of processors can be achieved.

3) The proposed FDTD algorithm can be extended from 2D to 3D. Suppression of spurious modes was achieved by means of transversal cuts of the layered FBAR structure [18]. The 3D model combined with the wave scattering analysis algorithm proposed by this study can be used to investigate the field components of such kind of structure and find out the underlying mechanisms.

4) A lateral transmission line model similar to Mason model can be set up regarding the lateral dimensions of the different resonator sections. Each resonator section can be seen as a transmission line for the propagating modes. Each propagating waveguide mode can be seen as a port, and the ports at the interface of two lateral resonator sections are connected over the scattering matrix. The lateral transmission line model covering the mechanical coupling and effective scattering of modes on the borders can be applied to design the lateral boundaries of resonators.

Bibliography

[1] E. L. Adler, "Matrix Methods Applied to Acoustic Waves in Multilayers," *IEEE Transactions on Ultrasonics, Ferroelectrics and Frequency Control*, vol. 37, no. 6, pp. 485–490, 1990.

[2] R. Aigner, J. Ella, H.-J. Timme, L. Elbrecht, W. Nessler, and S. Marksteiner, "Advancement of MEMS into RF-filter applications," *IEEE International Electron Devices Meeting*, pp. 897–900, 2002.

[3] R. Aigner, "MEMS in RF Filter Applications : Thin-film Bulk Acoustic Wave Technology," *Sensors Update*, vol. 12, no. 1, pp. 175–210, 2003.

[4] R. Aigner, J. Kaitila, J. Ella, L. Elbrecht, W. Nessler, M. Handtmann, T.-R. Herzog, and S. Marksteiner, "Bulk-acoustic-wave filters: performance optimization and volume manufacturing," *IEEE MTT-S International Microwave Symposium Digest*, vol. 3, pp. 2001–2004, 2003.

[5] R. Aigner, "SAW and BAW technologies for RF filter applications: A review of the relative strengths and weaknesses," *IEEE Ultrasonics Symposium*, pp. 582–589, Nov. 2008.

[6] R. Aigner and L. Elbrecht, " Design and Fabrication of BAW Devices," in *RF Bulk Acoustic Wave Filters For Communications*, K. Hashimoto, Ed., Boston: Artech House, 2009.

[7] D. N. Alleyne and P. Cawley, "A 2-dimensional Fourier transform method for the quantitative measurement of Lamb modes," *IEEE Ultrasonics Symposium*, pp. 1143–1146, 1990.

[8] D. Alleyne and P. Cawley, "A two dimensional Fourier transform method for the measurement of propagating multimode signals," *Journal of the Acoustical Society of America*, vol. 89, pp. 1159–1168, 1991.

[9] D. N. Alleyne and P. Cawley, "The interaction of Lamb waves with defects," *IEEE Transactions on Ultrasonics, Ferroelectrics and Frequency Control*, vol. 39, pp. 381–397, Jan. 1992.

[10] B. Auld, *Acoustic fields and waves in solids*, 2nd ed., Vol. I, Malabar, FL: Krieger Publishing, 1990.

[11] B. Auld, *Acoustic fields and waves in solids*, 2nd ed., Vol. II, Malabar, FL: Krieger Publishing, 1990.

[12] M. J. Avioli, " Lamb wave inspection for large cracks in centrifugally cast stainless steel," *EPRI report RP*, pp. 2405–2423, Georgetown University, 1988.

[13] Y. Bar-Cohen, and A. K. Mal, " Characterization of composite laminates using combined LLW and PBS methods," in *Review of Progress in Quantitative Nondestructive Evaluation*, (10b), D.O. Thompson, and D. E. Chimenti, Ed., Plenum Press, N. Y., 1555-1560, 1991.

[14] P. Bauerschmidt, R. Lerch, J. Machui, W. Ruile, and G. Visintini, "Reflection and transmission coefficients of SAW in a periodic grating computed by finite element analysis," *IEEE Ultrasonics Symposium*, pp. 421–423, 1990.

[15] F. Bi and B. Barber, "Improve MBVD Model to Consider Frequency Dependent Loss for BAW Filter Design," *IEEE Ultrasonics Symposium*, pp. 1025–1028, Oct. 2007.

[16] F. Z. Bi and B. P. Barber, "Bulk acoustic wave RF technology," *IEEE microwave magazine*, no. October, pp. 65–80, 2008.

[17] J. Blitz, G. Simpson, *Ultrasonic methods of non-destructive testing*, London: Chapman & Hall, 1996.

[18] H. Campanella, " Thin-film bulk acoustic wave resonators C FBAR: Fabrication, heterogeneous integration with CMOS technologies and sensor applications," Ph.D. dissertation, Université de Montpellier II (UM2) and Universitat Autònoma de Barcelona (UAB), 2007.

[19] C. K. Campbell, *Surface acoustic wave devices for mobile and wireless communications*, Application of Modern Acoustics, 1998.

[20] T. Chiba, "Optical Measurement and Numerical Analysis of SAW Propagation at Dispersive Delay Line on Y-Z $LiNbO_3$ substrate," *IEEE Ultrasonics Symposium*, pp. 1718–1721, 2003.

[21] L. Coldren and R. Rosenberg, "Surface-Acoustic-Wave Resonator Filters," *Proceedings of the IEEE*, vol. 67, no. 1, pp. 147–158, 1979.

[22] D. L. Conn, and J. F. Jackson, " In-line ultrasonic inspection of colded rolled strip," *Material Evaluation*, vol. 29, no. 2, 1971.

[23] D. Cushman and J. D. Crawford, "Semiconductor bulk acoustic resonator with suppressed lateral modes," U. S. Patent 6,381,820 B1, May 2002.

[24] N. Dai, A. Vafidis, and E. R. Kanasewich, "Wave propagation in heterogeneous, porous media: a velocity-stress, finite-difference method," *Geophysics*, vol. 60, no. 2, pp. 327–340, Apr. 1995.

[25] F. L. Degertekin and B. T. Khuri-Yakub, "Lamb wave excitation by Hertzian contacts with applications in NDE," *IEEE Transactions on Ultrasonics, Ferroelectrics and Frequency Control*, vol. 44, no. 4, pp. 769 –779, 1997.

[26] G. G. Fattinger and P. T. Tikka, "Modified Mach–Zehnder laser interferometer for probing bulk acoustic waves," *Applied Physics Letters*, vol. 79, no. 3, pp. 290–292, 2001.

[27] G. G. Fattinger, "BAW resonator design considerations - An overview," *IEEE International Frequency Control Symposium*, pp. 762–767, May 2008.

[28] D. A. Feld, R. Parker, R. Ruby, P. Bradley, and S. Dong, "After 60 years: A new formula for computing quality factor is warranted," *IEEE International Ultrasonics Symposium*, pp. 431–436, Nov. 2008.

[29] A. Gollwitzer, A. Lerner, and G. Fischerauer, "Interferometric Observation of Surface Acoustic Wave Phase Fronts," *IEEE International Frequency Control Symposium*, pp. 424–427, June 2006.

[30] K. F. Graff, *Wave Motion in Elastic Solids*, Dover Publications, 1975.

[31] S. Grondel, C. Paget, C. Delebarre, J. Assaad, and K. Levin, "Design of optimal configuration for generating A_0 Lamb mode in a composite plate using piezoceramic transducers," *Journal of the Acoustical Society of America*, vol. 112, no. 1, pp. 84–90, 2002.

[32] T. W. Grudkowski, J. F. Black, T. M. Reeder, D. E. Cullen, and R. A. Wagner, "Fundamental-mode VHF/UHF minature acoustic resonators and filters on silicon," *Applied Physics Letters*, vol. 37, no. 11, pp. 993–995, 1980.

[33] K.-y. Hashimoto, T. Omori, and M. Yamaguchi, “Extended FEM/SDA Software for Characterising Surface Acoustic Wave Propagation in Multi-Layered Structures,” *IEEE Ultrasonics Symposium*, pp. 711–714, Oct. 2007.

[34] K.-y. Hashimoto, K. Kashiwa, T. Omori, M. Yamaguchi, O. Takano, S. Meguro, and K. Akahane, “A fast scanning laser probe based on Sagnac interferometer for RF surface and bulk acoustic wave devices,” *IEEE MTT-S International Microwave Symposium Digest*, pp. 851–854, June 2008.

[35] K.-y. Hashimoto, Y. Watanabe, M. Akahane, and M. Yamaguchi, “Analysis of acoustic properties of multi-layered structures by means of effective acoustic impedance matrix,” *IEEE Ultrasonics Symposium*, pp. 937–942, 1990.

[36] J. Kaitila, “Review of Wave Propagation in BAW Thin Film Devices-Progress and Prospects,” *IEEE Ultrasonics Symposium*, pp. 120–129, 2007.

[37] J. Kaitila, M. Ylilammi, J. Ella, and R. Aigner, “Spurious Resonance Free Bulk Acoustic Wave Resonators,” *IEEE Ultrasonics Symposium*, pp. 84–87, 2003.

[38] K. Kashiwa, T. Omori, K.-y. Hashimoto, and M. Yamaguchi, “Improvement of Detection System for a Fast-Scanning and Phase-Sensitive Laser Probe for Surface Acoustic Wave Devices in 2 GHz Range,” *Japanese Journal of Applied Physics*, vol. 47, pp. 4108–4110, May 2008.

[39] R. A. Kline, and D. Hashemi, “ Ultrasonic guided-wave monitoring of fatigue damage development in bonded joints,” *Materials Evaluation*, vol. 45, 1987.

[40] J. V. Knuuttila, P. T. Tikka, and M. M. Salomaa, “Scanning Michelson interferometer for imaging surface acoustic wave fields,” *Optics letters*, vol. 25, pp. 613–615, May 2000.

[41] M. Koshiba, S. Mitobe, and M. Suzuki, “Finite-Element Solution of Periodic Waveguides for Acoustic Waves,” *IEEE Transactions on Ultrasonics, Ferroelectrics and Frequency Control*, vol. 34, no. 4, pp. 472–477, 1987.

[42] R. Krimholtz, D. Leedom, and G. Matthaei, “New equivalent circuits for elementary piezoelectric transducers,” *Electronics Letters*, vol. 6, no. 13, pp. 398–399, 1970.

[43] T. Kundu and K. Maslov, “Material interface inspection by Lamb waves,” *International Journal of Solids and Structures*, vol. 34, no. 29, pp. 3885–3901, 1997.

[44] K. Lakin, “Fundamental properties of thin film resonators,” *Proceedings of the 45th Annual Symposium on Frequency Control*, pp. 201–206, 1991.

[45] K. Lakin, “Modeling of thin film resonators and filters,” *1992 IEEE Microwave Symposium Digest MTT-S*, pp. 149–152, 1992.

[46] K. M. Lakin, “Numerical analysis of two dimensional thin film resonators,” *IEEE International Frequency Control Symposium*, pp. 502–508, 1993.

[47] K. M. Lakin, “Thin film resonator technology,” *IEEE 2003 FCS-EFTF Paper Wel A-4*, May 2003.

[48] K. M. Lakin, “Thin film resonator technology,” *IEEE Transactions on Ultrasonics, Ferroelectrics and Frequency Control*, vol. 52, pp. 707–716, May 2005.

[49] K. Lakin, “ Background and history,” in *RF Bulk Acoustic Wave Filters For Communications*, K. Hashimoto, Ed., Boston: Artech House, 2009.

[50] K. Lakin, “ Resonator and filter topologies,” in *RF Bulk Acoustic Wave Filters For Communications*, K. Hashimoto, Ed., Boston: Artech House, 2009.

[51] K. Lakin, J. Belsick, J. McDonald, and K. McCarron, “Improved Bulk Wave Resonator Coupling Coefficient For Wide Bandwidth Filters,” *IEEE Ultrasonics Symposium*, pp. 827–831, 2001.

[52] K. Lakin, K. McCarron, and R. E. Rose, “Solidly mounted resonators and filters,” *IEEE Ultrasonics Symposium*, pp. 905–908, 1995.

[53] K. M. Lakin and K. G. Lakin, “Numerical Analysis Of Thin Film BAW Resonators,” *IEEE Ultrasonics Symposium*, pp. 74–79, 2003.

[54] K. Lakin and J. Wang, “UHF Composite Bulk Wave Resonators,” *IEEE Ultrasonics Symposium*, pp. 834–837, 1980.

[55] K. Lakin, J. Wang, G. Kline, A. Landin, Y. Chen, and J. Hunt, “Thin film resonators and filters,” *IEEE Ultrasonics Symposium*, pp. 466–475, 1982.

[56] K. Lakin, J. Wang, and A. Landin, “Aluminum Nitride Thin Film and Composite Bulk Wave Resonators,” *IEEE International Frequency Control Symposium*, pp. 517–524, 1982.

[57] R. Lanz, “Piezoelectric thin films for Bulk Acoustic Wave Resonator applications: From processing to microwave,” Ph.D. dissertation, Ecole Polytechnique Fédérale, Lausanne, Suisse, 2004.

[58] J. D. Larson III, R. Ruby, and P. Bradley, “Bulk Acoustic Wave Resonators with Improved Lateral Mode Suppression,” U. S. Patent 6,215,375 B1, Apr. 2001.

[59] J. D. Larson III, P. D. Bradley, S. Wartenberg, and R. C. Ruby, “Modified Butterworth-Van Dyke Circuit for FBAR Resonators and Automated Measurement System,” *IEEE Ultrasonics Symposium*, pp. 863–868, 2000.

[60] J.-h. Lee, C.-m. Yao, K.-y. Tzeng, C.-w. Cheng, and Y.-c. Shih, “Optimization of Frame-like Film Bulk Acoustic Resonators for Suppression of Spurious Lateral Modes Using Finite Element Method,” *IEEE Ultrasonics Symposium*, pp. 278–281, 2004.

[61] S.-H. Lee, K. H. Yoon, and J.-K. Lee, “Influence of electrode configurations on the quality factor and piezoelectric coupling constant of solidly mounted bulk acoustic wave resonators,” *Journal of Applied Physics*, vol. 92, no. 7, pp. 4062–4069, 2002.

[62] R. Lerch, “Simulation of piezoelectric devices by two- and three-dimensional finite elements,” *IEEE Transactions on Ultrasonics, Ferroelectrics and Frequency Control*, vol. 37, pp. 233–247, Jan. 1990.

[63] A. Link, E. Schmidhammer, H. Heinze, M. Mayer, M. Schmiedgen, B. Bader, K. Wagner, and R. Weigel, “Suppression of Spurious Modes in Mirror-Type Thin Film BAW Resonators Using an Appropriate Shape of the Active Area,” *IEEE Ultrasonics Symposium*, pp. 1179–1182, 2005.

[64] M. Lowe, “Matrix techniques for modeling ultrasonic waves in multilayered media,” *IEEE Transactions on Ultrasonics, Ferroelectrics and Frequency Control*, vol. 42, pp. 525–542, July 1995.

[65] B. Y. R. Madariaga, “Dynamics of an expanding circular fault,” *Bulletin of the Seismological Society of America*, vol. 66, no. 3, pp. 639–666, 1976.

[66] T. Makkonen, A. Holappa, J. Ellä, and M. M. Salomaa, “Finite element simulations of thin-film composite BAW resonators,” *IEEE Transactions on Ultrasonics, Ferroelectrics and Frequency Control*, vol. 48, pp. 1241–1258, Sept. 2001.

[67] T. L. Mansfield, “ Lamb wave inspection of aluminum sheet,” *Material Evaluation*, pp. 96–100, 1975.

[68] S. Marksteiner, J. Kaitila, G. G. Fattinger, and R. Aigner, “Optimization of Acoustic Mirrors for Solidly Mounted BAW Resonators,” in *IEEE Ultrasonics Symposium*, pp. 329–332, 2005.

[69] K. Maslov and T. Kundu, “Selection of Lamb modes for detecting internal defects in composite laminates,” *Ultrasonics*, vol. 35, pp. 141–150, 1997.

[70] W.P. Mason, *Physical Acoustics and the Properties of Solids*, New York: D. Van Nostrand Co, 1958.

[71] J. Meltaus, T. Pensala, and K. Kokkonen, "Modelling of 2-D lateral modes in solidly-mounted BAW resonators," *2008 IEEE International Ultrasonics Symposium*, pp. 1544–1547, Nov. 2008.

[72] R. F. Milsom, H.-p. Löbl, and C. Metzmacher, "Simulation of second-order effects in SBAR and FBAR," *Second International Symposium on Acoustic Wave Devices for Future Mobile Communication System*, pp. 145–156, 2004.

[73] R. F. Milsom, H.-p. Löbl, C. Metzmacher, P. Lok, A. Tuinhout, and F. V. Straten, "2D model of solidly-mounted and membrane BAW devices," *IEEE Ultrasonics Symposium*, pp. 1802–1807, 2003.

[74] R. F. Milsom, H.-p. Löbl, F. Vanhelmont, A. B. M. Jansman, J.-w. Lobeek, and A. Tuinhout, "Comparison of Mode-Conversion , Energy-Trapping and Lateral Acoustic Coupling in FBAR and SBAR," *IEEE MTT-S International Microwave Symposium Digest*, pp. 229–232, 2005.

[75] A. Miyamoto, S.-i. Wakana, and A. Ito, "Novel optical observation technique for shear horizontal wave in SAW resonators on 42° YX-cut lithium tantalate," *IEEE Ultrasonics Symposium*, pp. 89–92, 2002.

[76] R. Monkhouse, P. Wilcox, and P. Cawley, "Flexible interdigital PVDF transducers for the generation of Lamb waves in structures," *Ultrasonics*, vol. 35, pp. 489–498, Nov. 1997.

[77] B. Morvan, A. Tinel, and J. Duclos, "Coupling of Lamb waves at a tee junction," *IEEE Ultrasonics Symposium*, pp. 565–568, 1999.

[78] B. Morvan, N. Wilkie-Chancellier, H. Duflo, A. Tinel, and J. Duclos, "Lamb wave reflection at the free edge of a plate," *Journal of the Acoustical Society of America*, vol. 113, no. 3, p. 1417, 2003.

[79] K. Nakamura, H. Sasaki, and H. Shimizu, "A Piezoelectric Composite Resonator Consisting of a ZnO Film on an Anisotropically Etched Silicon Substrate," *Japanese Journal of Applied Physics*, vol. 20, pp. 111–114, 1980.

[80] D. E. Newland, *An introduction to random vibrations and spectral analysis*, Longman Scientific & Technical, Wiley, 1984.

[81] T. Omori, Y. Tanaka, K. Hashimoto, and M. Yamaguchi, "Synthesis of Frequency Response for Wideband SAW Ladder Type Filters," *2007 IEEE Ultrasonics Symposium Proceedings*, pp. 2574–2577, Oct. 2007.

[82] W. Pang, R. C. Ruby, R. Parker, P. W. Fisher, M. A. Unkrich, and J. D. Larson III, "A Temperature-Stable Film Bulk Acoustic Wave Oscillator," *IEEE Electron Device Letters*, vol. 29, no. 4, pp. 315–318, 2008.

[83] T. Pensala and M. Ylilammi, "Spurious resonance suppression in gigahertz-range ZnO thin-film bulk acoustic wave resonators by the boundary frame method: modeling and experiment," *IEEE Transactions on Ultrasonics, Ferroelectrics and Frequency Control*, vol. 56, pp. 1731–1744, Aug. 2009.

[84] A. F. Peterson, S. L. Ray, and R. Mittra, *Computational Methods for Electromagnetics*, Piscataway, NJ: IEEE Press, 1998.

[85] W. H. Press, *Numerical recipes: The art of scientific computing*, 3rd ed., Cambridge University Press, 2007.

[86] A. Reinhardt, S. Ballandras, and V. Laude, "Simulation of transverse effects in FBAR devices," *IEEE MTT-S International Microwave Symposium Digest*, pp. 237–240, 2005.

[87] A. Reinhardt, V. Laude, M. Solal, S. Ballandras, and W. Steichen, "Investigation of spurious resonances in Thin Film Bulk Acoustic Wave Resonators," *IEEE International Ultrasonics, Ferroelectrics, and Frequency Control Joint 50th Anniversary Conference*, pp. 1698–1701, 2004.

[88] V. M. Ristic, *Principles of Acoustic Devices*, New York: Wiley, 1983.

[89] W. P. Rogers, " Elastic property measurement using Rayleigh-Lamb waves," *Research in Nondestructive Evaluation*, vol. 6, no. 4, pp. 185–208, Dec. 1995.

[90] J. L. Rose, *Ultrasonic waves in solid media*, Cambridge University Press, 1999.

[91] D. Rosén, J. Bjurström, and I. Katardjiev, "Suppression of spurious lateral modes in thickness-excited FBAR resonators," *IEEE Transactions on Ultrasonics, Ferroelectrics and Frequency Control*, vol. 52, pp. 1189–1192, July 2005.

[92] J. F. Rosenbaum, *Bulk Acoustic Wave Theory and Devices*, Boston, M.A.: Boston: Artech House, 1988.

[93] R. Rosenfeld, “Surface Acoustic Wave (SAW) Bandpass Filter Review,” *33rd Annual Symposium on Frequency Control*, pp. 220–222, 1979.

[94] R. R. Rowland, and W. Lichodziejewski, “ Lamb wave bond inspection,” *Material Evaluation*, vol. 31, no. 2, 1973.

[95] D. Royer, *Elastic Waves in Solids I*, Berlin, Germany: Springer-Verlag, 2000.

[96] R. Ruby, “Review and Comparison of Bulk Acoustic Wave FBAR , SMR Technology,” *IEEE Ultrasonics Symposium*, pp. 1029–1040, 2007.

[97] R. Ruby, “ FBAR Resonators and Filters,” in *RF Bulk Acoustic Wave Filters For Communications*, K. Hashimoto, Ed., Boston: Artech House, 2009.

[98] R. Ruby, “A decade of FBAR success and what is needed for another successful decade,” *2011 IEEE Symposium on Piezoelectricity, Acoustic Waves and Device Applications (SPAWDA)*, pp. 365–369, 2011.

[99] R. Ruby, P. Bradley, J. Larson III, and Y. Oshmyansky, “PCS 1900 MHz duplexer using thin film bulk acoustic resonators (FBARs),” *Electronics Letters*, vol. 35, no. 10, pp. 794–795, 1999.

[100] R. Ruby, P. Bradley, J. Larson III, Y. Oshmyansky, and D. Figueredo, “Ultra-Miniature High-Q Filters and Duplexers Using FBAR Technology,” *2001 IEEE International Solid-State Circuits Conference*, pp. 120–121, 2001.

[101] R. C. Ruby, P. Bradley, Y. Oshmyansky, A. Chien, and J. D. Lason III, “Thin Film Bulk Wave Acoustic Resonators (FBAR) for Wireless Applications,” *IEEE Ultrasonics Symposium*, pp. 813–821, 2001.

[102] R. Ruby, R. S. Fazzio, H. Feng, and P. D. Bradley, “Acoustic resonator performance enhancement using alternating frame structure,” U. S. Patent 2006/0071736 A1, Apr. 2006.

[103] R. Ruby, M. Small, F. Bi, D. Lee, L. Callaghan, R. Parker, and S. Ortiz, “Positioning FBAR technology in the frequency and timing domain,” *IEEE Transactions on Ultrasonics, Ferroelectrics and Frequency Control*, vol. 59, pp. 334–345, Mar. 2012.

[104] C. T. Schröder, “ On the interaction of elastic waves with buried land mines: An investigation using the finite-difference time-domain method ,” Ph.D. dissertation, School Elect. Comput. Eng., Georgia Inst. Technol., Atlanta, GA, 2001.

[105] C. T. Schröder and W. R. Scott, Jr., “A finite-difference model to study the elastic-wave interactions with buried land mines,” *IEEE Trans. on Geoscience and Remote Sensing*, vol. 38, no. 4, pp. 1505–1512, Jul. 2000.

[106] S. Sherrit, S. Leary, B. Dolgin, and Y. Bar-Cohen, “Comparison of the Mason and KLM equivalent circuits for piezoelectric resonators in the thickness mode,” *IEEE Ultrasonics Symposium*, pp. 921–926, 1999.

[107] B. K. Sinha, Q. H. Liu, and S. Kostek, “Acoustic waves in pressurized boreholes: a finite-difference formulation,” *J. Geophysical Research*, vol. 101, no. B11, pp. 25173–25180, Nov. 1996.

[108] J. E. A. Southin and R. W. Whatmore, “Finite element modelling of nanostructured piezoelectric resonators (NAPIERs),” *IEEE Transactions on Ultrasonics, Ferroelectrics and Frequency Control*, vol. 51, pp. 654–662, June 2004.

[109] J. T. Stewart and Y.-K. Yong, “Exact analysis of the propagation of acoustic waves in multilayered anisotropic piezoelectric plates,” *IEEE International Frequency Control Symposium*, pp. 476–501, 1993.

[110] Z. Su, L. Ye, and Y. Lu, “Guided Lamb waves for identification of damage in composite structures: A review,” *Journal of Sound and Vibration*, vol. 295, pp. 753–780, Aug. 2006.

[111] A. Taflove and S. C. Hagness, *Computational Electrodynamics: The Finite-Difference Time-Domain Method*, 3rd ed., Norwood, MA: Artech House, 2005.

[112] K. Telschow, V. Deason, D. Cottle, and J. Larson, “UHF acoustic microscopic imaging of resonator motion,” *IEEE Ultrasonics Symposium*, pp. 631–634, 2000.

[113] K. L. Telschow, V. A. Deason, D. L. Cottle, and J. D. Larson III, “Full-field imaging of Gigahertz film bulk acoustic resonator motion,” *IEEE Transactions on Ultrasonics, Ferroelectrics and Frequency Control*, vol. 50, pp. 1279–1285, Oct. 2003.

[114] R. Thalhammer, R. Aigner, I. Technologies, and O. H. Ring, “Energy loss mechanisms in SMR C type BAW devices,” *IEEE MTT-S International Microwave Symposium Digest*, pp. 225–228, 2005.

[115] R. Thalhammer, J. Kaitila, R. Aigner, S. Marksteiner, I. Technologies, and O. H. Ring, “Prediction of BAW resonator performance using experimental and numerical methods,” *IEEE Ultrasonics Symposium*, pp. 282–285, 2004.

[116] R. Thalhammer, J. Kaitila, S. Zieglmeier, and L. Elbrecht, "Spurious Mode Suppression in BAW Resonators," *IEEE Ultrasonics Symposium*, pp. 456–459, 2006.

[117] F. Thalmayr, " Wave scattering analysis as approach for improved BAW resonator design," Ph.D. dissertation, Chiba University, Chiba, Japan, 2010.

[118] F. Thalmayr, K.-y. Hashimoto, T. Omori, and M. Yamaguchi, "Power deduction from surface fields in multilayer waveguides," *IEEE Transactions on Ultrasonics, Ferroelectrics and Frequency Control*, vol. 57, pp. 405–411, Jan. 2010.

[119] F. Thalmayr, K.-Y. Hashimoto, T. Omori, and M. Yamaguchi, "Frequency domain analysis of lamb wave scattering and application to film bulk acoustic wave resonators," *IEEE Transactions on Ultrasonics, Ferroelectrics and Frequency Control*, vol. 57, pp. 1641–1648, July 2010.

[120] F. Thalmayr, K.-y. Hashimoto, M. Ueda, T. Omori, and M. Yamaguchi, "Quantitative Analysis of Power Leakage in an Film Bulk Acoustic Resonator Device at the Antiresonance Frequency," *Japanese Journal of Applied Physics*, vol. 49, p. 07HD11, July 2010.

[121] P. J. Torvik, "Reflection of wave trains in semi-infinite plates," *Journal of the Acoustical Society of America*, vol. 41, no. 2, pp. 346–353, 1967.

[122] J. Tsutsumi, M. Iwaki, Y. Iwamoto, and T. Yokoyama, "A Miniatuirized FBAR Duplexer with Reduced Acoustic Loss for the W-CDMA Applicaion," *IEEE Ultrasonics Symposium*, pp. 93–96, 2005.

[123] M. Ueda, T. Nishihara, S. Taniguchi, T. Yokoyama, J. Tsutsumi, M. Iwaki, and Y. Satoh, "Film Bulk Acoustic Resonator using High-Acoustic-Impedance Electrodes," *Japanese Journal of Applied Physics*, vol. 46, pp. 4642–4646, July 2007.

[124] J. S. Wang and K. M. Lakin, "Sputtered AlN films for Bulk-Acoustic-Wave Devices," *IEEE Ultrasonics Symposium*, pp. 502–505, 1981.

[125] K. Y. Wong and W. Y. Tam, " Analysis of the frequency response of SAW filters using finite-difference time-domain method," *IEEE Trans. on Microwave Theory and Techniques*, vol. 53, no. 11, pp. 3364–3370, Nov. 2005.

[126] D. C. Worlton, " Ultrasonic testing with Lamb waves," *Non-destructive Testing 15*, pp. 218–222, 1957.

[127] N. Wu, K.-y. Hashimoto, K. Kashiwa, T. Omori, and M. Yamaguchi, "Study on the Frequency Dependence of Lateral energy leakage in RF BAW device by fast-scanning laser probe system," *IEEE International Ultrasonics Symposium*, pp. 94–97, 2008.

[128] W. X. Yang and W. Y. Tam, "Spurious Wave Suppression in BAW Resonators with Frame-like Airgap," *IEEE International Frequency Control Symposium*, pp. 656–660, 2010.

[129] K. S. Yee, "Numerical solution of initial boundary value problems involving Maxwells equations in isotropic media," *IEEE Transactions on Antennas and Propagation*, vol. AP-14, no. 8, pp. 302–307, 1966.

[130] Y. Q. Zeng and Q. H. Liu, "Acoustic detection of buried objects in 3-D fluid saturated porous media: numerical modeling," *IEEE Trans. Geoscience and Remote Sensing*, vol. 39, no. 6, pp. 1165–1173, Jun. 2001.

[131] Q. Zou, D. Lee, F. Bi, R. Ruby, M. Small, S. Ortiz, Y. Oshmyansky, and J. Kaitila, "High coupling coefficient Temperature compensated FBAR resonator for oscillator application with wide pulling range," *IEEE International Frequency Control Symposium*, pp. 646–651, June 2010.

[132] European Patent: EP1317797B1.

[133] "*IEEE Standard on Piezoelectricity*," ANSI/IEEE Std. 176-1987.